RIKAGAKU KENKYUSHO
the Institute of Physical and Chemical Research
Wako-shi, Saitama Pref., JAPAN

'70

IPCR cyclotron Progress Report 1970

Vol. 4

Edited by Administration Committee of the IPCR Cyclotron

IPCR Cyclotron Progress Report 1970

Vol. 4

The Institute of Physical and Chemical Research
"RIKAGAKU KENKYUSHO" Wako-shi, Saitama, 351 JAPAN
December, 1970

This volume contains recent information of the IPCR Cyclotron, informal reports and abstracts of papers which will be published at scientific meetings or in publications by staff members, guests, and visitors.

All rights reserved. This report or any part thereof may not be reproduced in any form (including photostatic or microfilm form) without written permission from the publisher.

CONTENTS

1. INTRODUCTION

Eight years ago, the construction of our cyclotron was started, which may be compared to planting a young fruit-tree. Five years later, the cyclotron was completed and experiments using it were begun. Since then the fruit-tree has grown up gradually in these three years, and now we can say that we could have a good harvest of nice fruits.

Last year, we succeeded in making stable operation of heavy ion source and this year we obtained many important results using heavy ions. They are charge exchange of heavy-ion by colliding with gas molecules, nuclear transfer reactions, LET effect and irradiation effect on bacteria and chemical systems by heavy-ion bombardments.

Alpha particles and heavy-ions were used for elastic scattering by nuclei and also for production of new elements and many isomers. The g-factor measurements of isomer of ^{42}Ca, ^{90}Zr, ^{208}Pb, and ^{210}Po gave fundamental and interesting results for nuclear physics. Spin-flip reactions in Fe by protons were also measured. We ascertained nuclear fission of light elements by charged particles which can be used in the tracer techniques.

Artificially produced ^{61}Ni and ^{119}Sb were used for study of the Mösbauer effect, obtaining several important results in magnetism and radio-chemistry.

Many improvements were made in the cyclotron and measuring appratuses for nuclear physics and some studies have started for an expected new accelerator in this institute.

The above mentioned studies were mostly performed by the research workers of this institute, but certain researches have been performed by the outside people using our cyclotron. Machine time of two days per month is allotted to the outside people for irradiation and RI production. Irradiation is being used for example, in the tests of materials for nuclear breeder reactor, irradiation of semiconductors, activation analysis and neutron irradiation of tissues. ^{18}F, ^{52}Fe, ^{111}In, ^{26}Al, and other about 10 species of radio isotopes were produced and applied successfully in medicine and nuclear physics.

H. Kumagai

Hiroo Kumagai, Chairman
Administration Committee of
the IPCR Cyclotron

2. MACHINE OPERATION

During these four years the IPCR cyclotron was operated by a 24 h per day system without any serious fault. An overhaul was done in Jan. 1970. The movable liner was reconstructed[1] and thenceforth the range of beam energy has been changed as shown in Table 1.

With a new liner the stability of the cyclotron was improved owing to the reduction of vacuum discharge. The increase of maximum R-F frequency extended the upper limit of particle energies and the beam of O^{4+} was also used for experiments. It is noted that a beam of triton of about 20 MeV was successfully accelerated. The closed gas system including the ion source and the cyclotron itself was adopted. A careful system for the evacuation of tritium and the monitoring system of residual tritium activity were tested as described in this report.

Fig. 1 shows the actual operation obtained from the operation diary. Diverse kinds of particles and energies were present. The change of energies was so frequent, in some cases, six times a day. The beam extraction efficiency ranged from 40 % to 10 % depending on the operating conditions. It seemed that the best condition was not always realized when the particle or the energy was changed. The entrance part of the septum tungsten and the graphite part of the puller[2] was repaired in a period of about two months to keep the cyclotron in a better condition. The bad extraction efficiency is considered to be due to mismatching of the cyclotron resonance beam with the setting of the beam transport system, and the beam intensity of light ions is now limited by the heat loss at about 1.5 kW at the entrance part of the septum.

The machine time of 235 days was scheduled in the period from Nov. 24th, 1969 to Nov. 23rd, 1970. Any fault which needed a repair time of more than one day has not been found during this period. The integrated loss of machine time owing to small damages of some cyclotron components was less than 5 days. The actual machine operating time is shown in Table 2. This table is very much similar to that of the last Progress Report. This fact shows that the cyclotron is working very steadily.

During five months from March to August, the number of operators was decreased to five, which forced us to reduce the scheduled machine time. The reserved days were used for the repair of cyclotron components or the arrangement of beam transport system.

The scheduled subjects of machine time is listed in Table 3. No marked difference is found in comparison with that of 1969. There was some increase of machine time for the in-beam spectroscopy, i.e., for the measurement of magnetic moment of excited states. The demands for RI production from other organizations was so strong that the machine time for this purpose also increased to fulfill the requests only partly. On the contrary, the machine time for the radio chemistry has decreased. The main reason is that the machine worked so steadily because a short time use of the machine became efficient.

The authors are indebted to Y. Miyazawa and T. Karasawa for their information of the cyclotron operation condition.

(the editor)

Table 1. Machine operation time.

Indication of working time meter		
	Oscillator input power	Ion source input power
Nov. 21, 1969	2458.9 (h)	3594.5 (h)
Nov. 18, 1970	7539.1 (h)	9166.6 (h)
~ 8690 (h)	5080.2 (h) (58.4 %)	5572.1 (h) (64.5 %)

Schedule for this year (365 days)	
Scheduled machine time	235 (days)
Scheduled time for overhaul and installation	40 (days)
Vacation, holidays, and sundays	90 (days)

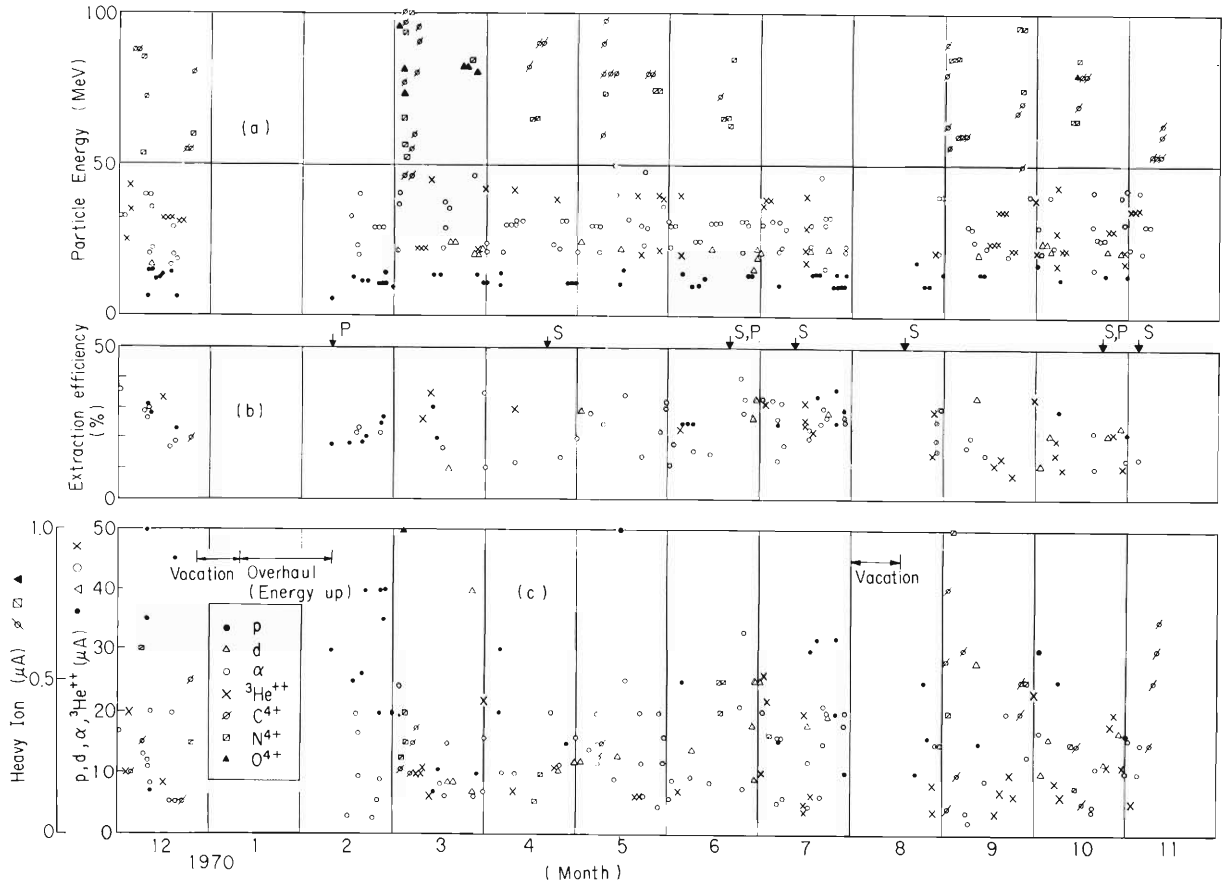

(a) Particle energies used for experiments.
(b) Beam extraction efficiency.
(the ratio of deflected beam current at 85 cm radius to that at 65 cm radius)
(c) Deflected beam currents which were actually employed in experiments.

Fig. 1. Plot obtained from the operation diary.
In the figure the arrows represent the repair of septum (S) or puller (P).

Table 2.

	Before the reconstruction of the liner	With the new liner
P	2.8 ~ 16 MeV	4 ~ 17.5 MeV
$^3He^{++}$	8.3 ~ 48	12 ~ 50
d	5.6 ~ 23	8 ~ 25
α	11 ~ 48	16 ~ 50
C^{4+}	39 ~ 95	48 ~ 100
N^{4+}	45 ~ 95	56 ~ 100
O^{4+}		70 ~ 95

Table 3. Scheduled machine time.

Period V, Nov. 24th, 1969 ~ Nov. 23th, 1970

Subject	Days	Percent
Heavy ion reaction	16.0 (14.0)	54.5 % (51.5 %)
Direct reaction	69.3 (66.5)	
In-beam spectroscopy	34.0 (28.0)	
RI production for nuclear spectroscopy	8.8 (11.0)	
Radiochemistry and RI production	11.1 (19.0)	22.9 % (26.5 %)
Radiation chemistry and radiation biology	20.0 (21.0)	
Solid state physics	19.5 (17.0)	
Analysis of nuclide	3.1 (4.5)	
Accelerator physics and machine improvement	14.3 (22.5)	17.1 % (19.0 %)
Experiments of charge exchange	6.9 (5.5)	
Machine inspection and repair	12.0 (16.0)	
Reserved for the machine time adjustment	7.0 (0)	
RI production for other organizations	13.0 (7.0)	5.5 % (3.0 %)
	235	

(Numbers in parenthesis are the figures in the Period IV from Nov. 1968 to Nov. 1969)

References

1) M. Odera : IPCR Cyclotron Progr. Rep., 4, 24 (1970).

2) Y. Miyazawa, T. Tonuma, A. Shimamura, T. Inoue, and T. Karasawa : IPCR Cyclotron Progr. Rep., 3, 4 (1969).

3. MACHINE DEVELOPMENT AND ACCELERATOR PHYSICS

3-1. Improvement of Radio-Frequency System
Increase of Resonant Frequency and Energy of Proton Beam

M. Odera, Y. Miyazawa, and O. Terajima

In the IPCR cyclotron designed as a multiparticle machine, the low resonant frequency which is necessary to accelerate heavy ions is obtained by a pair of movable liners above and below the dee. Originally removable of the liners to get higher frequency than 12 MHz was intended in case of acceleration of proton above 16 MeV. However, when routine operation of the cyclotron was started, the movable liner system was found very convenient in tuning the machine. Removable of the liners will necessiate change of present prescription of operation established. Other means must be devised to get higher resonant frequency without introducing much complexity in machine control.

Firstly, the movable liner was modified. As shown in Fig. 1, the cooling pipe was soldered to the dee side of the liner. Formerly the pipe was hidden from the dee to avoid high electric field at the pipe and hence sparking. But breakdown seems to occur at the places where a stronger field singularity exists such as dusts or scratches on the surface. Really, we have experienced a larger voltage holding capability of the new liners than older ones. Perhaps, dusts sent back by sparking has a small probability to settle in the concave parts of the pipe where the electric field is weak, whereas in the old liner of plane surface, the chance of escape of dusts from high electric field is small. On the other hand, concentration of field on the pipe surface means smaller decrease of dee capacity than calculated from the dee liner distance and pipe area. Measurement of resonant frequency yielded increase of maximum frequency by about 500 kHz. The increase corresponds to widening of a dee-liner gap of about 7 mm, though from a simple geometrical consideration the increase of about 9 mm can be expected assuming perfectly flat finish of surface of pipe and valley. Fig. 2 shows the new liners before installation between poles of the magnet. 17.5 MeV proton was obtained and extracted soon after the operation was resumed in February of this year.

Next, decrease of the volume of resonant cavity at the shorting plane was planned. For small perturbation at the boundary of a cavity the frequency can be expressed by

$$\omega^2 = \omega_a^2 \left\{ 1 + \int (H_a^2 - E_a^2)\, dv \right\}$$

where ω_a, H_a and E_a are the frequency, magnetic and electric field strengths for the concerned radiofrequency mode before the perturbation is applied. Integration is to be made over the volume which is removed. From this formula it is found that the increase of frequency of about 8 % is possible by suitably deforming the shorting plane. As coupling loops to the oscillator tube exist directly in front of the shorting plane at its foremost position, deformation must be made in a somewhat complex manner. C-shaped boxes made of copper plates were manufactured and attached to the shorting device. Fig. 3 shows its dimensions and relative configuration with the coupling loops. Fig. 4 is its photograph. Resonant frequency increased to nearly 13.5 MHz corresponding to 20 MeV of proton energy. Q value decreased moderately as expected but the oscillator was powerful enough to supply the loss. Removal or attaching of the copper box is

relatively easy. In Fig. 5 the resonant frequencies with the old and the new liners and with the boxes attached are compared.

At the end of overhauling period in Aug. 1970 the test operation with these boxes was made. However, after letting the acceleration chamber open for several days in the atmosphere of high humidity, vacuum sparking was severe. Proton energy of 18.5 MeV was the maximum at the end of the test run. In a better vaccum condition attainment of higher energy will be possible because low voltage operation at higher frequency is stable and it seems that out-gassing has prevented the higher level oscillation.

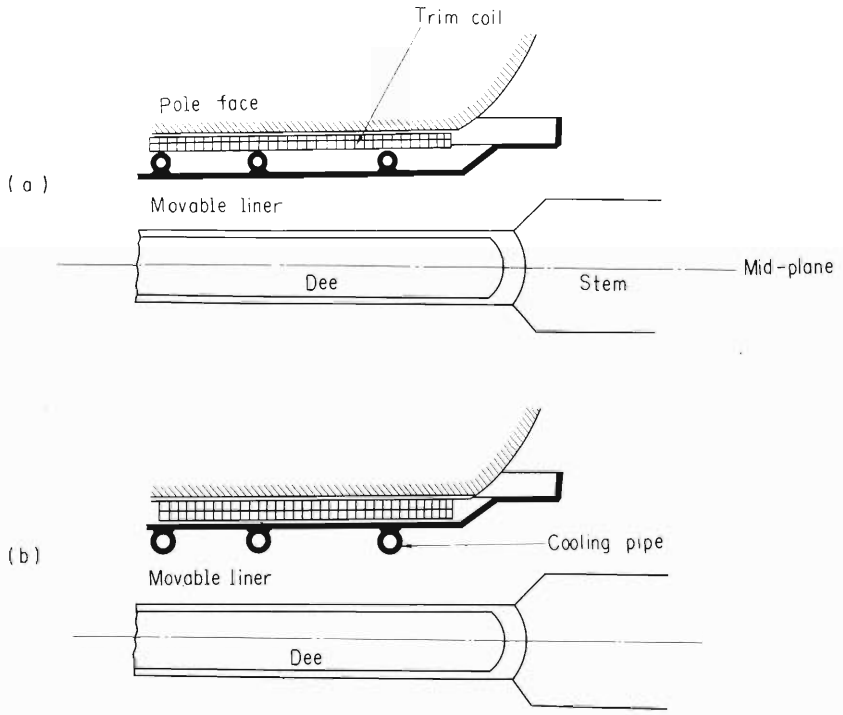

(a) Original configuration of the dee-liner system.

(b) Configuration of modified movable liner.

Fig. 1. Structure of movable liner.

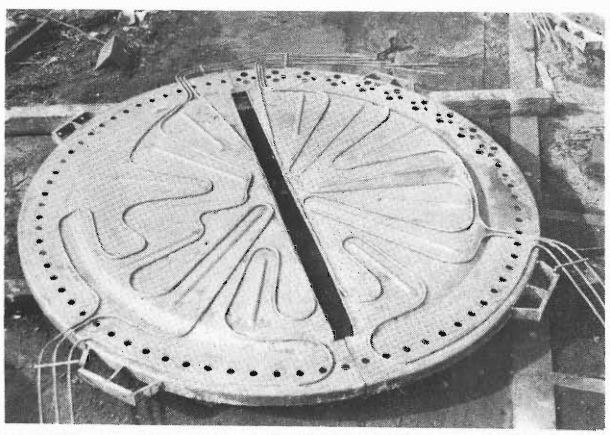

Fig. 2. Photograph of liner.

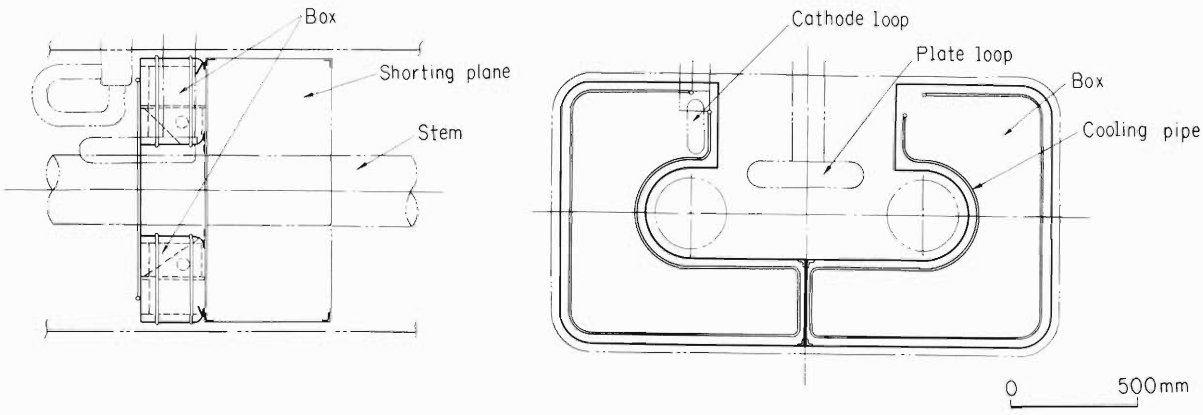

Fig. 3. Structure of the box to be attached to the shorting plane.

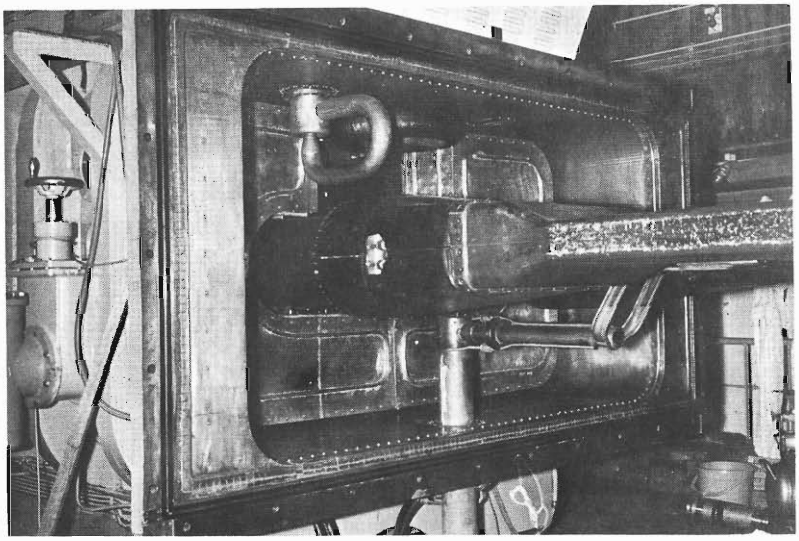

Fig. 4. Photograph of the box attached to the shorting plane.

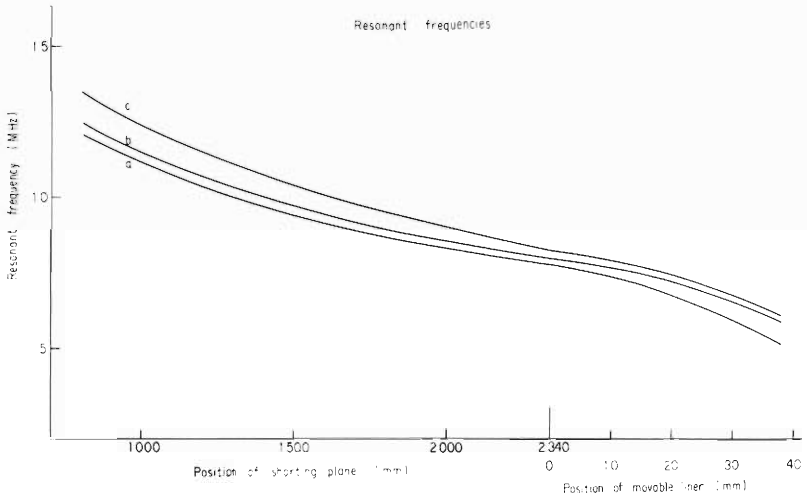

a. with old liners.

b. with new liners.

c. with new liners and deforming boxes.

Fig. 5. Resonant frequencies.

3-2. Improvement of Oscillator Power Supply

M. Odera and K. Ogiwara

It is well-known that stabilization of frequency and amplitude of accelerating radiofrequency voltage is prerequisite for successful operation of a cyclotron.

At present the frequency of our cyclotron is relatively stable after warming up of the radio frequency system and ripples of 100 and 300 Hz appearing in the amplitude envelope are objectionable. The percentage and form of ripple amplitude vary appreciably according to operating conditions suggesting interplay of several factors.

Fig. 1 shows a typical ripple waveform. The form was Fourier analyzed and

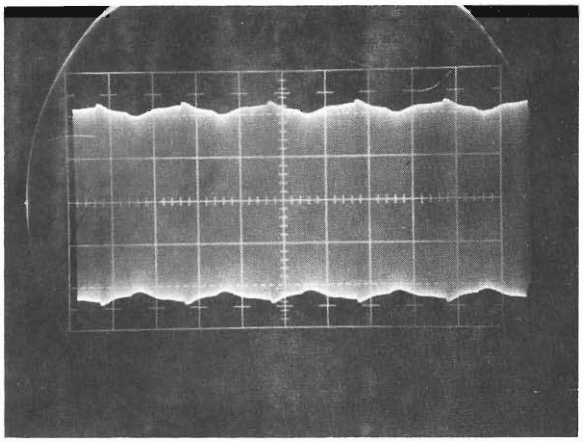

Fig. 1. Ripple waveform of r.f. envelope before filter improvement is made. Sweep 5 ms/cm, vertical 5 V/cm.

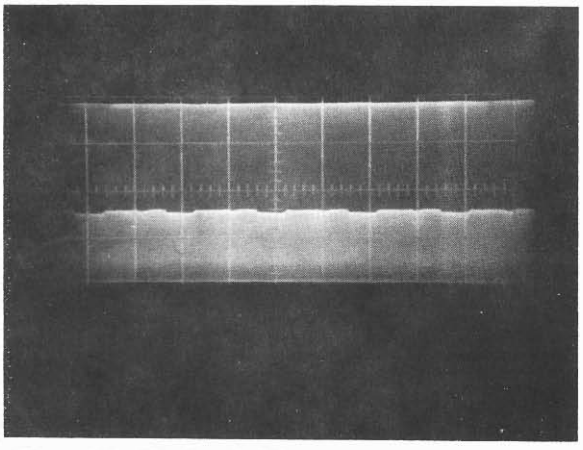

Fig. 3. R.f. ripple waveform after addition of 20 μF condenser to filter. Ion source off, oscillator filament DC heated, vertical 0.5 V/cm and 5 V/cm.

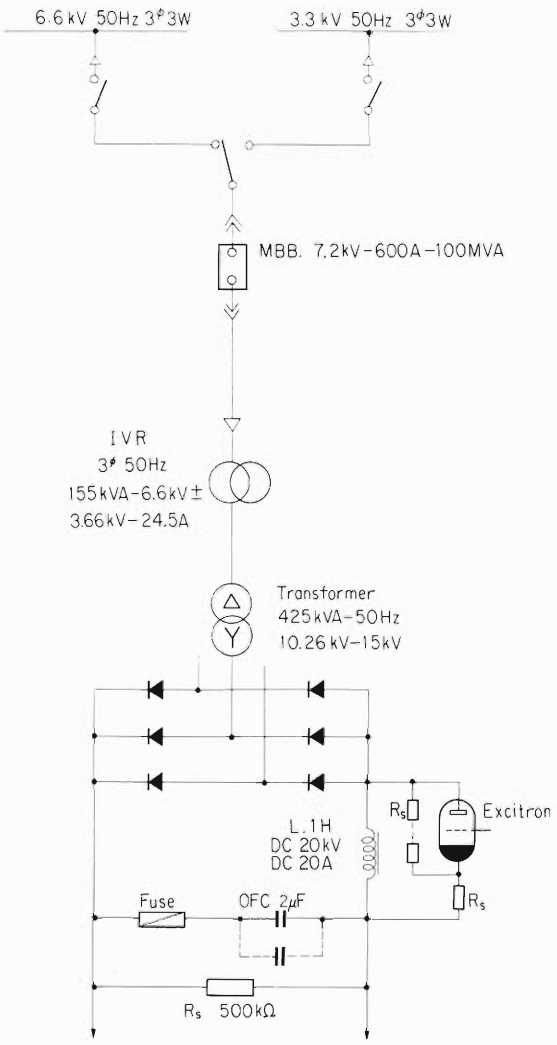

Fig. 2. Scheme of high voltage power supply.

percentage of each component was extracted. In the case of Fig. 1 the values are 6.95 % for 100 Hz, 2.4 % for 200 Hz, and 0.78 % for 300 Hz. As indicated in Fig. 2 the high voltage power supply is made of three-phase all-wave sillicon diode and has a relatively small-sized smoothing filter. Major part of 300 Hz must come from the power supply. 100 Hz component is to be expected from the oscillator filament heated by 50 Hz AC and small umbalance in the three phases of AC high voltage supply.

Ion source with its filament heated by three-phase all-wave rectified DC and single-phase all-wave rectified arc supply must also contribute 100 and 300 Hz components. This can be seen from change of shape of radio frequency envelope with and without arc "on". Since careful measurements of each phase of the induction-regulator and the step-up transformer revealed no essential defects in these elements and time-to-time fluctuations of balance of supply voltage and phase of each arm should be expected, improvement of ripple characteristics of the filter and DC heating of the oscillator filament were planned. A 20 μF oil-filled paper condenser was installed in Apr. 1970 in addition to a 2 μF one. Fig. 3 shows the ripple form at the dee cavity without arc and with the oscillator filament DC heated. Fig. 4 is the photograph when the tube filament is AC heated but the arc is off. Fig. 5 shows the effect of the ion source with the DC heated tube filament. In Fig. 6 combined ripples by AC heating filament and ion source working are indicated. These photographs show relative contributions of filament and ion source to the ripples of accelerating voltage separately.

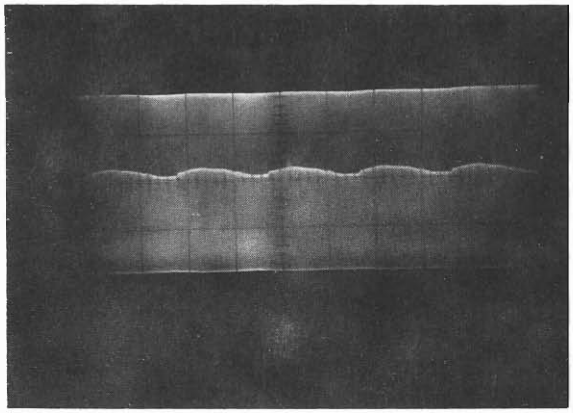

Fig. 4. R.f. ripple waveform. Ion source off, filament AC heated, vertical 0.5 V/cm and 5 V/cm.

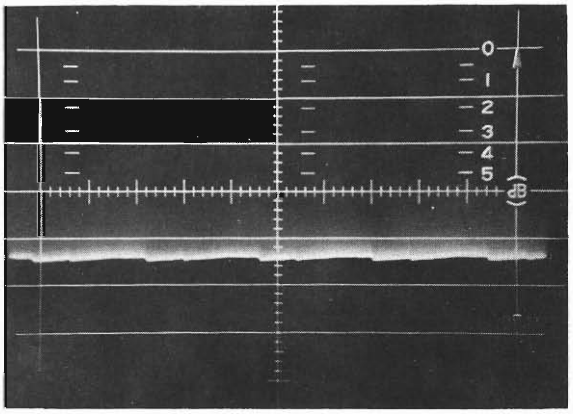

Fig. 5. R.f. ripple waveform. Ion source on, filament DC heated. vertical 0.5 V/cm.

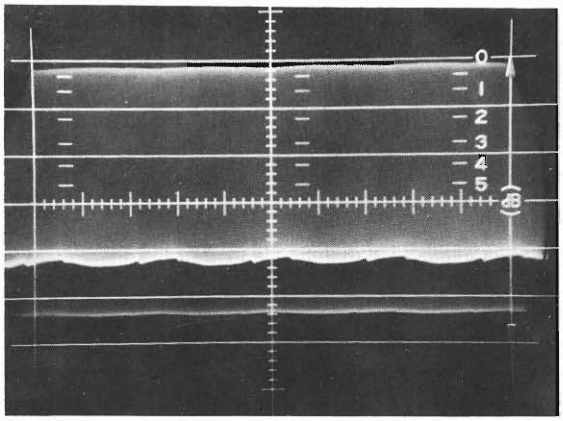

Fig. 6.

R.f. ripple waveform. Ion source on, filament AC heated. Upper and lower traces are waveforms to be compared with those of Fig. 1. Reduction of ripples can be seen. Vertical 0.5 V/cm and 5 V/cm.

3-3. Tritium Gas Circulation System for the Ion Source of Cyclotron and Monitoring of Tritium Gas

I. Kohno, A. Shimamura, I. Sakamoto, T. Tonuma,
S. Takeda, N. Nakanishi, K. Matsuda, K. Koda,
and T. Hamada

(1) Introduction

Tritium gas is supplied to the ion source in order to accelerate tritium ion by the cyclotron. As the tritium is a radioactive element (β-decay, E_{max} = 18 keV), it is necessary to prevent the gas from escaping to the atmosphere. Tritium gas should be, therefore, circulated in a closed system including the acceleration chamber of the cyclotron. This paper reports an outline of the circulation system of tritium gas, its operation, the acceleration of tritium ions and the results of contamination survey.

(2) Circulation system

Fig. 1 shows the circulation system of tritium gas, in which the gas is introduced between the valves V3 and V10 , with valves V3 , V10 , V17 being closed under operation of the circulating rotary pump. The flow rate of gas is controlled by the needle valve and supplied into the ion source. The gas flows through the circulating path (the broad line shown in the figure), with valves V1 , V11 , and V17 being closed during triton acceleration. The liquid nitorgen trap prevents H_2O, D_2O, and T_2O from circulation with the gas. The charcoal trap is used at room temperature which absorbs only a small amount of gas during acceleration. When the ion beam is guided to the beam transport system, the air valve V_N is operated in connection with the vacuum gauge in the focusing system and protects the circulation system against leakage of air.

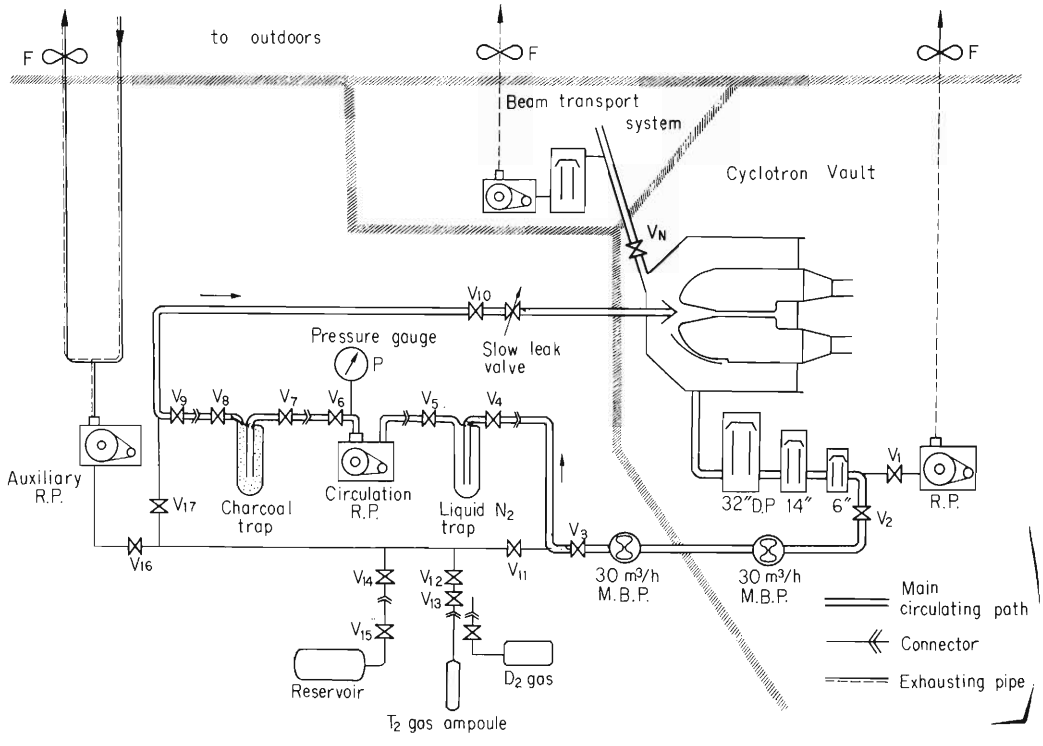

Fig. 1. Schematic diagram of the tritium circulation system.

After triton acceleration has been ended, tritium gas is recollected. The gas is collected in a space between the circulation pump and the closed valve V_{10}, and most of the gas is collected in a 5 ℓ reservoir by opening V_7, V_{14}, and V_{15}. Then the charcoal trap is cooled with liquid nitrogen and the valve V_{11} is opened. The residual gas is absorbed in the charcoal trap by circulating the gas in the closed path passing through the trap and the valve V_{11} by using the circulation pump. As 1_g of the charcoal absorbs tritium of 136 mℓ STP[1] at liquid nitrogen temperature, the charcoal of about 300 g in the trap can absorb 40 ℓ STP of tritium gas.

A very small amount of the residual tritium gas which is not absorbed by the charcoal trap is exhausted to outdoors using an auxiliary pump and a blower by closing V_{11} and opening V_{16}. A U-shaped PVC pipe of 50 ϕ in diameter and 10 m long on each side is placed from the circulation system to outdoors as shown in the Fig. 1. Both sides of the pipe are exposed to outdoors. And the blower placed at the outlet of the pipe exhaust the gas with air at a speed of 20 m/sec.

After the circulation system has been cleaned for half a day under this condition, the 5 ℓ reservoir and the charcoal trap are removed.

(3) Triton acceleration

40 mℓ STP of tritium gas ($\sim$100 Ci) diluted with 400 mℓ STP of deuterium gas were used.

When the tritium-D_2 mixture was not introduced to the ion source, the pressure gauge P (Fig. 1) indicated 371 Torr and it became 354 Torr when the sample gas was circulated through the needle valve. It was found that 95.4 % of the gas existed in a space between the circulation pump and the needle valve, and the remaining 4.6 % existed in the other part of the circulation system during operation. It is, therefore, able to keep almost all the tritium gas inside the circulation apparatus even if some troubles such as vacuum failure take place in the cyclotron.

The tritium ions (m/q = 3) were selectively accelerated with the intensity of 10 μA after passing through the deflector. This condition did not change during the operation of 15 h. After 15 h running, the gas was recollected and put out of use according to the steps described above.

Deuterium gas was admixed in place of hydrogen gas to avoid the contamination of H_3^+ ion into the beam. The contamination of hydrogen and deuterium ions was tested with a beam analyzing magnet and the elastic scattering spectrum, and was proved to be negligible.

(4) Monitoring of tritium

The quantity of the residual tritium was measured with an ionization chamber of collection type[2] and a liquid scintillation counter. The ionization chamber has a volume of 600 mℓ (Fig. 2) and the minimum measurable quantity of tritium is about 5×10^{-6} μCi/mℓ which is 2.5×10^{-3} times the maximum permissible concentration of tritium for a human body (2×10^{-3} μCi/mℓ).

When the tritium gas was circulated in the closed system, no tritium was detected in the vicinity of the apparatus, but at the exhaust port of the evacuation system of beam transport duct, a contamination of about 10^{-4} μCi/mℓ was observed (Table 1).

After 15 h operation the quantities of residual tritium were measured at several parts of the circulation system and the cyclotron, and the results are shown in Tables 2 and 3. At the exhaust of the blower for evacuating the circulation system $10^{-3} \sim 10^{-5}$ μCi/mℓ of tritium was detected just after the sample gas was absorbed

Table 1. Quantities of tritium leaking out from the circulating system.

Tritium quantity used in a run	1 Ci *	100 Ci
Surrounding the circulation system	Not detectable	Not detectable
At the exhaust port of auxiliary pump	Not detectable	Not detectable
At the exhaust port of evacuating beam transport duct		10^{-4} μCi/mℓ

* The operation test using 1 Ci tritium was performed before the test using 100 Ci.

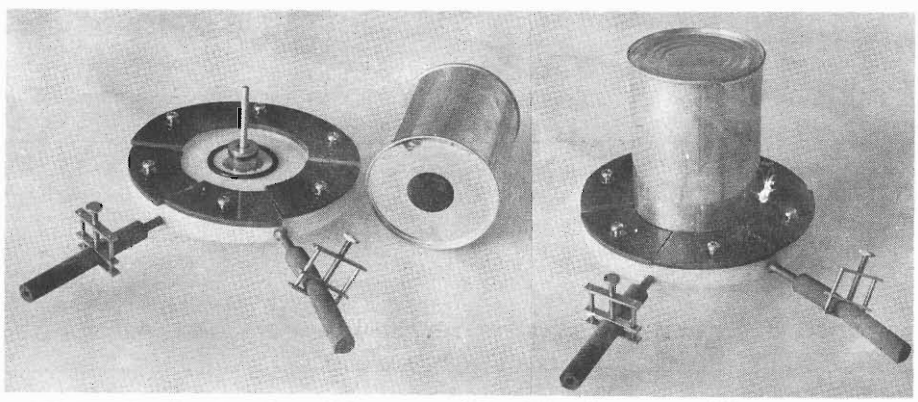

Fig. 2. Ionization chamber of collection type (the can is replaced when it is contaminated with tritium).

by the charcoal. In the oil of the auxiliary rotary pump 10 $\sim$ 100 μCi of tritium per mℓ of oil was detected with the liquid scintillation counter (Table 3). The tritium absorbed in the oil has been released slowly for a long time. Amounts of $10^{-2} \sim 10^{-3}$ μCi/mℓ were detected near the ion source and the acceleration chamber of the cyclotron just after they were exposed to the atmosphere. These values were decreased to 1/10 $\sim$ 1/100 after 2 weeks. In other places in the cyclotron vault the quantity of residual tritium gas was below 10^{-5} μCi/mℓ at all times.

(5) Conclusion

From this test it was concluded that tritium gas of 100 Ci (400 mℓ STP) is sufficient for accelerating the tritium ions in the cyclotron.

The circulation has been proved quite safe and it enabled a good recovery of tritium for disposal. The tritium concentration in the exhaust air of the blower to the atmosphere was well below the MPC. Concentrations up to 10^{-2} μCi/mℓ were found near the ion source and the accelerating chamber just after the exposure to the atmosphere and also contamination as much as 100 μCi/mℓ in the oil of the auxiliary rotary pump was found. These facts suggest a need of taking an appropriate safety precaution in the future operation.

Table 2. Residual tritium after operation.

Tritium quantity in sample gas	1 Ci			100 Ci		
Time after the circulation is stopped	immediate	2 days	70 days	10	1 day	15 days
Tritium after the circulation is stopped	10^{-3} $\sim 10^{-5}$	10^{-4}	7×10^{-5}	10^{-4} $\sim 10^{-5}$		
Ion source		10^{-4}			10^{-2} $\sim 10^{-3}$	10^{-4}
Acceleration chamber		not detectable			10^{-5}	not detectable
Exhaust part of cyclotron evacuating system					10^{-2}	

Unit of tritium quantity in the air is μCi/mℓ of air. Detection limit is 5×10^{-6} μCi/mℓ.

Table 3. Tritium quantity rested in the vacuum pump oil.

Tritium quantity used in a run	1 Ci		100 Ci
Time after the circulation is stopped	immediate	70 days	immediate
Circulation pump	1.2	1.0	19
Auxiliary pump	8.8	0.9	97

Unit of tritium quantity in the pump oil is in μCi/mℓ .

References

1) P.M.S. Jones and C.G. Hutcheson : Nature, 213, 490 (1967).
2) T. Miyake : Isotope News, Apr., p.19 (1970).

3-4. Charge Exchange Experiment (2)

Cross Sections for Electron Loss and Capture of Carbon Ions in Various Gases

T. Tonuma, Y. Miyazawa, T. Karasawa,
I. Kohno, T. Takahashi, and S. Konno

Carbon ions are accelerated in the IPCR cyclotron at energies of 3.2 $\sim$ 7.5 MeV/nucl., i.e. velocities of 2.5 $\sim$ 3.8 $\times 10^9$ cm/sec with C^{4+} charge state. When accelerated C^{4+} ions passed through some gaseous media, cross sections for electron loss and capture of carbon ions were measured.

Measurements were carried out by the same method which had been reported concerning the mathematical description and the experimental apparatus (shown in Fig. 1), procedure and conditions. The measurement of target gas pressure was improved by the use of a α-tron gauge.

(1) Cross sections for electron loss and capture of carbon ions

Fig. 2 shows the cross sections for electron loss and capture of carbon ions in H_2, He, N_2, Ne, Ar, Kr, and Xe gaseous media.

When C^{4+} ions passed through gas media except H_2 and He the cross sections of σ_{45}, σ_{46}, σ_{56}, and σ_{65} were given by the measured fractions of carbon ions with charge states 4,5 and 6 ; F_4, F_5, and F_6 at several gas pressures, where σ_{ij} means the cross sections which C^{i+} ions exchange to C^{j+} ions by losing or capturing an electron. In H_2 and He media only σ_{45} was measured because the present apparatus could not increase gas pressure in the collision chamber to attain several sets of values (F_4, F_5, F_6) for smaller cross sections in these media. The cross sections, σ_{46}, for loss of two electrons contain large errors compared with other cross sections. This fact is due to little variation of errors in a least-square fit to analyze data when a large change is given to the value of σ_{46}.

A detectable minimum current is now about 0.02 nA. The cross sections σ_{54} cannot be observed because a current of the equilibrium C^{4+} charge state is at least smaller than the above value. In order to observe the cross sections σ_{54}, which may exist at the degree $\sigma_{54} \simeq \frac{1}{2}\sigma_{65}$ theoretically, it is desirable to measure smaller current.

As shown in Fig. 2, in this velocity region the cross sections of σ_{45} and σ_{46} for single electron loss decrease monotonically with the ion velocity V and σ_{65} for single electron capture is proportional to $V^{-5} \sim V^{-7}$. Fig. 2 also shows that all cross sections for electron loss and capture increase with the atomic number Z_{med} of the medium gas.

(2) The relation of cross sections to Z_{med}

Fig. 3 shows the dependence of cross sections for single electron loss σ_{45} to the atomic number Z_{med} of the gas medium, the energy of carbon ions being a parameter. The cross section σ_{45} is nearly proportional to Z_{med}^2 up to $Z_{med} \sim 10$, and about $Z_{med}^{2/3}$ for the values more than 10. The latter may depend on a shielding effect of atoms of a heavy medium, that is, the decrease of the effective charge number of Z_{med}.

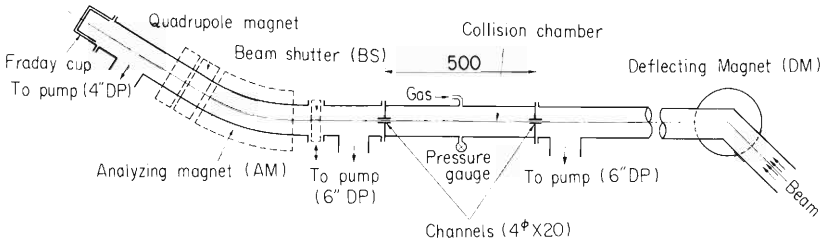

Fig. 1. Diagram of apparatus.

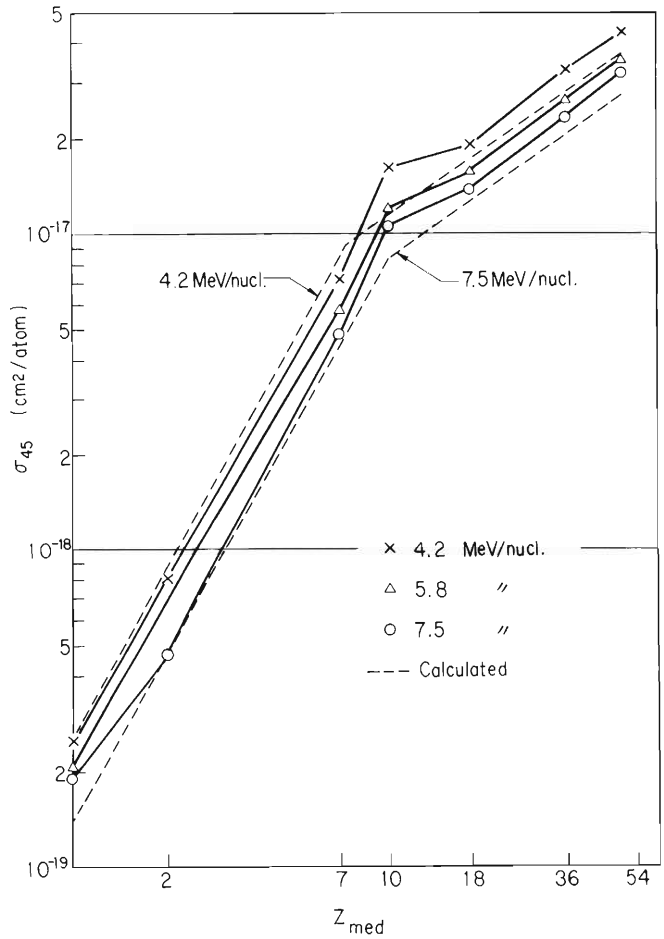

Fig. 3. The relation of the cross sections σ_{45} for single electron loss of carbon ions to the atomic number Z_{med} of the medium. Dotted lines are the values of σ_{45} calculated with Bohr's and Dmitriev's formulas.

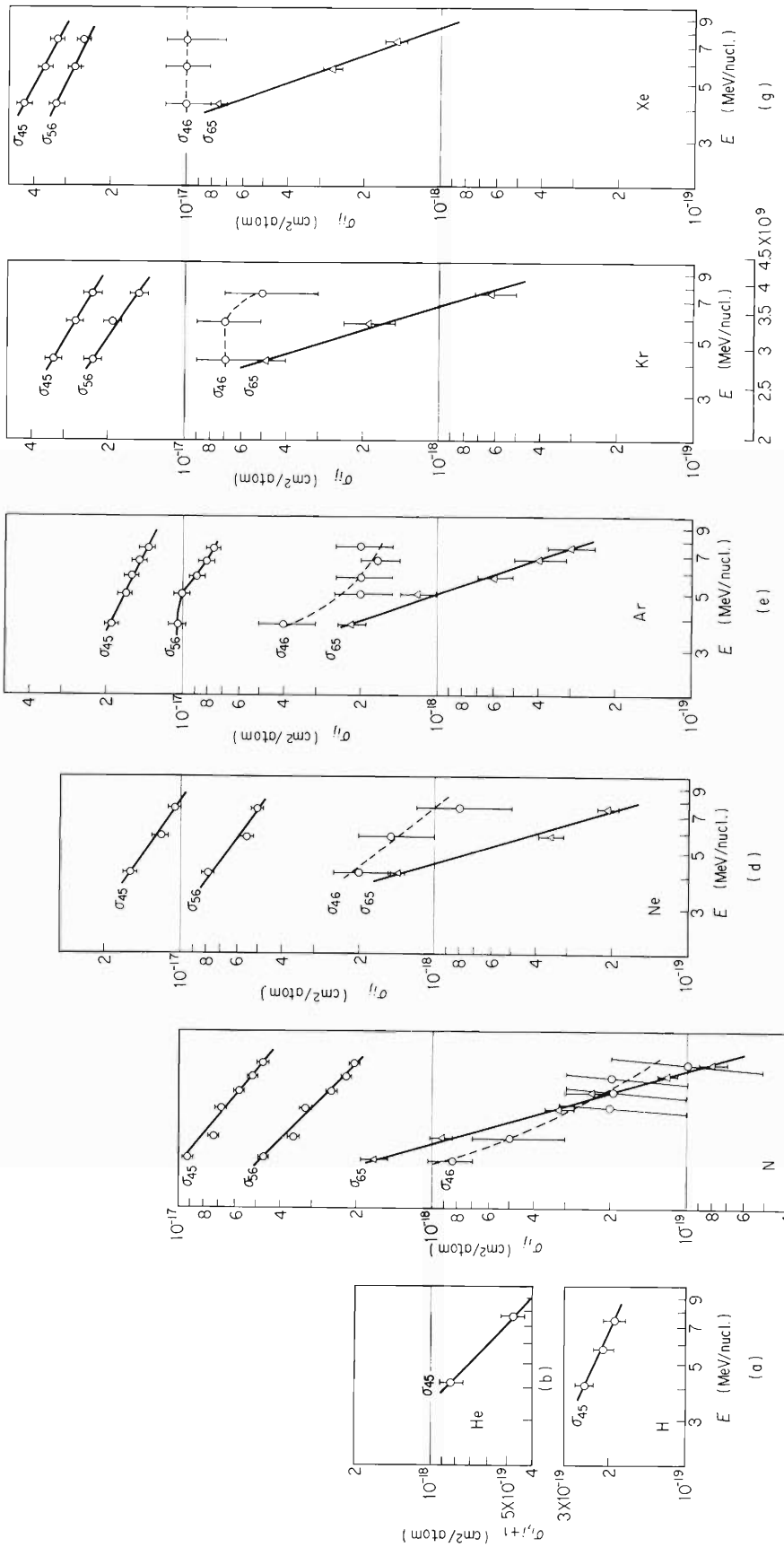

Fig. 2. Cross sections for electron loss and capture of carbon ions in H_2, He, N_2, Ne, Ar, Kr, and Xe as functions of ion energy.

Bohr[3] has already given a formula in the free-collision approximation without taking the shielding into account :

$$\sigma_{i,\,i+1} \simeq 4\pi a_0^2 \left(\frac{V_0^2}{UV}\right)^2 \left(Z_{med}^2 + Z_{med}\right) q_i \qquad (1)$$

Dmitriev[4] has generalized Bohr's formula derived in the free-collision approximation through a classical treatment of the scattering of an electron in the strongly shielded field of an atom :

$$\sigma_{i,\,i+1} \simeq \pi a_0^2 \; Z_{med}^{2/3} \; \frac{V_0^2}{UV} \; q_i \qquad (2)$$

where a_0 is the Bohr radius, v_0 is the atomic unit of velocity, v is an ion velocity, $U = (2I/\mu)^{1/2}$, I being the binding energy of the lost electron and μ the electron mass, and q_i is the number of electrons in the outmost shell.

The values calculated with the formulas (1) and (2), which are shown with dotted lines in Fig. 3, agree appeciably well with the measured values. The relation of σ_{56} to Z_{med} seems to be the same as that of σ_{45} to Z_{med}, though σ_{56} in H_2 and He media are not given.

Fig. 4 shows the dependence of the cross sections for single electron capture to Z_{med}. The values of σ_{65} are proportional to $Z_{med} \sim Z_{med}^{3/2}$, but differ from the values calculated with Bohr's formula[3] in which the cross section is proportional to $Z_{med}^{1/3}$ and Bohr and Lindhard's formula,[5] in which the cross section is proportional to Z_{med}^3.

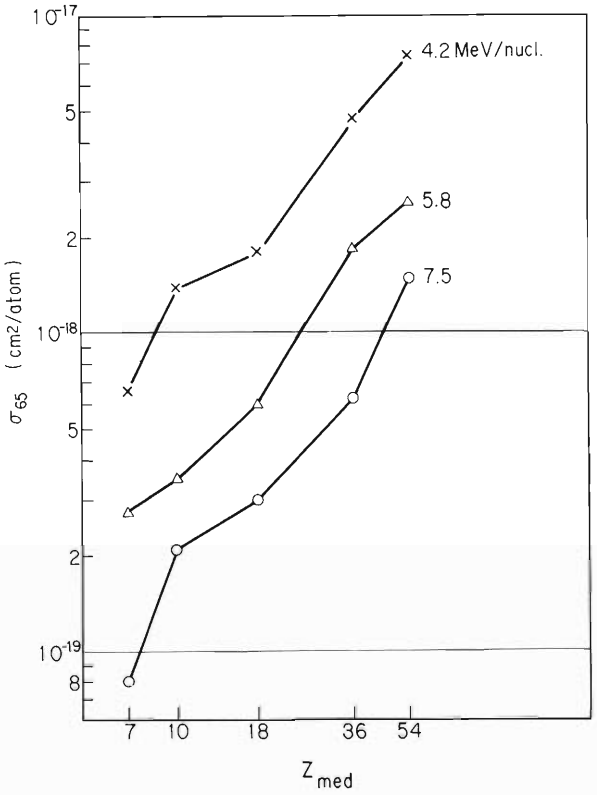

Fig. 4. The relation of the cross sections σ_{65} for single electron capture of carbon ions to the atomic number Z_{med} of the medium.

References

1) T. Tonuma, Y. Miyazawa, T. Karasawa, and I. Kohno : IPCR Cyclotron Progr. Rep., 3, 11 (1969).
2) T. Tonuma, Y. Miyazawa, T. Karasawa, and I. Kohno : Japan. J. Appl. Phys., 9, 1306 (1970).
3) N. Bohr : K. Danske Vidensk. Selsk. mat.-fys. Medd., 18, No. 8 (1948).
4) I. S. Dmitriev, V. S. Nikolaev, L. N. Fateeva, and Ya. A. Teplova : Sov. Phys. JETP., 15, 11 (1962).
5) N. Bohr and J. Lindhard : K. Danske Vidensk. Selsk. mat.-fys. Medd., 28, No. 7 (1954).

3-5. Status of Beam Bunch Selector Construction

Y. Chiba, T. Inoue, and M. Odera

It is well-known that the extracted beam of a cyclotron has a microscopic structure, that is, particles are bunched in a narrow phase angle of accelerating radiofrequency. The characteristic has been frequently used advantageously in some sort of research such as neutron time of flight spectroscopy and short life activity. Preliminary study of the time structure of our cyclotron indicated that the width of bunch of 2 ns is obtainable after making the magnetic analysis. Study of short life isomers of the order of 100 ns was already carried out using this characteristic.[1] To investigate longer life isomers and to make fast neutron measurements, construction of a beam bunch selector was planned. It is also useful in other fields such as solid state physics or radiation chemistry involving short life phenomena.

Beam deflection in the early stage of acceleration is most desirable for technical reasons, but the two-dee construction of our cyclotron leaves no space to install the device. Therefore, it was decided to select beam bunches at the site before the switching magnet. As shown in Fig. 1, use of this facility is possible in all of the experimental areas.

There is a relation among the angle of deflection θ, parameters of deflecting electric field and projectile such that :

$$\tan\theta = \frac{1}{2} \cdot \frac{Z}{A} \cdot \frac{A}{T} \cdot E \cdot L ,$$

where Z, A, and T are charge number, mass number and kinetic energy in MeV of the projectile to be deflected respectively. E is the deflecting transverse electric field in MeV/m and L is length of the deflector in meter. Table 1 gives the value of $E \cdot L$ necessary to deflect ions by 1/100 radian. As the space is limited, only L = 0.8 m is possible. Maximum field required becomes 6.25 kV/cm to deflect ions by 3 cm at the beam stopping slits which are located 3 m apart from the deflector.

Fig. 2 is the block diagram of the bunch selector. R.f. signal picked up from the cyclotron cavity is fed to a count-down circuit in the counting room via a variable delayline to adjust phase. Output pulse is shaped and is sent to the trigger circuit of high power pulse generator located in the cyclotron vault. The amplitude of the pulse needed at the deflector to cancel the deflecting field is that of the negative polarity of 10 kV to permit the gap of deflector plate of more than 1.5 cm. As maximum frequency of accelerating field is 13.5 MHz in this cyclotron, the pulse width must be narrow enough to let pass only one bunch, rejecting neighboring ones of 75 ns apart. To allow small jitter in the pulse generating system and shift of bunch in phase by drift of frequency or voltage of accelerating field, flat-topped pulse shape is desirable. Fig. 3 is an example of phase change by frequency variation measured at the exit port of accelerating chamber. It is seen that the phase drift can be moderate. Of course, after magnetic analysis range of drift must be greatly reduced. But considering a possibility of use of the beam just after deflection or in the straight course, a flat portion of $10 \sim 15$ ns must be provided. Thus the full width of 120 ns and the flat-top of 15 ns were chosen as design goal.

Large peak voltage and fast rise time require large peak current capability as

well as good high-frequency response to the last output tube of the pulser. Also a relatively large maximum duty factor near 10 % was proposed from the experimental consideration. Fulfillment of power and band width requirements with one tube is a rather formidable task. Our first choice was to use two tetrodes 8F66R in parallel which were the largest high-frequency tubes at the time of decision. Computer analysis of prototype circuits including the simulation of tube characteristics by simple functions and actual testing of them showed insufficient capability of 8F66R. Recently a new high-power high-frequency tube using vapor phase cooling has been manufactured by NEC (Nippon Electric Co.). Modification of test stand to incorporate this tube 8F68 is in progress.

On the other hand, mechanical construction of a deflecting electrode was completed in the machine shop of this institute and its vacuum testing was successful. Fig. 4 shows the dimensions of the deflector assembly. It is installed at the scheduled site and is now being used as beam steering device in place of a Helmholtz magnet which originally has been there. Fig. 5 is a photograph at the site.

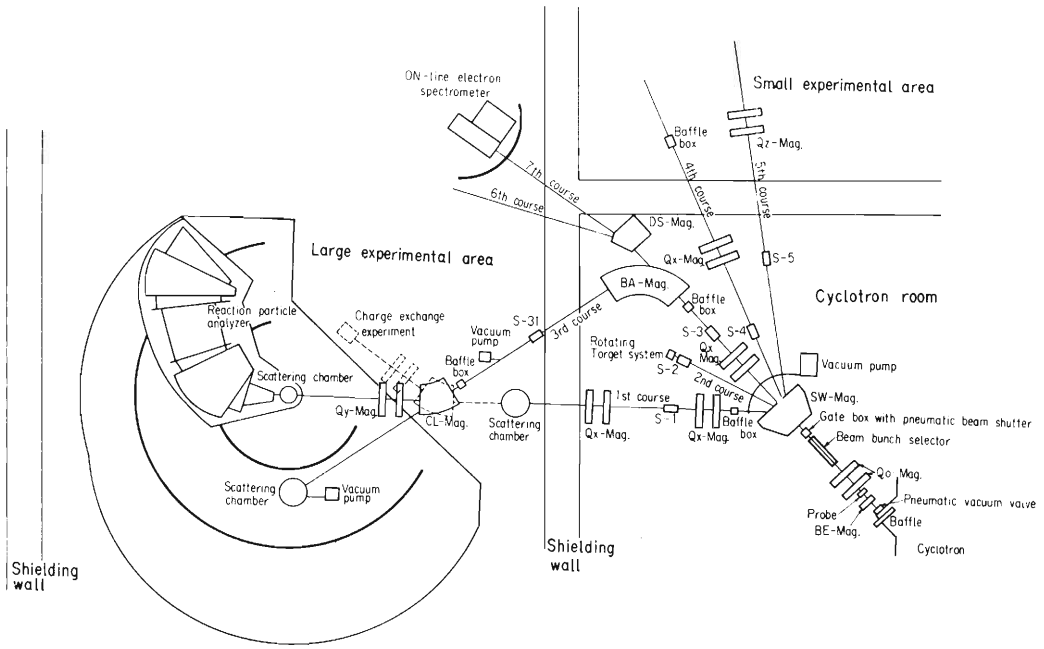

Fig. 1. Position of the beam bunch selector in the cyclotron vault.

Table 1. Values of EL to deflect ions by 1/100 radian.

Ions	A	Z	T (MeV)	E·L(MeV)
p	1	1	20	0.4
d	2	1	25	0.5
^3He	3	2	45	0.45
C^{4+}	12	4	100	0.5
N^{4+}	14	4	100	0.5

Vacuum testing of the deflector assembly was made with help of T. Tonuma and high-voltage sources at the test stand borrowed from the heavy-ion testing facility. Mechanical design of the deflector was made by N. Ohsawa who had been a member of this laboratory until last year.

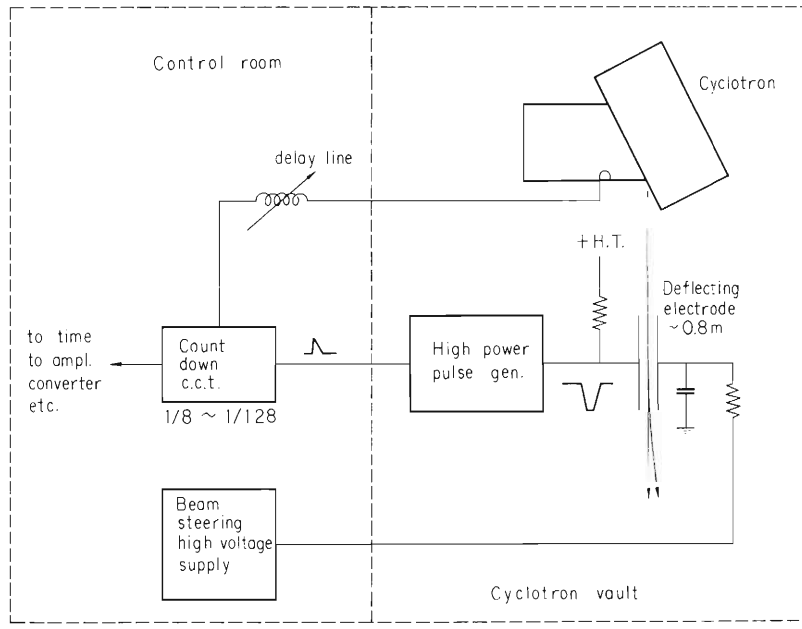

Fig. 2. Block diagram of the bunch selector.

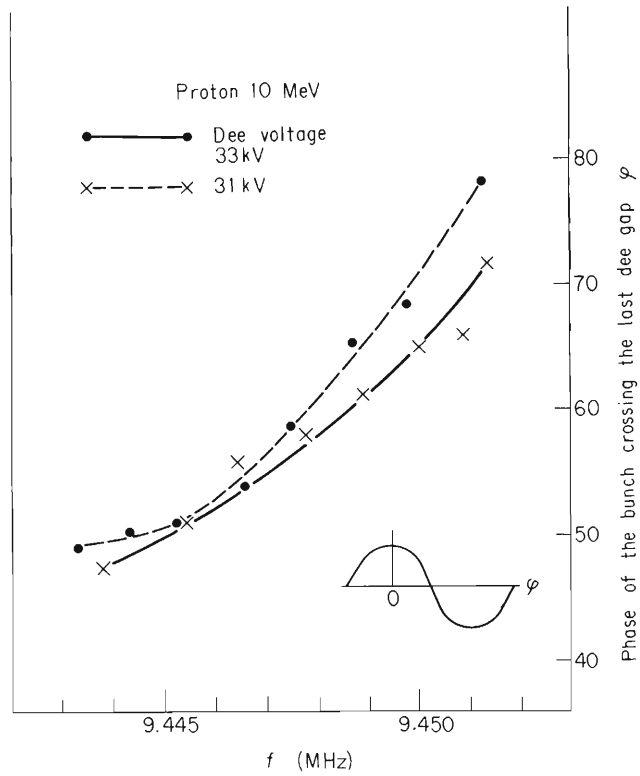

Fig. 3. Observed position of the bunch crossing the last dee gap as a function of frequency.

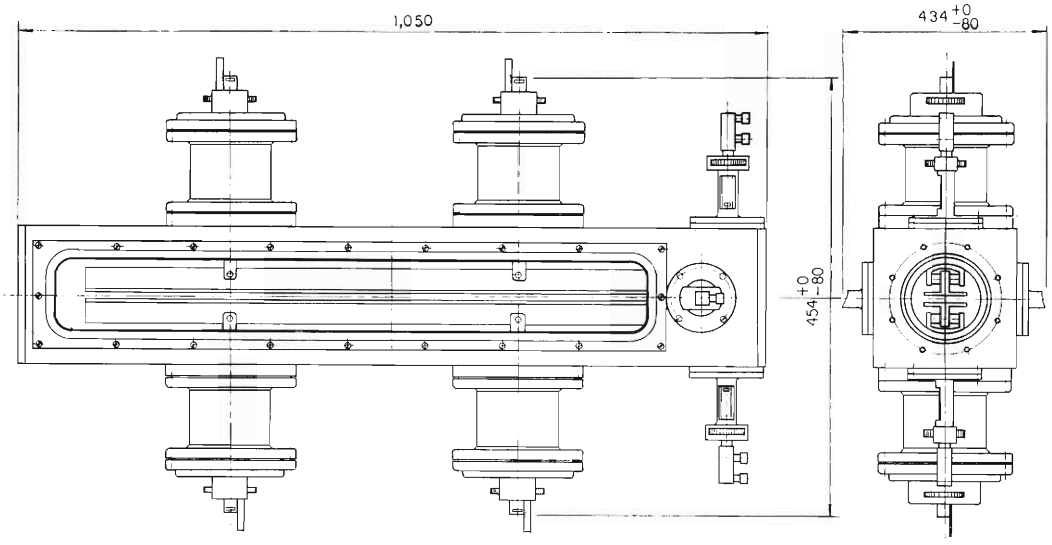

Fig. 4. Deflector assembly.

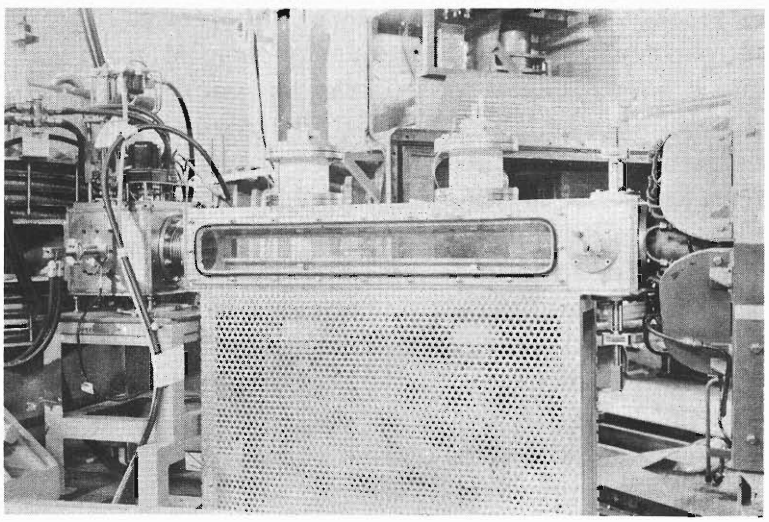

Fig. 5. Deflector at the site.

Reference

1) T. Yamazaki et al. : Phys. Rev. Letters, 24, 317 (1970) ; 25, 547 (1970) ; S. Nagamiya et al. : Nucl. Phys. (to be published).

3-6. Proposal of a Low Energy Multiparficle Linac

M. Odera

Recently the interest about acceleration of heavier nuclei than those of presently used as projectiles in a cyclotron, tandem Van de Graaff and linac is wide spread not only in nuclear physical research but also in other fields. Several projects are in progress[1), 2)] or under design study[3)~7)] to answer for this requirement.

One common problem is the ion source. Though there is some difference that the tandem V.d.G. accelerator needs negative ions and the others mostly positive ones, a considerable developmental work is necessary in both cases. Our laboratory has some experience in the design of multicharged heavy ion source which is being successfully used for acceleration of C, N, and O in the cyclotron.[8)] Another problem is the charge stripping and subsequent charge state selection in a suitable intermediate energy region to obtain higher energy with the least cost. We have a group of study of this phenomenon.[9)] Considering also other problems such as vacuum condition, large accelerating rate desirable to make the path length short, and beam extraction feasibility, we have found that a variable frequency linac is most suitable in acceleration of various heavy ions at least in the low energy region.

Our proposal is to use a shielded Lecher type resonator as the variable frequency cavity. A similar type of cavity is used in the heavy ion linacs of Manchester[10)] and Orsay.[2)] Main difference between our linac and the Manchester-Orsay's machine lies in the way of arrangement of stems or stubs and the drift tubes. Fig. 1 shows a schematic comparison. The latter is designed by combining a plural number of quarter wave resonators of Fig. 1 (a) into the shape indicated by (d) via (b) and (c). It has voltage distribution like (e). Our configuration (f) is much simpler and has a smaller number of drift tubes. It has smaller energy gain but allows a wide frequency change to accelerate ions of various m/q easily.

Maximum frequency of 33 MHz is chosen somewhat arbitrarily in a design example. In Table 1 the maximum frequencies to accelerate ions of various m/q for the same voltage gradient and the same length of drift tubes are tabulated. By the third harmonic acceleration the ions of m/q up to 81 can be used in principle. Fig. 2 shows an example of the linac system. Relatively low voltage of the injector was chosen to facilitate the supply of power, service and investigation for the heavy ion source on the high voltage terminal. As this is π mode linac, the length of one section from the center of a gap to that of the next gap is $1/2\beta\lambda$. Here, β is the ratio of velocity of ion to that of light and λ is the wave length of radio frequency in the free space. The values of β at injection is given in Table 1. The first section is 12.9 cm and so on. Assuming the peak voltage from drift tube to cavity wall to be 150 kV and the equilibrium phase angle of 25° before the peak and the transit angle of 24°, the eight sections altogether give a voltage gain of 2 MV in the distance of about 185 cm. The length of stem is 3 m.

Power loss in the cavity depends on several parameters which waits detailed studies of beam trajectory, probable emittance of injector beam, method of radial focusing, hence drift tube dimensions etc. Rough estimation gives around 40 kW for the above example.

This corresponds to an effective shunt impedance* of 60 MΩ per meter and allows CW operation.

Voltage gain of 2 MV is too small for a linac to be used as a nuclear research apparatus by itself. But the acceleration of all the elements in the periodic table may be possible by virtue of the frequency variation feasibility. Table 2 shows the energies of various ions obtainable.

Parallel operation of several cavities of high Q values is a task not very easy. Although the multicavity operation of proton or heavy ion linacs has been realized[11] or planned[3), 12] in some places, the frequency is always fixed. Frequency tuning and other controls have to take care of the only single frequency consideration. Anyhow, a multicavity variable frequency technique must be developed in the near future in order to realize a new type accelerator as a ring cyclotron planned[5), 6] or under construction.[13]

The following configuration may be possible. A similar second cavity working with the same frequency spectrum will have longer drift tubes owing to larger velocity of particles. Effective shunt impedance deteriorates much. If a maximum accelerating rate is required, a higher voltage operation than in the first cavity is necessary. The results will be 2.5 MV gain in 2 m with a power loss of around 160 kW. Use of a half-wave structure instead of a quarter-wave will reduce the loss. Table 3 shows the energies of various ions at the exit of the second cavity.

Further acceleration of light particles of small m/q with this low-frequency structure is no longer advantageous. Choice may be possible between the following two. One is the increase of frequency and the other is giving up of acceleration of light particles. First, we consider the latter case. If only ions of m/q larger than or equal to 4 are to be accelerated, the maximum frequency for each m/q can be doubled as indicated in Table 4. Practically, there is no need of the third harmonic acceleration for all kinds of elements. Rough estimation indicates that four similar cavities can give the energies to particles as shown in Table 5. These energies are high enough to give a moderate percentage of highly stripped charge state of ions by letting the particles pass through the stripping medium.

Next, we consider the increase of frequency at the exit of the cavity No 2. By making the characteristic impedance of Lecher line very low, a high resonant frequency can be obtained. For example, the structure indicated in Fig. 3 can have a high resonant frequency and a uniform voltage distribution along the drift tubes. Whether this structure and its power feeding line might have troubles of unwanted resonance in the wide frequency range or not must be investigated carefully. If this problem is solved and the cost of equipment is not very high, this higher frequency linac can be an equally good or better multicavity linac than that described above. Even the cavity No 2 can be replaced by this type with substantial reduction of the power loss.

The most difficult problem next to the multicavity operation in this proposal is radial focusing of particles of various velocities. As shown in Table 1, β has very low values at large m/q, where the magnetic quadrupole usually used in the proton linacs is not effective. Electric quadrupole may be usable in the low velocity range instead.[14] In this respect, the variable and low frequency characteristics of the cavity of this proposal are advantageous in reducing the necessary field strength for ions of large m/q. A tentative solution for the time being may be the use of grid focusing. If by the buncher technique the beam from injector can be bunched in a narrow phase angle, the alternating phase focusing[15] may be also possible. In the two methods the drift tubes of smaller diameter can be used than in the strong focusing scheme.

* Defined by (net voltage gain per unit length)^2 / power loss per unit length.

When the linac is used as an injector to a larger accelerator, fine adjustment of output energy may be desirable to make matching of two conveniently. This can be done for heavy ions of moderate energy by simply placing the stripping facility on a low voltage terminal of say, 300 kV, as shown in Fig. 4. Difference of the number of charges before and after stripping multiplied by terminal voltage gives changes of energy of the ion. By controlling the terminal voltage and its polarity, matching of the energies of two accelerators can be easily achieved.

Table 1. Maximum frequencies for various ions to be accelerated in the cavity of Fig. 2.

m/q	1	1.5	2	4	6	8	12*	16*	20*	24*	28*
f_{MHz}	33	26	23.4	16.5	13.7	11.7	28.6	24.8	22.1	20.2	18.7
β	0.024	0.02	0.017	0.012	0.01	0.0086	0.007	0.0062	0.0054	0.005	0.0046

* The third harmonic acceleration

Tabel 2. Energies of various ions accelerated in the cavity of Fig. 2.

Ion	P	α^{2+}	C^{3+}	O^{4+}	Ar^{5+}	Kr^{8+}	U^{10+}
Energy	2.25	4.50	6.75	9.0	11.15	18.0	22.5

Table 3. Energies of various ions at the exit of second cavity.

Ion	P	α^{2+}	C^{3+}	O^{4+}	Ar^{5+}	Kr^{8+}	U^{10+}
Energy	4.75	9.50	14.25	19.0	23.75	38.0	47.5

Table 4. Maximum frequencies for various ions when only ions of $m/q \geq 4$ are accelerated after passing through the second cavity.

m/q	4	6	8	12	16	20	24	28
f	33	27.4	23.4	19.1	16.5	14.8	13.5	12.5

Table 5. Final energies of various ions when four more cavities are used to accelerate ions of $m/q \geq 4$ after passing through the second cavity.

Ion	C^{3+}	O^{4+}	Ar^{5+}	Kr^{8+}	U^{10+}
Energy	48	64	80	128	160

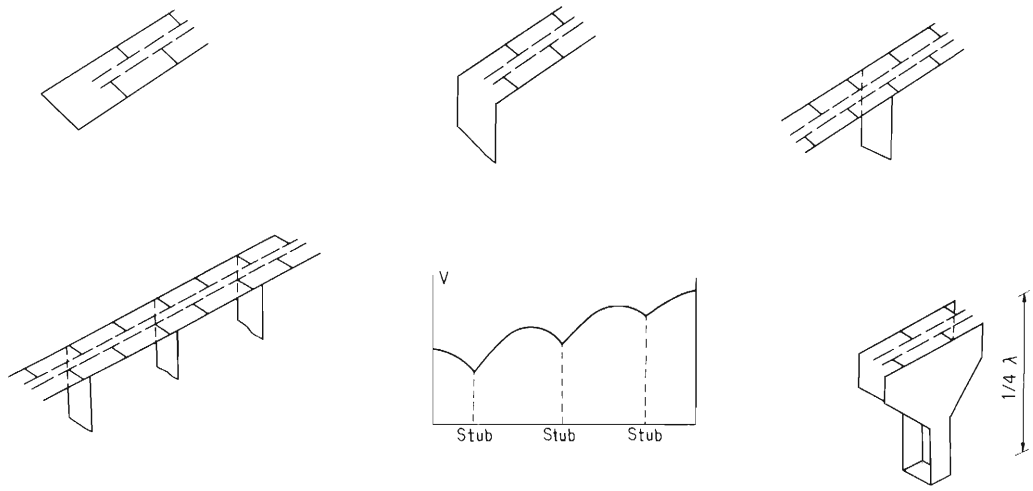

Fig. 1. Schematic comparison between Wideröe-Sloan-Lawrence linac of Manchester-Orsay and this proposal.

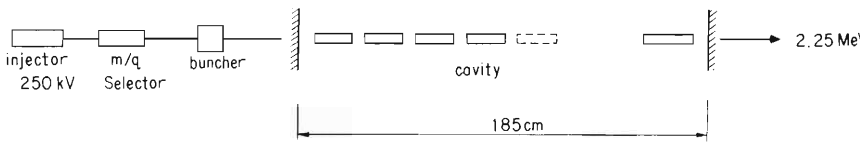

Fig. 2. An example of the initial section of the linac.

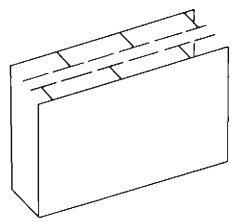

Fig. 3. A low impedance structure of the Lecher linac.

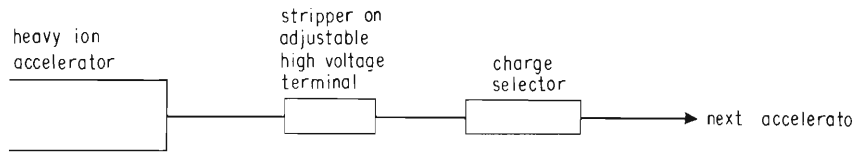

Fig. 4. A method of fine adjustment of energy of heavy ions.

References

1) D. Böhne et al. : "Linear Accelerators"(Ed. : P. M. Lapostolle and A. L. Septier), North Holland Publ., p. 1047 (1970) ; L. Grodzins : "Proc. Nucl. React. Heavy Ions, Heidelberg"(Ed. : R. Bock and W. R. Hering), North Holland Publ., p. 572 (1969).
2) M. Lefort et al. : "Proc. Nucl. React. Heavy Ions, Heidelberg"(Ed. : R. Bock and W. R. Hering), p. 557 (1969).
3) K. Blasche et al. : Ibid, p. 518.
4) H. Klein et al. : Ibid, p. 540.
5) A. Zucker : Ibid, p. 583.
6) G. C. Morrison : Ibid, p.601.
7) A. Chabert et al. : Ibid, p. 561.
8) I. Kohno et al. : Nucl. Instr. Methods, 66, 283 (1968).
9) T. Tonuma et al. : Japan. J. Appl. Phys., 9, 1306 (1970).
10) G. Nassibian et al. : Rev. Sci. Instr., 32, 1316 (1961).
11) E. L. Hubbard et al. : Rev. Sci. Instr., 32, 621 (1961) ; E. A. Day et al. : Ibid., 29, 457 (1958).
12) E. A. Knapp : "Linear Accelerators"(Ed. : P. M. Lapostolle and A. L. Septier), North Holland Publ., p. 601 (1970).
13) M. E. Rickey et al. : IEEE Trans. Nucl. Sci., NS 16, 397 (1969).
14) K. Blasche et al. : "Proc. Nucl. React. Heavy Ions, Heidelberg" (Ed. : R. Bock and W. R. Hering), North Holland Publ., p. 533 (1969) ; M. prome : "Linear Accelerators"(Ed. : P. M. Lapostolle and A. L. Septier), North Holland Publ., p. 785 (1970).
15) M. L. Good : Phys. Rev., 92, 538 (1953) ; Ya.B. Fainberg: Sov. Phys. Tech. Phys., 29, 506 (1959).

4. NUCLEAR PHYSICS

Scattering and Reactions

4-1. ^{24}Mg (d, ^{6}Li) ^{20}Ne Reaction

M. Odera, S. Takeda, and I. Kohno

Multinucleon transfer reaction can give insight to the cluster or many-quasi-particle structure of nuclei which cannot be easily obtained by other means such as direct single nucleon transfer reactions usually applied as probes of nuclear structure. Difficulty in the particle identification that hitherto hindered the study of this sort of reaction has been gradually solved by the developments of various techniques including the time-of-flight of charged particles,[1] the magnetic analysis[2] and the counter telescope with very thin ΔE counter[3]. Here the first result of a series of studies of s-d shell nuclei based on the (d, ^{6}Li) reaction made in this laboratory is described.

There are several reports on the 2p2n transfer reaction on light nuclei below ^{19}F by the (d, ^{6}Li) process[2),4),5] and the DWBA fit has been applied to some of them using a simple α-clustering model. The model seems to have been in moderate success in cases of light nuclei below ^{18}O.[4] Angular distribution from ^{19}F was not reproduced. The authors attributed the main reason of failure to the insufficient knowledge of optical model potential of ^{6}Li channel.[4] Recently Bethge et al. have made a detailed elastic scattering study of ^{6}Li and ^{7}Li from various targets and extracted relatively shallow potentials.[6] We performed measurements of (d, ^{6}Li) reaction on ^{24}Mg to know whether the simple α cluster pick-up model can survive in the 4N nuclei heavier than ^{19}F using these potentials.

An enriched target of purity of ^{24}Mg 99 % and thickness of 450 μ g/cm^2 was used. The energy of deuteron was 24 MeV and the average current was about 0.8 μa. Identification of particle specie was made by use of a Goulding type circuit and a ΔE-E solid state counter telescope. Since this reaction has a large negative Q value of -7.842 MeV and the energy of emitted particle rapidly decreases with angle, a very thin totally depleted counter is necessary as ΔE element to permit the identification of Li particles. Combination of 10μ and 2000μ, or in cases where the recording of deuteron was unnecessary, that of 10μ and 200μ was used.

Fig. 1 is a block diagram of the measuring circuit and Fig. 2 shows a typical particle spectrum obtained. Separation of α-particles is complete. Since the reaction emitting ^{7}Li has a large negative Q of -17.5 MeV, there is little possibility of detecting ^{7}Li in this experiment. Figs. 3 and 4 are examples of Li spectra resulted from the reaction induced in the 20μ g/cm^2 thick carbon and magnesium targets. It is seen that the cross section of carbon is larger by more than an order of magnitude. Therefore, use of targets free of carbon contamination as far as possible is required in the (d, ^{6}Li) study of magnesium or heavier nuclei. Figs. 5 and 6 indicate angular distributions obtained for ^{24}Mg, carbon and ^{46}Ti respectively. A diffraction like pattern is seen for the transition to the ground state of ^{20}Ne. Cross sections of the α pick-up reaction on ^{46}Ti is too small even at the forward angles to extend measurement to larger angles. But the undulation of differential cross section is perceptible. Increase of cross section with excitation of residual nuclei is to be noted in both nuclei.

Zero range DWBA analysis was tried to the ground state transition from ^{24}Mg. INS-DWBA-1 code[7] modified by S. Yamaji* was used with a computer FACOM 270-30 of this Institute. Optical model parameters of the exit channel are those of Pennsylvania

* We are indebted to him for use of his code.

group[6] and of Denes et al. modified as described later.[4] Table 1 gives the values of the parameters used in the analysis. Fig. 7 shows the calculated angular distributions of the elastic scattering of ^{6}Li from ^{20}Ne using these parameters. Incident energy is chosen at 18.6 MeV which corresponds to the laboratory energy of ^{6}Li in the exit channel. Potential of Denes et al. which is obtained from the data of ^{7}Li scattering on ^{12}C at 7.3 MeV gives rapid oscillation and has features very different from those of Pennsylvania group.

Alpha pick-up calculation was formulated following the prescription of Denes, Daehnik and Driko.[4] Four nucleons picked-up are assumed to have been coupled to zero spin in the d5/2 shell and have zero relative angular momentum in the target nuclei. Wave function of this quasi-α-particle has a number of nodes corresponding to energy quanta of the four nucleous added, viz, 5S state. Saxon Woods potential depth is adjusted to reproduce the separation energy or external tail of wave function of this α-particle. Fig. 8 shows the results of calculation. Peaks at around 50° and 70° are reasonably represented, but the steep rise at foremost angles never. Fig. 9 shows the effect of radial cut-off indicating a rather good cancellation of contribution to the radial integral from the interior of nucleus. Calculated angular distribution using the Pittsburgh potential[4] changes drastically with changes of various parameters. Really, the fit of Fig. 8 using the Denes' potential is obtained by use of the imaginary potential four-fold deep that of the original one.* The original potential gives a poor fit as shown in Fig. 10. Radial cut-off does not remedy this situation. Their Li potential seems not to have been suitable for heavier nuclei than ^{18}O as they guessed. Finite range calculation using the Pennsylvania potential is in progress.

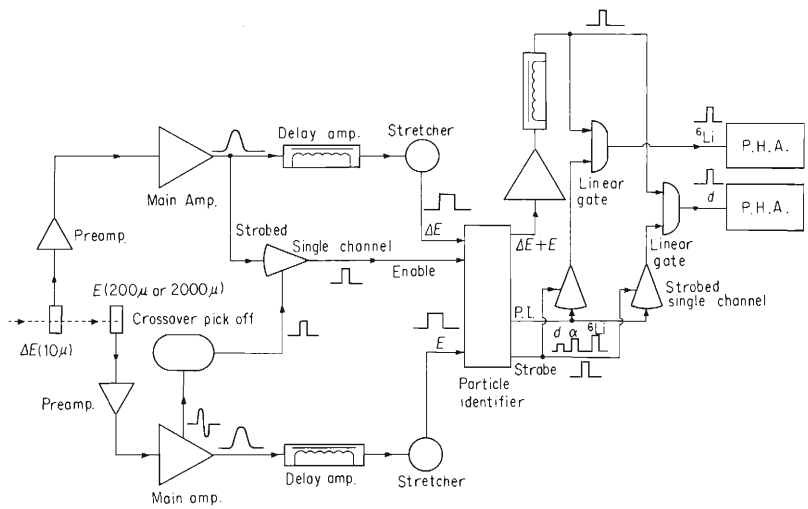

Fig. 1. Block diagram of measuring circuit.

* Their definition of attractive imaginary potential is of a surface absorption form given by

$$W(r) = W\, a\, \frac{d}{dr}\left[\left\{1+\exp\left(\frac{r-r_0A^{1/3}}{a}\right)\right\}^{-1}\right]$$

whereas, in the code DWBA-1 of S. Yamaji it is

$$W(r) = 4Wa\, \frac{d}{dr}\left[\left\{1+\exp\left(\frac{r-r_0A^{1/3}}{a}\right)\right\}^{-1}\right]$$

It is interesting to see a trend of the total cross section of (d, ^{6}Li) process with mass. Fig. 11 shows rough estimates incorporating the results of Denes et al. More α pick-up reactions from targets of varying mass will be useful to investigate the effects of shell filling to the nucleon correlation.

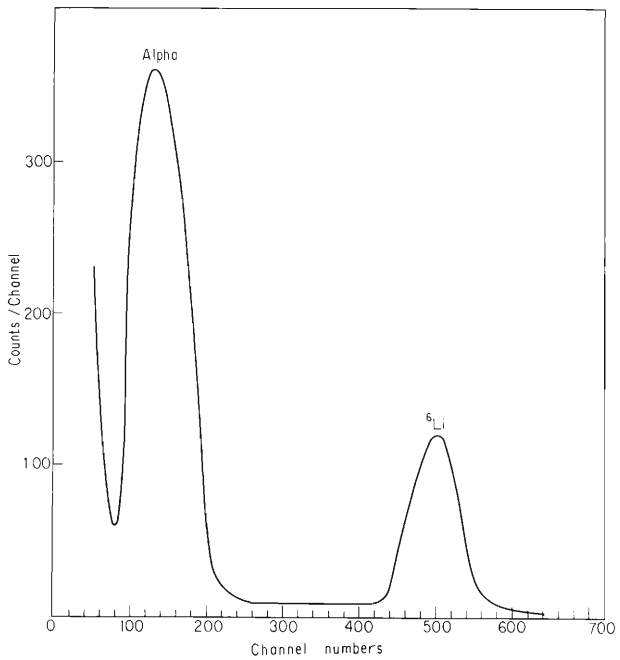

Fig. 2. Typical particle identifier output spectrum.

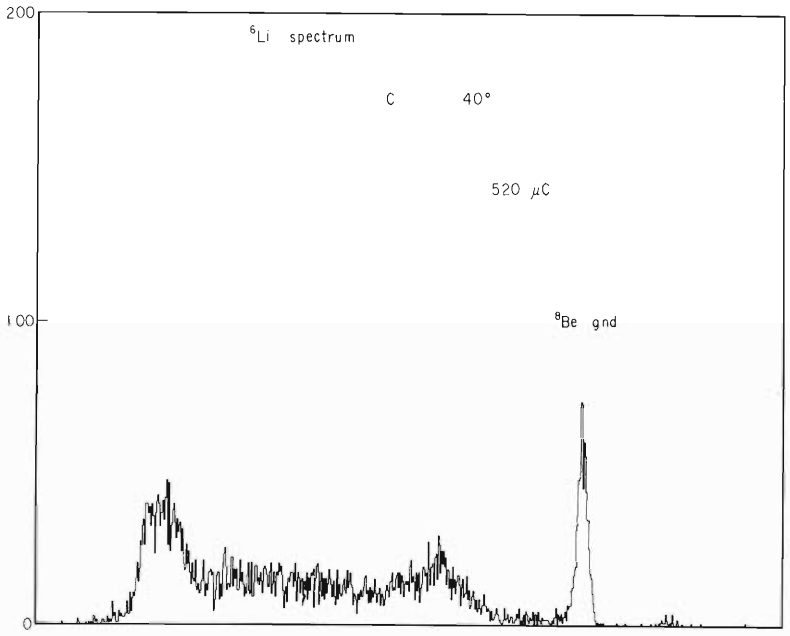

Fig. 3. Energy spectrum of ^{6}Li from ^{12}C.

Table 1. Optical model parameters of ^{6}Li used in the zero range DWBA analysis.

No.	V	W_V	W_d	r_V	r_W	a_V	a_m	r_c
1[6]	35.5	—	7.94	1.42	1.71	0.92	0.89	2.5
2[6]	65.5	12.0	—	1.48	1.43	0.41	1.48	2.5
3[4]	126.8	—	24.9	1.18	2.5	0.81	0.90	2.0

Parameters used for the form factor calculation are r = 1.50, a = 0.50, and V = 91.4 MeV.

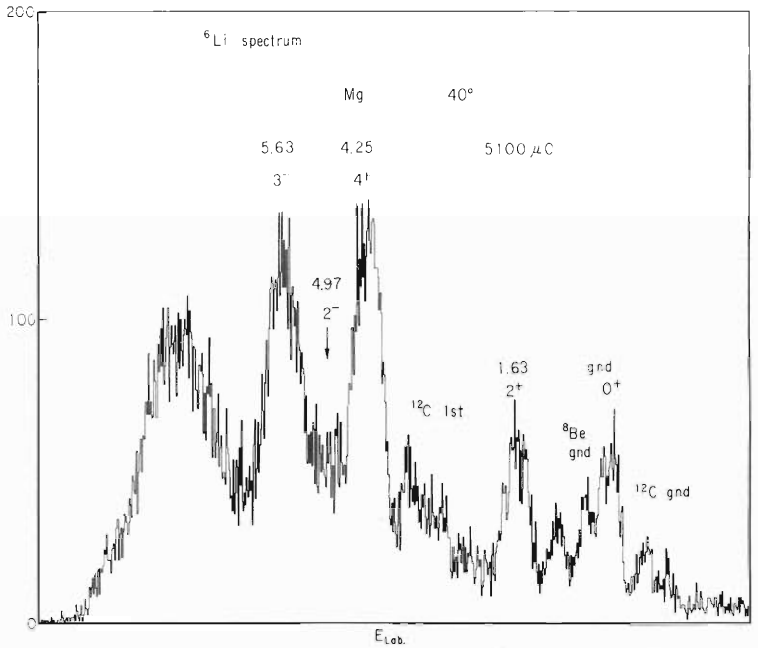

Fig. 4. Energy spectrum of ^{6}Li from ^{24}Mg.

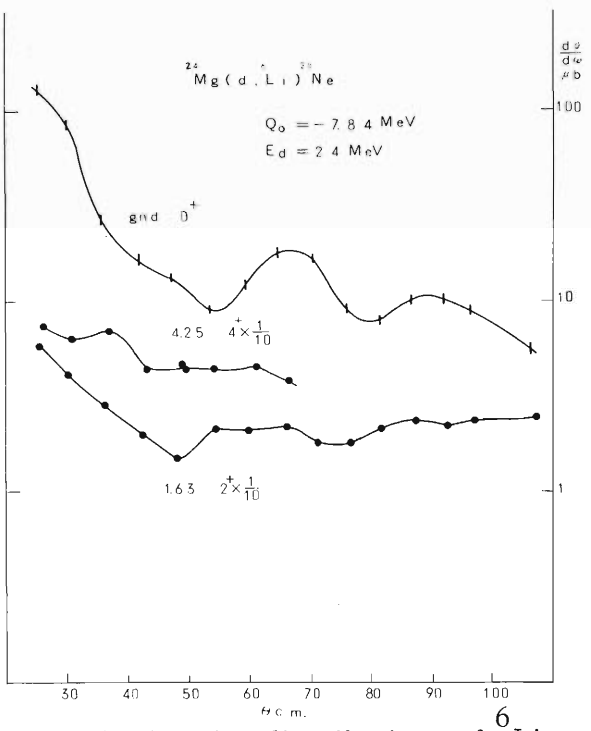

Fig. 5. Angular distributions of ^{6}Li from ^{24}Mg.

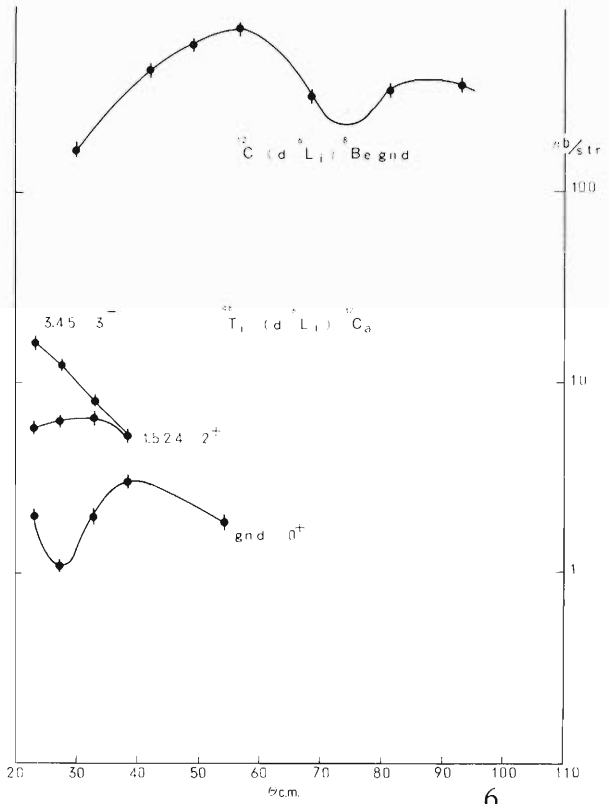

Fig. 6. Angular distributions of ^{6}Li from ^{12}C and ^{46}Ti.

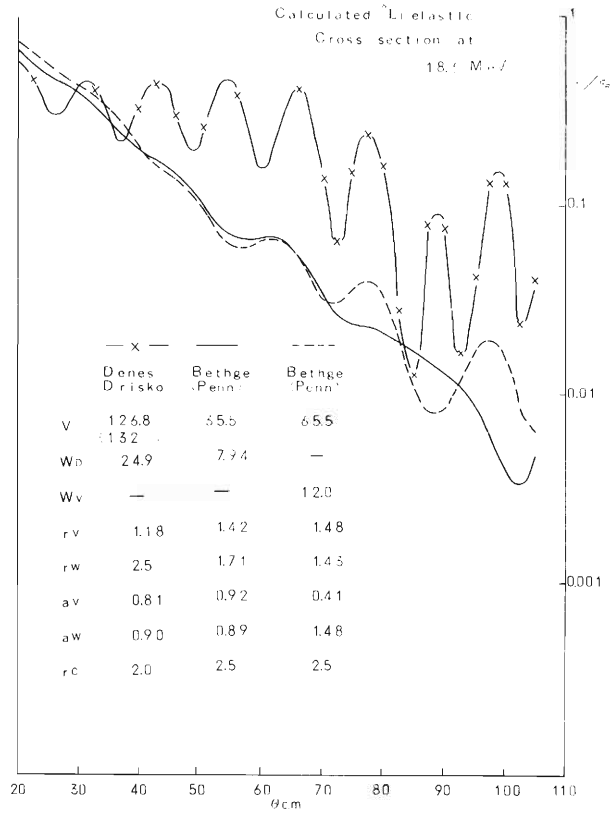

Fig. 7. Calculated elastic angular distributions of ^{6}Li of 18.6 MeV from ^{24}Mg.

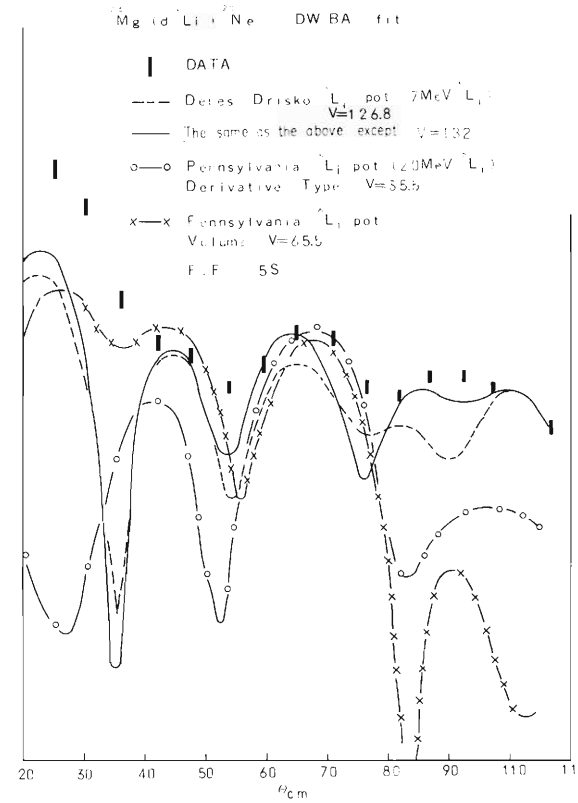

Fig. 8. Fit of DWBA calculations. Vertical bar indicates the experimental value.

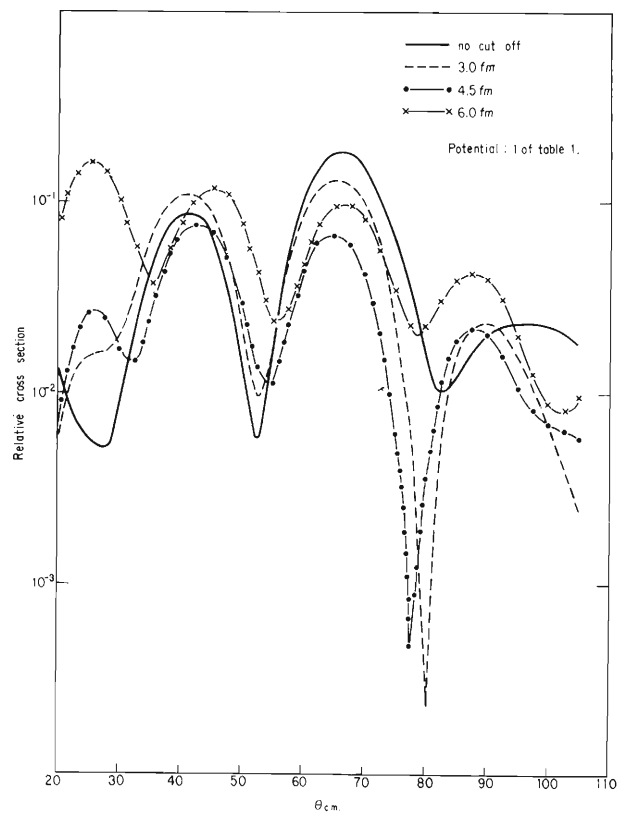

Fig. 9. Effect of radial cut-off. Optical parameter used is surface derivative potential of Bethge et al.[6)]

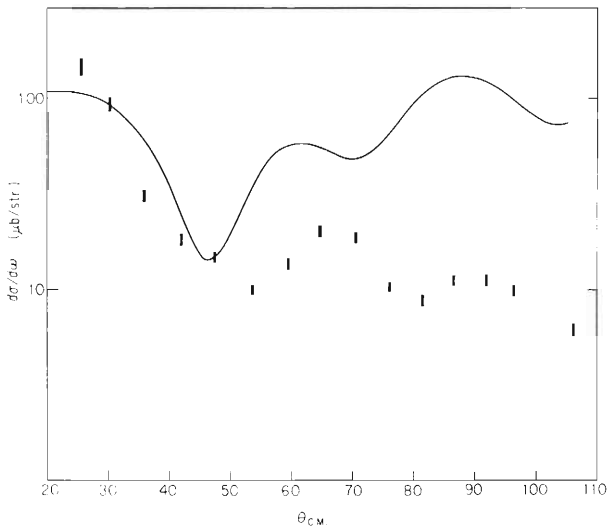

Fig. 10. Fits of DWBA analysis using the original Denes' potential.[4]

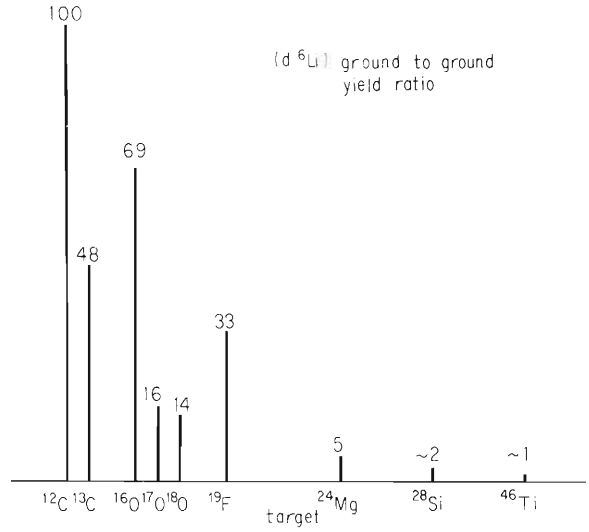

Fig. 11. Rough estimates of relative yield of ground to ground transition as a function of target mass.

References

1) D. S. Gemmel : IEEE Trans. Nucl. Sci., NS 11, 409 (1964).
2) W. W. Daehnick and L. J. Denes : Phys. Rev., 136, B1325 (1964).
3) H. H. Gutbrod et al. : "proc. Nucl. React. Heavy Ions, Heidelberg" (Ed. : R. Bock and W. R. Hering), North Holland Publ., p. 311 (1969) ; H. T. Fortune et al. : ibid., p. 307 ; C. Detraz et al. : ibid., p. 319.
4) L. J. Denes, W. W. Dehnick, and R. M. Drisko : Phys. Rev., 148, 1097 (1966).
5) W. Eichelberger et al. : Nucl. Phys., A149, 441 (1970).
6) K. Bethge, C. M. Fou, and R. W. Zurmühle : Nucl. Phys., A123, 521 (1969).
7) T. Udagawa et al. : Elastic Scat and DWBA 1, INS-PT-8.

4-2. Transfer Reactions Induced by ^{12}C Ions

S. Nakajima, I. Kohno, T. Tonuma, and M. Odera

Since the single nucleon or multi-nucleon transfer induced by heavy-ion nuclear reactions is of great interest from theoretical and experimental points of view, considerable efforts have been paid to the study of it. This study is more difficult compared to stripping and pick-up reactions with light nuclei for several reasons:

(i) It is difficult to identify the detected heavy particles and to obtain a good energy resolution.

(ii) A mechanism of the reaction is not well understood for one-nucleon and multi-nucleon transfer.

(iii) The structures of projectile and detected nucleus are complex.

A ΔE-E counter telescope was used to identify the heavy particles and a preliminary study of the one-nucleon transfer reaction was carried out.

(1) Performance of heavy-particle identification scheme by counter telescope

The counter telescope consists of a 10 μ , 20 μ , or 30 μ surface barrier SSD of planer transmission type as ΔE and a 200 μ surface barrier SSD as E-counter. The pulses are processed by the Nuclear Data 4096 channel P.H.A. in the two-dimensional mode. The electronic block diagram of measurement is shown in Fig. 1. Fig. 2 shows a two-dimensional spectrum obtained from the reactions induced by ^{12}C on ^{12}C. In the figure ^{10}B and ^{11}B particles are separated and can be identified. Fig. 3 shows the spectra of ^{10}B and ^{11}B particles obtained from this two-dimensional spectrum.

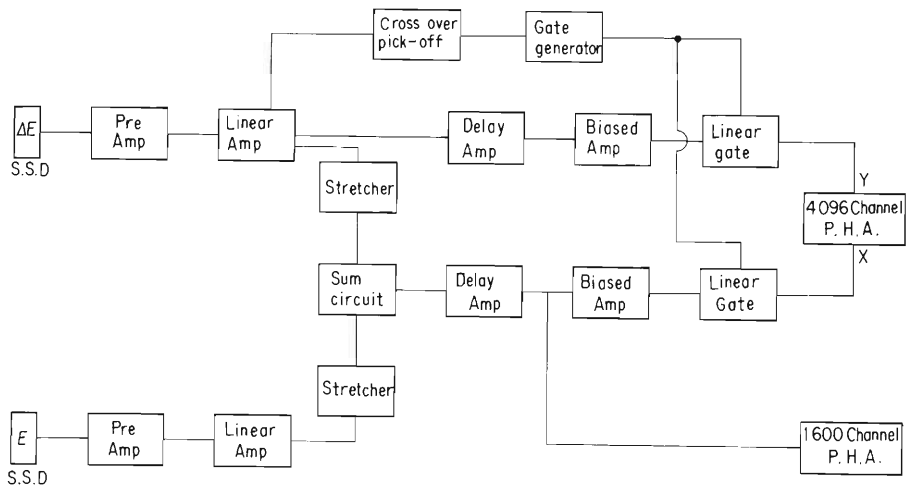

Fig. 1. Electronic block diagram.

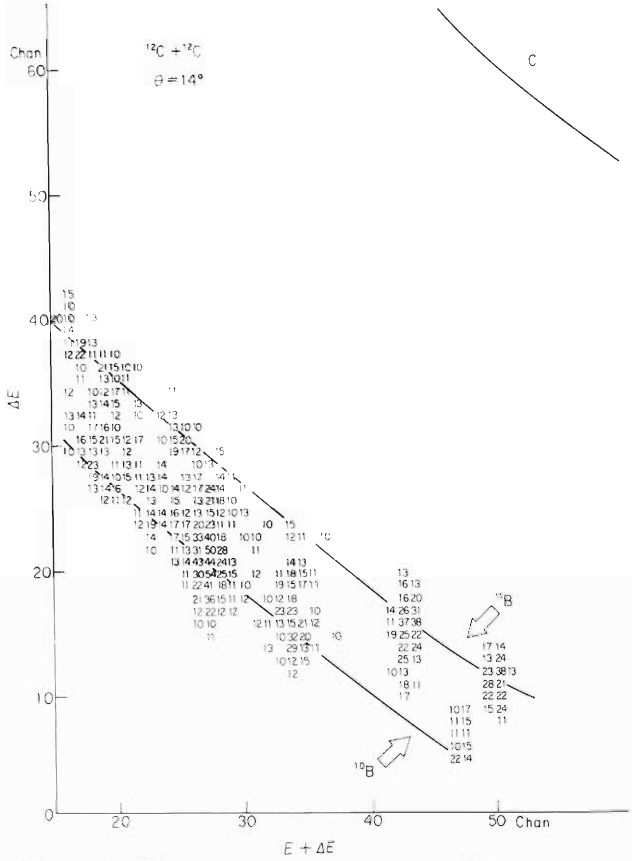

Fig. 2. Spectrum of energy and mass to charge ratio obtained from the reactions induced by ^{12}C on ^{12}C.

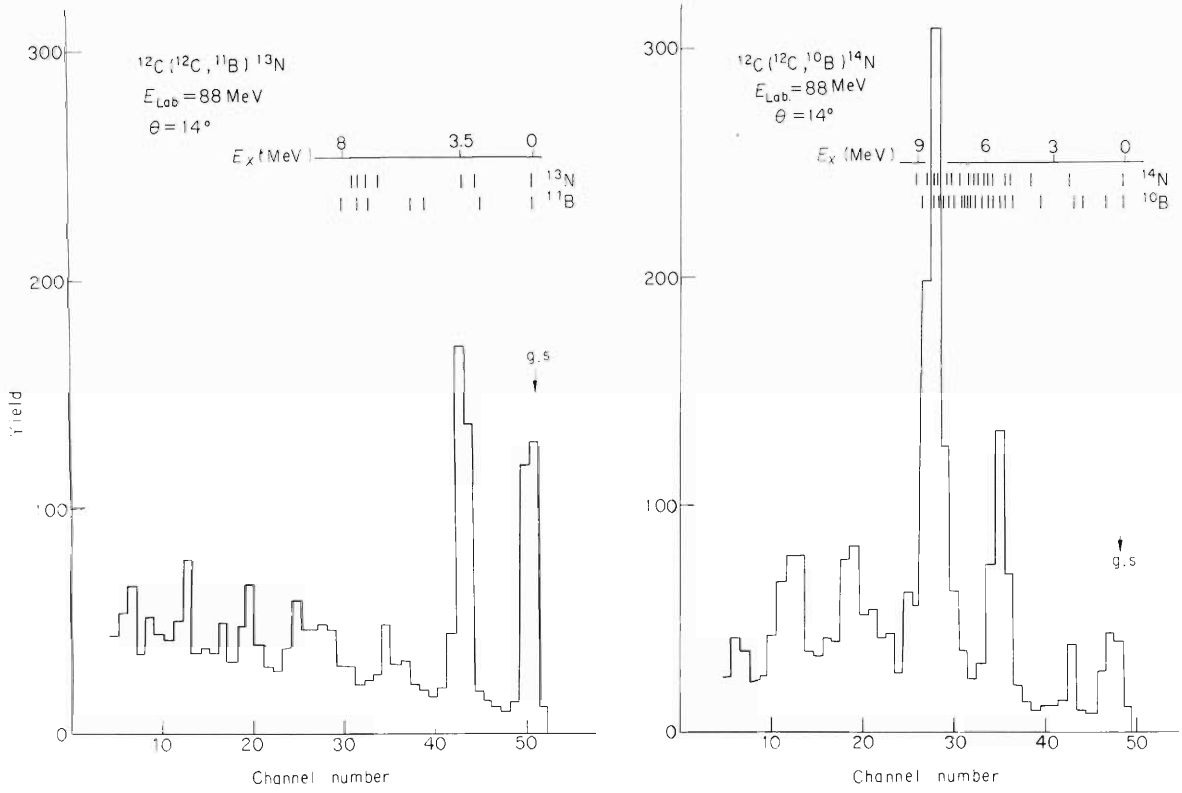

Fig. 3. Energy spectra of ^{10}B and ^{11}B.

(2) $^{27}Al\ (^{12}C,\ ^{13}N)^{26}Mg$ reaction

For studying the reaction mechanism of a one-nucleon transfer, an experiment on the $^{27}Al(^{12}C,\ ^{13}N)^{26}Mg$ reaction was performed at energy of 80 MeV. Fig. 4 shows an energy spectrum of the detected ^{13}N particles at the angle of 15 degrees. The energy resolution is 880 keV. There are some peaks corresponding to the ground state, 1.8 and 2.9 MeV excited states of ^{26}Mg and the ground state of ^{13}N.

In Fig. 5 is shown the angular distribution of both ground levels. This angular distribution shows a diffraction pattern and not a single maximum feature which has been found and explained by the grazing collision mechanism.

Measurements at higher and lower energies are in progress to see the effect of bombarding energy to the angular pattern.

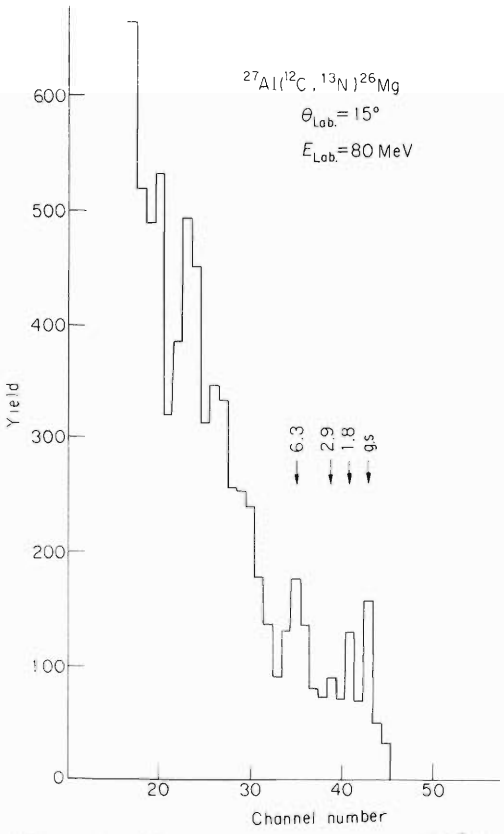

Fig. 4. Energy spectrum of ^{13}N produced from the reaction $^{27}Al\ (^{12}C,\ ^{13}N)\ ^{26}Mg$.

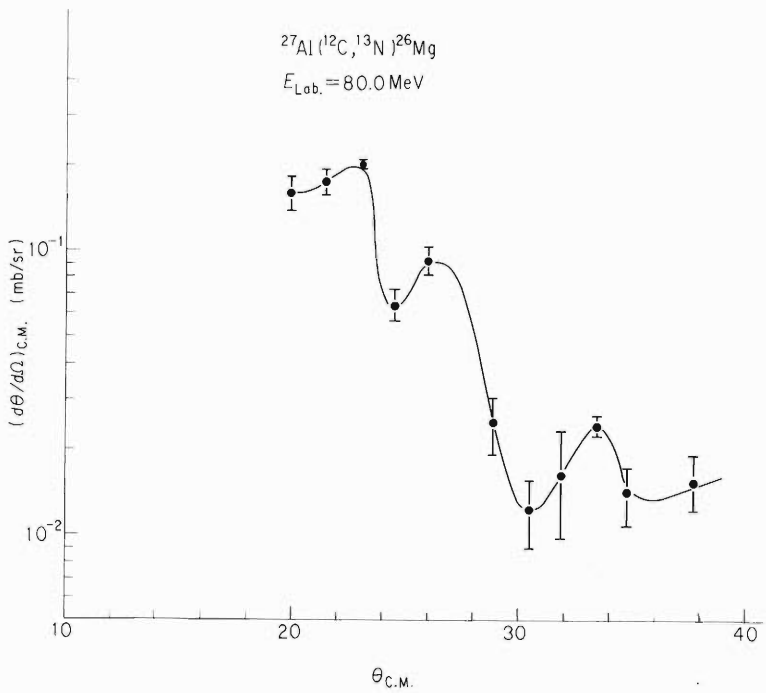

Fig. 5. Angular distribution in the reaction $^{27}Al\ (^{12}C,\ ^{13}N)\ ^{26}Mg$.

4-3. Inelastic Scattering of Alpha Particles from Even Molybdenum Isotopes

K. Matsuda, Y. Awaya, N. Nakanishi, and S. Takeda

It is now generally recognized that nuclear inelastic scattering strongly excites quadrupole and octupole collective states and the macroscopic DWBA analysis gives a measure of the collectiveness with the deformation parameter β_L. The analysis with a microscopic model, of course, gives a different approach to the collectiveness for the excitations with protons and alpha particles. This difference exists in the isobaric dependence, the exchange effect and the interaction form factor, etc.

As the value of β_L, a parameter to connect the scattering results to the nuclear structure, is considered to be not so accurate as the B(E λ) of the electromagnetic transition. The relative ratio of β_L in isotopes, however, is believed to be a more definite quantity free from some ambiguities of the DWBA analysis.

The present experiment is intended to give an accurate determination of the relative value of β_L for the inelastic alpha scattering of molybdenum isotopes. Inelastic scattering experiments of protons from the same isotopes were already performed in this Laboratory[1] and reported. Table 1 gives the level energies involved and the measured target thickness. Fig. 1 is an example of emitted alpha spectra. Fig. 2 gives angular distributions of elastic scattering ratio and fit of optical model analysis.[2] In this analysis the parameters of radius and diffuseness are fixed as those that give an overall best fit. Figs. 3 and 4 give angular distributions for quadrupole and octupole collective excitations respectively. In the processing of these results,

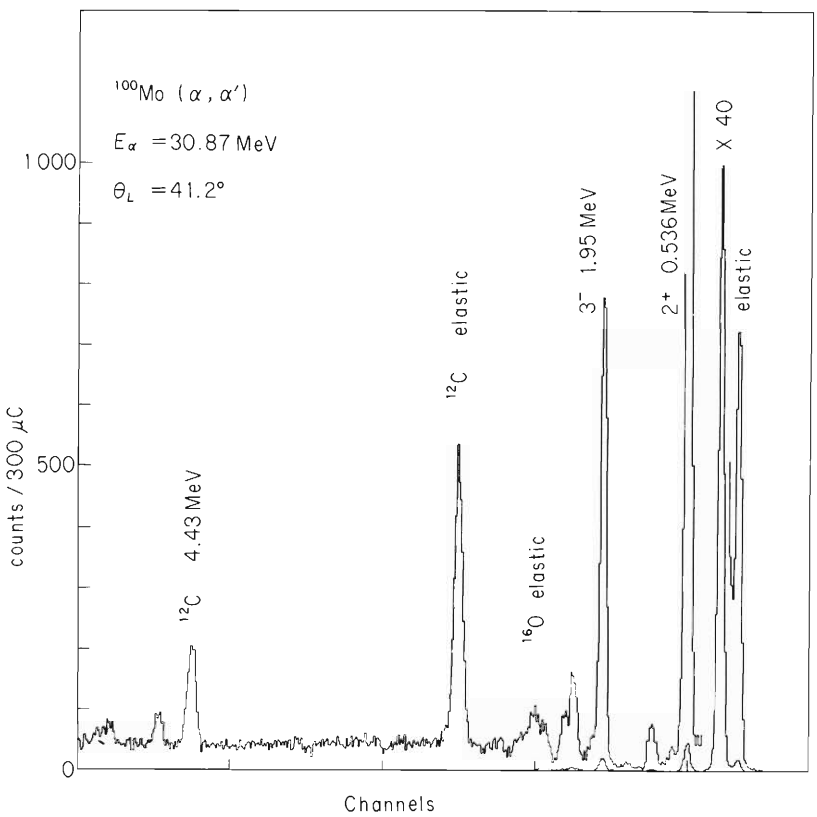

Fig. 1. Emitted alpha spectrum from ^{100}Mo (α,α').

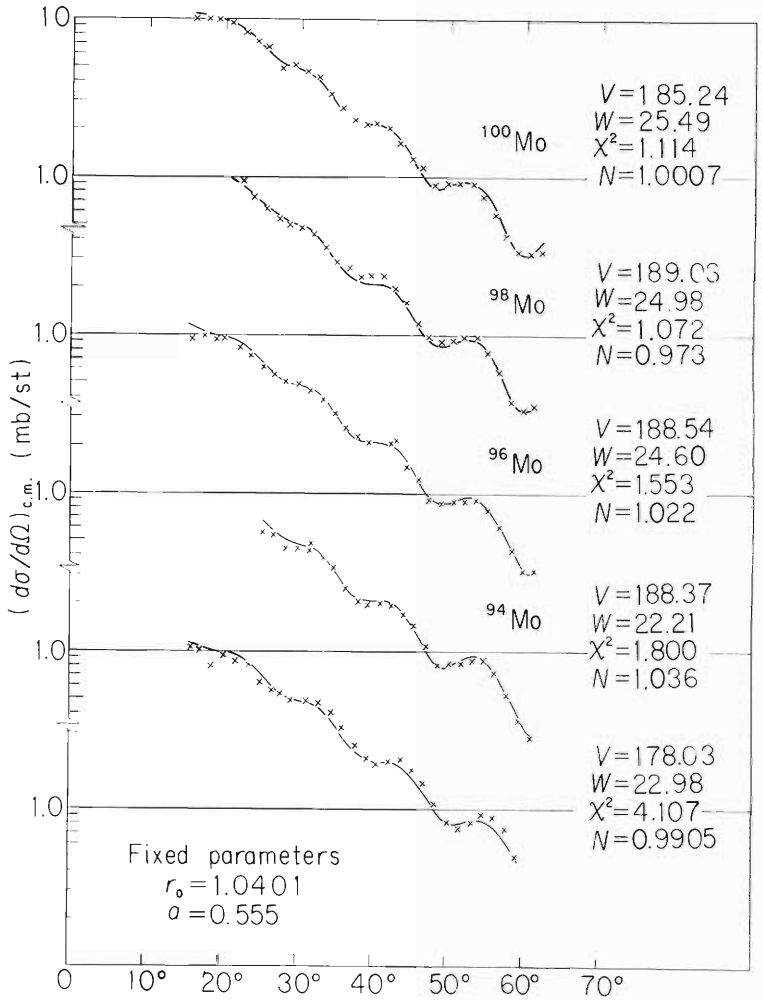

Fig. 2. Elastic cross section ratio of 30.87 MeV alpha particles from even molybdenum isotopes. Solid curves give the optical model calculations obtained with the search code. The radius parameter r_0 and the diffuseness parameter a are fixed to those given. Values of χ^2 are given with errors of 5 %. Values of N are recommended normalizations for better fitting.

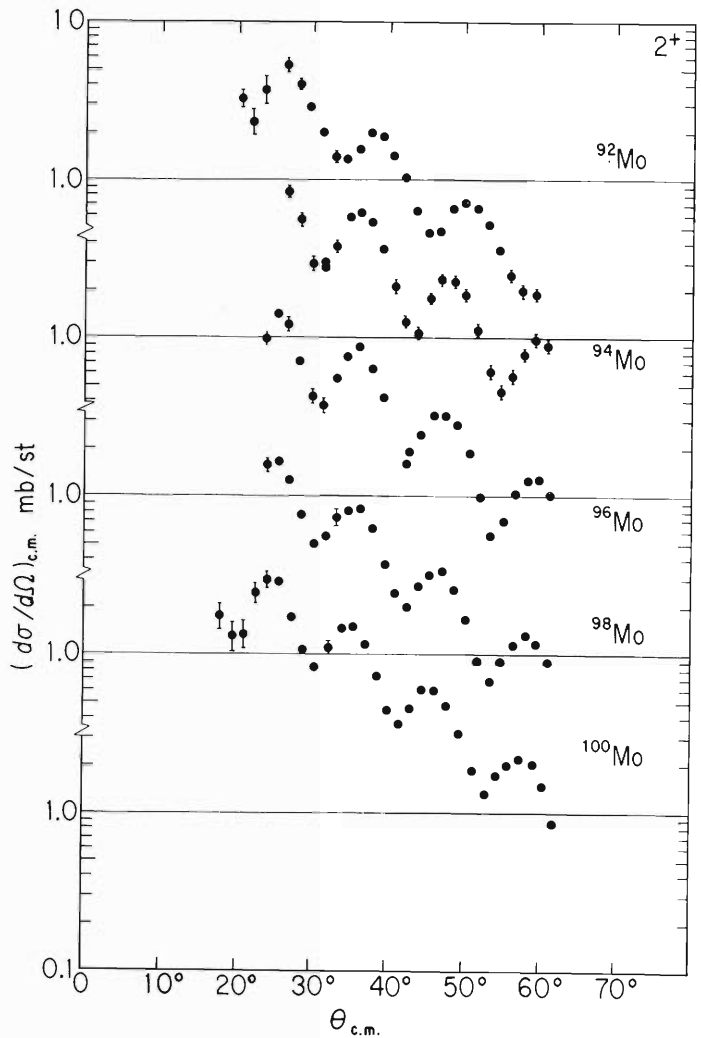

Fig. 3. Angular distributions for the quadrupole collective excitation of even molybdenum isotopes.

relative errors within five percent will be given to each data point except those indicated by error bars. The DWBA analysis with the macroscopic form factor is now in progress.

Table 1. The excitation energies of collective 2^+ and 3^- states in even molybdenum nuclei and the thickness of targets.

	Excitation energy (MeV)		Target thickness (mg / cm^2)		
	2+	3^-	(α , α)	Th- α	Th- α
^{92}Mo	1.54	2.90	0.715	0.717	0.724
^{94}Mo	0.871	2.56	0.876	0.914	0.931
^{96}Mo	0.778	2.25	1.00	0.959	0.951
^{98}Mo	0.787	2.03	0.774	0.804	0.838
^{100}Mo	0.536	1.95	1.06	1.08	1.13

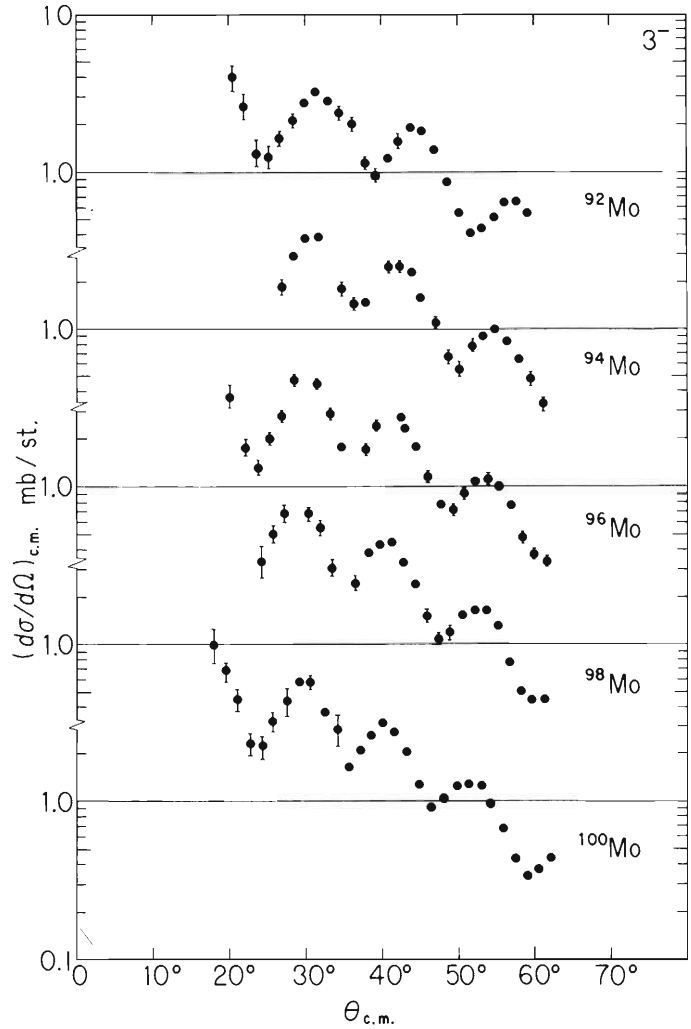

Fig. 4. Angular distributions for the octupole collective excitation of even molybdenum isotopes.

References

1) T. Wada, K. Matsuda, Y. Awaya, N. Nakanishi, and S. Takeda : IPCR Cyclotron Progr. Rep., 3, 36 (1969).
2) T. Wada : ibid., 2, 87 (1968).

4-4. The Spin-Flip in the $^{54, 56}$Fe(p, p') Reaction

T. Wada, S. Motonaga, Y. Chiba, T. Fujisawa,
S. Kobayashi,* K. Katori,** and A. Stricker***

A microscopic model[1] has been used to describe the inelastic scattering. According to this model, it is expected that there should be some differences in the inelastic scattering of proton from the first 2^+ states of ^{54}Fe and ^{56}Fe. Existing data show the differences in the cross section and asymmetries at 18.6 [2] and 19.6 MeV.[3] But the spin-flip probability is quite similar at 19.6 MeV.[3]

For the further test, we measured the excitation functions of the cross sections and the spin-flip probabilities from these two nuclei from 10.0 MeV to 14.0 MeV, and the angular distributions at several energies. The ^{54}Fe target is a self-supporting enriched foil with thickness 3.07 mg/cm^2 which was obtained from ORNL. The ^{56}Fe target is a

Table 1.

(a) Optical parameters for ^{54}Fe.

Ep (MeV)	V (MeV)	Ws (MeV)	a_I (fm)
12.0	53.80	9.24	0.536
13.0	53.48	8.99	"
14.0	53.16	8.74	"

(b) Optical parameters for ^{56}Fe.

Ep (MeV)	V (MeV)	Ws (MeV)	a_I (fm)
10.0	55.23	10.16	0.56
12.0	54.59	9.66	"
14.0	53.95	9.16	"

Other parameters are the same and the following, r_R = 1.17 fm, a_R = 0.75 fm, r_I = 1.32 fm, V_{so} = 6.2 MeV, r_{so} = 1.17 fm, a_{so} = 0.75 fm, r_c = 1.20 fm.

* Kyoto University.
** Argonne National Laboratory, U.S.A.
*** Basel University, Switzerland.

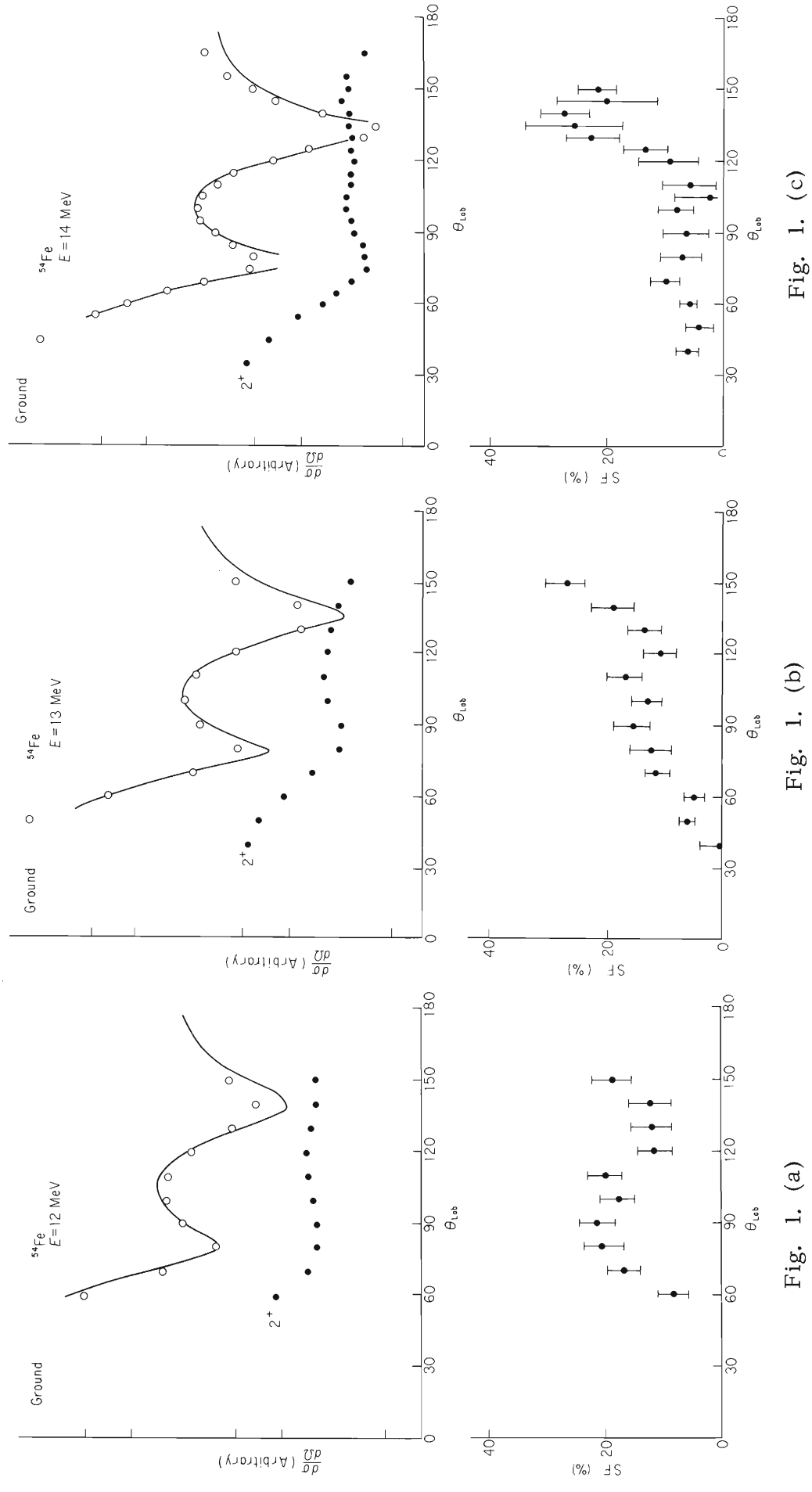

Fig. 1. (a)

Fig. 1. (b)

Fig. 1. (c)

Fig. 1. The angular distributions of elastic and inelastic proton scattering cross sections and spin flip probabilities for ^{54}Fe.

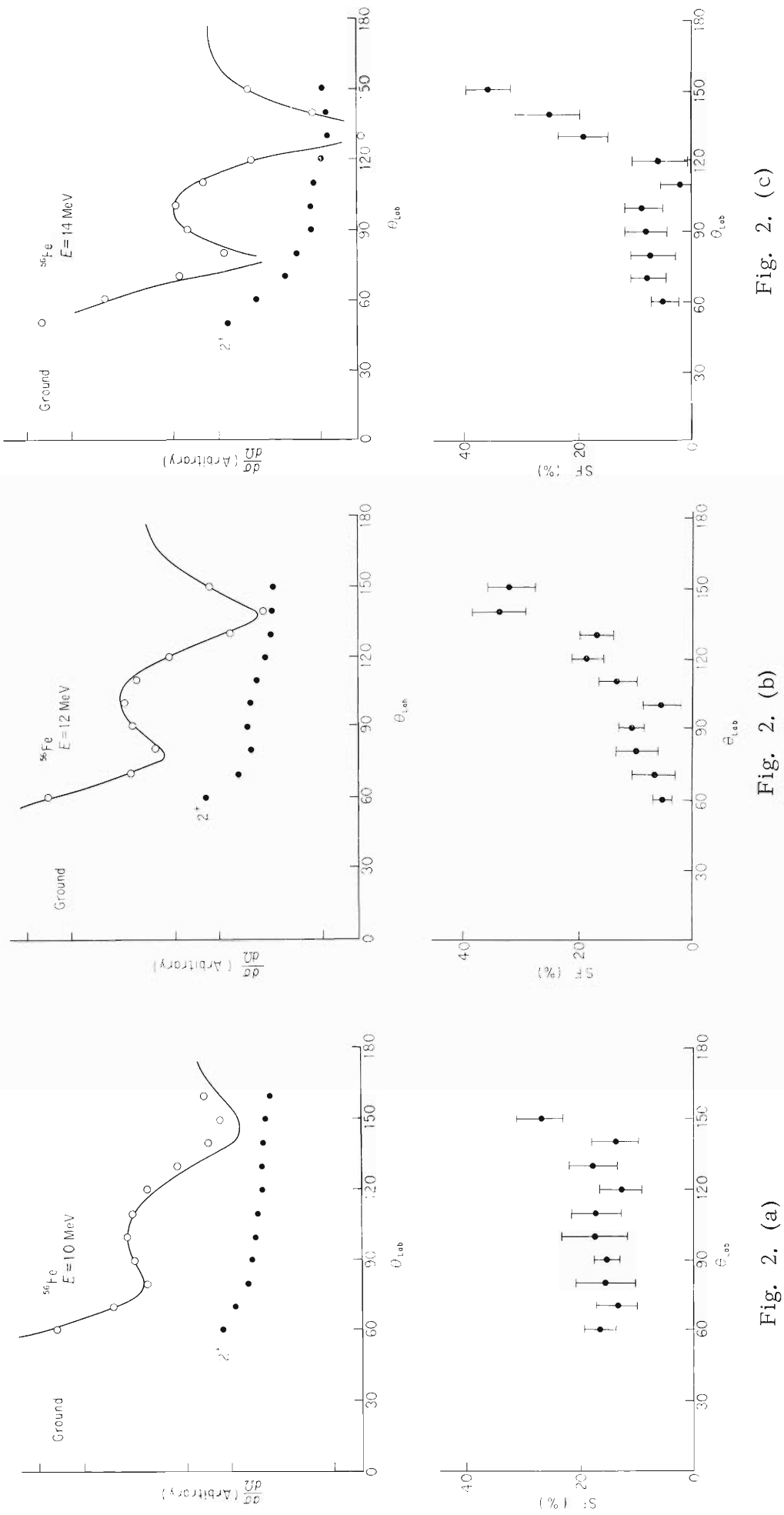

Fig. 2. (a)

Fig. 2. (b)

Fig. 2. (c)

Fig. 2. The angular distributions of elastic and inelastic proton scattering cross sections and spin flip probabilities for ^{56}Fe.

self-supporting foil of natural iron with thickness 2.93 mg/cm^2. The experimental conditions are the same as previously reported.[4]

Figs. 1 and 2 show the angular distributions of the elastic- and inelastic-scatterdng cross sections and the spin-flip probabilities. The solid curves are the results of preliminary optical-model calculation. The optical potential parameters are shown in Table 1 which were calculated from the equations of Ref. 5).

Below the threshold energy of (p,n) reaction plus 5 MeV, it is said that the contribution from a compound process is large.[6] This may correspond to the broad peak at about 90 degree. Q-value of (p, n) reactions are −9.6 MeV for ^{54}Fe and −5.4 MeV for ^{56}Fe. At 14.0 MeV where the compound process is considered to be small, there is some difference in spin-flip probability at the backward angle. The data reduction of the excitation functions are now in progress.

References

1) N. K. Glendenning and M. Veneroni : Phys. Rev., 144, 839 (1966) ; G. R. Satchler : Nucl. Phys., 77, 481 (1966).
2) C. Glashausser, R. de Swiniarski, J. Thirion, and A. D. Hill : Phys. Rev., 164, 1437 (1967).
3) D. L. Hendrie, C. Glashausser, J. M. Moss, and J. Thirion : Phys. Rev., 186, 1188 (1969).
4) S. Kobayashi, S. Motonaga, Y. Chiba, K. Katori, A. Stricker, T. Fujisawa, and T. Wada : J. Phys. Soc. Japan, 29, 1 (1970).
5) F. D. Becchetti, Jr. and G. W. Greenlees : Phys. Rev., 182, 1190 (1969).
6) D. H. Wilkinson : "Isospin in Nuclear Physics", North Holland Publ.,(1969).

4-5. The (^{3}He, ^{3}He), (^{3}He, ^{3}He'), and (^{3}He, α) Reactions of ^{12}C

T. Fujisawa, H. Kamitsubo, S. Motonaga, K. Matsuda,
F. Yoshida, H. Sakaguchi,* and K. Masui*

Differential cross sections of (^{3}He, ^{3}He), (^{3}He, ^{3}He'), and (^{3}He, α) reactions of ^{12}C have been measured at incident energies of 24.0, 29.2, 34.7, and 39.6 MeV.

The elastic scattering was investigated in order to see the sets of optical potential parameters,[1] and the inelastic scattering and the (^{3}He, α) reaction to study the reaction mechanism. The ^{12}C target was a self-supporting foil of natural carbon with thickness of 1.29 mg/cm^2. The reaction products were observed with a ΔE-E counter telescope consisting of two silicon surface barrier units of which the thickness was 100 μm or 50 μm for ΔE-counter and 1000 μm for E-counter. Pulses from the E and ΔE-counters were fed into a particle identifier (ORTEC MODEL 423).

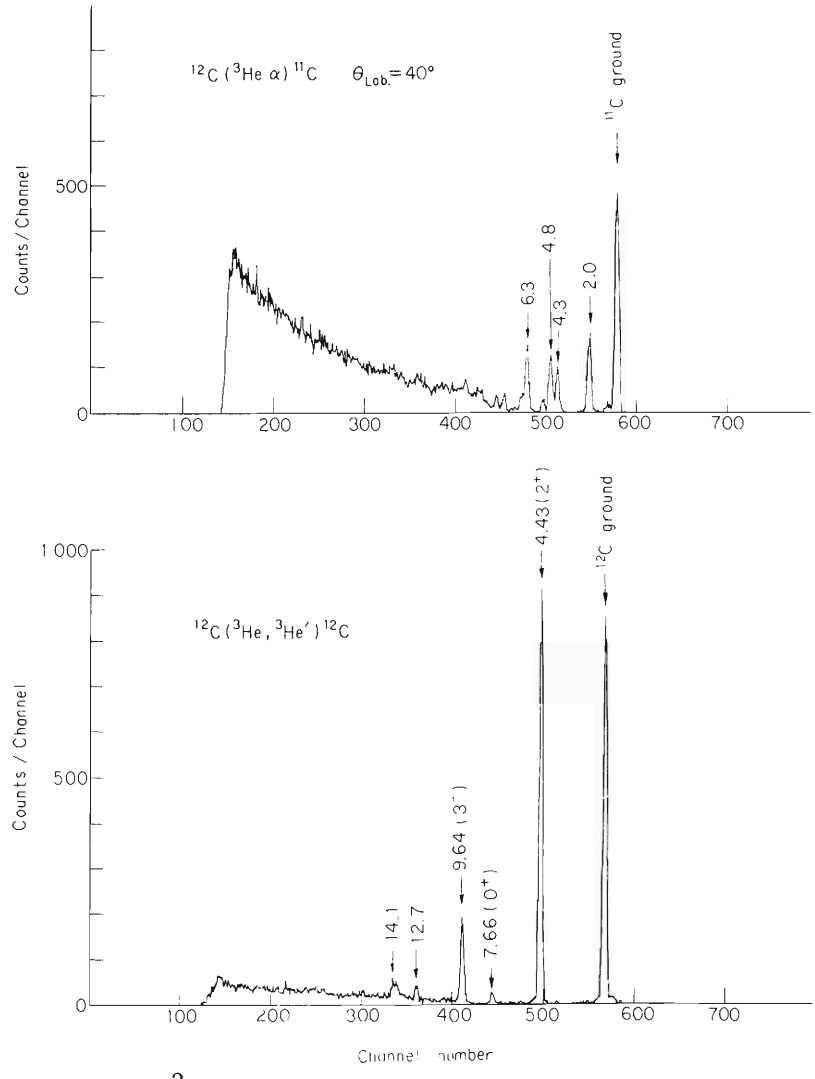

Fig. 1. Typical ^{3}He and α-particle spectra of ^{12}C (^{3}He, ^{3}He)^{12}C and ^{12}C (^{3}He,α)^{11}C reactions.

* Permanent address : Department of Physics, Kyoto University.

In Fig. 1, typical energy spectra of ^3He and α particles from ^{12}C are shown. Fig. 2 shows the differential cross section of $^{12}C(^3He, ^3He)\ ^{12}C$ reaction and the predicted curves from optical model as follows :

$$V(r) = -\left\{ V_0 f(X_R) + i4W \frac{d}{dX_D} f(X_D) + Vso \frac{(V \cdot L)}{r} \left(\frac{\hbar}{m\pi c}\right)^2 \frac{d}{dr} f(Xso) \right\} + V_c(r)$$

where $f(X_i) = \left\{1 + \exp(X_i)\right\}^{-1}$

$X_i = (r - r_i M^{1/3}) / a_i$

M : atomic mass number.

V_c : Coulomb potential due to a uniformly charged sphere of radius $1.4\ M^{1/3}$ fm.

σ : Pauli spin matrix.

L : Orbital angular momentum of the incident particle.

Table 1. Optical-model parameters that predict the curves in Fig. 2. Value of a_{so} and r_{so} are taken equal to those of real part and r_R is fixed.

Potential number	Incident energy (MeV)	V_0 (MeV)	r_R (fm)	a_R (fm)	W (MeV)	r_D (fm)	a_D (fm)	V_{so} (MeV)	θ_{max} for χ^2 fit	χ^2/N
1	24.0	142.3	1.1	.718	13.43	1.314	.823	0	82.5	8.2
2	29.2	135.0	1.1	.700	14.34	1.097	.907	0	72.1	4.5
3	34.7	129.3	1.1	.751	14.72	1.205	.834	0	62.6	17.7
4	39.6	123.0	1.1	.823	17.0	1.416	.657	0	58.5	11.2
5	24.0	139.9	1.1	.681	10.96	1.298	.921	3.609	129.5	67.4
6	29.2	134.0	1.1	.660	10.70	1.323	.882	7.70	127.8	53.1
7	34.7	124.6	1.1	.793	15.14	1.566	.605	4.75	164.4	43.7
8	39.6	124.2	1.1	.808	14.73	1.561	.611	4.48	172.2	28.3

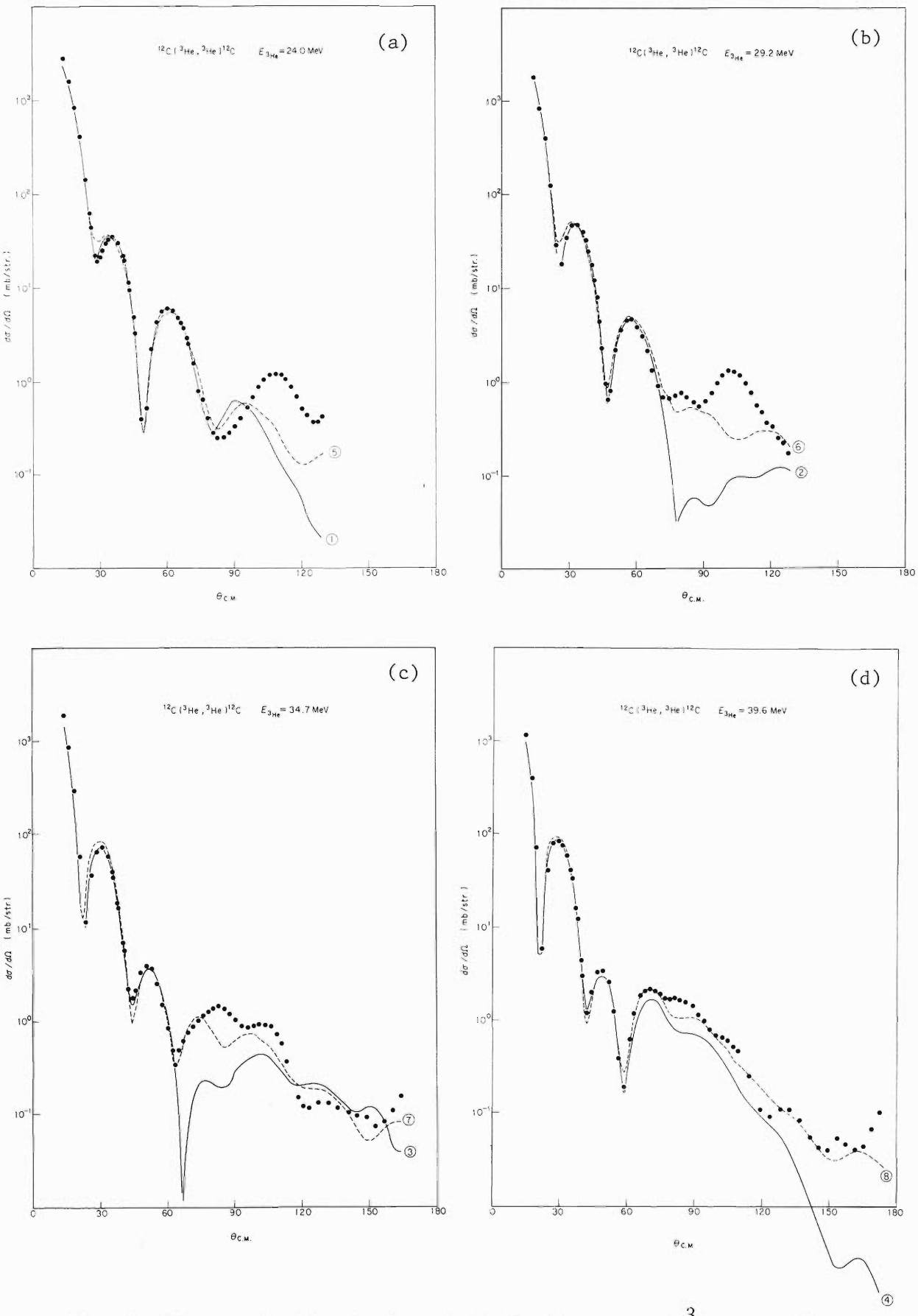

Fig. 2. The angular distribution of elastically scattered ^{3}He particles from ^{12}C. The curves are obtained from optical model prediction. The optical parameters are shown in Table 1.

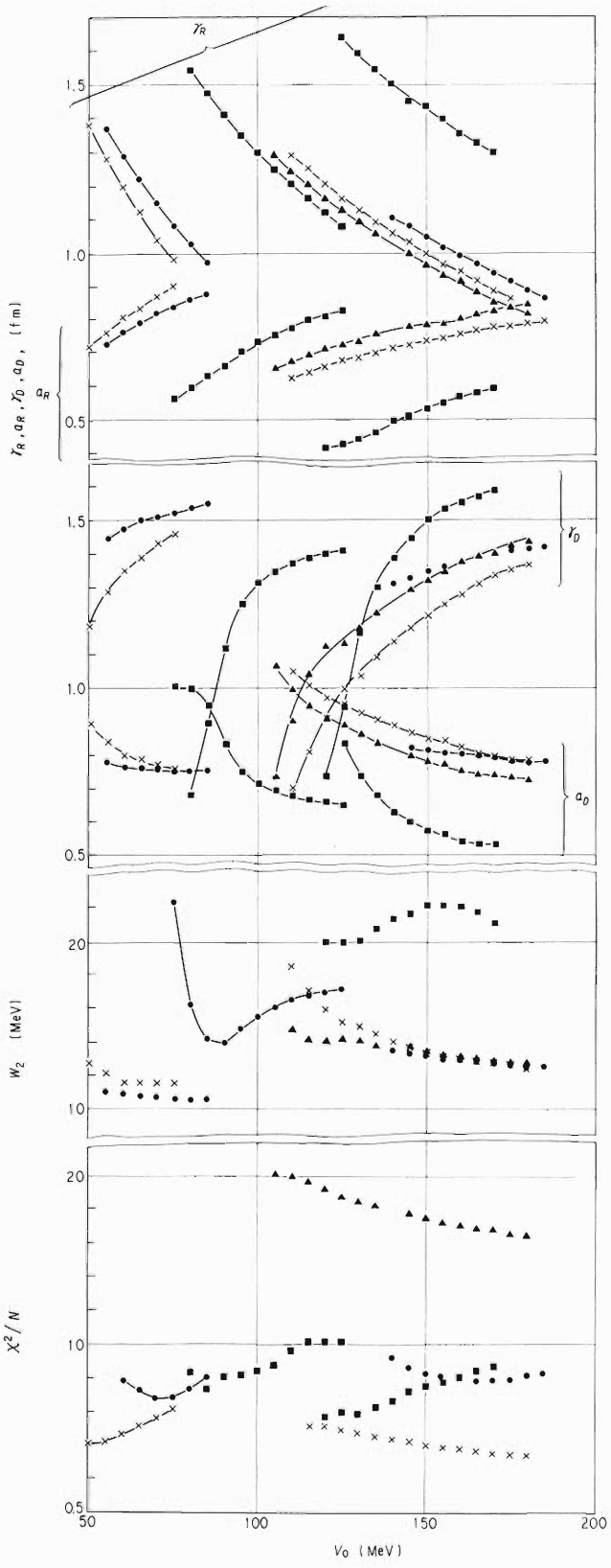

Fig. 3. Potential ambiguities given by five-parameter search at given values of V_0. The fits were done at forward three peaks of the angular distribution.

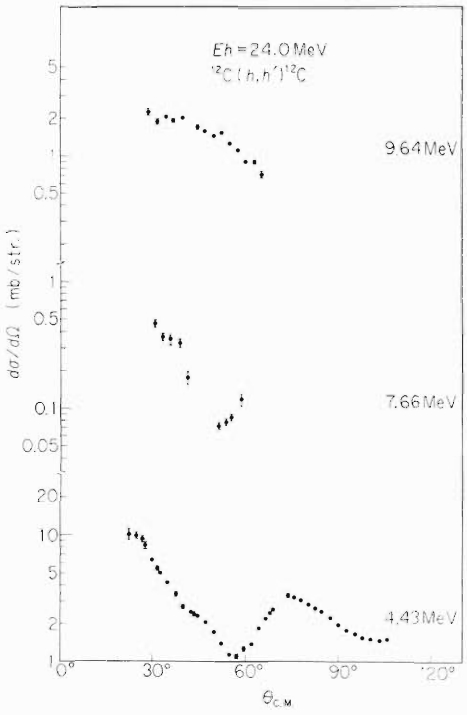

Fig. 4(a)

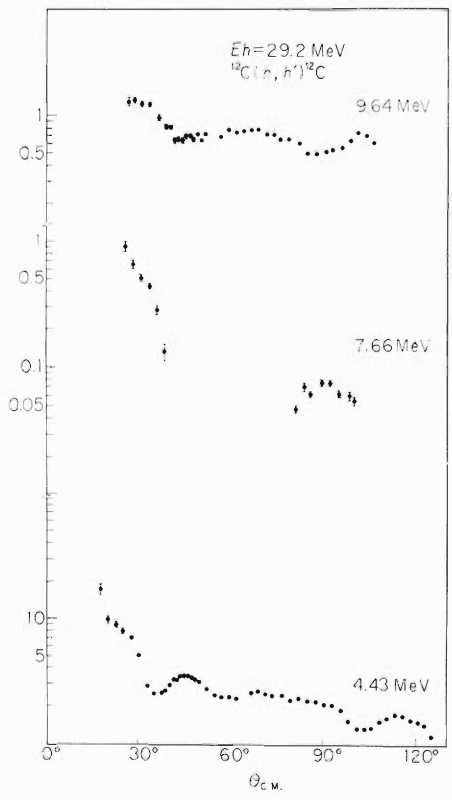

Fig. 4(b)

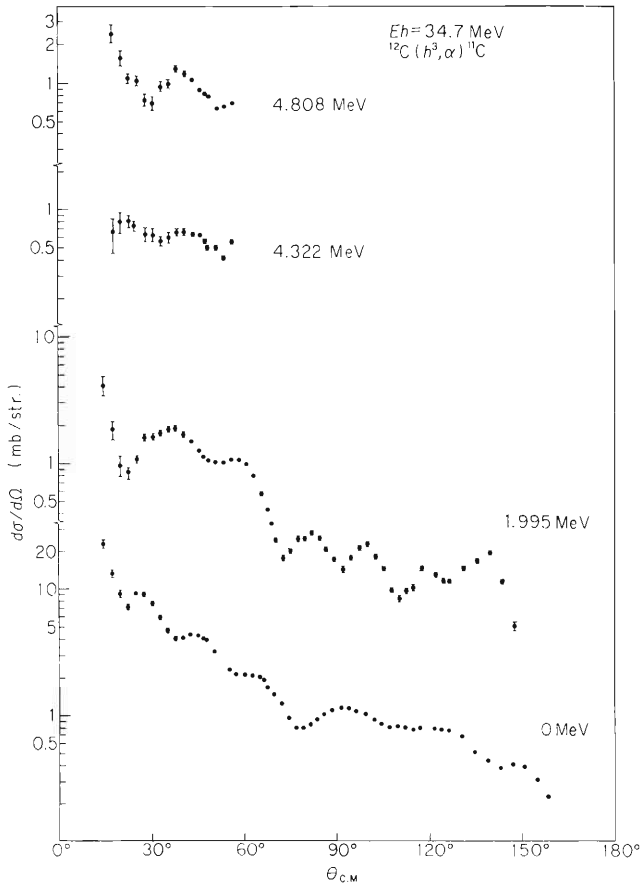

Fig. 4(c)

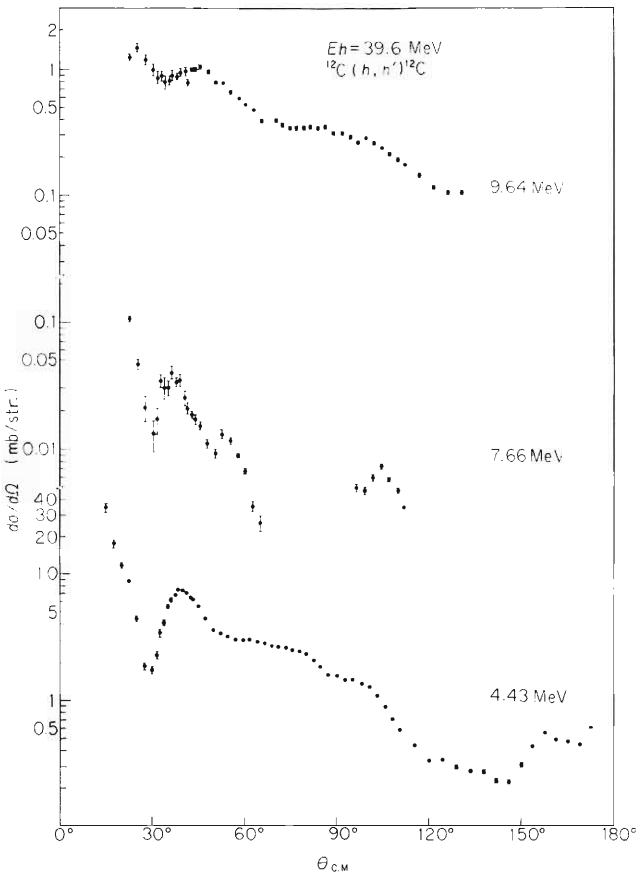

Fig. 4(d)

Fig. 4. ^{3}He-particle angular distribution of inelastic scattering from ^{12}C.

The fits were carried out at forward three peaks of differentical cross section with the "SEARCH" code[2] and so the fits of backward angle are not good. In Fig. 2, the prediction of optical potential with spin orbit coupling potential is shown. At the backward angle, the fit is fairly good. Fig. 3 shows ambiguity of the optical parameter. More detailed analysis will be done in the future. Figs. 4 and 5 show the differential cross sections of $^{12}C(^{3}He, ^{3}He')^{12}C$ and $^{12}C(^{3}He, \alpha)^{11}C$ reactions respectively. It is interesting that the cross sections are very large. DWBA analysis will also be done in the future.

The authors would like to express their sincere thanks to Dr. S. Kusuno for his help in analysis and Mr. T. Wada for the use of his "SEARCH" code.

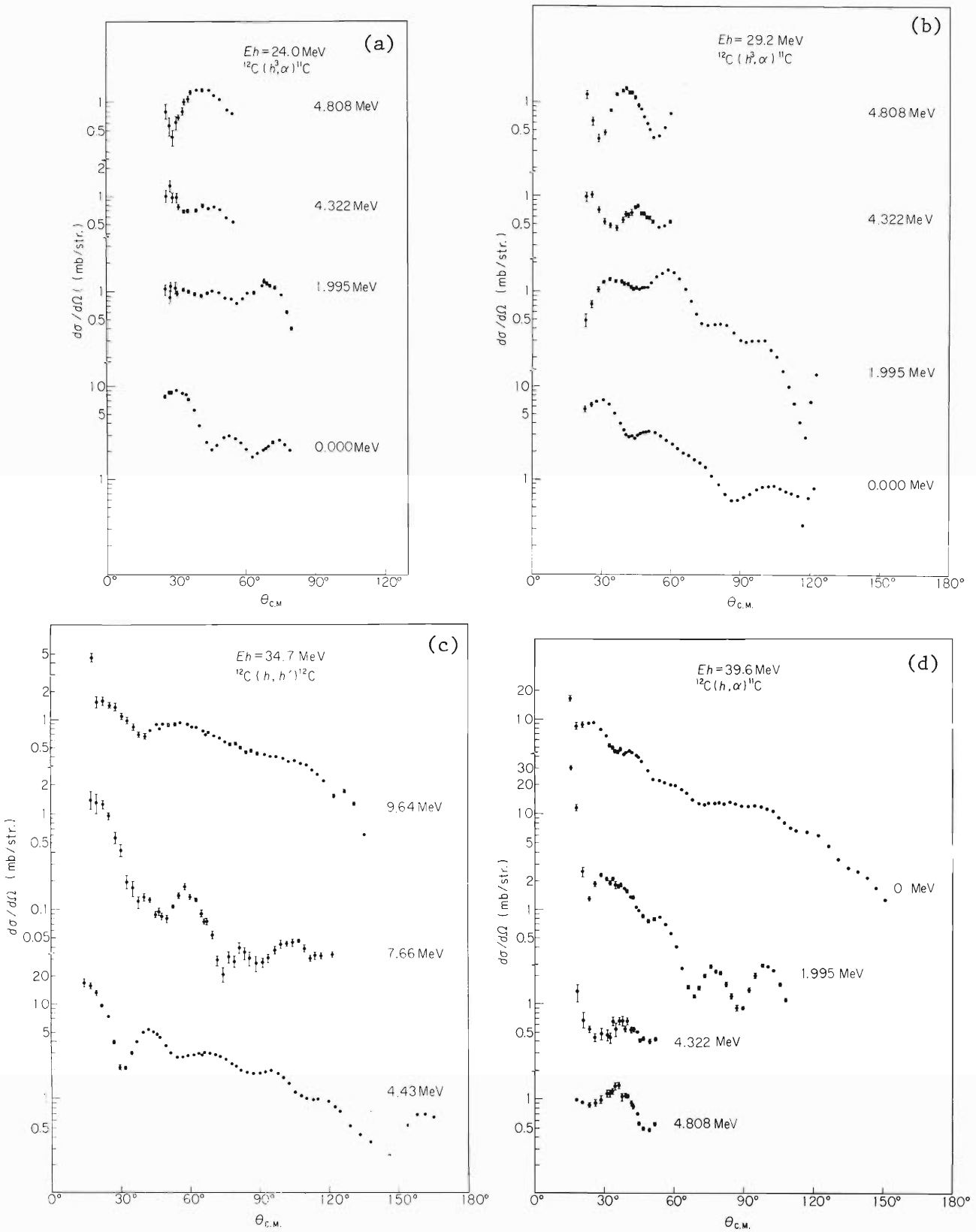

Fig. 5. Angular distribution of α - particles of $^{12}C(^{3}He,\alpha)^{11}C$ reaction.

References

1) T. Fujisawa et al. : IPCR Cyclotron Progr. Rep., 2, 77 (1968).
2) T. Wada : ibid., p. 87.

4-6. Finite-Range Calculation of Two Nucleon Transfer Reaction

S. Yamaji

Two methods of calculation of the two nucleon transfer reaction were discussed in order to compare the formulation of Glendenning to be called the "cluster" calculation with that of Lin-Yoshida to be called the "micro" calculation.[1] As an example, the cross section of the reaction $^{12}C(h, p)^{14}N(0^+, 2.31\ MeV)$ in the zero-range DWBA was calculated.[2]

A code was made for the calculation of the cross section of the two nucleon transfer reaction without a zero-range approximation, that is, with a finite-range interaction by modifying the code INS-DWBA-4.* The formulation is given in Refs. 1), 4), and 5). The finite-range calculation needs much time. For example, in the case of $^{12}C(h, p)^{14}N$ (Eh = 25.3 MeV), it takes about 10 and about 120 minutes to calculate the cross sections of "cluster" and "micro" respectively, using a computer HITAC 5020 E. So only a few cases of the finite-range calculation are reported here, assuming that the state of the captured particles is $(P1/2)^2_0$.

Before discussing the results of the finite-range calculation, we return to the zero-range calculation of Ref. 2) to compare "micro" with "cluster". This is useful to examine the condition that makes the difference between the finite-range calculations of "micro" and "cluster" so large. Cn in the expression of the spectroscopic amplitude is proportional to $(1-\alpha)^n$. The expression of α corresponding to "cluster" is given by

$$\alpha^{c)} = \frac{\nu}{2C'} = \frac{2\nu}{\nu + 6\eta^2},$$

and for "micro"

$$\alpha^{(m)} = \frac{2\nu}{\nu + 8\eta^2} + \frac{\dfrac{8\nu\eta^4}{(\nu + 8\eta^2)^2}}{\beta^2 + \dfrac{2\nu\eta^2 + 12\eta^4}{\nu + 8\eta^2}}$$

In Fig. 1 $\alpha^{(m)}$ is shown as a function of β for the cases of η = 0.1, 0.2, and 0.4 fm^{-1}, where β is the inverse of the interaction range ξ. The value of $\alpha^{(m)}$ approaches that of $\alpha^{(c)}$ as the interaction range ξ becomes large. But even in case the range is very long, for example, ξ = 3.2 fm, $\alpha^{(m)}$ is nearly equal to $2\nu/\nu + 8\eta^2$ as can be seen in Fig. 1. So, in a reasonable interaction range, we may consider that

$$\alpha^{(m)} = \frac{2\nu}{\nu + 8\eta^2} \quad \text{and} \quad \alpha^{(c)} + \frac{2\nu}{\nu + 6\eta^2},$$

and that the difference between "cluster" and "micro" does not bring about an appreciable difference of the angular distribution of the cross section. The angular distribution is rather affected by the drastic change of $\alpha^{(m)}$ according to the change of the value η. By fitting the calculated cross section to the experimental results, it is difficult to examine which method is better.

* H. Yoshida : Code INS-DWBA-4.

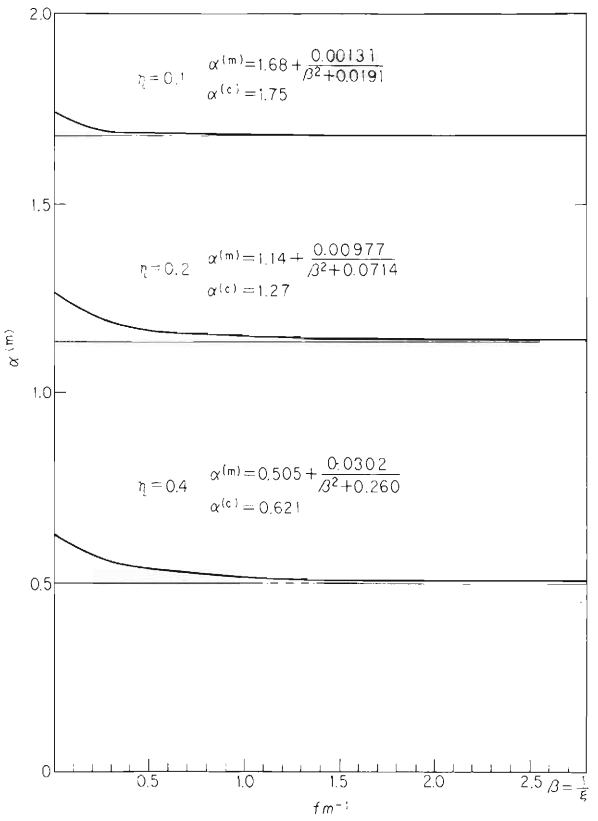

Fig. 1. Behavior of $\alpha^{(m)}$ as a function of the interaction range.

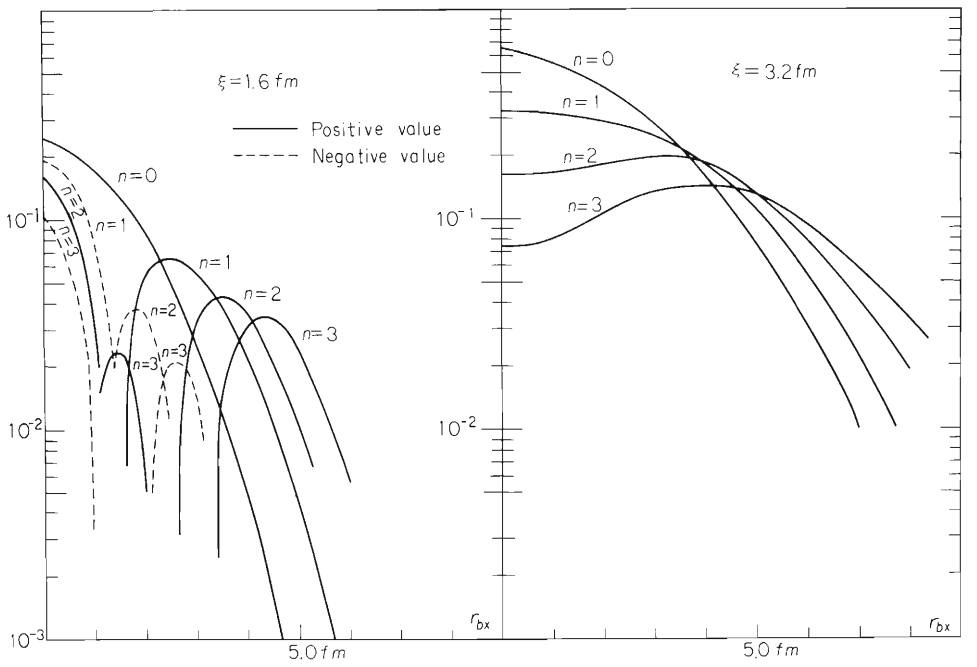

Fig. 2. Behavior of the effective interaction $D^{(m)}(r_{bx}) / \psi_{00}(r_{bx})$ for "micro". The spread η of the projectile ^{3}He is taken to be 0.2 fm^{-1}.

The reason that we may regard $\alpha^{(m)} \approx \alpha^{(c)} = \frac{2\nu}{6\eta^2 + \nu}$ in the very long range interaction with $\xi \gg \{1/\nu \text{ and } 1/\eta\}$ is also mentioned as follows : In the range of $|\vec{r}|$ in which the intrinsic state of the captured particle varies appreciably, it can be considered reasonable that the interaction $\exp\left\{-\frac{(\vec{r}_{bx} \pm \frac{1}{2}\vec{r})^2}{\xi^2}\right\} \approx \exp(-\frac{r_{bx}^2}{\xi^2})$, where $\vec{r}_{bx}$ is the vector between the particles x and b and $\vec{r}$ is that between nucleons in the captured particle x.

Then it is inferred that as the interaction range ξ becomes large, the difference between "micro" and "cluster" decreases and the difference between "zero-range" and "finite-range" increases.

In the finite-range calculation, the difference between "micro" and "cluster" consists in the expression $D^{(n)}(r_{bx})$. In Fig. 2 the behavior of $D^{(n)}(r_{bx})/\psi_{00}(4b\eta^2, r_{bx})$ is shown in the cases of the interaction range ξ = 1.6 and 3.2 fm. The spread η is fixed at 0.2 fm^{-1}. The "micro" is characterized by the fact that the interaction range is effectively given by the expression $\xi' = \frac{1}{\sqrt{B(1 - \frac{B}{4C})}}$ and ξ' is larger than ξ . For example, ξ' = 1.32, 1.46, 2.03, and 3.42 fm for ξ = 0.4, 0.8, 1.6, and 3.2 fm, respectively.

The contributions of (N, n) to the calculated cross section are expressed as $\sigma^{(m)}(N, n)$ and $\sigma^{(c)}(N, n)$. Suffixes (m) and (c) correspond to "micro" and "cluster",

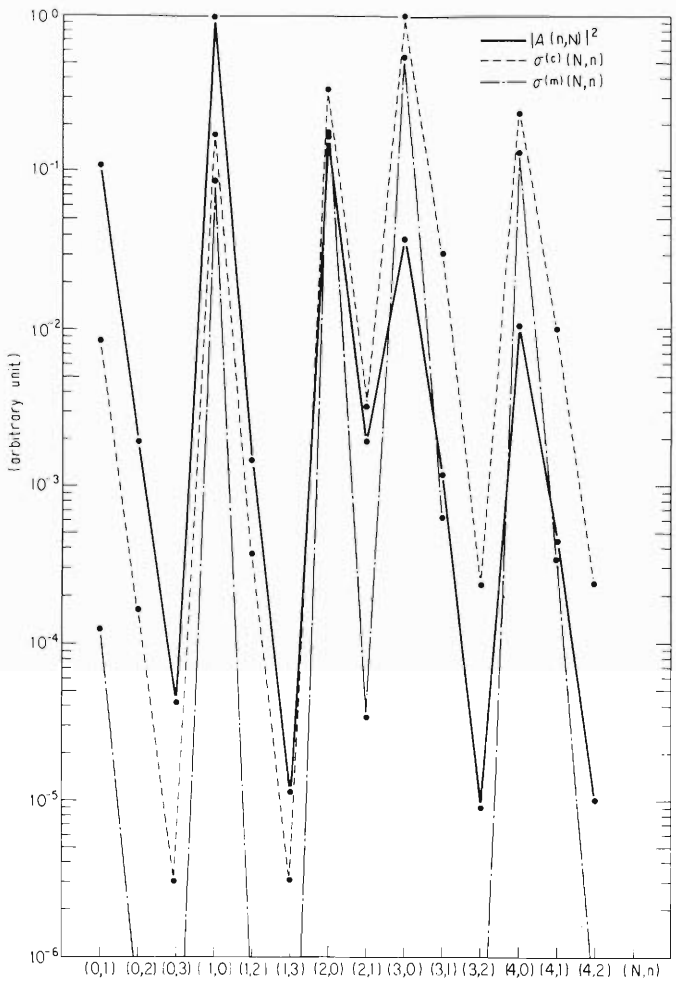

Fig. 3. Total cross section corresponding to each (N,n). We take $|A(o, 1)|^2$ = 1.0 and $\sigma^{(c)}(3,0)$ = 1.0. The interaction range is taken to be 2 fm.

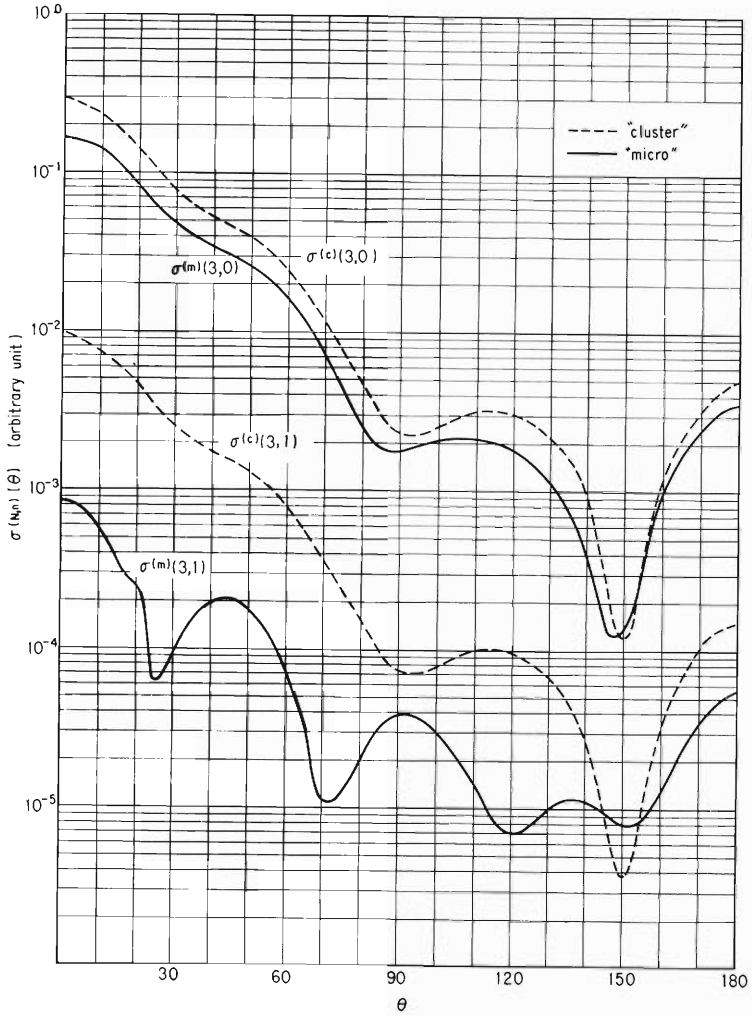

Fig. 4(a)

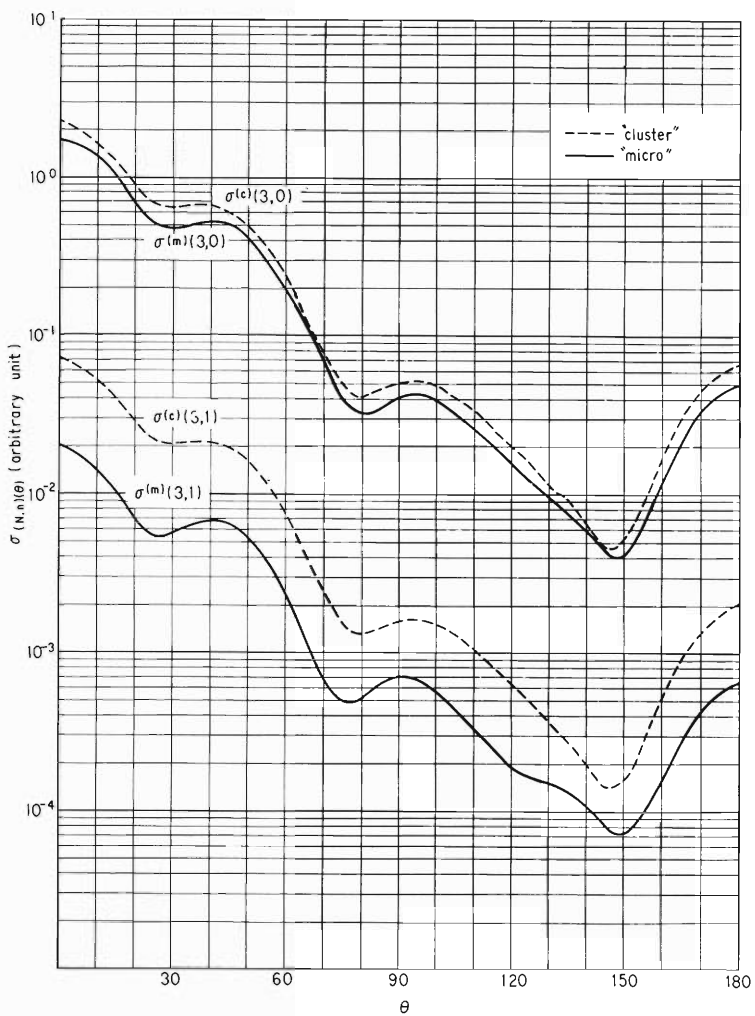

Fig. 4(b)

Fig. 4. Comparison between "micro" and "cluster" corresponding to the terms N = 3. The interaction range is taken to be 1.6 fm in Fig. 4 (a) and 3.2 fm in Fig. 4 (b).

respectively. The cross sections of main terms of (N, n) are shown in Fig. 3. The same parameters as those of Ref. 2) are used in these calculations. The range of the intergration of r_{bx} is taken to be 2.0 fm to save the computing time, although this value is too small for the case of the interaction range ξ = 2.0 fm to obtain the exact calculated values. But the whole behavior of the relative values are obtained nearly correctly form this figure.

As $D^{(n)}(r_{bx})$ of "micro" has nodes and varies rapidly, $\sigma^{(m)}(N, n)$ decreases more rapidly than $\sigma^{(c)}(N, n)$ as the node n increases. Although only up to terms of N = 4 are shown in Fig. 3, $\sigma^{(c)}(N, n)$ decreases more slowly than $|A(n, N)|^2$ and we took up to terms of N = 12 for the numerical calculations.

In Figs. 4 (a) and 4 (b), the calculated differential cross sections $\sigma^{(m)}(3,n)$ and $\sigma^{(c)}(3, n)$ are shown. They are main terms as can be seen form Fig. 3. The scale is arbitrary, but relative contributions of each term are given correctly in these figures, if we take the same strength concerning the interaction of ξ = 1.6 and 3.2 fm. As the contributions of term of n = 0 are very large compared with those of terms of $n \neq 0$ and angular distributions of $\sigma^{(m)}(3, 0)$ and $\sigma^{(c)}(3, 0)$ are very similar, the differential cross sections of both "micro" and "cluster" are supposed to be similar in the "finite-range" calculation. The difference between "micro" and "cluster" is found to become small as the interaction range becomes large from Figs. 4 (a) and 4 (b). This is the same as in the "zero-range" case.

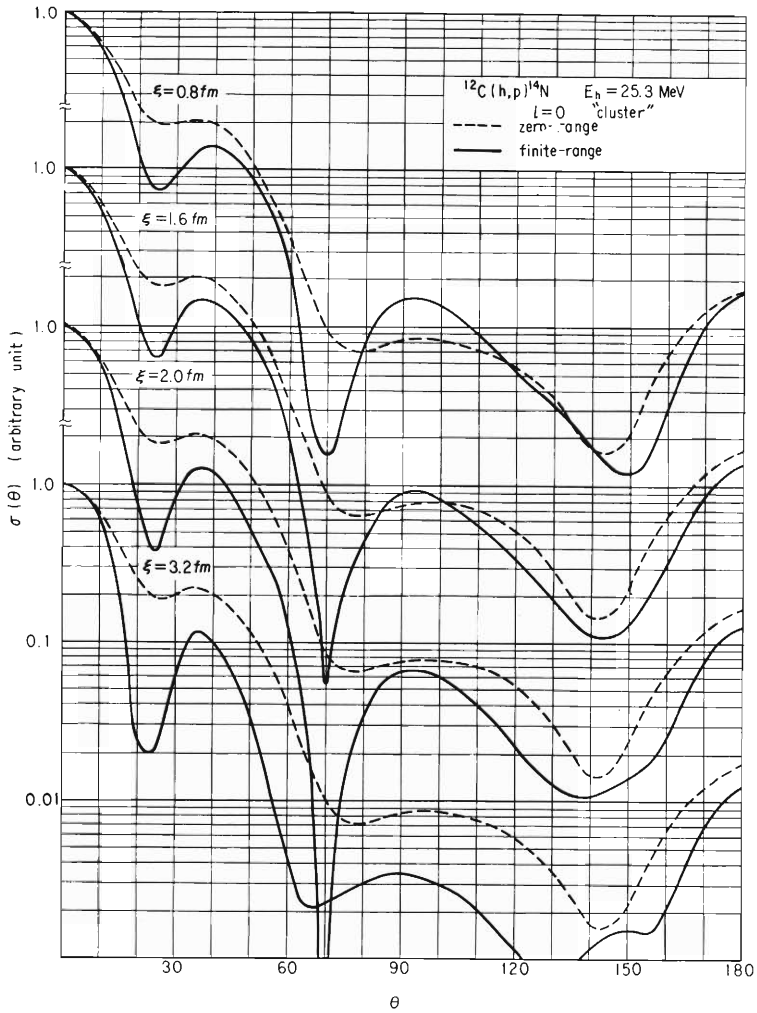

Fig. 5. Comparison between the "zero-range" calculation and the "finite-range" calculation.

Although we must calculate DWBA amplitudes corresponding to each (N, n) term and sum over them to obtain the cross section $\sigma(\theta)$ of "micro" and "finite-range", we obtain the cross section $\sigma(\theta)$ by calculating the form factor $\sum_{N,n} A(n, N)\phi_{Nl}(\nu \cdot r_{xA})$ in the "cluster" and "finite-range" calculation because of the independence of $D^{(n)}(r_{bx})$ of n. In the numerical calculation it is much easier in the "cluster" case than in the "micro" case.

In Fig. 5, the cross sections $\sigma(\theta)$ corresponding to ξ = 0.8, 1.6, 2.0, and 3.2 fm are shown. From this figure, we can see that the difference between "zero-range" and "finite-range" becomes large as the interaction range ξ increases, and that the more drastic difference appears at the backward angle.

The absolute values of $\sigma(0^{\circ})$ are shown in Table 1. The strength of the interaction used in this calculation was determined form Ref. 2).

The numerical calculation of the cross section is examined in more detail by taking the case of ξ = 2.0 of Fig. 5 as an example. As this calculation corresponds to "cluster", $D^{(n)}(r_{bx})$ is independent of n and of a Gaussian type with the spread $\frac{1}{\sqrt{2\eta^2 + 1/\xi^2}} \approx 1.74$ fm. The radial dependence of the captured particle is the same as that of the form factor of the "cluster" and "zero-range" case given in Fig. 2 of Ref. 2).* Using such radial dependences, we show the expression $\beta_{\ell m}(r_b, r_a, \theta)$ at $\theta = 0^{\circ}$ in Fig. 6, where

$$\beta_{\ell m}(r_b, r_a, \theta) = \frac{1}{i^{\ell}\sqrt{2\ell+1}} \int d\hat{r}_a \int d\hat{r}_a \, \chi_b^{(-)*}(\vec{k}_b, \vec{r}_b) \, f_{\ell m}(\vec{r}_b, \vec{r}_a) \, \chi_a^{(+)}(\vec{k}_a, \vec{r}_a).$$

The notations of the above expression are given in Refs. 1) and 3).

Table 1. Absolute values of the cross section at the forward peak.

The strength of the interaction used here are obtained by the condition that a neutron and a proton are bound at 2.226 MeV in the Gaussian well $V_{np} \exp(-r^2_{np}/\xi^2)$.[2)]

Interaction-range (fm)	Interaction strength V_{np} (MeV)	Cross section (mb/sr)	
		Zero-range	Finite-range
0.8	212	0.019	0.032
1.6	64	0.049	0.074
2.0	45	0.065	0.096
3.2	22	0.10	0.14

* In Fig. 2 the form factors of 4 cases corresponding to ξ = 0.4, 0.8, 1.6, and 3.2 fm are shown. But as can be seen from the expression of C_n of Ref. 1), the radial dependence of the normalized form factor is independent of ξ. As the results of the 4 cases are quite the same, it was enough to show only one case previously.

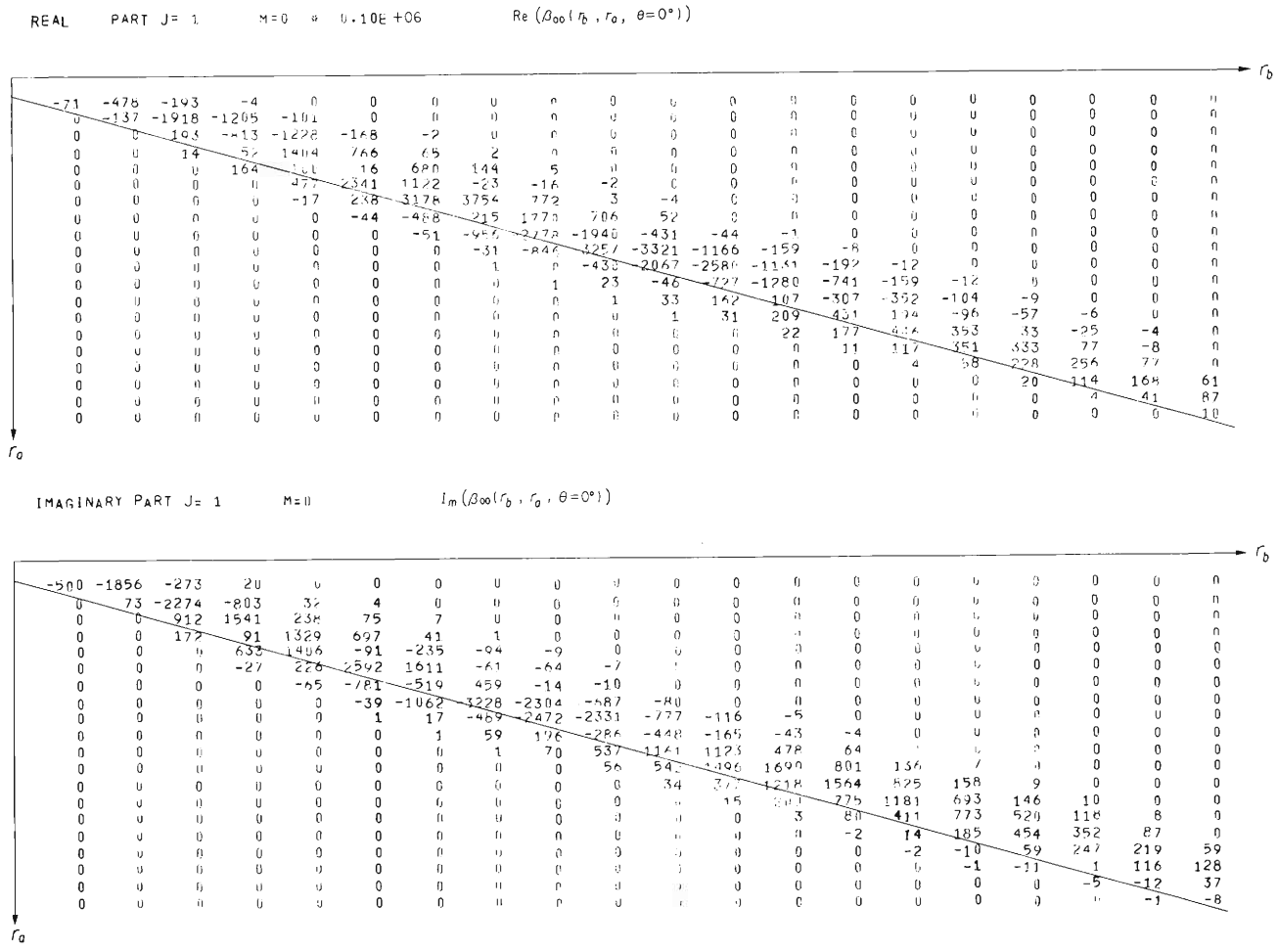

Fig. 6. Values of $\beta_{00}(r_b, r_a, \theta = 0^\circ)$. $\xi = 2.0$ fm.
The values of $\beta_{00}(r_b = \frac{A}{B} r_a, \theta = 0^\circ)$ correspond to the points on the diagonal line. The interval of r_b is 0.85 fm from these points. The interval of r_a is 0.4 fm. For example, we can see from this figure that

$$R_e\beta_{00}\left\{(r_b = 0.4 \times \frac{6}{7} = 0.34,\ r_a = 0.4,\ \theta = 0^\circ)\right\} = -71 \times 10^{-6}$$

$$R_e\beta_{00}\left\{(r_b = 0.4 \times \frac{6}{7} \times 4 = 1.4,\ r_a = 0.4 \times 4 = 1.6,\ \theta = 0^\circ)\right\} = 52 \times 10^{-6}$$

$$R_e\beta_{00}\left\{(r_b = 0.4 \times \frac{6}{7} \times 4 + 0.85 \times 2 = 3.1,\ r_a = 0.4 \times 4 = 1.6,\ \theta = 0^\circ)\right\} = 766 \times 10^{-6}$$

$$R_e\beta_{00}\left\{(r_b = 0.4 \times \frac{6}{7} \times 4 - 0.85 = 0.52,\ r_a = 0.4 \times 4 = 1.6,\ \theta = 0^\circ)\right\} = 14 \times 10^{-6}$$

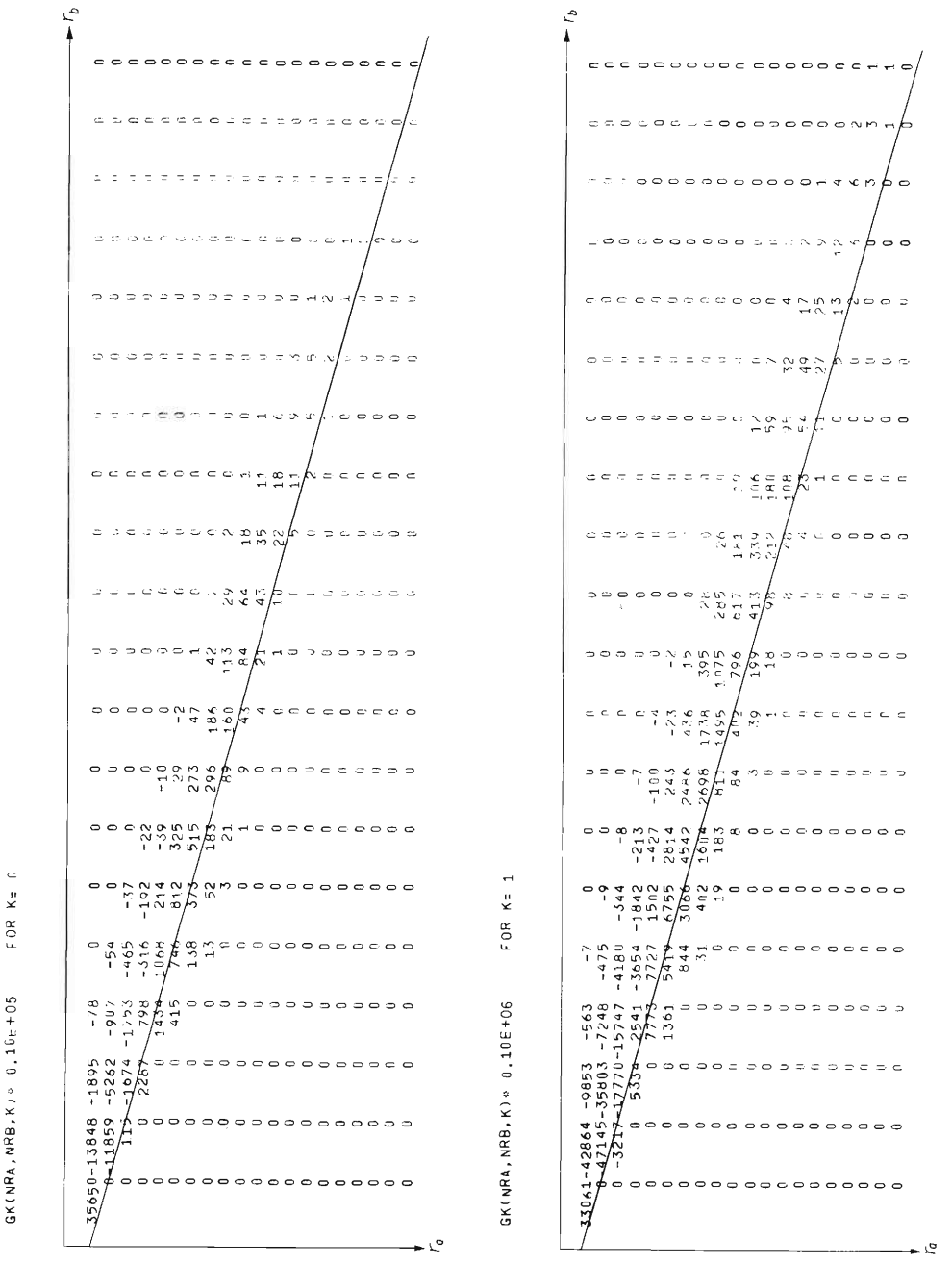

Fig. 7. Values of the form factors $g_K(r_b, r_a^{52})$. $\xi = 2.0$ fm.

Fig. 6 is convenient to see where the nuclear reaction mainly occurs. Moreover we can examine the validity of the "zero-range" approximation. If the value $\beta_{\ell m}(r_b = \frac{A}{B} r_a, r_a, \theta)$ which is the diagonal value in Fig. 6 is nearly proportional to the integral $\int \beta_{\ell m}(r_b, r_a, \theta)\, dr_b$ which corresponds to the sum of $\beta_{\ell m}(r_b, r_a, \theta)$ over the horizontal line in Fig. 6, the zero-range approximation is thought to be fairly good.

Finally the form factor of the finite-range calculation $g_K(r_b, r_a)$ is shown in Fig. 7, where $g_K(r_b, r_a)$ is proportional to

$$\int_{-1}^{1} \sum_{N,n} D^{(n)}(r_{bx})\, A(n, N)\, \phi_{Nl}(r_{xA})\, P_K(\mu)\, d\mu.$$

The detailed expression of this quantity is given in Refs. 4) and 5).

References

1) S. Yamaji : IPCR Cyclotron Progr. Rep., 2, 83 (1968).
2) S. Yamaji : ibid., 3, 47 (1969).
3) S. Yamaji and C. L. Lin : Genshikaku Kenkyu, 14, 366 (1969).
4) T. Une, T. Yamazaki, S. Yamaji, and H. Yoshida : Reference Manual for INS-DWBA-3, Institute of Nuclear Study, University of Tokyo (1965).
5) N. Austern, R. M. Drisko, E. C. Halbert, and G. R. Satchler : Phys. Rev., 133, B3 (1964).

4-7. Rotations and $K^{\pi}=1^{+}$ States of Deformed Even-Even Nuclei

S. Kusuno* and T. Kammuri**

In the framework of Bohr's model[1] treating deformations of order two, we have three Euler angles and two deformation parameters corresponding to rotations of the whole nucleus, β-vibrations ($K^{\pi}=0^{+}$) and γ-vibrations ($K^{\pi}=2^{+}$), respectively. The degree of freedom corresponding to $K^{\pi}=1^{+}$ is found to be related with rotations, if we consider the relation between the K = 1 components of angular momentum and spherical harmonics of rank two :

$$\ell_{+1} = (\text{sign of } \Delta n_z)\cdot m(\omega_z \pm \omega_\perp)(4\pi/15)^{1/2}\, r^2\, Y_{2+1}, \qquad (1)$$

where $\pm$ corresponds to the selection rules (ΔN, Δn_z, $\Delta \Lambda$) = (0, $\pm$ 1, +1) and ($\pm$2, $\pm$1, +1), respectively. In Eqn. (1), we assume the simplest anisotropic harmonic oscillator potential without spin-orbit force. According to the cranking model,[2] the moment of inertia of the nucleus is given by

$$J = 2\hbar^2 \Sigma_\nu \left| \langle \nu \left| \hat{J}_{+1} \right| o \rangle \right|^2 / \varepsilon_\nu \qquad (2)$$

Where $\hat{J}_{+1}$ is the K = 1 component of the total angular momentum of nucleus $\hat{J}_{+1} = -\frac{1}{\sqrt{2}}(\hat{J}_1 + \hat{J}_2)$ and ε_ν is excitation energy of the $K^{\pi}=1^{+}$ two-quasiparticle state $|\nu\rangle$ relative to the quasiparticle vacuum $|o\rangle$. If we consider the system without intrinsic spins, Eqns. (1) and (2) seem to imply the spurious character of the $K^{\pi}=1^{+}$ vibrations, because Eqn. (2) corresponds to the zero-energy solution of the dispersion equation of random-phase approximation. This inference, however, is not correct from the theoretical point of view.

Recent experimental data concerning $K^{\pi}=1^{+}$ states[3)~8)] require more detailed treatment than the simple two-quasiparticle picture of Gallagher and Soloviev.[9] Table 1 shows several $K^{\pi}=1^{+}$ states found mainly by off-beam spectroscopy. Energy gap parameters calculated by Nilsson and Prior[10] are also shown. These data show that we should take into account some correlations neglected. The spurious character of the $K^{\pi}=1^{+}$ vibrations should be disposed of according to Ref. 11).

Our Hamiltonian consists of the single-particle term, the pairing and the (spin)-quadrupole forces[12), 13)] :

$$\begin{aligned}
\bar{H} &= \bar{H}_{sp} - G\bar{P}^{+}\bar{P} - \frac{1}{2}\sum_{s=0}^{1} \chi_s \sum_\mu \bar{Q}_\mu^{(s)+}\, \bar{Q}_\mu^{(s)}, \\
\bar{H}_{sp} &= \sum_i (\varepsilon_i - \lambda)\, C_i^{+} C_i, \\
\bar{P}^{+} &= \frac{1}{2}\sum_i C_i^{+} C_{\tilde{i}}^{+}, \\
\bar{Q}_\mu^{(s)} &= \sum_{ij} (T_\mu^{(s)})_{ij}\, C_i^{+} C_j = (-)^s\, \bar{Q}_{\tilde{\mu}}^{(s)+},
\end{aligned} \qquad (3)$$

* On leave of absence from University of Osaka, Japan.

** Present adress, Københavns Universitet, Niels Bohr Institutet, Denmark.

Table 1. Observed $K^{\pi} = 1^{+}$ states.

Nucleus	$KI^{\pi} = 11^{+}$ (keV)	Configuration	Δp (keV)	Δn (keV)	Reference	Remarks
^{156}Gd	1966	$\frac{5^+}{2}[413] - \frac{3^-}{2}[411]_p$	1099.0	1040.0	3)	Four $I^{\pi} = 1^{+}$ levels Decay of ^{156}Eu
^{160}Dy	2085.3		1001.1	939.9	4)	$I^{\pi} = 1^{+}, 2^{+}, 3^{+}, 4^{+}$ Decay of $^{160}H_0$
^{162}Dy	1745	$\frac{3^-}{2}[521] - \frac{5^-}{2}[523]_n$	968.0	876.2	5)	$I^{\pi} = 1^{+}, 2^{+}, ..., 6^{+}$ ^{163}Dy (d, t)
^{170}Yb	1659.41±0.21 1775.70±0.20		872.6	759.7	6)	Two sets of $I^{\pi} = 1^{+}, 2^{+}$ Six $K^{\pi} = 1^{+}$ levels Decay of ^{170}Lu
^{172}Yb	2008	$\frac{5^-}{2}[512] - \frac{3^-}{2}[521]$	843.7	705.2	7)	$I^{\pi} = 1^{+}, 2^{+}, 3^{+}, 4^{+}$ ^{173}Yb (d, t)
^{178}Hf	1430		820.0	654.1	3)	
^{188}Os	1843.3 2099.5	$\frac{1^-}{2}[510] - \frac{3^-}{2}[512]_n$ $\frac{3^+}{2}[402] - \frac{5^+}{2}[402]_p$			8)	Decay of ^{188}Ir

where C_i^+ and C_i are the creaption and annihilation operators for the single-particle state i. The single-particle Hamiltonian has diagonal matrix elements ϵ_i, and λ is a Lagrange multiplier used in order to fix the average number of particles in the ground state. We denote by G and χ_s the strength of the pairing and quadrupole (s = 0) or spin-quadrupole (s = 1) forces, respectively. The $(T^{(s)}_{\mu})_{ij}$ are the matrix elements of the single-particle quadrupole moments $i^2 r^2 \; Y_{2\mu}$ (s = 0) and spin-quadrupole moments $i^2 r^2 \; [\sigma \otimes Y_2]_{2\mu}$ (s = 1). In treating the intrinsic excitations, we should subtract the rotational Hamiltonian

$$H_{rot} = \frac{\hbar^2}{2J}(\hat{J}^2 - \hat{J}_3^2) = \frac{\hbar^2}{2J} \sum_{\mu = \pm 1} \hat{J}_{\mu}^{+} \hat{J}_{\mu} \,, \qquad \hat{J}_{\mu} = \sum_{ij} (\hat{J}_{\mu})_{ij} C_i^{+} C_j = -(\hat{J}_{-\mu})^{+}, \tag{4}$$

from the original one. If we introduce the quasiparticle operators α_i^{+} and α_i by

$$C_i^{+} = u_i \, \alpha_i^{+} + v_i \, \alpha_{\tilde{i}} \,, \tag{5}$$

the intrinsic Hamiltonian is written as

$$
\begin{aligned}
&H = H_0 + H_1 + H' + H'', \\
&H_1 = \Sigma_i E_i \alpha_i^+ \alpha_i, \\
&H' = -\frac{1}{2}\chi_0 \Sigma_\mu Q_\mu Q_{\tilde{\mu}} - \frac{1}{2}\chi_1 \Sigma_\mu S_\mu S_{\tilde{\mu}} - \frac{1}{2J}\Sigma_\mu I_\mu I_{-\mu}, \\
&Q_\mu = \sqrt{2}\,\Sigma_p L_p^{(0)\mu} X_p, \\
&S_\mu = i^\mu \sqrt{2}\,\Sigma_p L_p^{(1)\mu} P_p, \\
&I_\mu = i^\mu \sqrt{2}\,\Sigma_p J_p^\mu P_p,
\end{aligned}
\tag{6}
$$

where we have Introduced new variables

$$
\begin{aligned}
X_{ij} &= \frac{1}{\sqrt{2}}(\alpha_i^+ \alpha_{\tilde{j}}^+ + \alpha_{\tilde{i}} \alpha_j) \equiv X_p, \\
P_{ij} &= \frac{i}{\sqrt{2}}(\alpha_i^+ \alpha_j^+ - \alpha_{\tilde{i}} \alpha_j) \equiv P_p, \\
L_p^{(s)\mu} &= (u_i v_j + (-)^s v_i u_j)(T_\mu^{(s)})_{ij}, \\
J_p^\mu &= (u_i v_j - v_i u_j)(\hat{J}_\mu)_{ij}.
\end{aligned}
\tag{7}
$$

Here, H_0 and E_i are the expectation values of H with respect to the quasiparticle vacuum and the quasiparticle energy. We neglect H '', which contains the remaining part of the Hamiltonian. We introduce the canonical transformation further given by

$$
\begin{aligned}
Y_q &= \Sigma_p \lambda_{qp} X_p, \\
\Pi_q &= \Sigma_p \mu_{qp} P_p .
\end{aligned}
\tag{8}
$$

Then, the total Hamiltonian is diagonalized by

$$
\begin{aligned}
\left[Y_q, H \right] &= iB_q \Pi_q, \\
\left[\Pi_q, H \right] &= -iC_q Y_q.
\end{aligned}
\tag{9}
$$

This set of equations gives the following secular equation :

$$
\begin{vmatrix}
A - J/2\hbar^2 & D & E \\
\hbar^2\omega^2 D & B - 1/2\chi_0 & \hbar^2\omega^2 F \\
E & F & C - 1/2\chi_1
\end{vmatrix} = 0,
\tag{10}
$$

where

$$A = \Sigma_p \frac{\varepsilon_p (J_p^{\mu})^2}{\varepsilon_p^2 - \hbar^2\omega^2}, \qquad B = \Sigma_p \frac{\varepsilon_p (L_p^{(0)\mu})^2}{\varepsilon_p^2 - \hbar^2\omega^2}, \qquad C = \Sigma_p \frac{\varepsilon_p (L_p^{(1)\mu})^2}{\varepsilon_p^2 - \hbar^2\omega^2},$$

$$D = \Sigma_p \frac{L_p^{(0)\mu} J_p^{\mu}}{\varepsilon_p^2 - \hbar^2\omega^2}, \qquad E = \Sigma_p \frac{\varepsilon_p L_p^{(1)\mu} J_p^{\mu}}{\varepsilon_p^2 - \hbar^2\omega^2} \qquad F = \Sigma_p \frac{L_p^{(0)\mu} L_p^{(1)\mu}}{\varepsilon_p^2 - \hbar^2\omega^2} \tag{11}$$

In the limit of zero-energy excitation $\hbar\omega = 0$, Eqn. (10) reduces to the modified expression for the moment of inertia,[14]

$$\frac{1}{2\hbar^2} J = A_0 + \frac{2\chi_1 E_0^2}{1 - 2\chi_1 C_0}, \tag{12}$$

where A_0 etc. are values of A etc. at $\hbar\omega = 0$. Eqn. (12) is the cranking-model expression

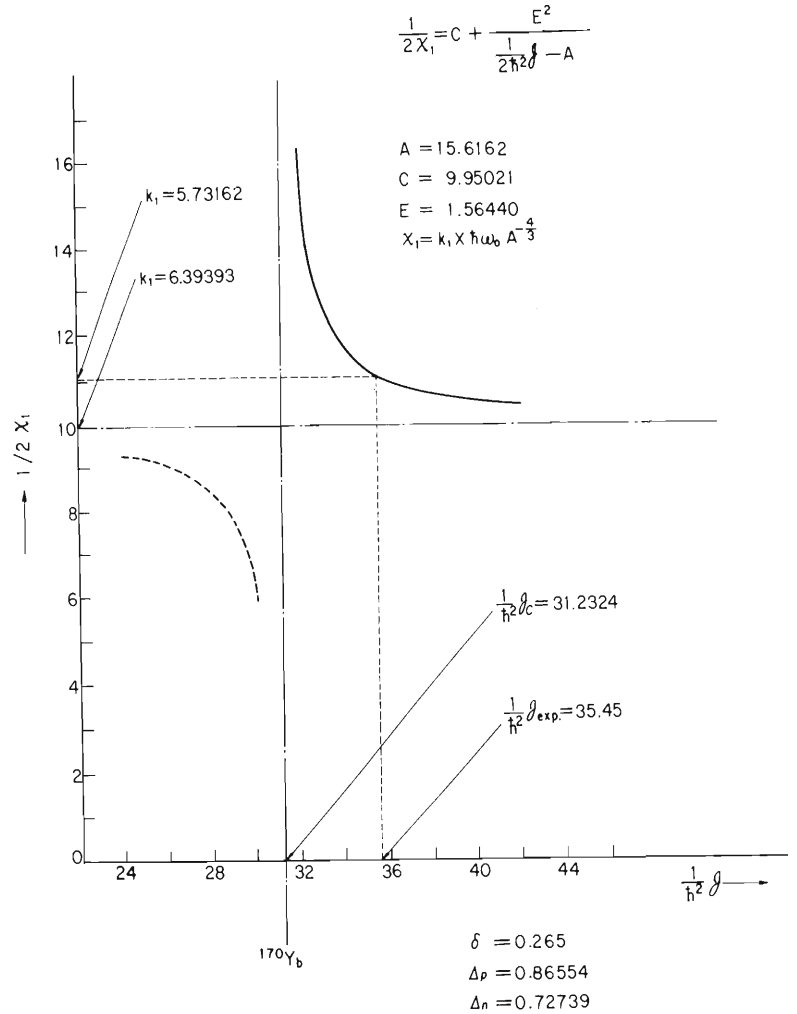

Fig. 1. Relation between the moment of inertia and the strength of the spin-quadrupole force χ_1. Quantities J_c and J_{exp} are cranking-model and observed moment of inertia, respectively.

for the moment of inertia in the limit of $\chi_1 = 0$. Another types of spin-dependent correlations such as $\sigma \cdot \sigma$ [15] and $\ell \cdot s$ [16] can give the same expressions. Therefore, we can measure the spin-dependent correlations by comparing Eqn. (12) with observed moment of inertia. Excitation energy of $K^\pi = 1^+$ states are obtained by solving Eqn. (10), or

$$\frac{1}{2\chi_1} = S(\hbar\omega), \tag{13}$$

with

$$S(\hbar\omega) = C + \frac{\frac{2\hbar^2}{J} E^2(1-2\chi_0 B) + \hbar^2 w^2 \cdot 2\chi_0 \left\{(1 - \frac{2\hbar^2}{J} A)F^2 + \frac{4\hbar^2}{J} \cdot DEF\right\}}{(1 - \frac{2\hbar^2}{J} A)(1 - 2\chi_0 B) - \frac{4\hbar^2}{J} \cdot \chi_0 \cdot \hbar^2\omega^2 D^2}, \tag{14}$$

where it should be noted that the relation between J and χ_1 is fixed according to Eqn. (12).

Numerical caluculation is applied to ^{170}Yb, where six $I^\pi K = 1^+1$ states are identified.[6] As the single-particle Hamiltonian, we take that of Nilsson[17] with the parameters of case A of Ref. 10). Deformation parameter δ is taken to be 0.265. Three

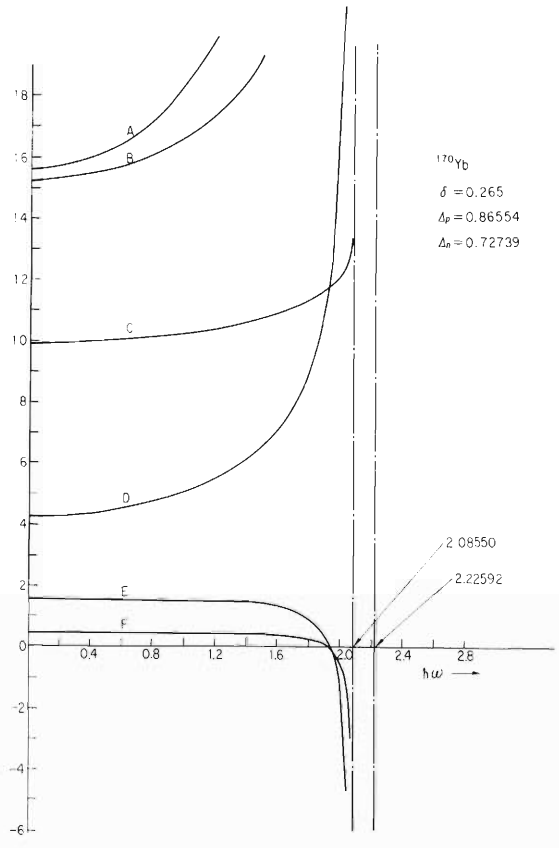

Fig. 2. Behaviors of quantities defined by Eqn. (11) vs. excitation energy $\hbar\omega$.

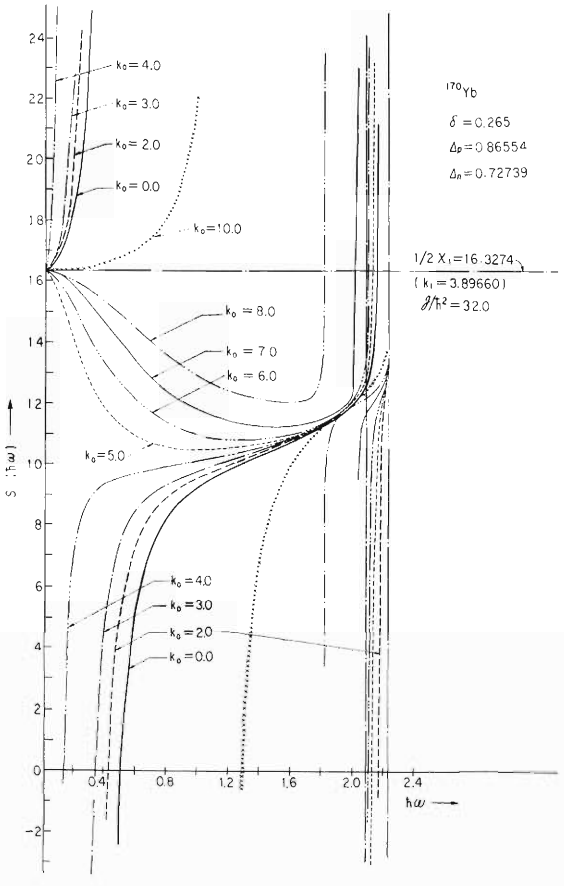

Fig. 3. Behaviors of dispersion Eqn. (13) vs. excitation energy $\hbar\omega$. Solutions are obtained at the intersections of S($\hbar\omega$) with $\frac{1}{2\chi_1}$ line.

major shells are taken into account, viz., N = 3 − 5 and N = 4 − 6 for proton and neutron systems, respectively. Strength of the pairing force is $G_p \times A$ = 23.8 MeV and $G_n \times A$ = 17.5 MeV, from which energy gap parameters Δ_p = 0.86554 MeV and Δ_n = 0.72739 MeV are obtained. Strength parameters of (spin) - quadrupole force is defined by $\chi_s = k_s \times \hbar\omega_0(\delta) \times A^{-4/3}$ MeV. Fig. 1 shows the relation between χ_1 and J . Usual cranking-model expression for $J/\hbar^2$ is 31.23 MeV^{-1}, which corresponds to $k_1 = 0.0$. We obtain $k_1 = 5.73$ in order to give the observed $J/\hbar^2 = +35.45\ MeV^{-1}$. This result is consistent with Ref.13). Fig. 2 shows the behavior of quantities defined by Eqn. (11), where the lowest two-quasiparticle energy is 2.0855 MeV. Excitation energy of $K^\pi = 1^+$ states are obtained by the dispersion equation shown in Fig. 3. In order to see the nature of this equation, the moment of inertia is fixed near the cranking-model value, $J/\hbar^2 = 32.0\ MeV^{-1}$ and k_0 is varied. Most probable value of k_0 is found to be 8.0 in order to explain the observed lowest excitation energy 1.659 MeV. This value of k_0 is also consistent with Ref. 13) Other values give excitation energies of almost two-quasiparticle picture.

If we would use only spin-quadrupole forces to explain the $K^\pi = 1^+$ states, we could have lower excitation energies. This treatment, however, has a spurious character related with rotations. Electromagnetic structures of the $K^\pi = 1^+$ states are now being studied by the authors.

References

1) A. Bohr : K. Danske Vidensk. Selsk. mat.-fys. Medd., 26, No. 14 (1952).
2) D. R. Inglis : Phys. Rev., 96, 1059 (1954).
3) Dzhelepov and Shestopalova : Nuclear Structure, Dubna Symposium 1968, p. 39 (IAEA, Vienna 1968).
4) E. Grigoriev et al. : Izv. Akad. Nauk SSSR, ser. fiz., 33,635 (1969).
5) A. Bäcklin et al. : Phys. Rev., 160, 1011 (1967).
6) B. A. Balalaev et al. : Izv. Akad. Nauk SSSR, ser. fiz., 32, 730 (1968).
7) D. G. Burke and B. Elbek : K. Danske Vidensk. Selsk. mat.-fys. Medd., 36, No. 6 (1967).
8) T. Yamazaki and J. Sato : Nucl. Phys., A130, 456 (1969).
9) C. J. Gallagher, Jr. and V. G. Soloviev : K. Danske Vidensk. Selsk. mat. -fys. Medd., 2, No. 2 (1962).
10) S. G. Nilsson and O. Prior : K. Danske Vidensk. Selsk. mat. -fys. Medd., 32, No. 16 (1961).
11) D. J. Thouless : Nucl. Phys., 22, 78 (1961).
12) L. S. Kisslinger : Nucl. Phys., 35, 114 (1962).
13) N. I. Pyatov : Ark. Fys., 36, 667 (1966) ; M. Chernej, N. Pyatov, and K. Zheleznova : Izv. Akad. Nauk SSSR, ser, fiz., 31, 550 (1967) ; M. Chernej and N. Pyatov : Preprint Dubna E4-3134 (1967) ; A. Kuliev and N Pyatov : Nucl. Phys., A106, 689 (1968).
14) B. L. Birbrair and K. N. Nikolaev : Phys. Letters, 32B, 672 (1970).
15) Z. Bochnacki and S. Ogaza : Nucl. Phys., A102, 529 (1967) ;
A. Chernyshev and L. Rapopor : Sov. J. Nucl. Phys., 7, 208 (1968) ;
S. Gabrakov, A. Kuliev, and N. Pyatov : Preprint Dubna, E4-4774 (1969).
16) R. Broglia, A. Molinari, and B. Sorensen : Nucl. Phys., A109, 353 (1968) ;
S. T. Belyaev and B. A. Rumiantsev : Phys. Letters, 30B, 444 (1969).
17) S. G. Nilsson : K. Danske Vidensk. Selsk. mat. -fys. Medd., 29, No. 16 (1955).

5. NUCLEAR PHYSICS
Nuclear Spectroscopy

5-1. In-Beam Gamma-Ray Spectroscopy Utilizing Heavy Ions

T. Inamura, S. Nagamiya, A. Hashizume,
Y. Tendow, and T. Katou

By use of natural beam beunches of heavy ions obtained from the Cyclotron, energy spectra and time distributions of γ-rays from various (HI, xn) reactions were measured. Half-lives of isomeric states produced can be determined within the time range from 10 to 300 ns in the present stage. In the experiments Ge(Li) detectors were used "in-beam" to observe γ-rays, and time-energy two-dimensional analyses were performed with a ND 4096 pulse-height analyzer. A block diagram of the electronic apparatus used is shown in Fig. 1. A simplified diagram of the experimental arrangement is also shown in Fig. 2. Our HI "in-beam" γ-ray spectroscopic studies are summarized in the following three parts.

(1) Excited levels in ^{82}Sr and ^{84}Sr

Energy vs. time spectra of γ-rays from ^{74,76}Ge(^{12}C, 4n)^{82,84}Sr reactions were measured in order to search for isomeric states in ^{82,84}Sr isotopes. The result of this experiment showed that there is no isomer with a half-life longer than 10 ns in ^{82,84}Sr. Excited levels of these isotopes, as shown in Fig. 3, are quasi-rotational. These results indicate that contrary to the prediction of Talmi and Unna[1] the seniority scheme with a core of $^{88}_{38}Sr_{50}$ collapses for ^{84}Sr having $(g_{9/2})^{-4}$ and $(g_{9/2})^{-2}(p_{1/2})^{-2}$ configurations; this shows a sharp contrast to the case of ^{92}Mo with $(g_{9/2})^4$ and $(g_{9/2})^2(p_{1/2})^2$ configurations for which the seniority scheme is very good.[1), 2)] Experiments as for more neutron-deficient Sr isotopes and ^{86}Zr are now under planning to study the character of the Z(or N) = 38 core and the effect of neutron-proton correlation.

(2) Delayed γ-transitions in Hg, Pb, Po, and Rn isotopes

High spin isomeric states in the closed-shell region are of interest from the

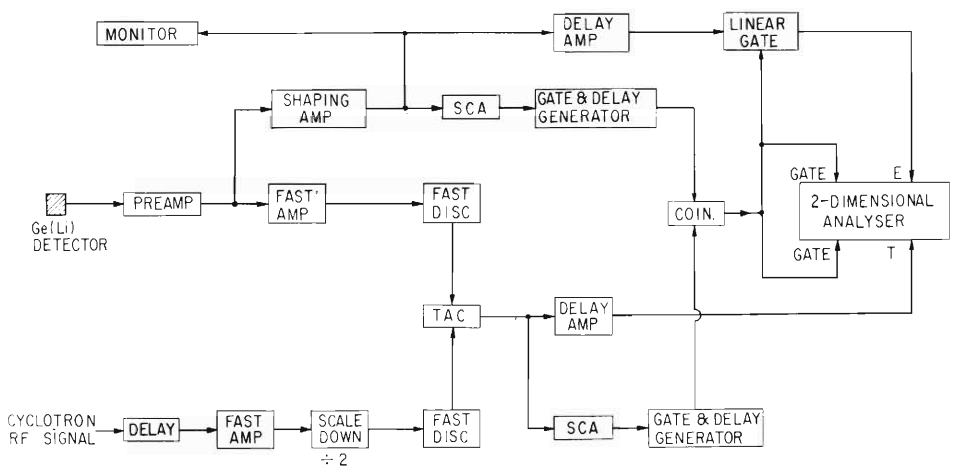

Fig. 1. Block diagram of electronic apparatus used in the nanosecond time analysis experiment.

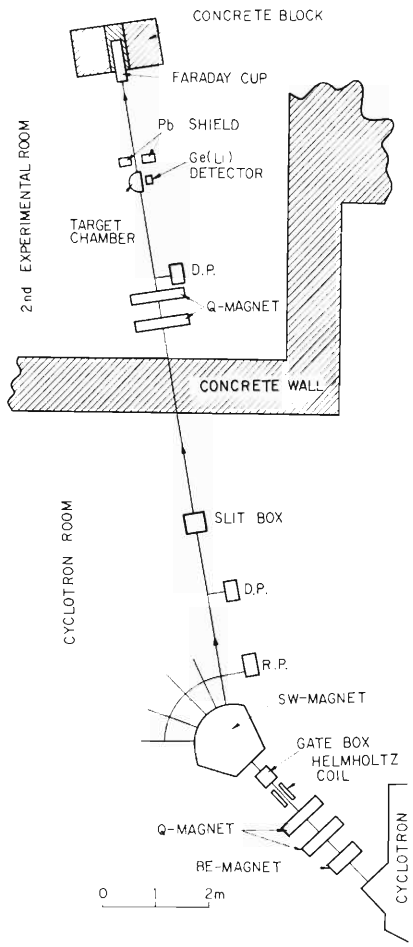

Fig. 2. Simplified diagram of the experimental arrangement used in the measurements of HI-reaction γ-rays.

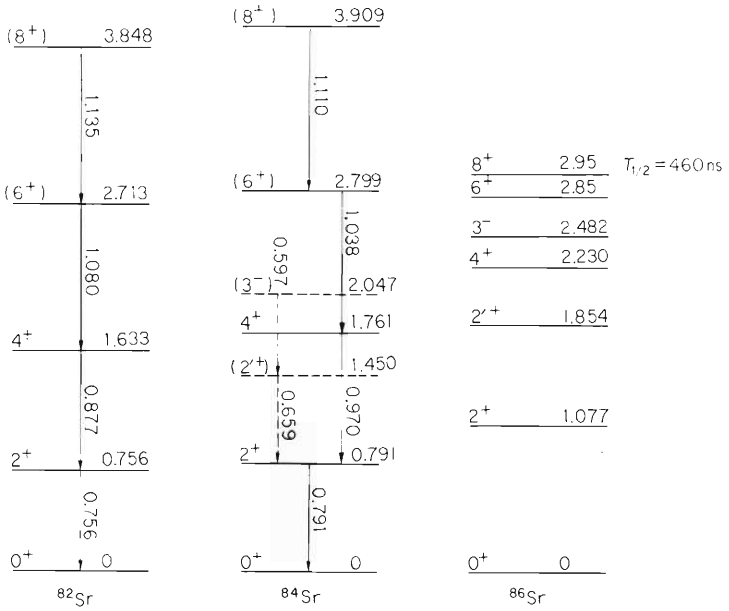

Fig. 3. Excited levels in ^{82}Sr and ^{84}Sr isotopes. Excited levels in ^{86}Sr[3] are shown for comparison.

viewpoint of the shell model, since such states can be described as the states with almost pure configurations.[4] By the nanosecond time analysis, we have found delayed γ-transitions in the nanosecond region in ^{190}Hg, ^{194,196}Pb, $^{200\text{-}203}$Po, and ^{206}Rn isotopes.

^{190}Hg isotope

Excited levels up to spin 6^+ have been known,[5] and this assignment was confirmed in the present measurement of γ-rays from the ^{181}Ta(^{14}N, 5n)^{190}Hg reaction. The $2^+ \rightarrow 0^+$, $4^+ \rightarrow 2^+$, and $6^+ \rightarrow 4^+$ transitions, however, were found to have a half-life, $T_{1/2} = 26 \pm 1$ ns. Decay curves for these transitions observed are shown in Fig. 4. Very recently Ton et al.[6] measured half-lives of the $(6^-, 7^-)$ level situated above the 6^+ level or at about this excitation energy in even Hg isotopes (A = 194~200) and found that the enhancement of the $(6^-, 7^-) \rightarrow (4^-, 5^-)$ E2 transition speed with respect to the single-particle estimate is systematically increasing with decreasing mass number. By extrapolation of the energy systematics for the $(6^-, 7^-)$ and $(4^-, 5^-)$ levels in Hg isotopes (A = 192-198)[7], the energy of the corresponding E2 transition in ^{190}Hg is expected to be

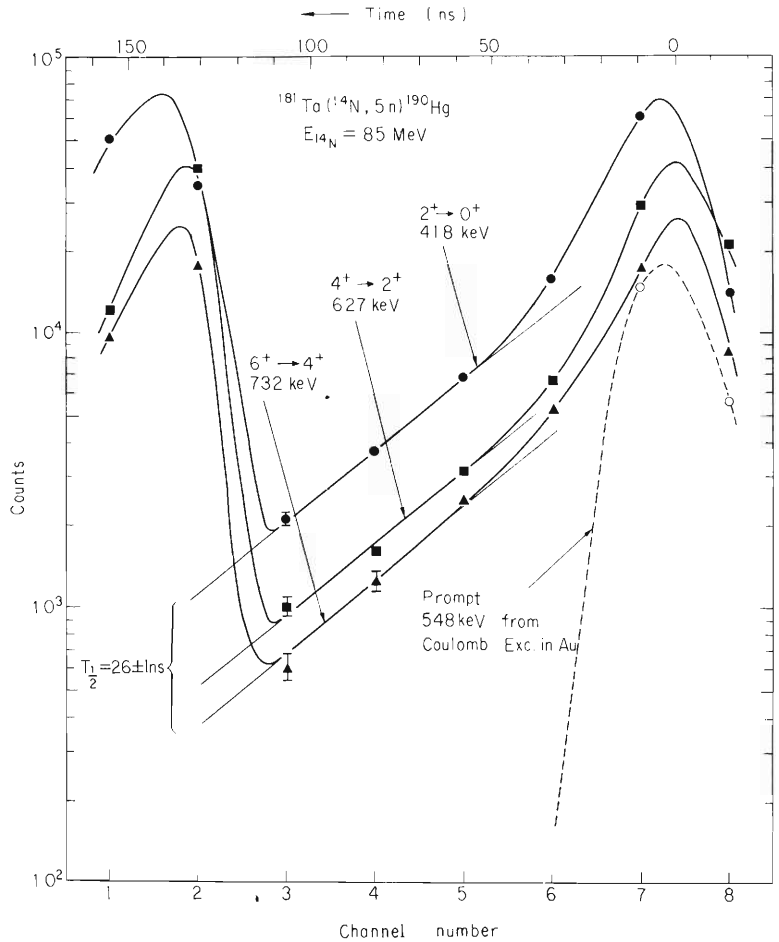

Fig. 4. Decay curves for the $2^+ \rightarrow 0^+$, $4^+ \rightarrow 2^+$, and $6^+ \rightarrow 4^+$ transitions in ^{190}Hg observed in the ^{181}Ta (^{14}N, 5n) reactions.

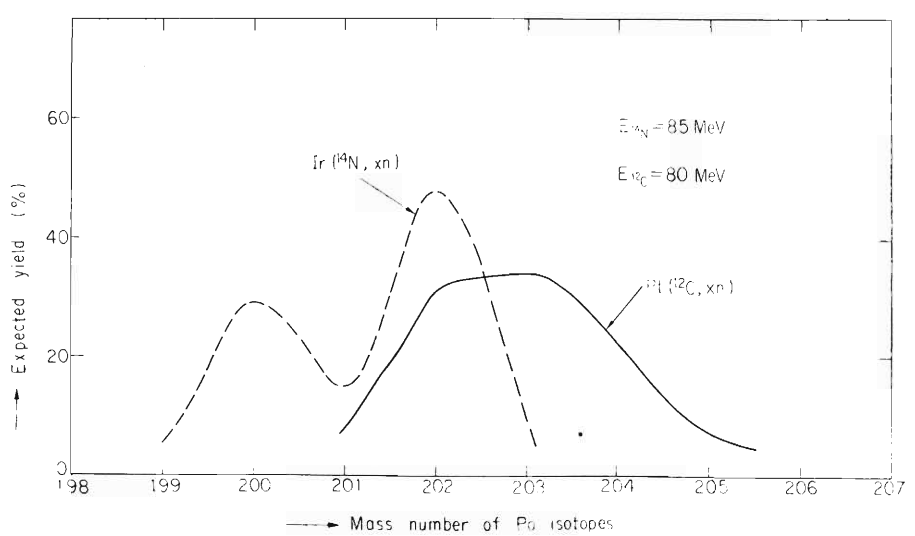

Fig. 5. Mass number distributions of reaction products expected in the Pt (^{12}C, 4n) and Ir (^{14}N, 5n) reactions.

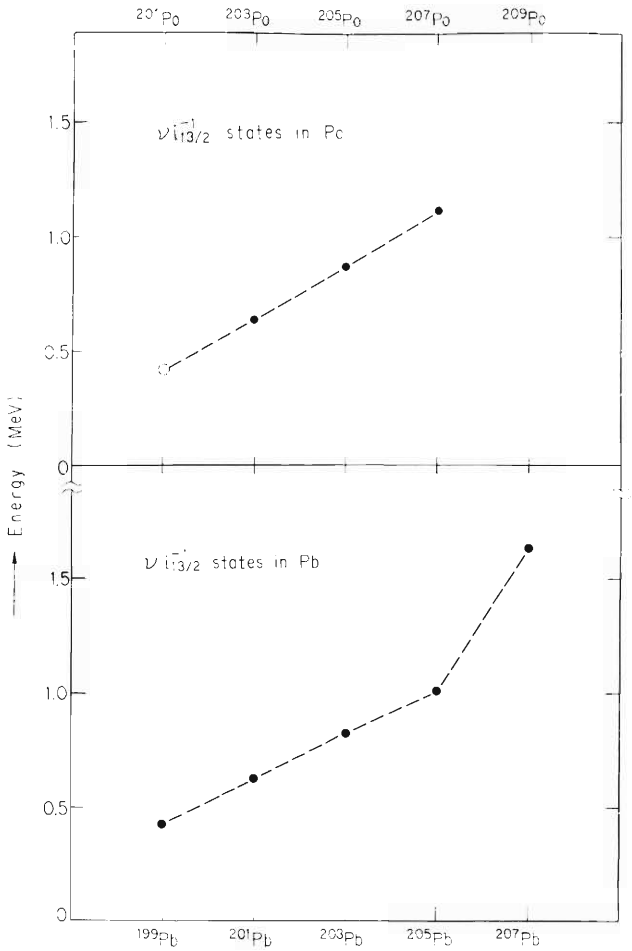

Fig. 6. Energy systematics of the $\nu(i_{13/2})^{-1}$ states in odd Pb and odd Po isotopes.

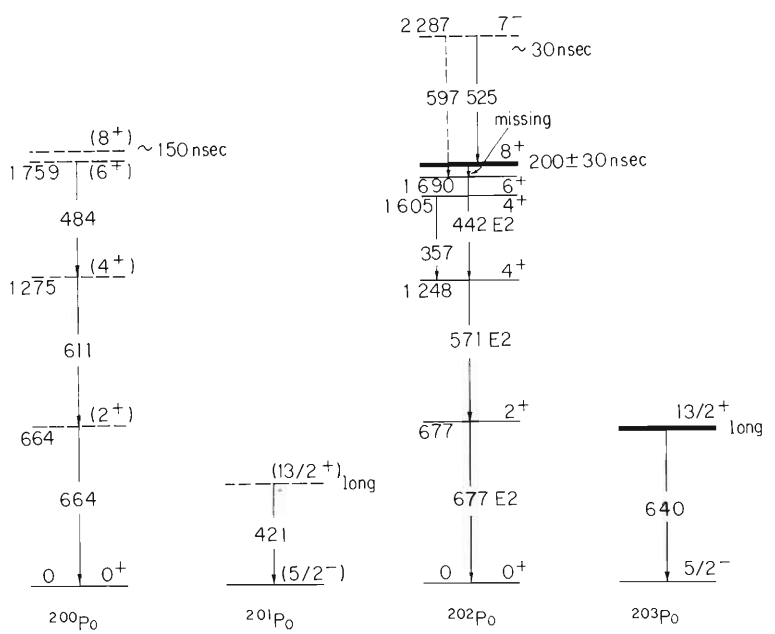

Fig. 7. Proposed levels in neutron deficient Po isotopes.

about 180 keV. If the 26 ns half-life observed is ascribed to this E2 transition, the transition speed becomes that of the single-particle estimate. This is probably not compatible with the result of Ref. 6). The 26 ns half-life in ^{190}Hg may suggest that there are high spin states with almost pure particle (hole) configurations in even Hg isotopes.

$^{194, 196}$Pb isotopes

Irradiating the natural Re target with 85 MeV ^{14}N ions, we observed γ-ray energy vs. time spectra in the $^{185, 187}$Re(^{14}N, 5n)$^{194, 196}$Pb reactions. Gamma-rays of 576, 964, 1035, and 1047 keV were found to have half-lives in the nanosecond region ($\lesssim$ 100 ns), and γ-rays of 340 and 420 keV with more longer lifetimes ($>$ 100 ns) were also found. Identification of these γ-rays cannot be made without ambiguity at present. This identification will be performed using enriched Re targets in the near future.

200-203Po isotopes

We observed energy spectra and time distributions of γ-rays from the Pt(^{12}C, 4n) and Ir(^{14}N, 5n) reactions. Since the natural targets of Pt and Ir were used in this measurement, the mass numbers of reaction products were distributed as shown in Fig. 5. From this mass distribution the γ-rays observed were identified as follows :

(i) High yield in both Pt(^{12}C, 4n) and Ir(^{14}N, 5n) reactions should be attributed to ^{202}Po.
(ii) High yield in Pt(^{12}C, 4n) but low yield in Ir(^{14}N, 5n) to ^{203}Po.
(iii) Rather high yield in Ir(^{14}N, 5n) but low yield in Pt(^{12}C, 4n) to ^{201}Po.
(iv) High yield in Ir(^{14}N, 5n) but not in Pt(^{12}C, 4n) to ^{200}Po.

Yamazaki[4] and Broda et al.[8] have found that the $(h_{9/2})^2 8^+$ isomeric sates appear in even Po isotopes (A = 204 − 210). The present observation shows that such an isomeric 8^+ state exists also in ^{202}Po and probably in ^{200}Po. Half-lives of these 8^+ states in ^{202}Po and ^{200}Po were determined as $T_{1/2}$ = 200 + 30 ns and $T_{1/2} \approx 150$ ns, respectively. As for ^{202}Po we tentatively placed the 7^- state with a half-life $\approx$30 ns at 2277 keV.

Long-lived isomeric states were observed in ^{201}Po and ^{203}Po and identified to be the $\nu(i_{13/2})^{-1}$ states on the basis of the energy systematics of the $\nu(i_{13/2})^{-1}$ states in the odd Pb and Po isotopes. The energy systematics is shown in Fig. 6.

Partial level schemes proposed in the present study and the isomeric states observed are summarized in Fig. 7.

^{206}Rn isotope

Energy spectra and time distributions of γ-rays from the ^{197}Au(^{14}N, 5n)^{206}Rn reaction were measured and the 560, 578, and 632 keV γ-rays were found with two distinct half-lives, $\approx$ 20 ns and $\gtrsim$ 100 ns. From the prompt relative yields of these cascade γ-rays, the 632, 560, and 578 keV γ-rays were tentatively assigned to the $2^+ \rightarrow 0^+$, $4^+ \rightarrow 2^+$, and $6^+ \rightarrow 4^+$ transitions in ^{206}Rn, respectively. Other γ-rays of 156, 600, and 665 keV were observed also as delayed, and it was identified with certainty that the 600 keV γ-rays decay with a half-life $\approx$ 20 ns and the 665 keV γ-rays decay with a half-life $\gtrsim$ 100 ns. We cannot establish the decay scheme of ^{206}Rn at present without any ambiguity. It is, however, notable that the excited levels in ^{206}Rn are likely to be explained quite similarly as in even Po isotopes.[4] Fig. 8 shows a tentative decay scheme of ^{206}Rn together with the decay scheme of ^{204}Po[4] for comparison.

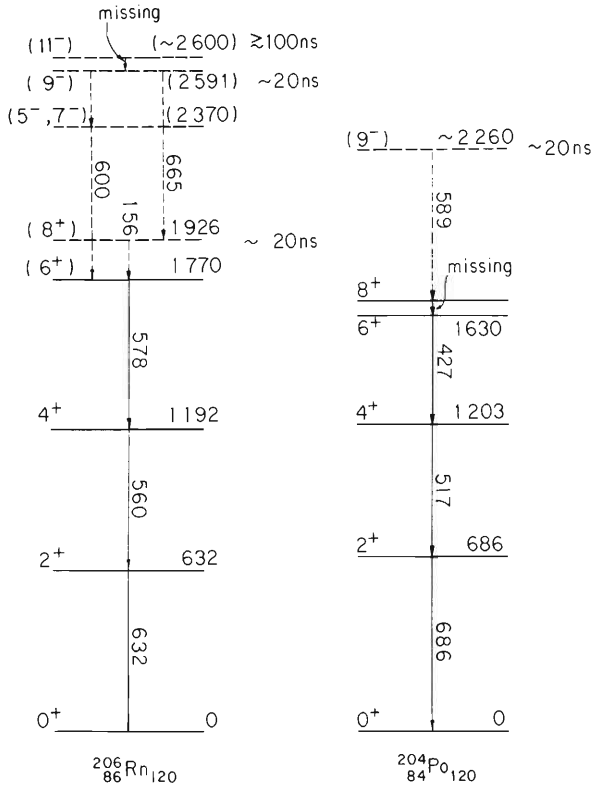

Fig. 8. A tentative decay scheme of ^{206}Rn. The decay scheme of ^{204}Po[4] is shown for comparison.

(3) On the possibility of shape isomeric states in ^{120}Xe and ^{126}Ba

Arseniev et al.[9] and Kusuno[10] theoretically predicted that the energy surface of ^{120}Xe and ^{126}Ba nuclides have two distinct minima ; one corresponds to prolate deformation and the other to oblate deformation which is predicted to be the equilibrium shape of the ground state. This suggests that some delayed γ -transitions should be observed in ^{120}Xe and ^{126}Ba because of "shape isomerism". [10), 11)]

From experimental point of view one can expect the delayed γ -rays associated with the ground band $2^+ \rightarrow 0^+$ transition in the nuclides of interest, since any γ -decay from the prolate nuclear states to the ground band states finally passes through the first 2^+ state to the ground state. By means of a two-dimensional 16 (E) × 256 (T) channel setting, we measured time distributions of the 322 keV ($2^+ \rightarrow 0^+$) γ -rays in ^{120}Xe and the 256 keV ($2^+ \rightarrow 0^+$) γ -rays in ^{126}Ba produced in the ^{109}Ag (^{14}N, 3n) and ^{115}In (^{14}N, 3n) reactions, respectively. The result of these measurements shows that there are no isomers in the time range from 20ns to 100ns populated at a fraction of more than 10^{-1} of the total population of the ground state.

Conlon and Elwyn[12] measured γ -ray time distributions in the microsecond region for ^{120}Xe and ^{126}Ba produced by (^{12}C, xn) reactions and found no isomers with lifetimes of 5 μs or more.

Taking account of these results, we feel at present, as suggested by Arseniev et al.,[9] that γ -deformation of the nuclides plays a crucial role in the formation of nuclear shape isomers. Further experimental and theoretical studies are now in progress.

References

1) I. Talmi and I. Unna : Nucl. Phys., 19, 225 (1960).
2) J. Ball et al. : Phys. Letters, 29B, 182 (1969) ; J. M. Jaklevic et al. : ibid., p. 179 ; R. Van Lieshout et al.: ibid., 9, 164 (1964) ; K.E.G. Löbner : Nucl. Phys., 58, 49 (1964).
3) M. Ishihara : Private communication, (1970) ; R. G. Anns et al. : Nucl. Phys., A148, 625 (1970).
4) T. Yamazaki : Phys. Rev., C1, 290 (1970).
5) J. Burde, R. M. Diamond, and F. S. Stephens : Nucl. Phys., A92, 306 (1967).
6) H. Ton et al. : ibid., A153, 129 (1970).
7) R. F. Petry, R. A. Naumann, and J. S. Evans : Phys. Rev., 174, 1441 (1968).
8) R. Broda et al. : Communication of the Joint Institute for Nuclear Research, Dubna, E6-5197 (1970).
9) D. A. Arseniev, A. Sobiczewski, and V. G. Soloviev : Nucl. Phys., A126, 15 (1969).
10) S. Kusuno : Private communication, (1970).
11) M. Wakai, K. Harada, and N. Ohnishi : Proc. of the Dubna Conf., (1968).
12) T. W. Conlon and A. J. Elwyn : Nucl. Phys., A142, 359 (1970).

5-2. Magnetic Moment of Isomeric States in Closed-Shell Region

T. Yamazaki, T. Nomura, T. Katou,
and S. Nagamiya

For these few years a number of isomeric states in the doubly closed-shell region have been identified. Since these states have almost pure shell-model configurations, magnetic moment of such states will provide much information on the magnetic core polarization, the effects of mesonic exchange current, and so on.

Here we report on g-factor measurements of the $\left[\pi h_{9/2}\, \pi i_{13/2}\right]$ 11^- state of ^{210}Po, the $\left[\pi h_{9/2}^2\ \nu p_{1/2}^{-2}\right]$ 8^+ state of ^{208}Po, the $\left[\pi g_{9/2}^2\right]$ 8^+ states of ^{92}Mo and ^{90}Zr, and the $\left[\nu f_{7/2}^2\right]$ 6^+ state of ^{42}Ca. These states were populated in compound reactions with α-particles from the cyclotron in this laboratory.

(1) Experimental procedure

A sketch of our experimental set-up is shown in Fig. 1. Accerelated α-particles were deflected by a switching magnet and focused at a spot nearly 4 mm long and 2 mm wide on the target, when necessary, at a spot 2 mm long and 1 mm wide. The γ-rays from the reactions were detected by a 4.5 mm $\times$4.5 cm diameter NaI(Tl) counter, or sometimes, by a 30 cc Ge(Li) detector. A magnetic field was applied perpendicularly to the plane of beam-detector with an electromagnet whose apparatus is shown in Fig. 1. The pole pieces of the magnet were made of Fe-Co alloy by which the magnetic field up to $\sim$33 kG can be produced. Excitation curves of the magnet are shown in Fig. 2.

Most of the measurements were carried out by the time-differential spin rotation method. For the g-factor measurement of the 380 nsec 8^+ state of ^{208}Po we used the stroboscopic resonance method. The principle of the latter method is as follows. If the lifetime of excited nuclei is longer than a period of excitation with beam bursts of a cyclotron, an anisotropy of γ-rays from the excited aligned nuclei in a magnetic field is smeared out unless the period of the excitation coincides with an integral multiple of half the Larmor period of the excited nuclei. Thus we can determine the Larmor period by observing such an anisotropy as a function of the strength of the applied magnetic field and searching for a maximum of the anisotropy. The stroboscopic resonance occurs when

$$n \frac{\pi}{\omega_L} = T_B, \qquad (1)$$

where ω_L is the Larmor frequency, T_B the period of a pulsed beam and n an arbitrary integer. Natural beam bursts of a cyclotron are suitable for utilizing this method.

Typical electronics arrangements are shown in Figs. 3 and 4. Levels strongly populated in α-induced reactions are shown in Fig. 5. We used metallic thick targets in these experiments.

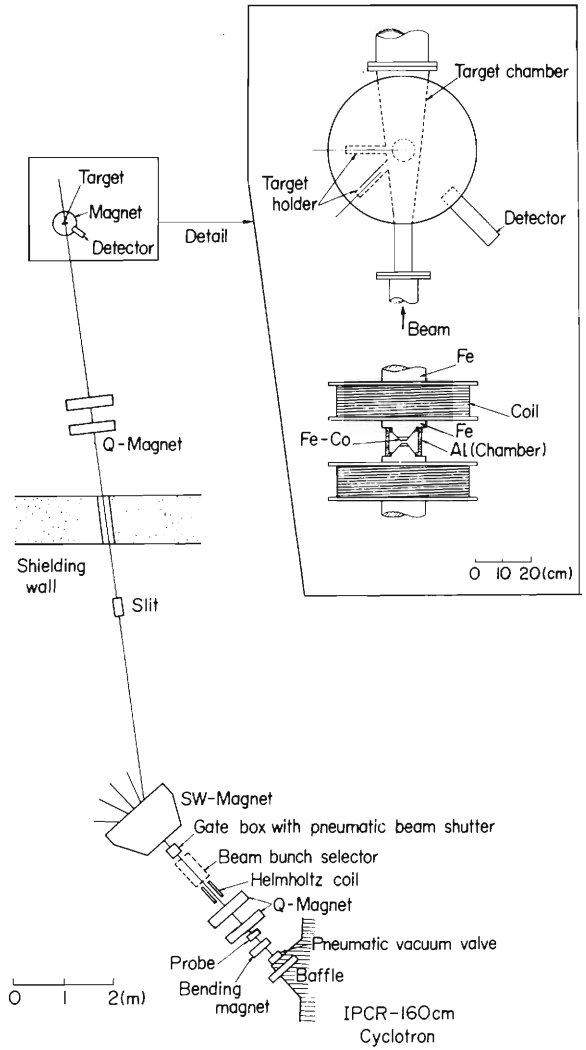

Fig. 1. Experimental apparatus in the present g-factor measurement.

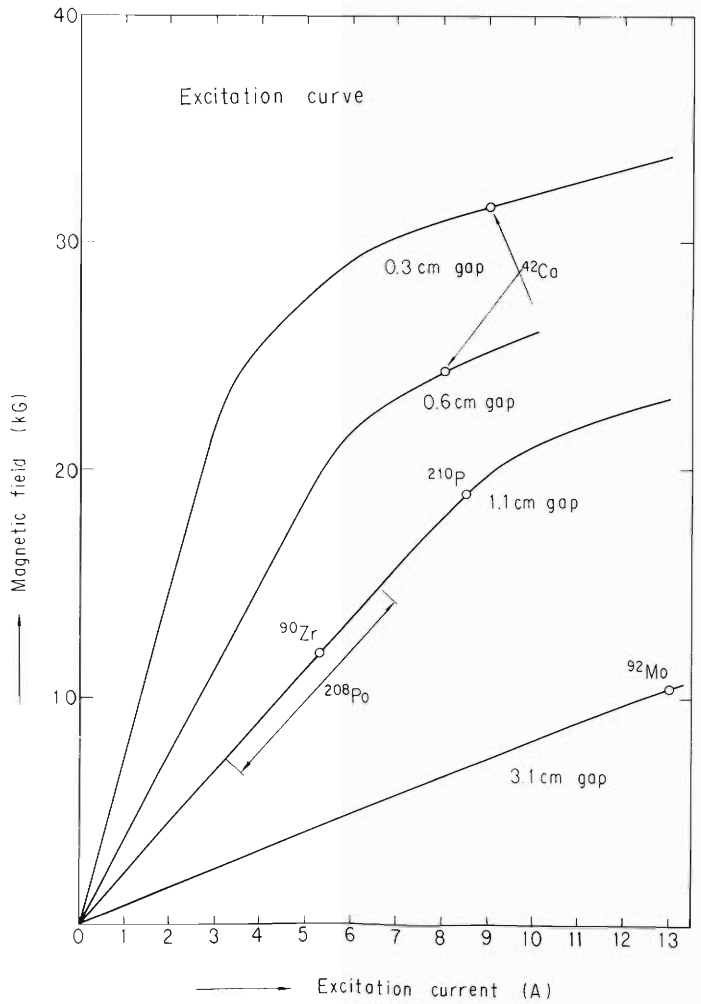

Fig. 2. Excitation curves of the magnet used. The four curves correspond to the four kinds of pole pieces. The pole piece and the strength of the magnetic field utilized in each experiment are indicated in this figure.

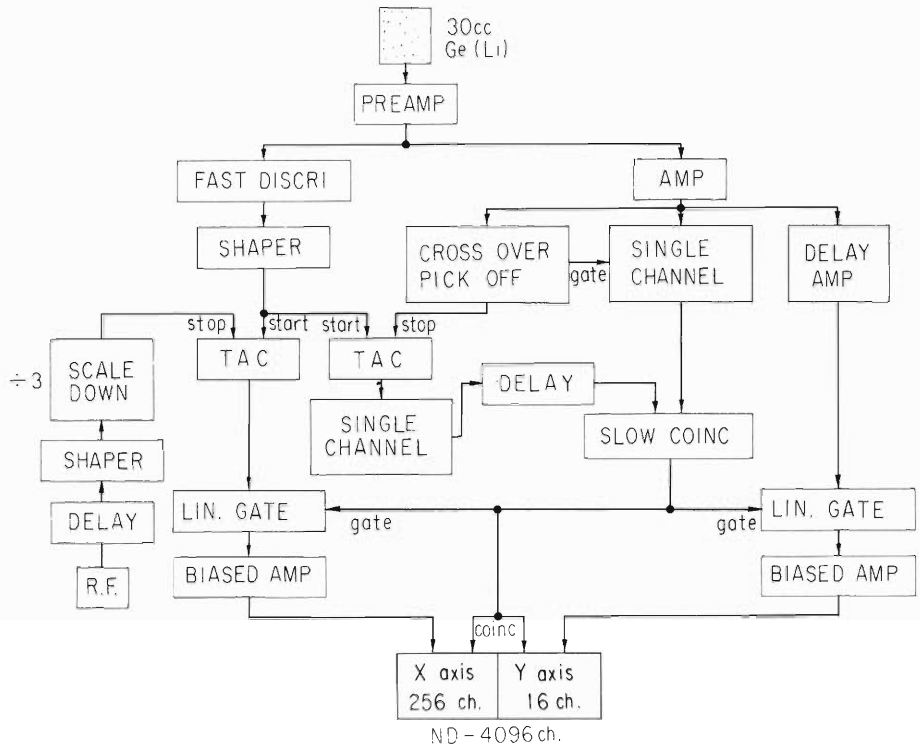

Fig. 3(a)

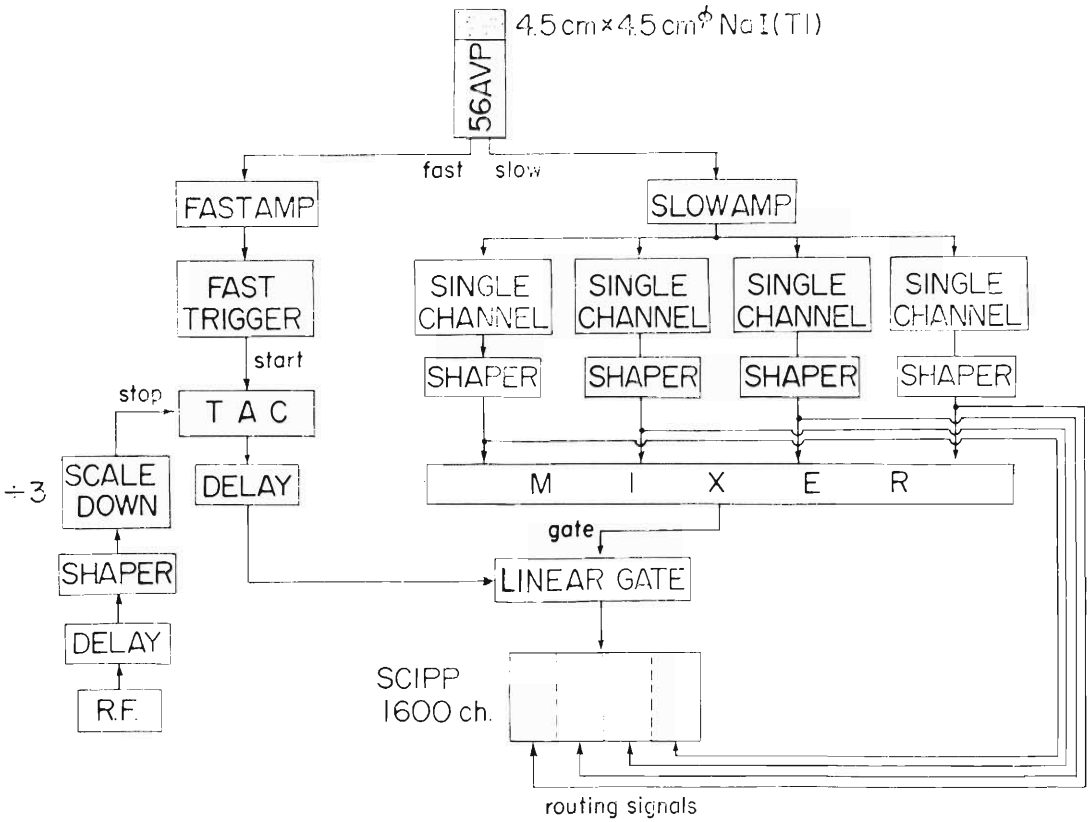

Fig. 3(b)

Fig. 3. Electronics arrangement for the time-differential spin rotation method. (a) is used for the g-factor measurement of the 11^- state of ^{210}Po, and (b) is used for the 8^+ states of ^{90}Zr and ^{92}Mo and also for the 6^+ state of ^{42}Ca.

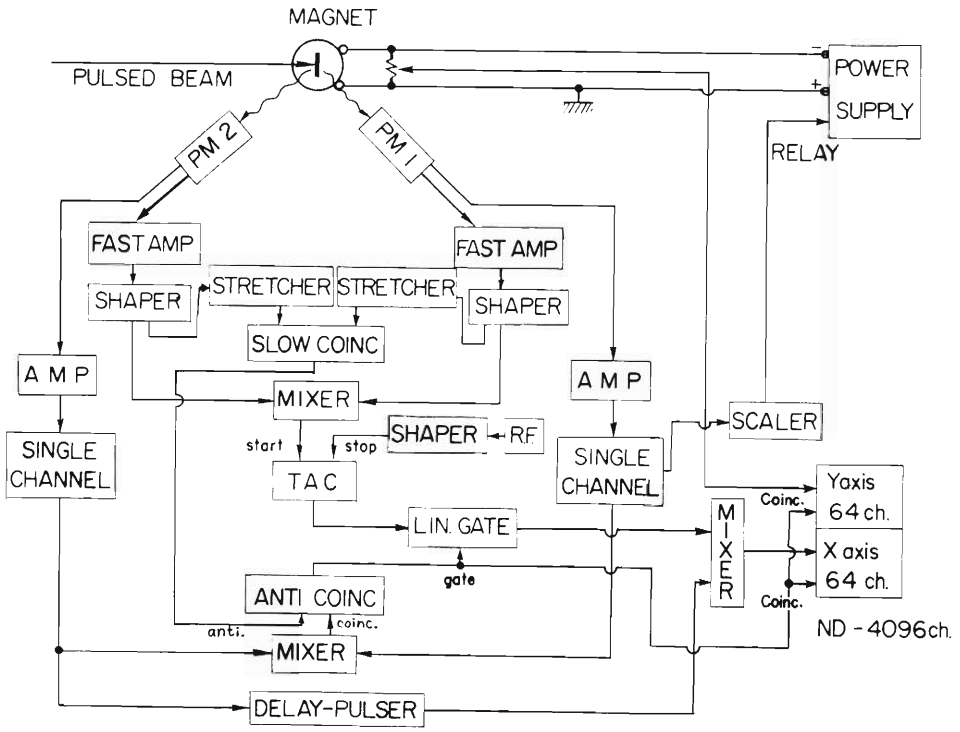

Fig. 4. Electronics arrangement for the stroboscopic resonance method utilized for the g-factor measurement of the 8^+ state of ^{208}Po.

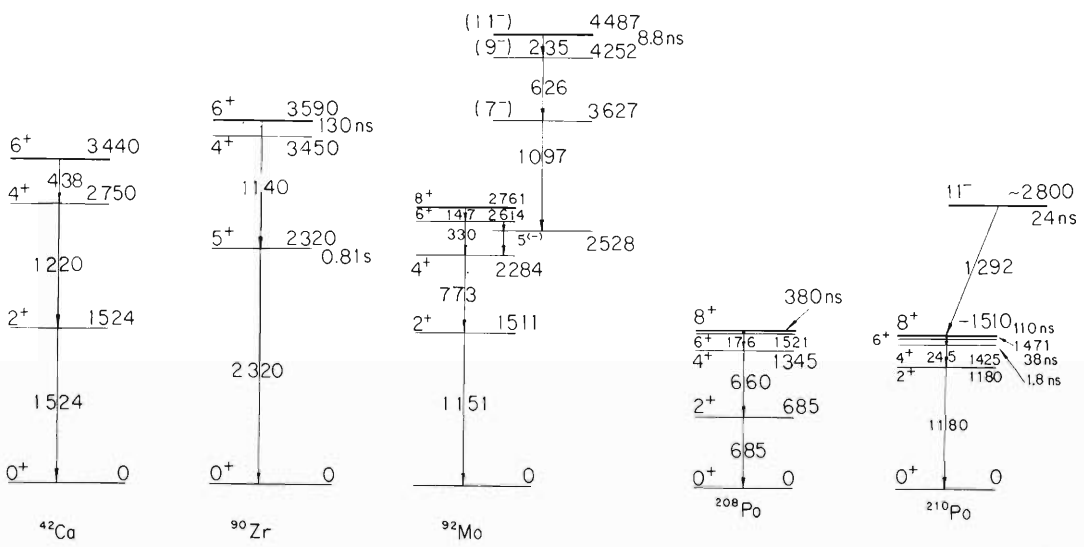

Fig. 5. Levels strongly populated in the α-induced reactions.

Table 1. g-Factors of proton states in the ^{208}Pb region.

Nucleus	I^{π}	Configuration Proton	Configuration Neutron	g_{exp}	$g_{schmidt}$	Spin polarization effect	L. S. force effect	Other correction	g_{cal}	$g_{exp} - g_{cal}$
$^{210}_{84}Po_{126}$	11^-	$h_{9/2}$	$i_{13/2}$	1.090 ± 0.016[a]	1.038	−0.017	~0	−0.014[c]	1.007	0.083 ± 0.016
$^{210}_{84}Po_{126}$	8^+	$h^2_{9/2}$	—	0.911 ± 0.010[b]	0.490	+0.144	+0.01	—	0.644	0.267 ± 0.010
$^{208}_{84}Po_{124}$	8^+	$h^2_{9/2}$	$P^{-2}_{1/2}$	0.902 ± 0.006[a]	0.490	+0.158	+0.01	−0.003[d]	0.655	0.247 ± 0.006
$^{209}_{83}Bi_{126}$	$9/2^-$	$h_{9/2}$	—	0.9067	0.490	+0.160	+0.01	—	0.660	0.247

a) Obtained after the Knight shift correction of 1.47 %.[1), 9)]

b) From Ref. 3).

c) Effect of the $\left| \left[\pi h^2_{9/2} \right] 8^+ ; (\hbar\omega_3)3^- ; 11^- \right\rangle$ mixing.[1)]

d) Effect of the surface vibration of the ^{206}Pb core.[9)]

Table 2. g-Factors of proton states in the ^{88}Sr region.

Nucleus	I^{π}	Configuration: Protom	Configuration: Neutron	g_{exp}	$g_{schmidt}$	Spin polarization effect: AH[b]	Spin polarization effect: MZB[c]	L. S force effect	g_{cal}	$g_{exp} - g_{cal}$
$^{90}_{40}Zr_{50}$	8^+	$g_{9/2}^2$	—	1.355 ± 0.018[a]	1.510	− 0.23	—	− 0.01	1.27	0.08 ± 0.02
$^{93}_{41}Nb_{52}$	$9/2^+$	(60∼70 %) $p_{1/2}^2\, g_{9/2}$ +(40∼30 %) $g_{9/2}^3$	$d_{5/2}^2$	1.3707	1.510	− 0.19 ∼ − 0.17	—	− 0.01	1.31 ∼ 1.33	0.05 ± 0.02
$^{92}_{42}Mo_{50}$	8^+	(70∼80 %) $p_{1/2}^2\, g_{9/2}^2$ +(30∼20 %) $g_{9/2}^2$	—	1.409 ± 0.016[a]	1.510	− 0.15 − 0.13	—	− 0.01	1.35 ∼1.37	0.05 ± 0.03
$^{87}_{37}Rb_{50}$	$3/2^-$	$p_{3/2}^{-1}$	—	1.8340	2.529	− 0.67	− 0.73	− 0.03	1.77 ∼1.83	0.03 ± 0.03
$^{89}_{39}Y_{50}$	$1/2^-$	$p_{1/2}$	—	− 0.2747	− 0.529	0.0	+0.04	+0.07	− 0.46 ∼ − 0.42	0.17 ± 0.03

a) Obtained after the Knight shift correction of 0.87 %.[2]
b) Calculated by using the formula of Arima and Horie.[4] For ^{90}Zr and ^{92}Mo the effects of the $|g_{9/2}g_{7/2}; 8^+)$ mixings are also included in this column.
c) Calculated by Mavromatis, Zamick, and Brown.[5]

Table 3. g-Factors of neutron states in the ^{40}Ca regions.

Nucleus	I^{π}	Neutron configuration	g_{exp}	$g_{schmidt}$	1st-order spin polarization effect b)	L. S force effect	g_{cal}	$g_{exp} - g_{cal}$
$^{41}_{20}Ca_{21}$	$7/2^-$	$f_{7/2}$	-0.4557	-0.5466	0	+0.01	-0.537	0.08
$^{42}_{20}Ca_{22}$	6^+	$f^2_{7/2}$	-0.516 ± 0.020 a)	-0.5466	+0.07	+0.01	-0.467	-0.05 ± 0.02
$^{43}_{20}Ca_{23}$	$7/2^-$	$f^3_{7/2}$	-0.3763	-0.5466	+0.13	+0.01	-0.407	0.03

a) Present result.

b) Calculated by Arima and Horie.[4]

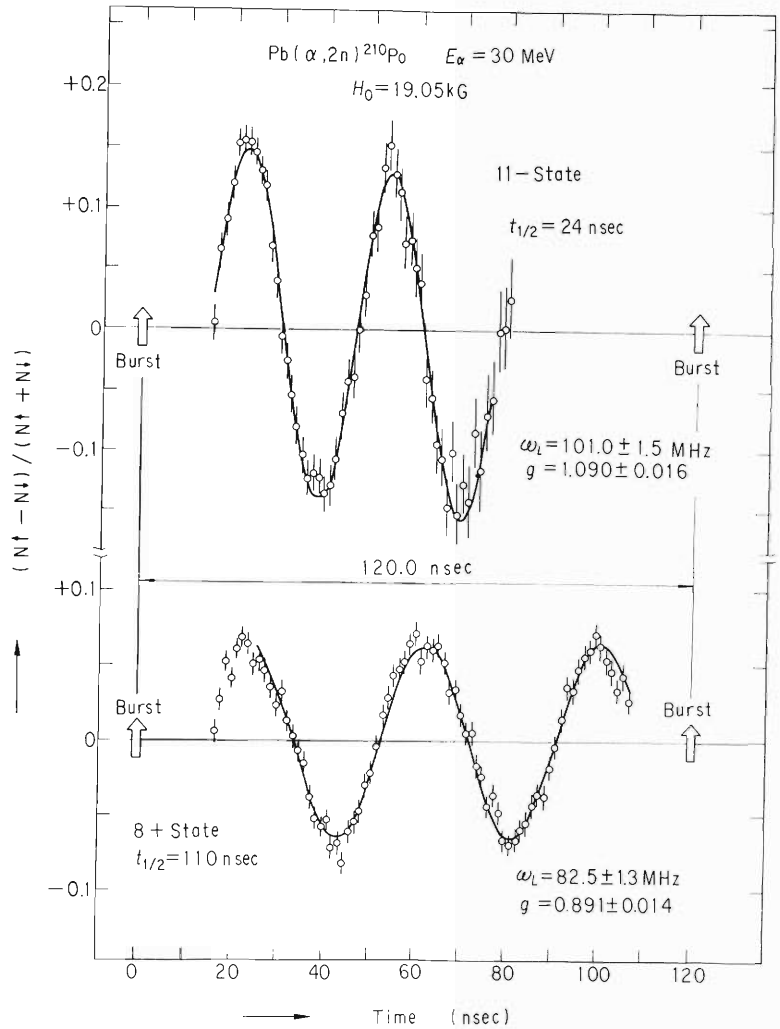

Fig. 6. Time-differential pattern $R(t) = (N^{\uparrow} - N^{\downarrow})/(N^{\uparrow} + N^{\downarrow})$ for the 11^- state of ^{210}Po (upper) and for the 8^+ state of ^{210}Po (lower), where counts $N^{\uparrow}$ and $N^{\downarrow}$ correspond to the external magnetic field up and down, respectively. The g-factor of the 8^+ state was measured for the check of this experiment, which turned out to be compatible with the previous one.[3)]

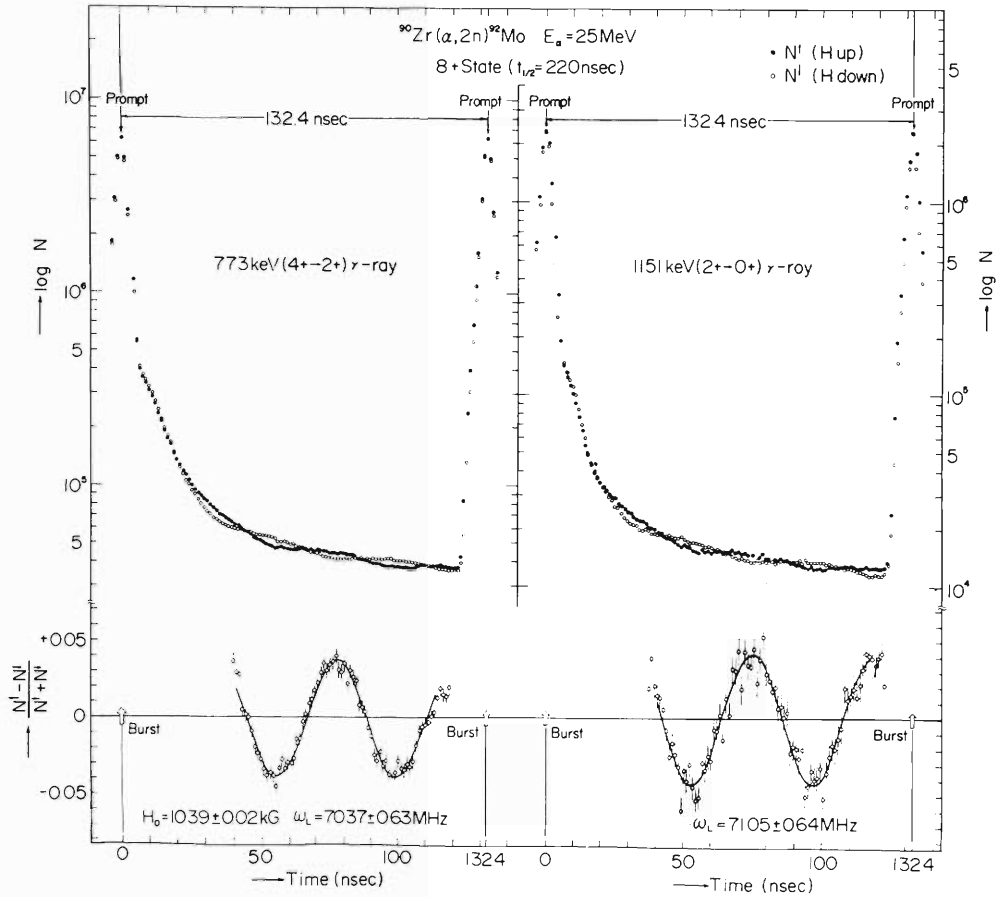

Fig. 7. Time distributions of γ-rays and the time-differential patterns R(t) for the 8^+ state of ^{92}Mo.

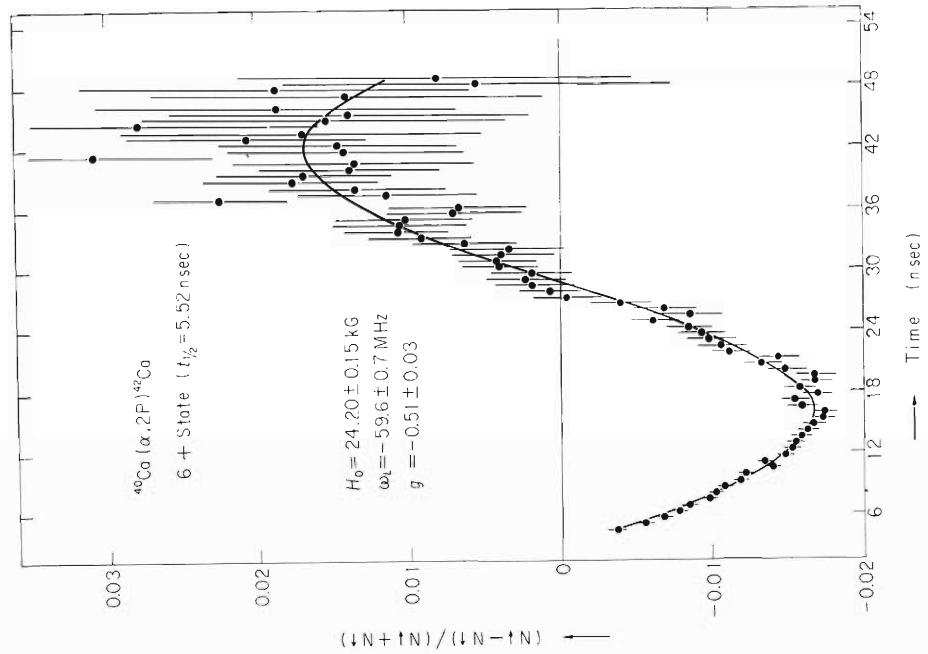

Fig. 9. Time-differential pattern R(t) for the 6^+ state of ^{42}Ca.

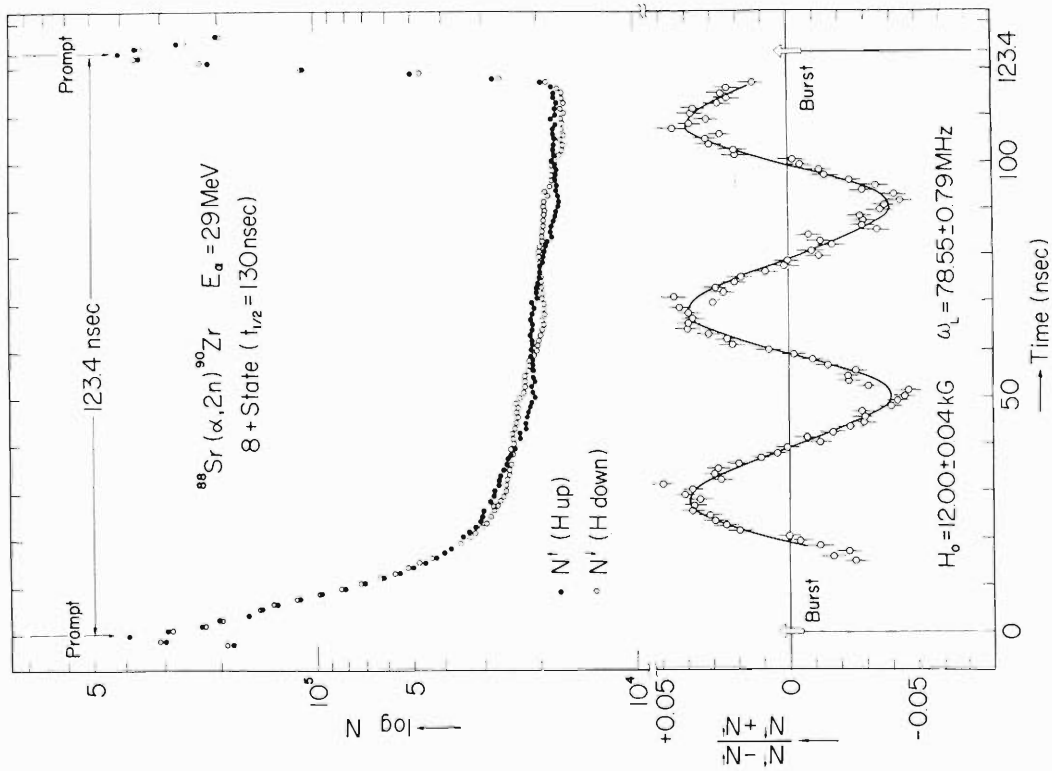

Fig. 8. Time distribution of γ-rays and the time-differential pattern R(t) for the 8^+ state of ^{90}Zr.

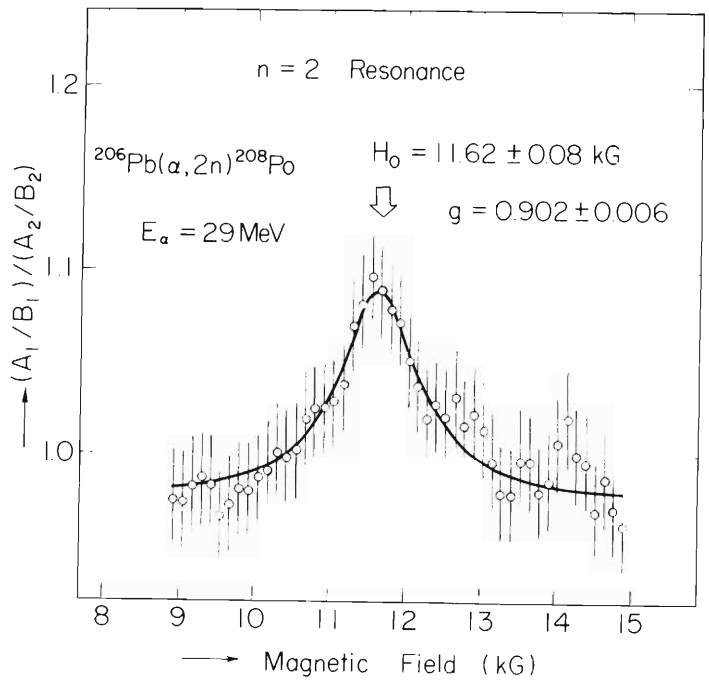

Fig. 10. Stroboscopic resonance for the 8^+ state of ^{208}Po.

(2) Results and discussion

The results are shown in Figs. 6 ~ 10 and summarized in Tables 1 ~ 3. The following points are to be noted.

(i) M1 spin polarization

In the ^{208}Pb and ^{88}Sr regions the observed changes of the g-factors (from one-particle state to two-particle state) are well accounted for by the M1 spin polarization mechanism although the absolute values are not explained by this mechanism. In general, the corrections to the g-factors due to the M1 spin polarization are too small for the $j = \ell - \frac{1}{2}$ orbitals but rather large for the $j = \ell + \frac{1}{2}$ orbitals. This fact infers, as described later, that g_ℓ factor of the proton is larger than 1.

The g-factor of the 6^+ state of ^{42}Ca gives an anomalous value in view of the M1 spin polarization. According to the current theories the deviation of the g-factor of the 6^+ state from the Schmidt value should be larger than that of the $7/2^-$ state of ^{41}Ca, but, the present value gives the opposite result. This point is open to further investigation.

(ii) Anomalous g_ℓ factor of the proton

Since in the $\{\pi i_{13/2} \ \pi h_{9/2}\}\ 11^-$ state of ^{210}Po the spin contribution to the g-factor is nearly cancelled out, the g-factor of this state is expected to be nearly equal to g_ℓ. The experimental value of this state clearly shows that $g_\ell = 1.09 \pm 0.02$. It is to be noted that the g-factors in the ^{88}Sr region also give a positive evidence for this conjecture. Such evidences are shown in Figs. 11 and 12.

In the ^{208}Pb region it has long been left as a question why the magnetic moment of ^{209}Bi deviates largely from the Schmidt value. According to our analysis this anomaly can be ascribed to the anomalous g_ℓ factor.

The mesonic exchange current is believed to be the main source of this anomalous g_ℓ factor. Miyazawa[7] and recently Chemtob[8] gave $g_\ell \approx 1.1$, which is in good agreement with the present result. Details of discussion are described in Refs. 1) and 2).

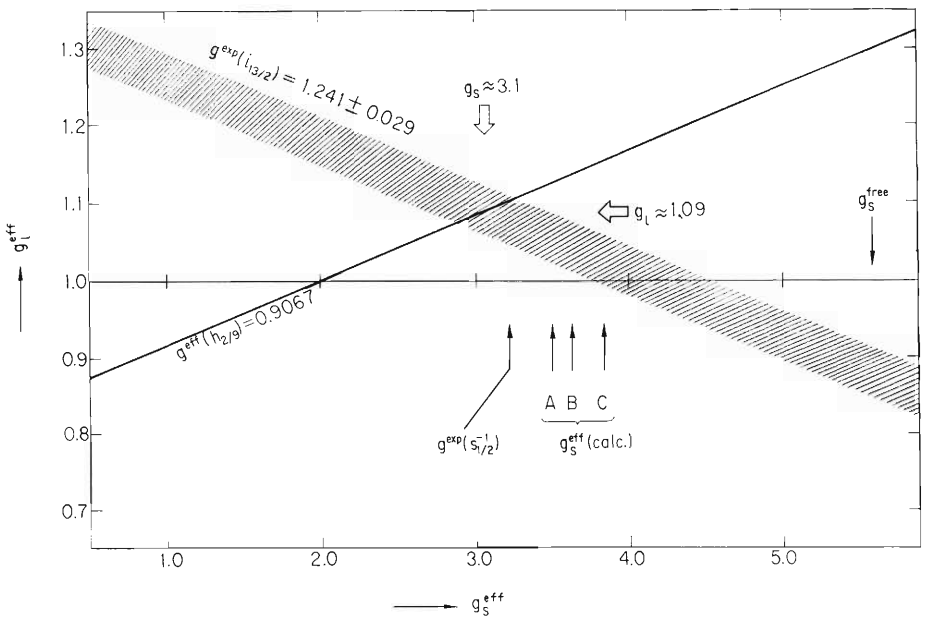

Fig. 11. Evidence of the anomalous g_ℓ factor in the ^{208}Pb region. By assuming that the g-factor is renormalized as a single-particle operator of $g_{exp} = g_\ell^{eff} + \frac{1}{2\ell+1}(g_s^{eff} - g_\ell^{eff})$ for $j = \ell \pm 1/2$, we plot the relation between g_s^{eff} and g_ℓ^{eff} by use of the observed g_{exp}. For the high spin orbital such as the $h_{9/2}$ or the $i_{13/2}$ orbital it is believed that the value of g_s^{eff} as well as g_ℓ^{eff} is independent of the orbital. The g_s^{eff}'s from the calculation of the core polarization are indicated, A: $g_s^{eff}(i_{13/2})$, B: $g_s^{eff}(h_{9/2})$ both by Arima and Horie,[4] and C: $g_s^{eff}(h_{9/2})$ by Blomqvist et al.[6]

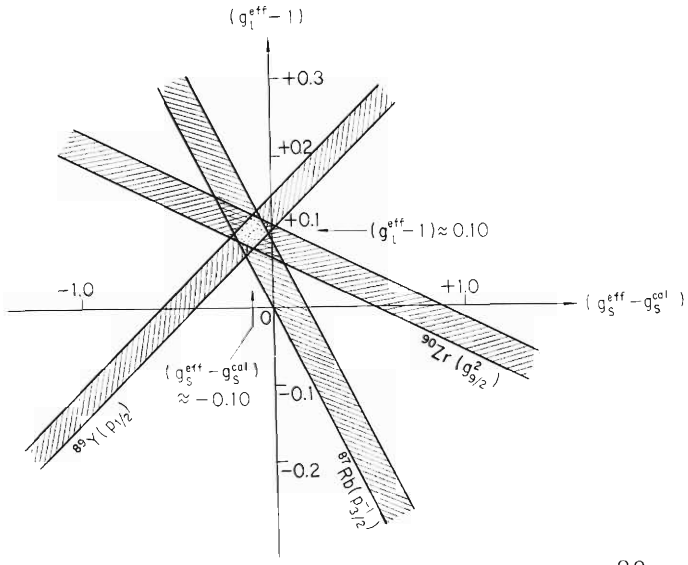

Fig. 12. Evidence of the anomalous g_ℓ factor in the ^{88}Sr region. Since in this region the corrections to the g-factors due to the M1 spin polarization and L·S force depend on the orbitals, we plot $(g_\ell^{eff} - 1)$ vs. $(g_\ell^{eff} - g_s^{cal})$ with given $(g_{exp} - g_{cal})$'s where $g_{exp} - g_{cal} = \left[g_\ell^{eff} \pm \frac{1}{2\ell+1}(g_s^{eff} - g_\ell^{eff})\right] - \left[1 \pm \frac{1}{2\ell+1}(g_s^{cal} - 1)\right]$. The g_s^{cal} includes the effects of the M1 spin polarization and L·S force.

References

1) T. Yamazaki, T. Nomura, S. Nagamiya, and T. Katou : Phys. Rev. Letters, 25, 547 (1970).
2) S. Nagamiya, T. Katou, T. Nomura, and T. Yamazaki : Phys. Letters, 33B, 574 (1970). (A full report will be published in an early date.)
3) T. Yamazaki, T. Nomura, T. Katou, T. Inamura, A. Hashizume, and Y. Tendow: Phys. Rev. Letters, 24, 317 (1970) ; IPCR Cyclotron Progr. Rep., 3 (1969).
4) A. Arima and H. Horie : Prog. Theor. Phys., 12, 623 (1954).
5) H. A. Mavromatis, L. Zamick, and G. E. Brown : Nucl. Phys., 80, 545 (1966).
6) J. Blomqvist, N. Freed, and H. O. Zetterström : Phys. Letters, 18. 47 (1965).
7) H. Miyazawa : Prog. Theor. Phys., 6, 801 (1951).
8) M. Chemtob : Nucl. Phys., A123, 449 (1969).
9) S. Nagamiya, T. Nomura, and T. Yamazaki : ibid., A159, 653 (1970).

5-3. The Nuclear Level Structure of ^{171}Yb

Y. Tendow, Y. Awaya, T. Katou, and A. Hashizume

The level structure of the deformed odd nucleus ^{171}Yb was investigated by use of a Ge(Li) gamma-ray spectrometer and the coincidence technique.

The ^{171}Yb nucleus was induced from electron capture and positron decay of ^{171}Lu (half-life 8.3 days) which was produced through the (α, 2n) reaction by bombardment of natural Tm_2O_3 with alpha-particle beams of 30 MeV energy from the IPCR cyclotron.

Gamma-ray sources were prepared by the radio chemical separation method using cation resin columns and an appropriate eluent.

Gamma-ray spectra were measured with a 23 cm^3 Ge(Li) detector which was put into an annular-type NaI(Tl) scintillation for the purpose of suppression of Compton-scattering. The whole system was surrounded by Pb shields of 10 cm in thickness to attain a low background condition. The large volume detector and the Compton suppression arrangement unveiled many previously unobserved weak gamma-ray peaks. (Table 1) The low energy gamma-ray and X-ray spectra were measured with a Si(Li) X-ray. spectrometer. (Fig. 1)

In order to determine the position of these transitions in the decay scheme, coincidence measurements were performed by use of the 23 cm^3 Ge(Li) and 3 × 3 inch NaI (Tl) detector system. (Figs. 2 and 3) The coincidence measurements revealed that some new weak gamma-rays are attributable to the transitions to the members of 95.26 keV $7/2^+$ rotational band from other higher-lying rotational bands. Coincidence works using the 23 cm^3 Ge(Li) -- Si(Li) X-ray system are now being continued.

A preliminary measurement of the 95.26 keV $7/2^+$ [633] isomeric state was

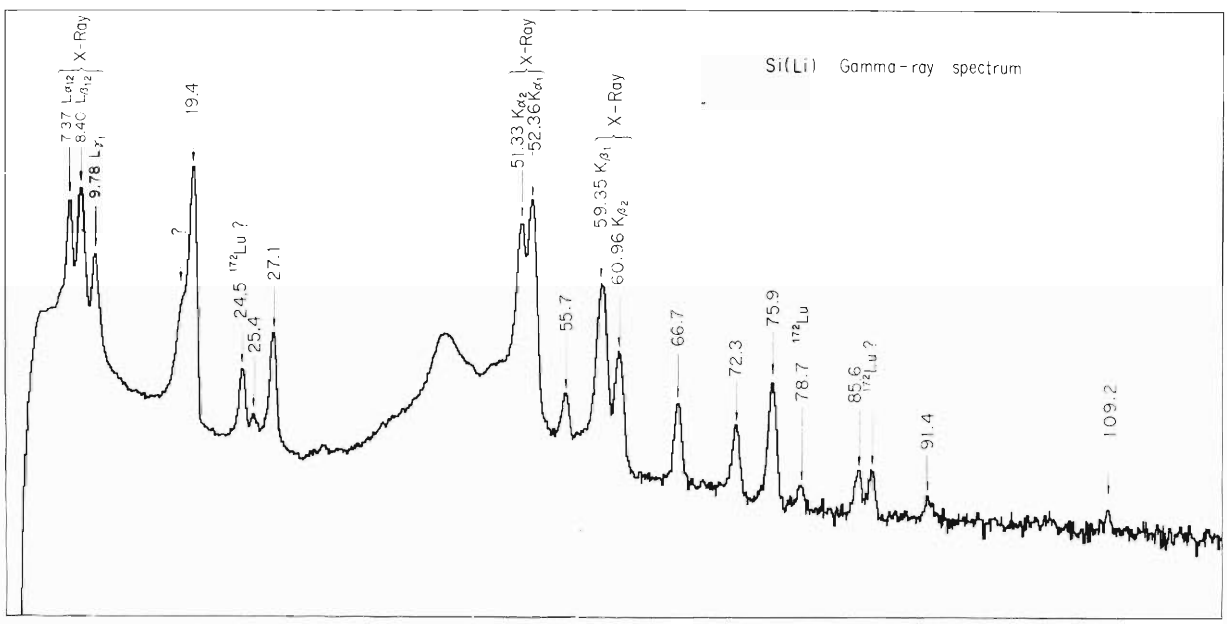

Fig. 1. Low energy gamma-ray spectrum measured with the X-ray Si(Li) spectrometer.

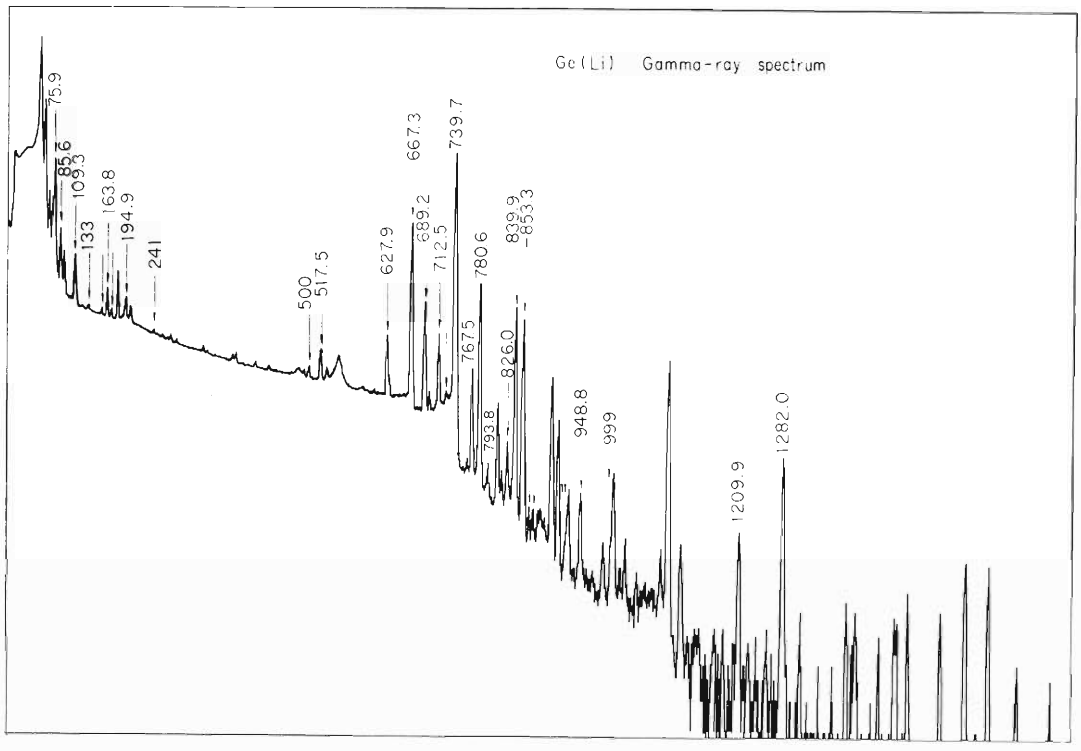

Fig. 2. Gamma-ray single spectrum measured with the Ge (Li) spectrometer.

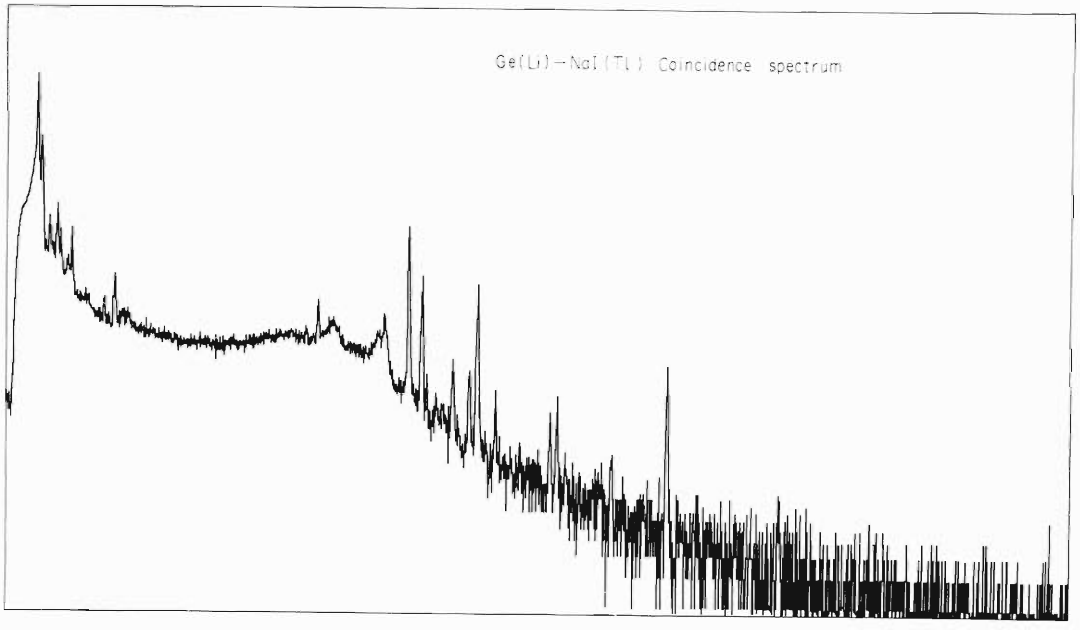

Fig. 3. Coincidence spectrum. (Gated with 70~90 keV gamma-rays).

Table 1. List of gamma-ray energies.

Energy (KeV)	Energy (KeV)	Energy (KeV)
9.2	163.8	793.8
19.4	194.9	826.0
27.1	241 ?	839.9
46.5	500 ?	853.3
55.7	517.5	863 ?
66.7	627.9	869 ?
72.4	667.3	926 ?
75.9	689.2	928 ?
85.6	712.5	948.8
91.4	725 ?	999 ?
109.3	739.7	1209.9
133 ?	767.5	1282.0 ?
154.7	780.6	

performed by the in-beam lifetime measurement technique using a mechanical beam chopper. Data analysis is now in progress. A preliminary value of lifetime is about 2 msec.

Taking into account all of these data together with the internal conversion electron data measured with 50 cm iron-free beta-ray spectrometer, the level scheme of ^{171}Yb nucleus was constructed and discussed.

5-4. The Conversion Electron Spectrum in the Decay of ^{147}Gd

A. Hashizume, Y. Tendow, Y. Awaya, and T. Katou

Succeeding to measurements of γ-rays with a Ge(Li) detector ,[1] the spectrum of conversion electrons emitted in the decay of ^{147}Gd has been obtained by an air core β-ray spectrometer. The method of chemical separation was the same as explained previously except a column of 30 cm in height in place of 50 cm was used for an ion exchange separation process. To charge effluent in the condensation and purification processes, an aspirator was used to constrain the effluent to flow into the column. Thus the total time necessary for the chemical separation to have a carrier-free radioactive source is shortened to 20 h compared to 60 or 70 h by the conventional method. This improvement is essential because the half-life is 35 h.

The spectrum of conversion electrons is shown in Figs. 1 and 2. There are so many peaks that the data have been processed by a computer. From the readings of a program counter of air core spectrometer, the $B\rho$ values are calculated by a calibration curve and transition energy is evaluated assuming K, L, M, and N electrons for each peak. This transition energy is compared to that of γ-rays.

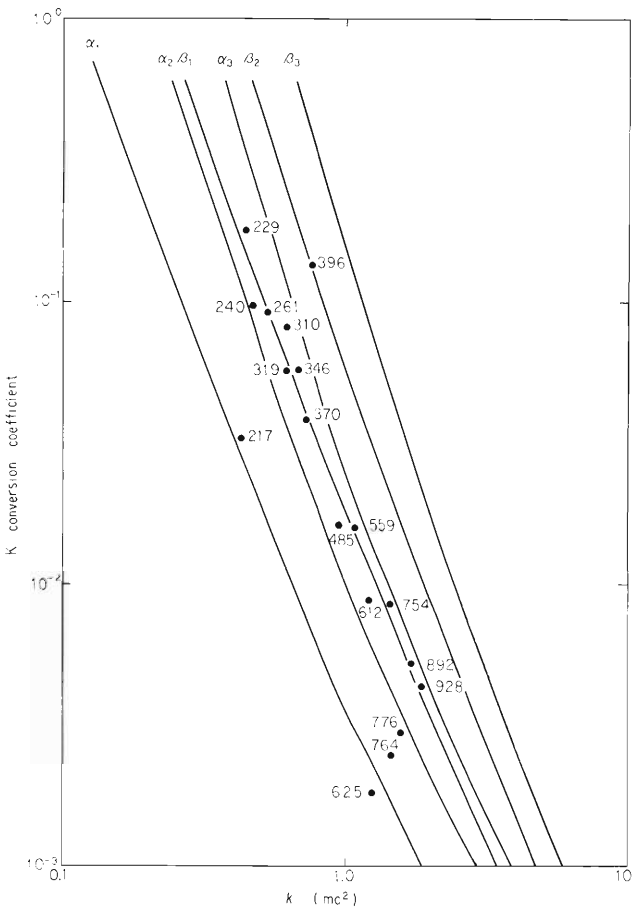

Fig. 3. K-conversion coefficient of transitions in ^{147}Eu, the number of each plot representing the transition energy in keV.

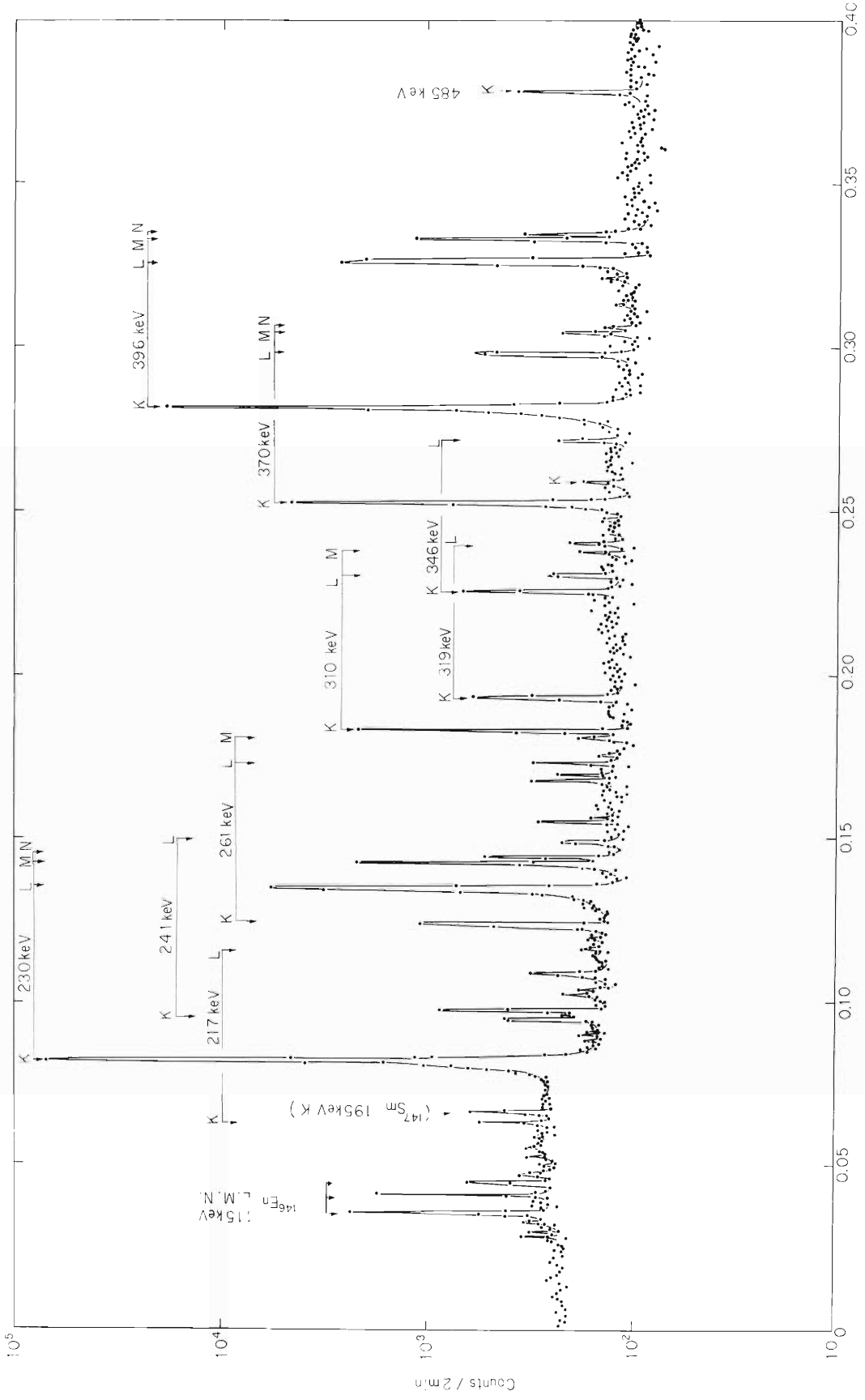

Fig. 1. Conversion electron spectrum in the decay of ^{147}Gd setting the apperture of the buffle at 60 mm. The source of 0.6 × 20 mm^2 was used. The current range is 8 to 17.6 A.

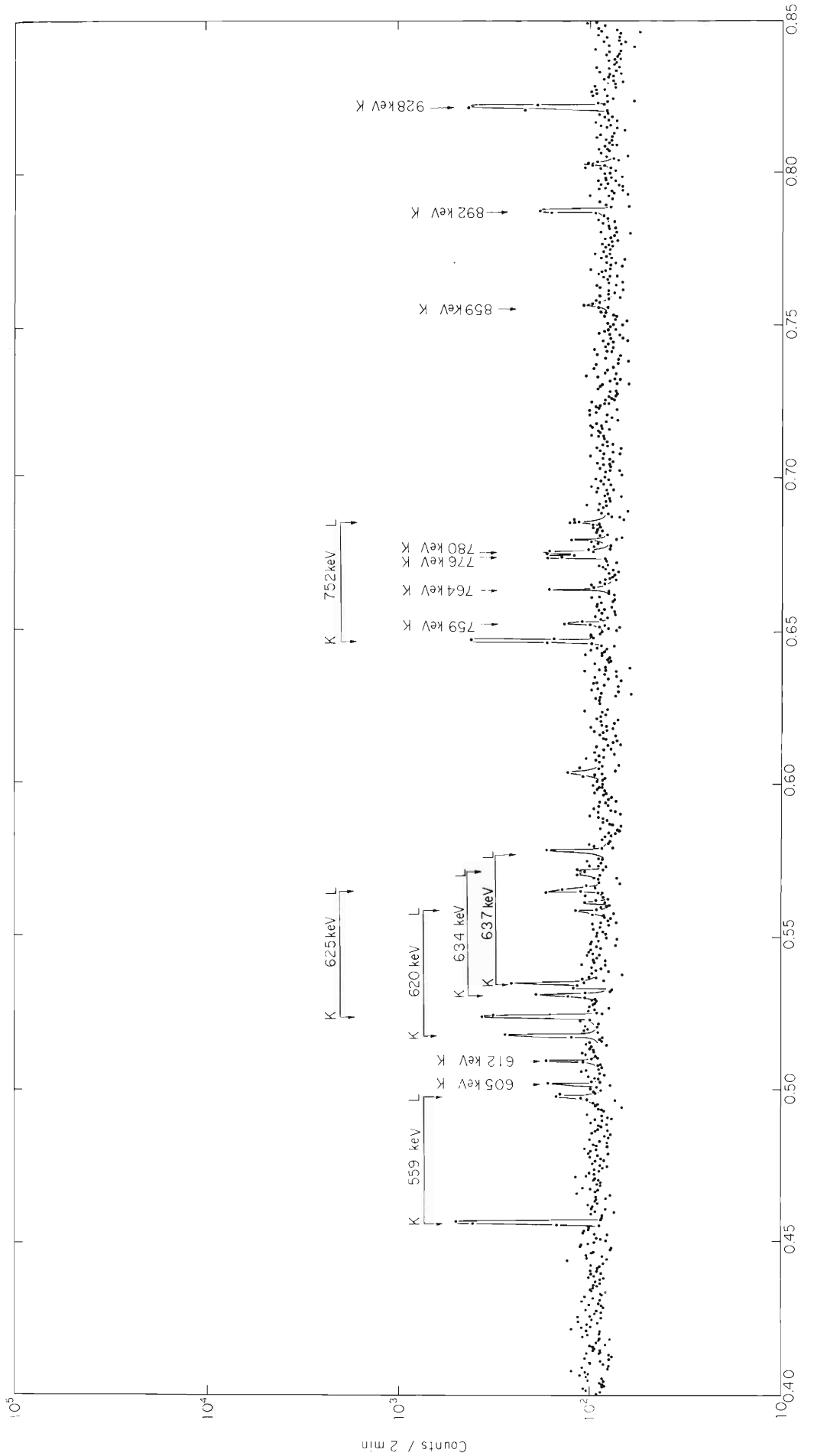

Fig. 2. Higher energy part of the conversion electron spectrum. The current range is 17.6 to 28.4 A.

It is known that the 396 keV transition is of M2 type and α_k of another transition was obtained normalizing the above-mentioned transition to a theoretical α_k (M2). The results are shown in Fig. 3. The subshell ratio of L-electrons of 229 and 396 keV transitions was also measured. To make the decay scheme conclusively, it is necessary to perform a γ - γ coincidence experiment with Ge (Li) - Ge (Li) detectors.

Reference

1) A. Hashizume, Y. Tendow, Y. Awaya, and T. Katou : IPCR Cyclotron Progr. Rep., 3,68 (1969).

5-5. New Neutron Deficient Radioisotope ^{81}Y Produced by Heavy Ions

A. Hashizume, T. Katou, Y. Tendow, Y. Awaya,
and T. Hamada

On the neutron deficient radioisotopes of yttrium, the mass numbers down to 82 have been known. The odd isotopes of this element are interested in because the proton number 39 lies near the submagic number 40 filling $p_{1/2}$ orbitals. From the systematics of half-lives from ^{87}Y to ^{82}Y, the half-life of ^{81}Y was estimated in the order of 1 min. Making extrapolation about the mass of yttrium, 80.9445 has been obtained for ^{81}Y, and assuming this value of mass the Q-value is estimated at about 71.5 MeV for ^{75}As(C, 6n) ^{81}Y reaction.

Natural arsenic targets were bombarded with 70, 80, 90, and MeV ^{12}C ions. The irradiation time was 10 min for each sample. After 3 or 4 min from the end of bombardment, the γ-rays emitted from the produced radioisotopes were measured with a 23 mℓ Ge(Li) detector. Then decays were followed for 2 h and, from the area of photopeaks of each spectra, the half-lives of produced isotopes were determined. In the second step, As targets were dissolved in 6N HNO_3 with yttrium and strontium carrier and a 12 % NH_4F solution was added to obtain precipitate of yttrium fluoride. The time necessary for this chemical separation was about 4 min.

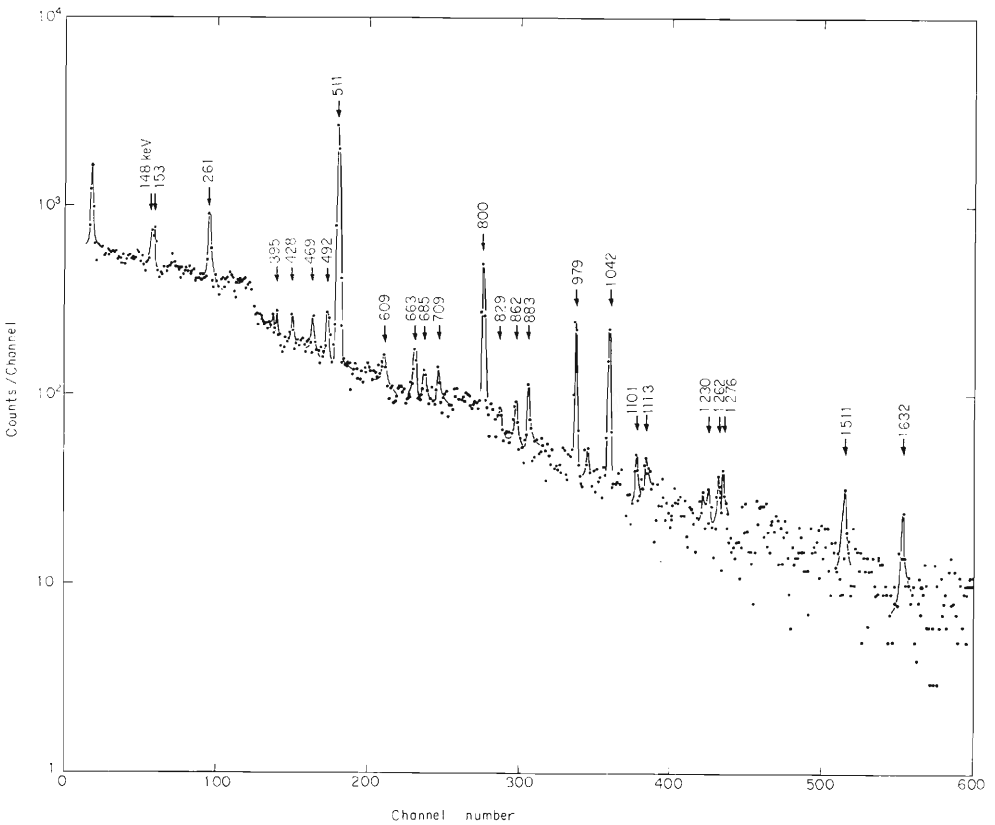

Fig. 1. Gamma-ray energy spectrum. Arsenic target was bombarded with 90 MeV C ions and subsequently yttrium fraction was precipitated.

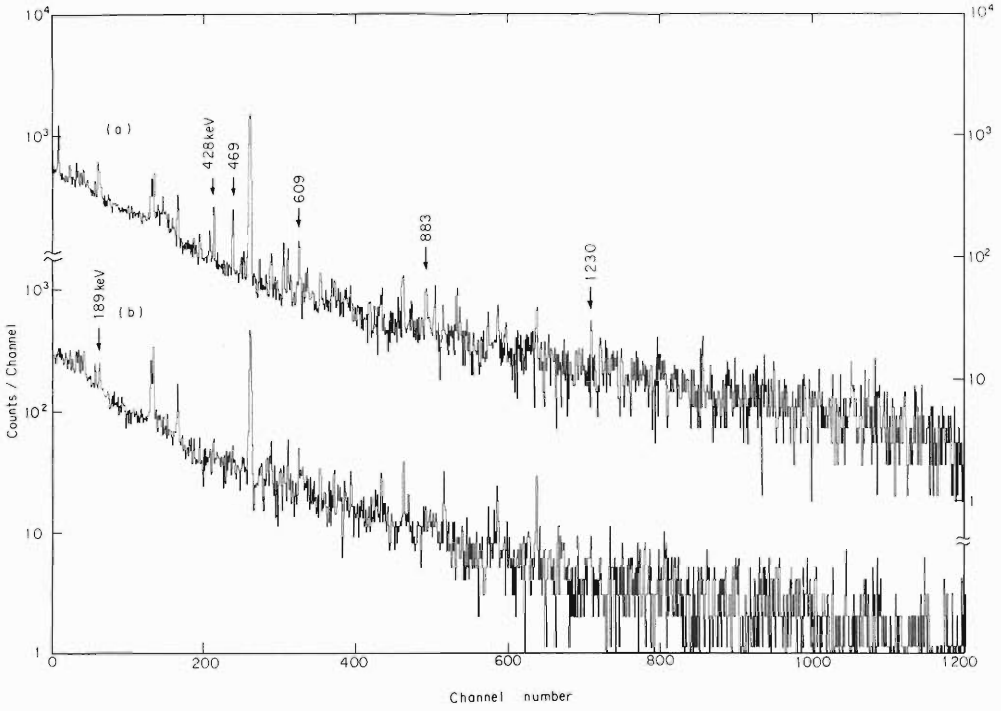

Fig. 2. Gamma-ray spectrum when electrodeposited arsenic target was bombarded by 90 MeV C ions. Gurve "a" was started to count 2.6 min and curve "b" was started 17.8 min after the bombardment, respectively.

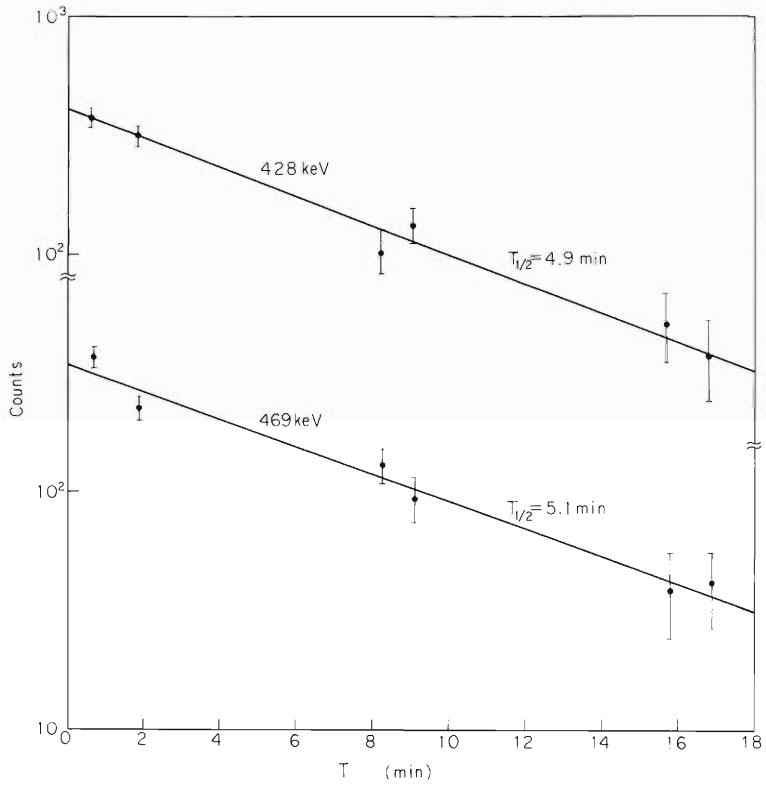

Fig. 3. Decay curves taken with 428 and 469 keV transitions.

Fig. 1 shows a γ-ray spectrum emitted from the yttrium fraction, when a thick As target is bombarded with 90 MeV C ions. Fig. 2 shows γ-ray spectra without chemical separation, but thin electrodeposited As targets on a platinum plate was used. In this case As was dissolved in conc HNO_3 and measured. Curve "a" was taken 2.6 min after bombardment and curve "b" shows a spectrum taken 17.8 min after bombardment. From the figures, 428 and 471 keV transitions belonging to Y fraction are highly excited in 90 MeV and decays with 5.0 min (Fig. 3). The 609, 883, and 1230 keV transitions are also of short life and found in Y fraction, but they are also observed when the target is bombarded with 70 MeV. If ^{81}Y is produced, it decays in such a way that $^{81}Y \longrightarrow {}^{81}Sr \begin{matrix} \nearrow {}^{81m}Rb \\ \searrow {}^{81}Rb \end{matrix} \times \begin{matrix} \nearrow {}^{81m}Kr \\ \searrow {}^{81}Kr \end{matrix} \longrightarrow {}^{81}Br$.

The 189 keV transition in Fig. 2 decays with a half-life of 4.7_5 h and it attributes the decay of ^{81}Rb to the metastable state ^{81}Kr of which the first excited state is reported to be 190 keV. The growth of these γ-rays is a proof that ^{81}Y has been produced.

Thus it is concluded that ^{81}Y decays with the half-life of 5.0 min emitting γ-rays of 428 and 469 keV.

6. NUCLEAR INSTRUMENTATION

6-1 The Ion Optical Properties of Particle Analyzer Determined by Scattered Proton Beams

N. Nakanishi, S. Motonaga, K. Matsuda, S. Takeda
M. Hemmi, H. Nakajima, and Y. Awaya

The beam optical properties of a reaction perticle analyzer have been measured by two methods, i.e. a floating wire method and a method using scattered proton beams. The former method and the results were reported previously,[1] so the latter and the results are described in this report.

The reaction particle analyzer was designed to satisfy the requirements : (i) momentum resolution of $\Delta P/P \leqq 5 \times 10^{-4}$, (ii) luminosity of 3×10^{-3} str., (iii) large dispersion. (iv) small vertical magnification, and (v) straight focal line. The shape of the magnetic field and the optical properties of the analyzer were described in Ref. 2). The set-up is illustrated schematically in Fig. 1.

Measurements were made using proton beams from the IPCR cyclotron. The proton beams are analyzed at energy resolution of 0.1 % by a beam analyzing magnet and scattered by a gold target at the center of a scattering chamber (A in Fig. 1). The thin gold target was prepared by vacuum evaporation onto a Polyvinyl Formvar backing. The magnet system is set at a scattering angle (lab.) of 19°. The proton beams are focused on the target to a rectangle 1.2 mm wide and 7.0 mm high. The elastically scattered proton beams are detected using a silicon surface barrier detector, which is set normally to the beam direction.

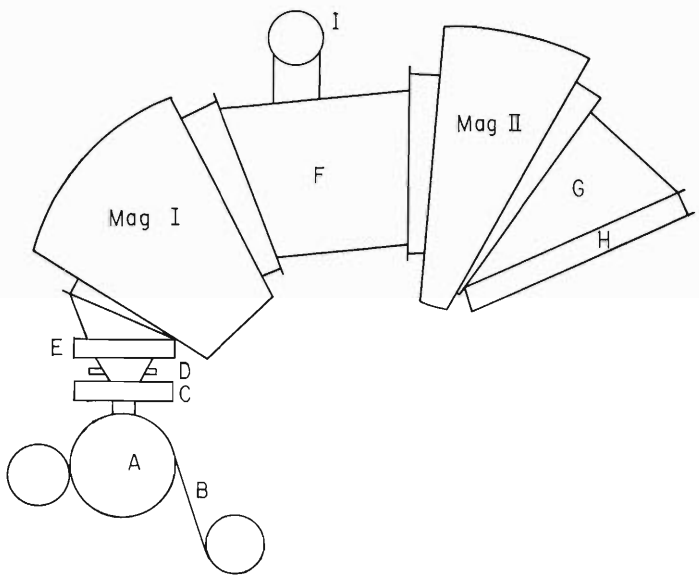

A: Scattering chamber
B: Sliding membrane
C: Slit box
D: Pneumatic value
E: Baffle box (horizontal slit)
F: Connecting vacuum chamber
G: Triangle vacuum chamber
H: Detector chamber
I: Vacuum pump

Fig. 1. Set-up of the reaction particle analyzer.

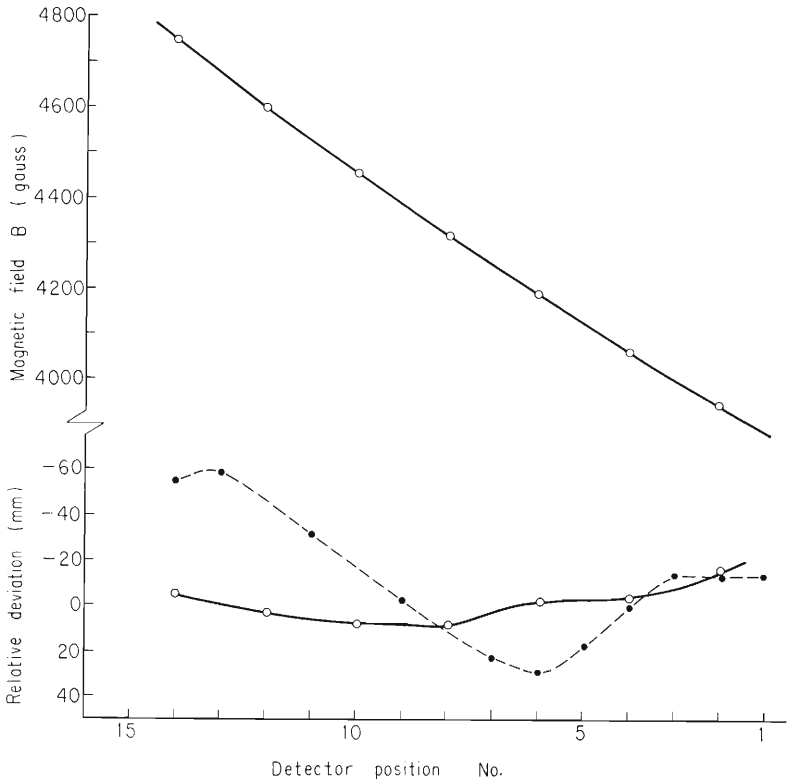

Fig. 2. Magnetic field strength and relative focusing point versus detector positions in the detector chamber. The broken line shows a behavior in the case of carbon steel chambers (F,G in Fig. 1).

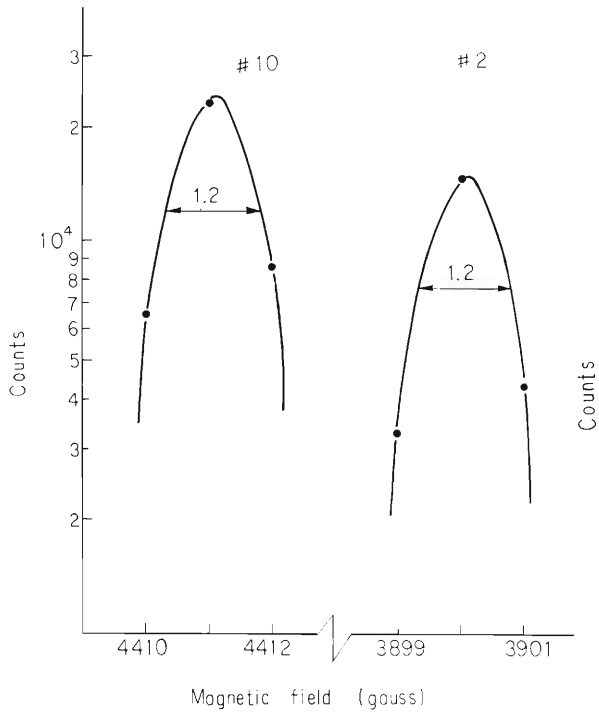

Fig. 3. Proton peaks at the detector positions 2 and 10.

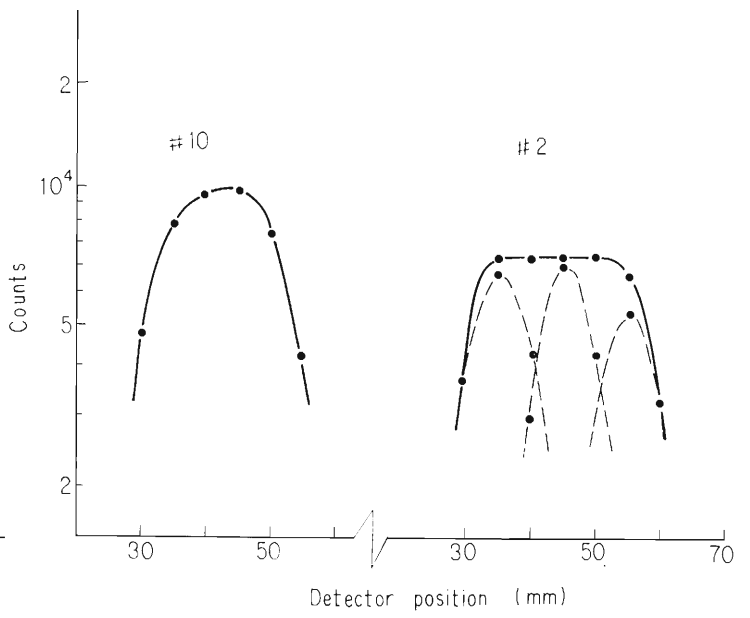

Fig. 4. Beam aspects in the vertical direction at the detector positions 2 and 10.

(1) Horizontal focusing line

A horizontal focusing point is determined to search an intersecting point of two beams with different entrance angles at a given magnetic field strength. Elastically scattered proton beams are led to the magnet I through a horizontal slit (E in Fig. 1). The slit limits the path of beams, and varies the entrance angle to the magnet and the acceptance angle of the magnet. Proton beams are used at an energy of 10.5 MeV. A defining slit of 1 mm in width and 5 mm in height is mounted in front of a detector. Fig. 2 shows the relative focal points and the magnetic field strength corresponding to various detector positions. In the figure closed circles represent experimental values in the case of stainless steel vacuum chambers and open circles in the case of carbon steel vacuum chambers. It can be seen that the effects of materials of vacuum chambers (F, G in Fig. 1) are remarkable. Fig. 3 shows typical examples of yield curves at the focusing points. It may be seen that the energy resolution $\Delta E/E$ is more less equal to 6×10^{-4}. When the focusing line, being curved, is replaced by a straight line, the energy resolution reduces to about 8×10^{-4}. Nuclear emulsions are mounted along the straight line and tests are in progress.

(2) Beam aspect in vertical direction

The beam aspects in the vertical direction are measured in the neighborhood of the horizontal focusing line in order to check the median plane of the system and to provide references for the luminosity. Proton beams are used at an energy of 14.0 MeV. The magnetic field strength is determined so as to obtain a maximum yield in the

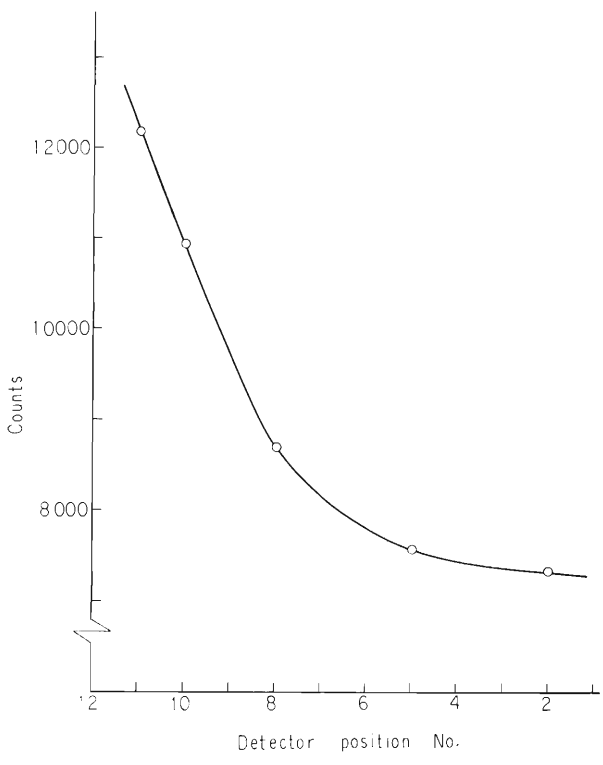

Fig. 5. Relative peak value versus detector positions.

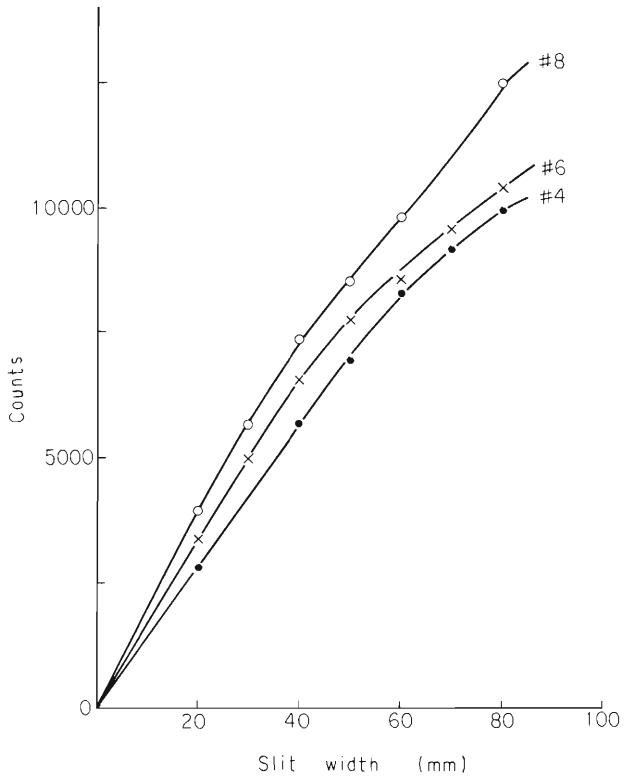

Fig. 6. Peak value versus horizontal width of slit (E in Fig. 1) at the detector positions 4, 6, and 8.

vicinity of horizontal focusing line. At this time, a slit with 5 mm width and 1 mm height is mounted in front of a detector. The yield curves along the vertical direction are measured for the magnetic field strength obtained by the above procedures. Fig. 4 shows some typical examples. Broken lines represent the components of each position at the vertical slit (C in Fig. 1). Preliminary measurements have been done also on the relative yield along the horizontal focusing line and the effect of the horizontal slit (E in Fig. 1) for some horizontal focusing points. These results are shown in Figs. 5 and 6 respectively.

References

1) S. Motonaga, N. Nakanishi, K. Matsuda, M. Hemmi, H. Ono, and Y. Awaya : IPCR Cyclotron Progr. Rep., 3, 77 (1969).
2) N. Nakanishi and K. Matsuda : Nucl. Instr. Methods, 57, 245 (1967).

6-2. Polarized Ion Source

S. Motonaga, M. Hemmi, T. Fujisawa, and Y. Yamazaki

Fabrication and test of RF transition unit and ionizer of atomic beam type polarized ion source which will be installed in the cyclotron are now under way.

Measurements of polarization and beam intensity with low energy deuteron will begin early in 1971. Also, investigations of high pressure dissociator with a Laval nozzle arrangement are on the way for the purpose of obtaining intense flux of the atomic beam.

(1) RF transitions

Radio-frequency transitions are used changing the population of the hyperfine states of the atom in order to increase the nuclear polarization. The adiabatic passage method proposed by Abragam and Winter are used. We have chosen the system of the adiabatic transitions as shown in Table 1, which shows the proposed operating scheme for hydrogen and deuterium and particle polarization after the strong field ionizer. The vector polarization changes its sign by reversing the direction of the axial magnetic field of the ionizer.

With reference to the energy diagrams of Figs. 1 (a) and (b), direct transitions between the states 1 and 3 for hydrogen and between 2 and 4 for deuterium are forbidden. In weak field the states between them are equispaced, making transitions from states 1 to 2 and 3 possible for hydrogen. The same applied to the deuterium case.

In the weak field transition, the oscillating magnetic field should be directed perpendicularly to the static field. It is supplied by a coil wound about a 1.5 cm diameter

Table 1. RF transition parameter.

Particle	Transition	Frequency (Mc/s)	Static field (gauss)	Gradient ΔH	Polarization P_z, P_{zz}
Hydrogen	π_{123}	10.2	8～10	2	−1
Deuterium	σ_{26}	378	40	5	$+\frac{1}{3}$, +1
	σ_{35}	"	117	15	$+\frac{1}{3}$, −1
	π_{36}	"	70	5	$+\frac{2}{3}$, 0
	π_{1234}	10.2	11	3	$-\frac{2}{3}$, 0

π - static and RF field, perpendicular
σ - static and RF field, parallel

quartz tube through which the beam passes.

The transitions σ_{26} and σ_{35} for deuterium are used in almost all of polarized deuteron sources operating at present. The oscillating field is to be parallel to the static field. Therefore it is produced by a hairpin loop, formed by a couple of 5 cm long plates parallel to the beam and bridged at one side. The transition frequency was chosen at 380 Mc/s in our case. The static field changes from 39 to 117 gauss, depending on the transition scheme. The static field H_0 is produced by an electromagnet. Typical field profiles can be achieved as shown in Fig. 2.

(2) Strong field ionizer

Strong field ionizer and its vacuum system are under construction. Basic design is similar to that discribed by Glavish. The atomic beam is ionized by electron collision in a cylindrical region 1 cm diameter and 10 cm long, where 1500 gauss magnetic field parallel to the axis is present.

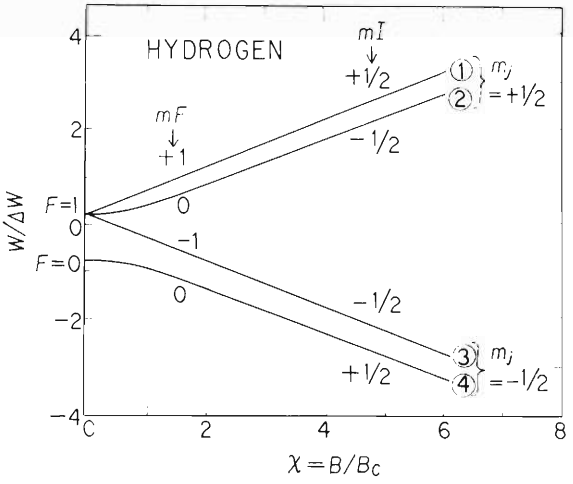

Fig. 1(a) Hyperfine structure levels of hydrogen.

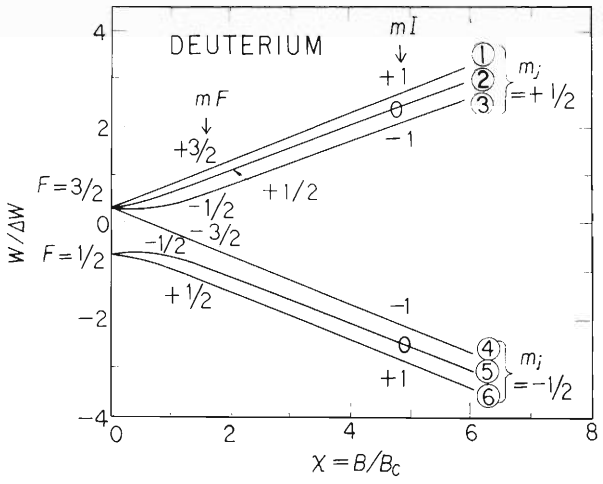

Fig. 1(b) Hyperfine structure levels of deuterium.

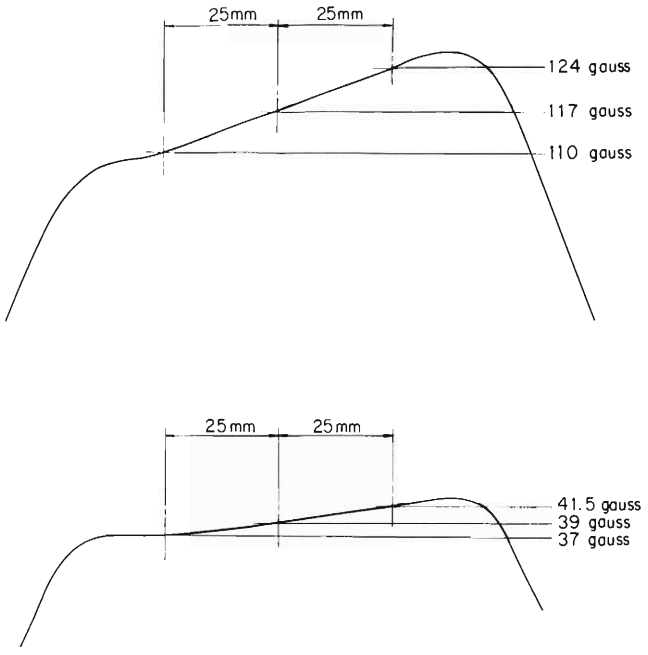

Fig. 2. Field profiles of RF transition magnet at two typical operating levels.

6-3. An On-Line Electron Spectrometer

A. Hashizume, T. Inamura, and J. Fujita

A high resolution, double focused sector type electron spectrometer has been constructed for the study of conversion electrons emitted through de-exciting processes of nuclei after nuclear reactions. This spectrometer will provide useful information for the "in-beam" spectroscopic sutdy together with a Ge(Li) detector for the measurement of γ-rays.

(1) Spectrometer

The special feature of the spectrometer consists in the arrangement of exciting coils of magnet and the setting of shims to make the fringing field effects minimum.[1] Thus we are enabled to get high resolution and high transmission realizing a large magnet pole gap. Each pole with a conical surface is placed symmetrically to the medium plane to provide a field distribution in the radial direction with $\beta = 1/4$. The mean radius of trajectory of electrons is 34.0 cm and the energy range of electrons to be measured is from 50 keV to 4 MeV. The spectrometer can be turned on a rail, allowing to detect electrons emitted from a target at 90, 125, and 180° to the beam direction. A simplified cross sections is shown in Fig. 1.

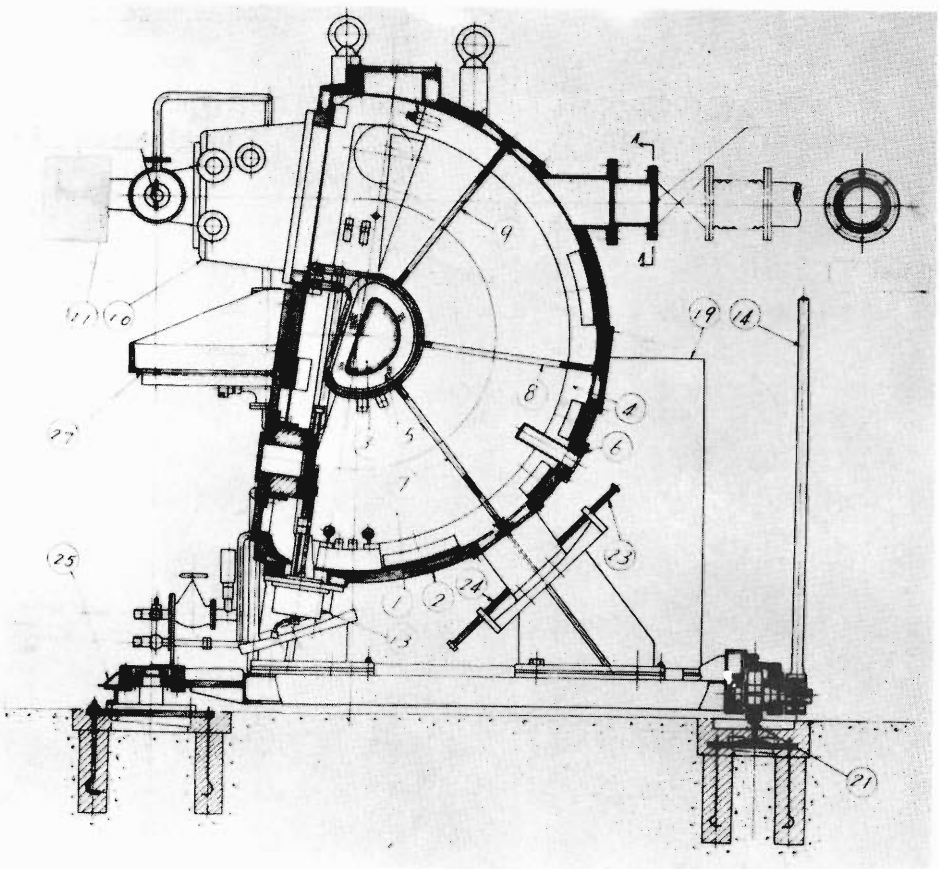

Fig. 1. A cross section of on-line electron spectrometer.

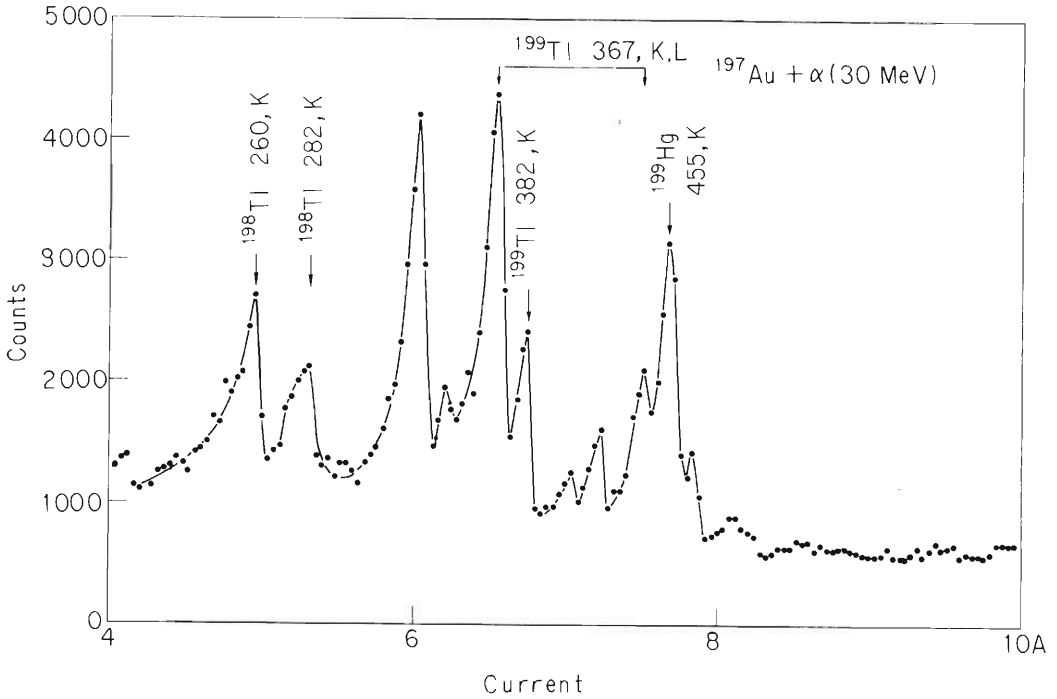

Fig. 2. A conversion electron spectrum from ^{197}Au target bombarded with 30 MeV α - particles. The K and L conversion electrons from $3/2^+ \rightarrow 1/2^+$ 367 keV transition in ^{199}Tl and K peak from $9/2^- \rightarrow 3/2^+$ 382 keV have been observed. The peak at 6.04 A is not yet assigned, it may correspond the 353 keV $5/2^+ \rightarrow 3/2^+$ transition reported by β-decay of ^{199}Pb but there is energy discrepancy of 19 keV.

The coil current is controlled by using twenty four 2SC159A power transistors in parallel. This power supply has three current ranges of 20, 40, and 55 A. The maximum output voltage is 60 V. The current can be varied stepwise manually or automatically at intervals of 0.01, 0.05, 0.1, and 0.5 % of each full scale. The current stability attained is $\pm$ 0.85 $\times$ 10^{-5}/10 h. In case of automatic scanning, the advance signal is taken from the output of a current integrator which advances at the same time one channel of a multiscaler. The details are described in the next section.

A target chamber is attached at the position of a usual β-ray source chamber. The beam extracted from the cyclotron is transported and focused at the source spot by two sets of quadrupole magnet pairs. The typical beam intensity is 200 nA with 1.5 mm height and 20 mm width. The electrons are detected by a lithium drifted silicon semiconductor detector. Its small volume and pulse height discrimination allow us to make a lower background than other detector systems. The momentum resolution of 0.16 % has been obtained by K-lines of ^{137}Cs. The overall "in-beam" performance of the spectrometer has been tested with Au target bombarding α -particles of 30 MeV. A spectrum obtained is shown in Fig. 2. In the figure de-exciting electrons in ^{199}Tl are observed.

(2) Automatic scanning system

A block diagram of the automatic scanning system is shown in Fig. 3. A count-down scaler coupled to a current integrator gives one pulse to the scanning controller

every time when total beam charge from the cyclotron reaches a quantity set beforehand to be appropriate for the measuring time and the statistical charge amount. On receipt of the scaler pulse, the scanning controller generates "start", "clock", and "current advance" pulses which control the analyzer in the multiscaler mode and the

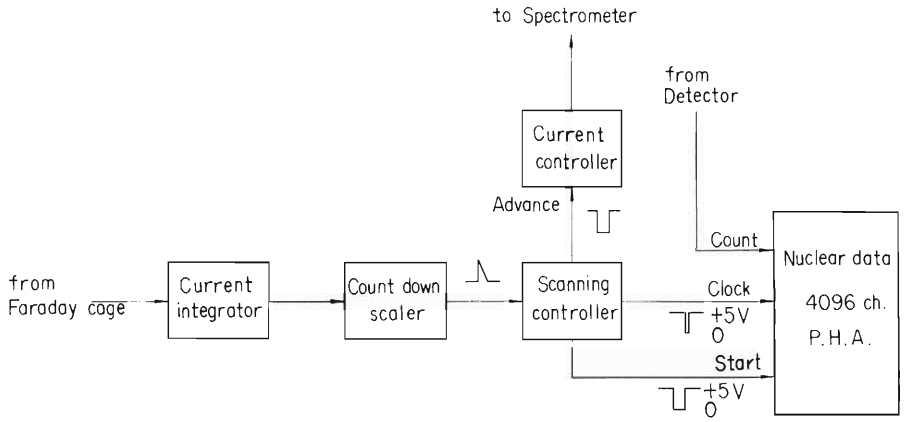

Fig. 3. Block diagram of automatic scanning system of the β-ray spectrometer.

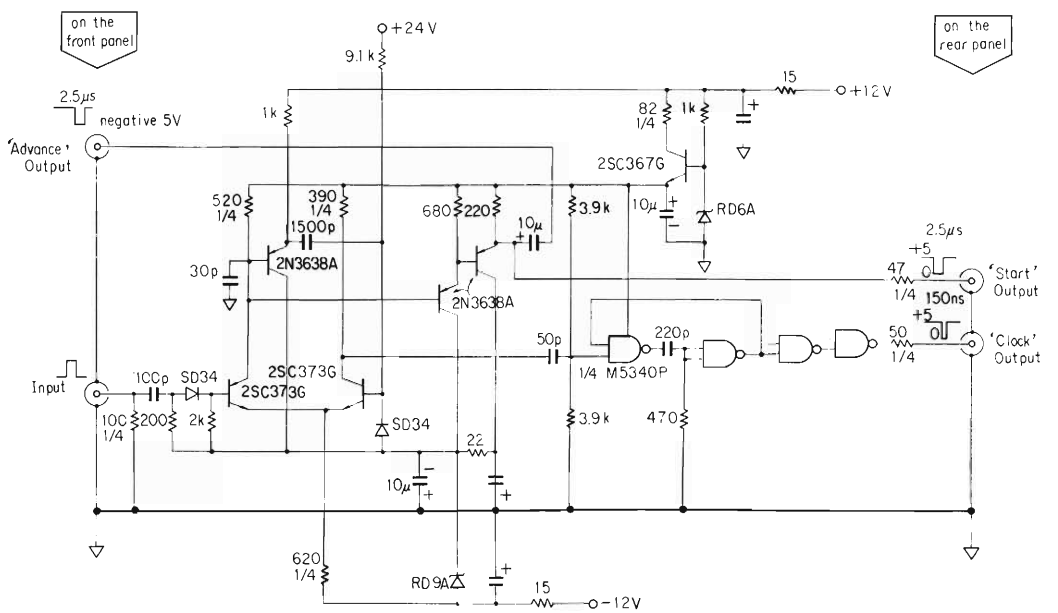

Note. 1. Capacitors 4.7μF, 35 V tantalum except those marked.

Note. 2. Resistors 1/8 W, 5 % carbon except where marked.

Note. 3. The mark of ∇ indicates chassis ground.

Note. 4. ⊐ is the quarter part of nand gate M5340P manufactured by Mitsubishi Electric Co. Ltd.

Fig. 4. Circuit schematics of the scanning controller.

spectrometer. The current advance pulse is sent to the current controller which changes the exciting current of magnet with a given step. Simultaneously the start pulse with a width of 2.5 μ sec enables the analyzer to start multiscaling. Also the clock pulse with a width of 120 nsec starts scaling. The next clock pulse produced after counting per channel advances the channel of the analyzer, which corresponds to the change of the spectrometer current. Once started, the scaling continues to the last channel. In usual measurements the period of counting per channel is long enough to neglect the transient time of the current controller, since it is less than 1 sec. Thus a momentum spectrum is automatically obtained in the memory of the analyzer. Circuit schematics of the scanning controller is shown in Fig. 4.

Reference

1) H. Yamamoto, K. Takumi, and H. Ikegami : Nucl. Instr. Methods, 65, 253 (1968).

6-4. Gate and Delay Generator Composed of all Home-Made Elements

J. Fujita

A gate and delay generator with almost the same specifications as ORTEC module was made of all home-made elements. Delay time stability to temperature change from 25^{o} to 50^{o} C is within 0.7 % over the delay range. Good performance was obtained in operation for a longer time than one day.

(1) Description

It is often needed in nuclear experiments to gate a logic circuit or to make one pulse coincident with another. The gate and delay generator is enough to satisfy the necessities. It gives continuous variable delay to an initial trigger. The width and amplitude of the delayed gate pulse are also variable and its polarity is arbitrarily selected.

(2) Circuit description

Block diagram and circuit schematics are shown in Figs. 1 and 2 respectively. C1 and R8 differentiate an input pulse. D1 sends only the positive part to the base of T1. T1 to T4 form a delay time univibrator which width is determined by the multiples of ohmic drop across R4, coupling condenser C3 or C4 and the inverse of charging current from a current source T4. Delay range switch selects either C3 or C4. The 10-turn delay potentiometer VR1 on the front panel changes the charging current. The output pulse of the delay univibrator switches on an emitter follower T5 normally at an off-state through which a "Delay period" pulse is supplied. The "Delay period" pulse is clipped with a differentiating circuit consisting of R12, R13, and L1, and the negative portion causes T6 to conduct on. A "Delayed marker" burst is fed out at the emitter of T6. The positive burst at the collector of T6 triggers a "Delayed gate" univibrator which period is approximately proportional to the products C9 (R22 + VR2). The amplitude of the "Delayed gate" pulse is controlled by VR2. A phase splitter T10 generates two pulses of equal amplitude but opposite polarity. These pulses are fed out through the separate cascaded emitter followers T11, T13 and T12, T14.

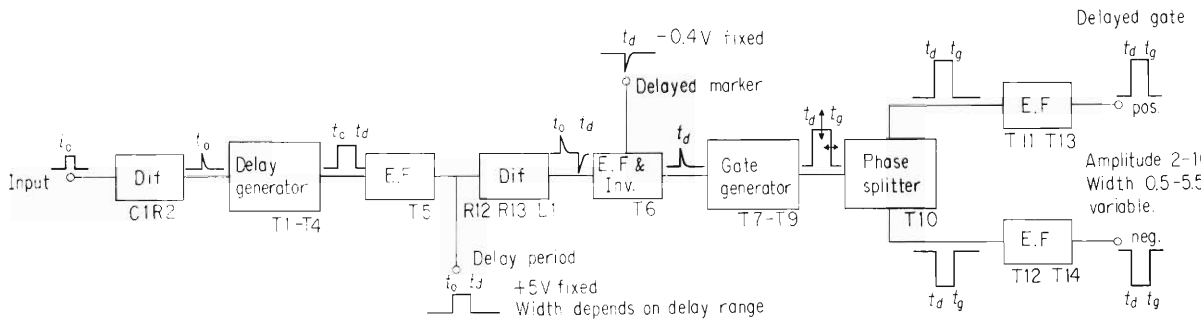

Fig. 1. Block diagram of a gate and delay generator.

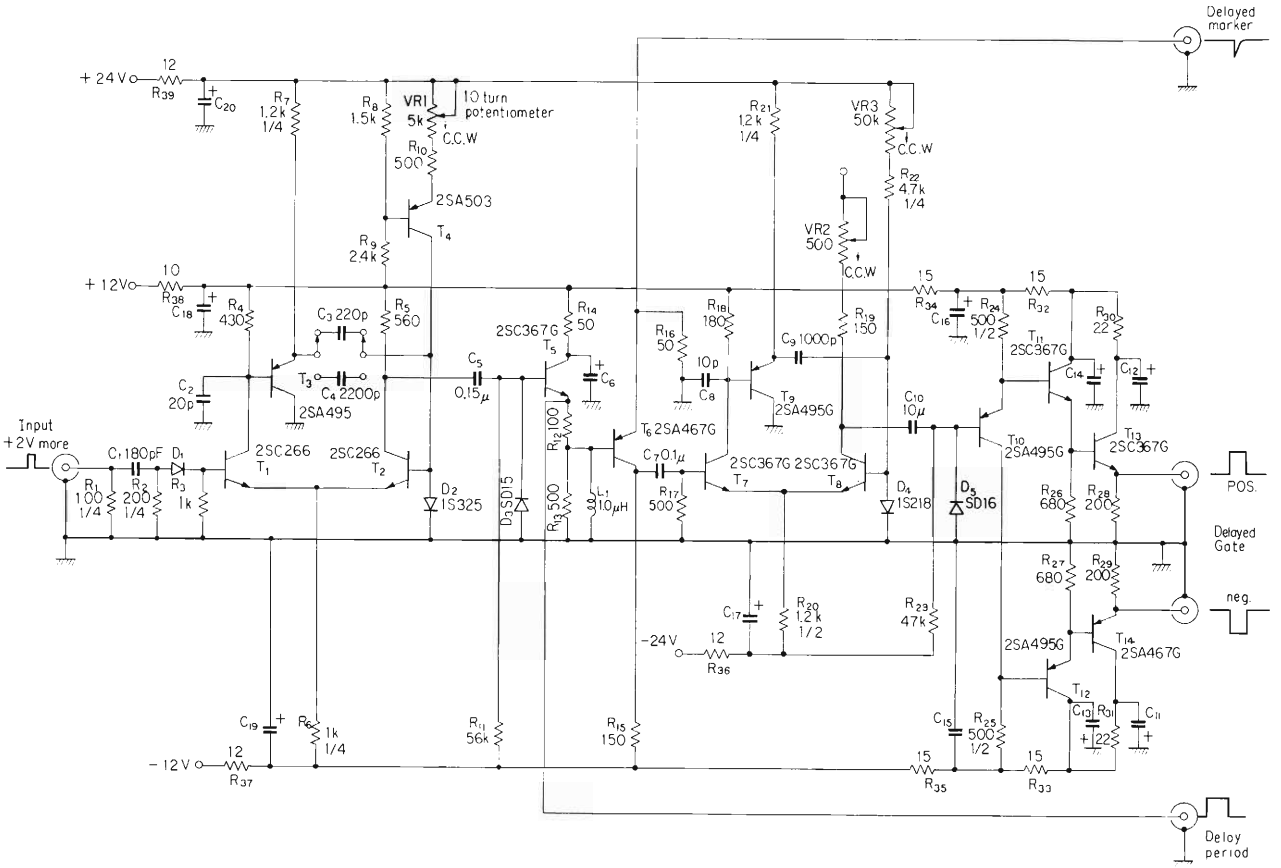

Note. 1. Capacitors 4.7μF 35 V tantalum except those marked.
Note. 2. Resistors 1/8 W, 5 % carbon except where marked.

Fig. 2. Circuit schematics of a gate and delay generator by all home-made elements.

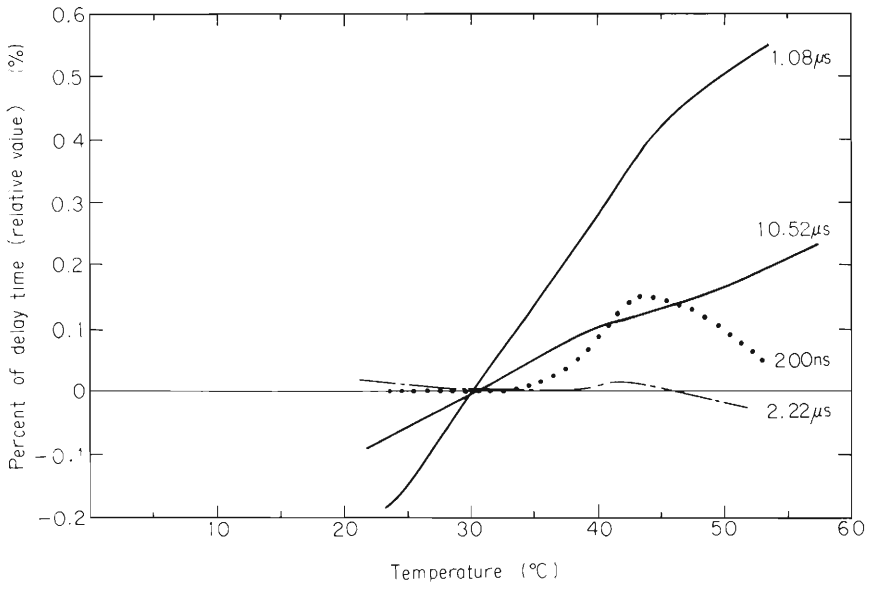

Fig. 3. Delay time stability versus temperature.

(3) Test performance

In an exact measurement of time interval such as an experiment of time of flight, the gate and delay generator must provide a stable delay for a long time, especially in temperature change.

Temperature stability of delay time between an initial pulse and the "Delayed marker" is measured with ORTEC 416 gate and delay generator, ORTEC 437 time to pulse height converter and TMC 400 channel pulse-height analyzer. Adoption of silicon diode 1S325 to D2 and polystyrol condenser to C3 and C4 guarantees stability within 0.03 % per degree of delay time at a temperature range 25° to 50 °C, as shown in Fig. 3. Germanium diode shows characteristics opposite to silicon one, the delay time decreases as temperature increases and the stability becomes worse about ten times.

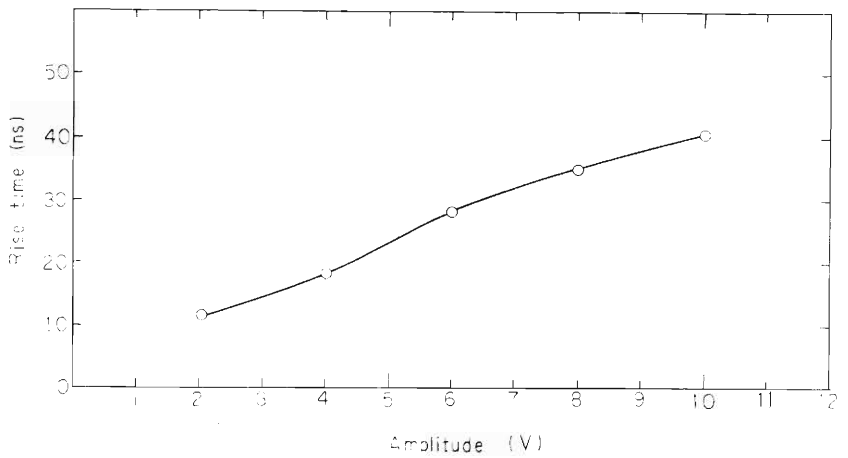

Fig. 4. Dependence of rise time on amplitude in positive 'Delayed gate' pulse.

Rise time of the "Delayed gate" pulse depends on its amplitude because of a long lead wire connecting between R19 and amplitude control VR2 on the front panel, as shown in Fig. 4.

Specifications of input and output pulses are as follows :

Input	Positive 2V minimum with less 60 nsec rise time.
Outputs	
Delay period	Tr $\leq$ 30 nsec. Positive 5V fixed. Width equal to delay time.
Delayed marker	Tr $\leq$ 9 nsec. Negative 0.4 V, width 26 nsec.
Delayed gate	Amplitude variable from 2 to 10V. Width 0.5 to 5.5 μsec. Tr less than 40 nsec, and depends on amplitude. (see Fig. 4)

6-5. The Test Performance of a Multi-Detector System in a Broad Range Magnetic Spectrometer

J. Fujita and S. Takeda

A previous report[1] has given an outline of a multi-detector system used in a broad range magnetic spectrometer. Performance of the preamplifier and test results of the whole system are reported here.

(1) Performance of preamplifier

There are needed 50 preamplifiers with the same specifications. Also they must be of low noise enough to detect 1 MeV protons with least energy loss. Therefore, they were designed taking consideration of low cost, simple gain adjustment, compactness and low noise. The size of the preamplifier-module is $94 \times 30 \times 230$ mm^3. Each module includes two channels of the preamplifiers. The circuit of the preamplifier is schematically shown in Fig. 1. It consists of an input charge sensitive amplifier and an output voltage amplifier. Noise with no input capacitance is within 15 keV (fwhm) as shown in Fig. 2. Fig. 3 shows the relative amplitude of the preamplifier output pulse versus input capacitance. Actual total input capacitance with that of the detector included is within 100 pF. The open loop gain of the charge sensitive stage is calculated to be about 250 times by the curve in Fig. 3. This is a little small to be used together with a thinner detector and a longer input cable.

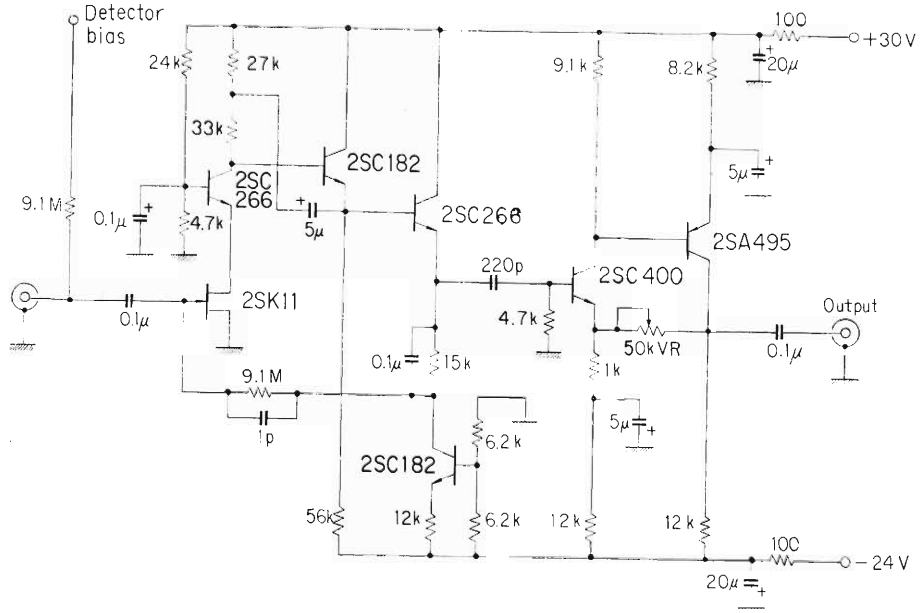

Fig. 1. Schematical circuit of preamplifiers used in a position detecting system.

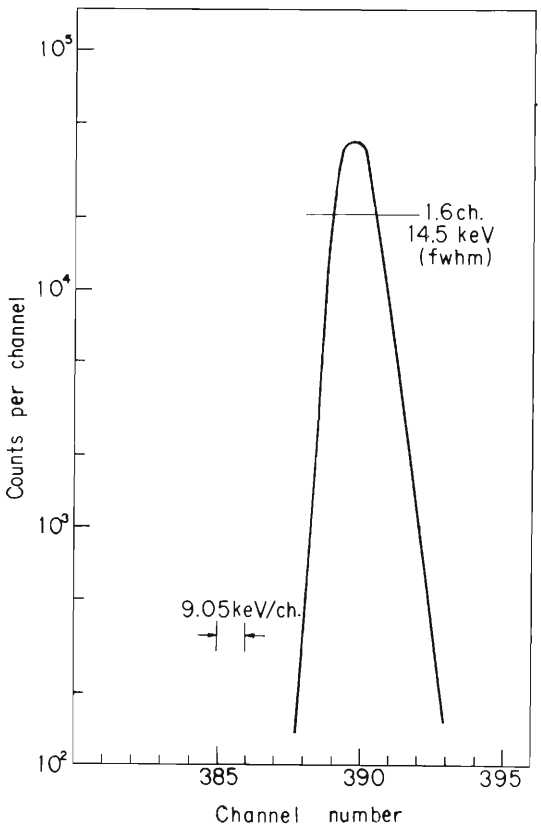

Fig. 2. Noise of the preamplifier with no input capacitance.

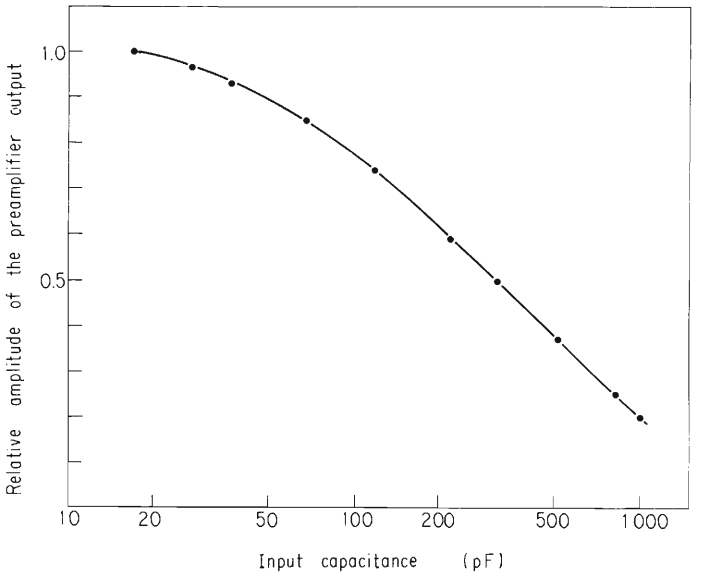

Fig. 3. Preamplifier output voltage as a function of input capacitance.

(2) Test results

We could not make a test of the multi-detector system because of deterioration of the 50 multi-detector-array.

The test was made using other two detectors instead of the noisy detectors. The detectors are 200 μ thick and 20 mm^2 in sensitive area. The test system is shown by the block diagram in Fig. 4. The two detectors are connected to the fourth and the eighth ones of 25 position preamplifiers. An α-ray source with energy 5.47 MeV is placed at equal distance from the two detectors.

The energy resolution at the total adder output is 114 keV (fwhm) as shown in Fig. 5. The graph on the right hand side of Fig. 4 shows that the counts of the fourth and the eight channels are almost equal. These results show equal efficiency of preamplifiers and at the same time good performance of the whole electronic system from the preamplifiers to the pulse height analyzer.

As a result, if new multi-detectors with about 1 mm thickness and noise within 20 keV (fwhm) are used, the detecting and recording system is enough to detect 30 MeV protons analyzed by a broad range magnetic spectrometer. In this case the noise at the total adder output will be within 200 keV (fwhm).

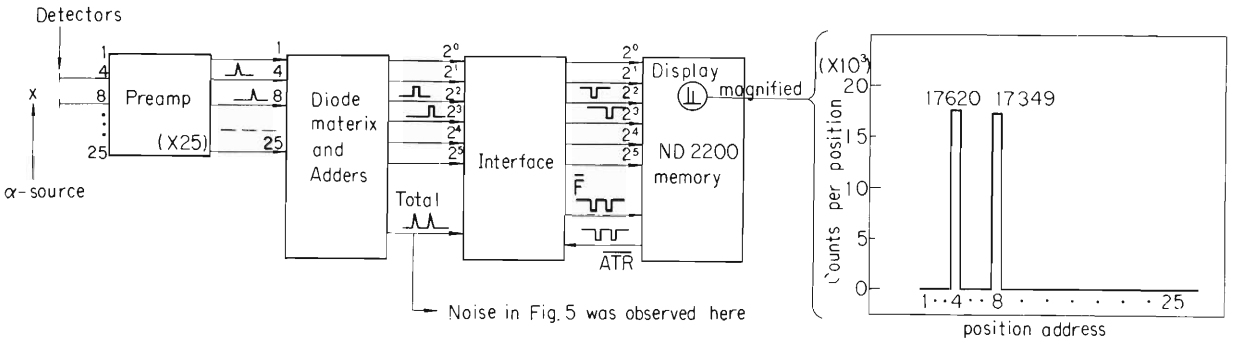

Fig. 4. Block diagram and counting result of a modified test system.

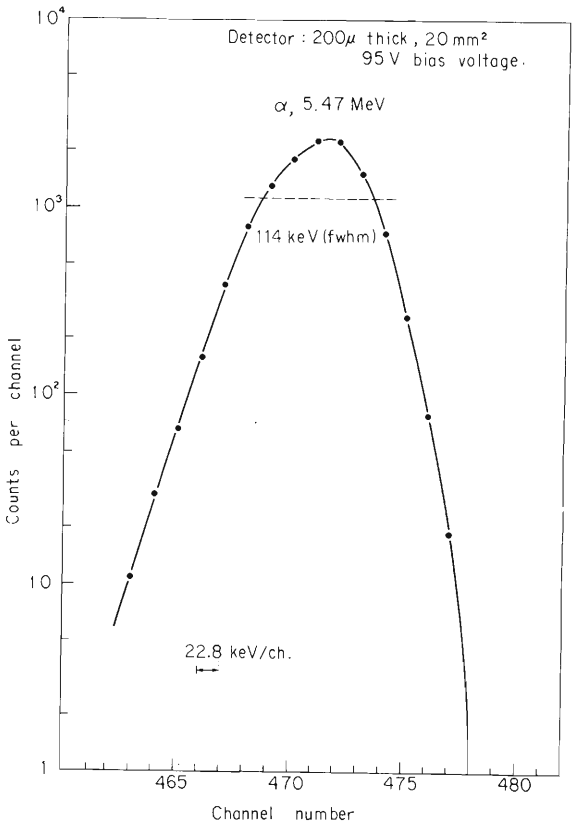

Fig. 5. Energy resolution at the total adder output in the modified test system.

Reference

1) S. Takeda, J. Fujita, and T. Inoue : IPCR Cyclotron Progr. Rep., 2,116 (1968).

7. RADIOCHEMISTRY

7-1. A New Radio-Tracer Method for the Measurement of the Escape of Carbon and Fluorine from Melts of Pure Substances

T. Nozaki, Y. Yatsurugi, and N. Akiyama

Although the knowledge of the behaviour of impurity carbon in the fusion of pure elements is very important in their further purification, suitable methods for the required study have not yet been fully developed. Usual physical and chemical methods are of little use, and ordinary radio-tracer techniques involve difficulties in the tracer incorporation and in the reliable measurement of subnanogram quantities of ^{14}C. As to the similar study of impurity fluorine no adequate technique has been found, either.

We, as well as other workers, in studying the charged-particle activation analysis of high-purity elements, have found that fairly high activities of ^{11}C and ^{18}F are formed by the fission and spallation of the matrix itself when silicon or aluminium is bombarded by ^{3}He- or α-particles of relatively low energies.[1)~4)] Our results for the thick-target saturation activities of ^{11}C and ^{18}F for the ^{3}He and α reactions on silicon (natural isotopic composition) are shown in Fig. 1. We have made use of the fission and spallation reactions for the carrier-free incorporation of ^{11}C and ^{18}F tracers into semiconductor silicon, and have thus obtained new information about the escape of carbon and fluorine from its melt.

Silicon disks (about 1g) of varying contents of carbon (30 p.p.b. to 3 p.p.m.) and oxygen (10 p.p.b to 15 p.p.m.)[1)] were bombarded by ^{3}He-particles (40 MeV, 1 to 5 μamp. 20 min). After the removal of the surface contaminations by etching, the disk was divided into two portions and the ratio of gross activities in them was determined. One portion was then placed on a semiconductor silicon rod or in a quartz dish sustained in a quartz fusion tube without any contact with its side wall. The fusion of the sample was carried out by radio-frequency heating either in a vacuum or in a high-purity helium stream. During the fusion, a grey or brownish sublimate deposite onto the side wall around the melt ; the amount was usually from 0.1 to 1 mg in the fusion in a quartz dish and much less in that on silicon. The gaseous activity evolved from the melt was either once trapped and then analyzed by radio-gaschromatography or carried away with the stream for the continuous monitoring of the ^{11}C evolution ; it was then absorbed in a small trap. After the fusion, the ^{11}C in the sublimate and the fused silicon and also in the other portion of the bombarded silicon was separated chemically,[1)] and the activities in the portions and in the trap were measured and compared. The ^{18}F activites, on the other hand, were determined nondestructively from the decay curves of the annihilation radiations.

The results so far obtained include : (1) a small part of the ^{11}C escaped from the melt almost instantaneously when the silicon was fused ; (2) in the fusion on a silicon rod, no further escape was observed ; in the fusion in a quartz dish, the escape continued until most of the ^{11}C disappeared from the melt ; (3) in a vacuum, almost no gaseous ^{11}C was found, but the sublimate contained a notable ^{11}C activity ; in helium, a main portion of the ^{11}C which had left the melt was found as ^{11}CO ; (4) no marked differences due to the original bulk contents of carbon and oxygen were found ; (5) most of the ^{18}F (more than 90 %) was found to escape, within a few minutes, from the melt onto the inside wall. Also, the ^{24}Na and ^{22}Na formed simultaneously with ^{11}C and ^{18}F were found to behave much like ^{18}F. Fig. 2. shows the continuous evolution of gaseous ^{11}C activity into a helium stream ; the silicon sample containing about 50 p.p.b.

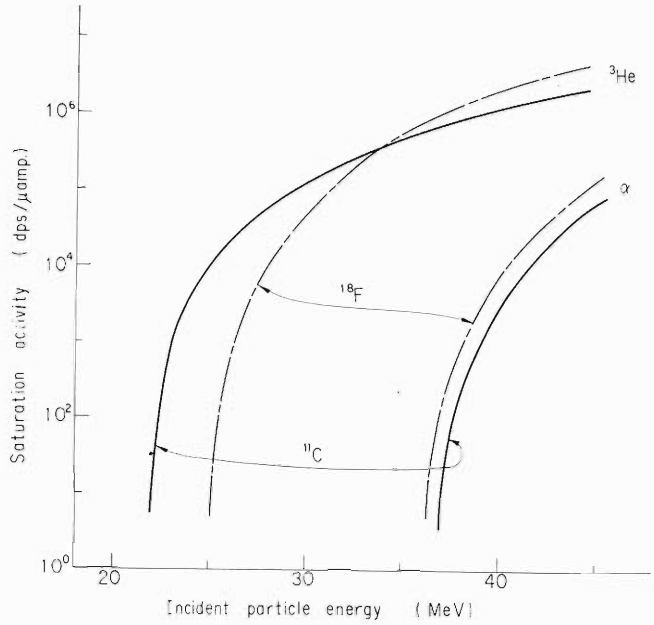

Fig. 1. Thick target saturation activities of ^{11}C and ^{18}F for the ^{3}He and α reactions on silicon.

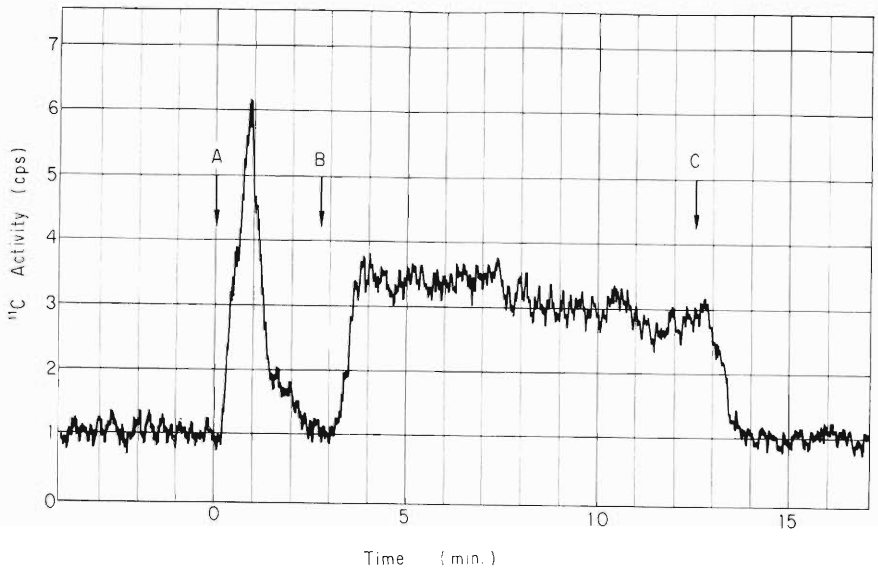

A: melting of the silicon sample
B: contact of the melt with quartz
C: solidification of the melt

Fig. 2. Evolution of gaseous ^{11}C from a silicon melt.

of both carbon and oxygen was fused on semiconductor silicon, and after a few minutes the melt was brought into contact with the quartz-tube wall. The reaction of a p.p.b. level of carbon with trace quantities of oxygen is thus clearly demonstrated.

These results give information valuable in the industrial zone-refining of semiconductor silicon. It is sure that similar techniques are applicable also to some other matrices.

References

1) T. Nozaki, Y. Yatsurugi, and N. Akiyama : J. Radioanal. Chem., 4, 87 (1970).
2) M. Deyris and Ph. Albert : Compt. Rend., C 262, 1675 (1966).
3) N. Chevarier, J. Giroux, M. D. Tran, and J. Tousset : Bull. Soc. Chim. France, 1967, 2893.
4) H. Lo Rook and E. A. Schweikert : Anal. Chem., 41, 958 (1969).

7-2. A Mössbauer Spectroscopic Study of the Chemical State of ^{119}Sn after the EC Decay of ^{119}Sb in Metal and Inorganic Compounds of Antimony

F. Ambe, H. Shoji,* S. Ambe,
M. Takeda,** and N. Saito

Mössbauer emission spectroscopy offers a unique way of studying the chemical consequences of nuclear decay in the solid.[1] We report here on our recent study of the chemical state of ^{119}Sn atoms after the EC decay of ^{119}Sb by this technique.

In the various Sn(II) and Sn(IV) compounds so fat studied, no change in the oxidation state of tin atoms has been observed after the IT decay of ^{119m}Sn,[2] except for the special compound in which the Sn(IV) atoms are surrounded by reducing ligands.[3] This fact led us to study the chemical state of ^{119}Sn atoms arising from another source nuclide, ^{119}Sb, which decays by electron capture directly to the Mössbauer level of ^{119}Sn. Will the ^{119}Sn atoms be distributed between the Sn(II) and Sn(IV) states following the EC decay of ^{119}Sb in Sb(III) compounds ? Little attention has been paid to this nuclide[4] because its half life is relatively short (38.0 h) and its production requires an accelerator. We established a procedure for preparing ^{119}Sb by the cyclotron and measured the Mössbauer emission spectra of metal and compounds of antimony labeled with ^{119}Sb. The oxidation state of ^{119}Sn atoms after the EC decay of ^{119}Sb was found to be dependent on the physicochemical properties of the host antimony compounds and in some Sb(III) compounds the ^{119}Sn atoms were found to be distributed between the Sn(II) and Sn(IV) states.

^{119}Sb was produced by the d-bombardment of a tin plate with a natural isotopic abundance. The ^{119}Sb in the target was radiochemically separated from tin, and metal and compounds of antimony labeled with ^{119}Sb were prepared. With those as the source, the Mössbauer spectra of ^{119}Sn were measured. The source was maintained at liquid nitrogen temperature in a cryostat and was driven in the constant acceleration mode by means of an electromechanical feed-back type transducer against a barium stannate standard absorber at rest (room temperature). The 23.8 keV Mössbauer γ-rays were detected with a thin NaI scintillator, and the counts were stored in a Hitachi 400-channel pulse-height analyzer.

Typical spectra obtained are shown in Fig. 1. Antimony metal labeled with ^{119}Sb gave a single peak in the region of Sn(0), as might be expected from the high electric conductivity of metal. The observed isomer shift, 2.7 mm/sec (versus $BaSnO_3$, the sign is as in usual absorption spectra), was in close agreement with the value reported for β-tin. As may be seen in the figure, $^{119}Sb_2S_3$ showed two emission peaks with isomer shifts of 3.8 and 1.4 mm/sec, indicating that the ^{119}Sn atoms appearing after the EC decay of ^{119}Sb in this compound are distributed between the Sn(II) and Sn(IV) states. This result may be said to be worthy of note, since the IT decay of ^{119m}Sn generally gives rise to only one oxidation state of tin, as has been described above. The emission spectrum gave, however, only one peak in the region of Sn(II) in the case of another chalcogenide of trivalent antimony, $^{119}Sb_2Te_3$, which is a semiconductor. Thus, it can be concluded that the chemical fate of ^{119}Sn atoms is highly dependent on the physicochemical properties of the host antimony compound.

* Visiting scientist from Tokyo University of Education.
** Visiting scientist from the University of Tokyo.

Similar studies are now in progress on other compounds of antimony and also on metal and compounds of tellurium labeled with ^{119m}Te.

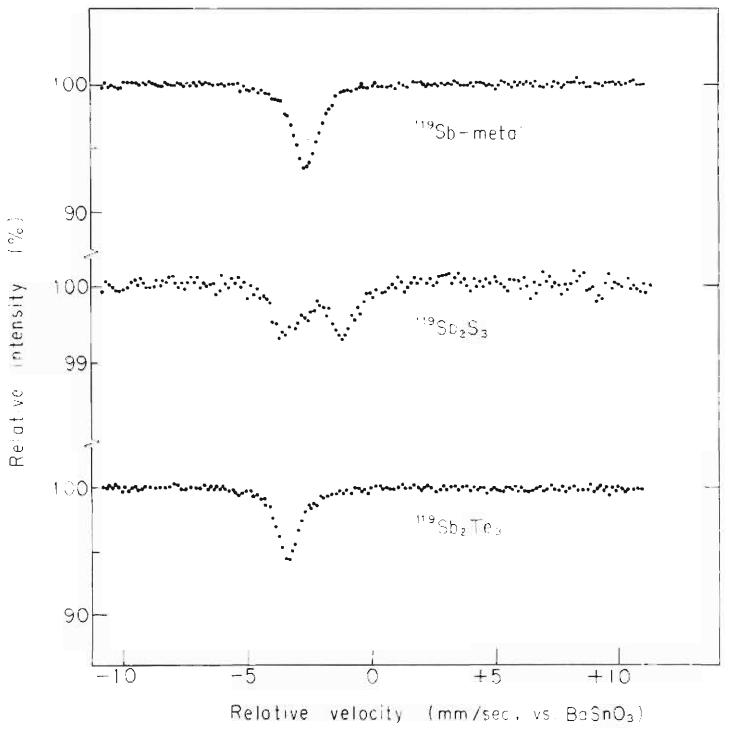

Fig. 1. Mössbauer emission spectra of ^{119}Sb-labeled metal and compounds of antimony at liquid nitrogen temperature (absorber: barium stannate at room temperature).

References

1) G. K. Wertheim : Phys. Rev., 124, 764 (1961).
2) See comments by R. H. Herber : "Proc. Symp. of the Faraday Society", No. 1. The Mössbauer Effect, p. 19, 101 (1967).
3) H. Sano and M. Kanno : Chem. Commun., 1969, 601.
4) P. A. Pella and J. J. Spijkerman : NBS Technical Note, 451, 90 (1969).

7-3. Charge States of Ions Produced by the Electron-Capture Decay of ^{109}Cd

M. Aratani, M. Inarida, and N. Saito

Measurements have been made of the charge distribution of the ions produced by the electron-capture decay of ^{109}Cd (453d) on the solid surface. The apparatus employed was a pulse-counting-mode magnetic spectrometer, consisting of an ion-source chamber, an analyzer tube, a detector, and 3-channel-pumping systems. The ion-source chamber

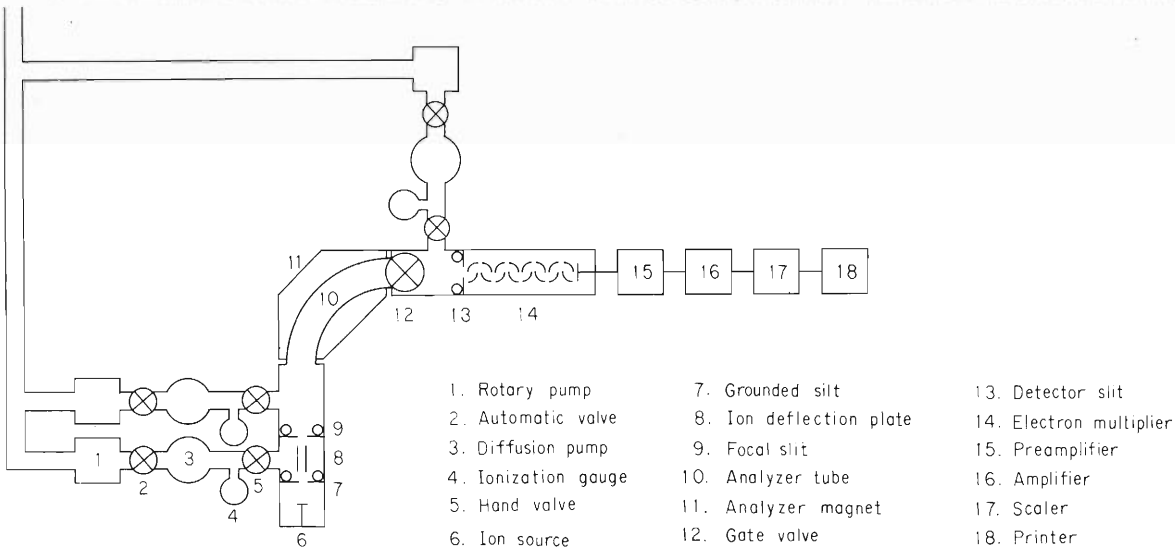

Fig. 1. Charge spectrometer for solid RI.

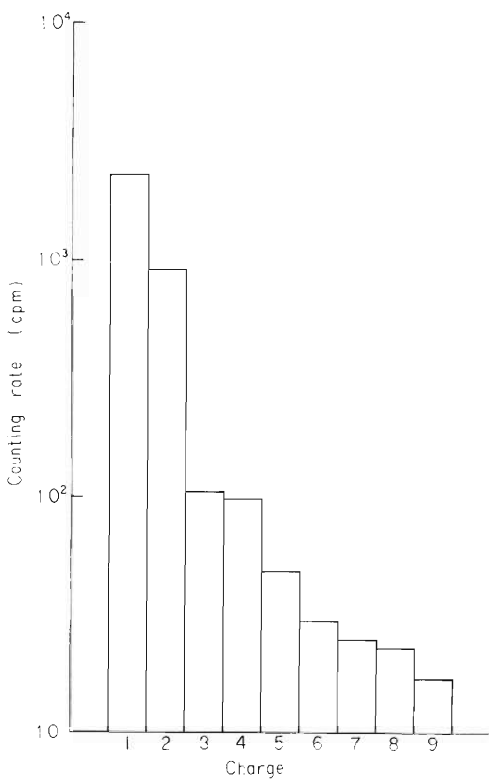

Fig. 2. Charge States of ions produced by the electron-capture decay of ^{109}Cd.

had a demountable mesh electrode made of stainless steel (Fig. 1).

The radionuclide, ^{109}Cd, produced by the ^{109}Ag (d, 2n) ^{109}Cd nuclear reaction was isolated without an isotopic carrier by means of the solvent-extraction procedure developed by the authors. A HCl solution of carrier-free ^{109}Cd was dropped on the mesh, which was left in a desiccator and later mounted in the ion-source chamber. The radioactivity at this stage was approximately thirty thousand c.p.m. Immediately after the mounting the ion-source chamber was evacuated to 10^{-7} Torr.

A high-tension voltage of 5000 V at the maximum was applied to the mesh electrode. The ions produced by the electron-capture decay of ^{109}Cd on the solid surface were pulled out through a grounded slit, analyzed by the magnetic field, and counted using a 16-stage, Cu-Be electron multiplier.

^{109}Cd decays to the first excited state of ^{109}Ag. Emitting 87.7 keV gamma rays (E3), the state deexcites to the ground state of ^{109}Ag ; it has a life time of 40 sec. The gamma transition has an internal conversion coefficient larger than unity.

The charge spectrum of the atoms produced by the decay is illustrated in Fig. 2. The most abundant ion species is singly-charged.

8. RADIATION CHEMISTRY AND RADIATION BIOLOGY

8-1. The Radiolysis of an Aqueous Ferrous Ammonium Sulfate Solution with C-, N-, and O-Ion Radiations

M. Imamura, M. Matsui, and T. Karasawa

The radiolysis of an aqueous ferrous ammonium sulfate solution was investigated by using carbon-, nitrogen-, and oxygen-ion radiations over a wide range of energy. The primary purpose of this study was to examine the possibility of determining radiation dose with the solution (Fricke solution) as well as to establish the irradiation arrangement. A series of the experiments revealed quite interesting features about the radiolysis mechanism of water at a limiting linear energy transfer (LET) and about the specific effects of heavy-ion radiations.[1] These features as well as the experimental procedures different from those for proton and helium-ion experiments[2] are described below in three sections.

(1) Irradiation

The heavy ions accelerated at energies between 50 and 100 MeV were shot into solution. Ions traversed a thin gold foil (2μ), an exit window (10μ Al), air layer (10 mm) and a cell window (10μ mica) before entering solution. Energies of ions entering solution (E_s) were obtained from the range-energy curves given by Northcliffe;[3] the range of E_s extended 31~77 MeV for C-ions, 17~78 MeV for N-ions and 58 MeV for O-ions. The principal difference between protons (or helium ions) and heavy-ions is that the former can be regarded as charge-invariant over most of the energy region, while the latter can not. With an increase in the atomic number of the ion, there is an expansion of the velocity region in which charge variation is of importance. Fortunately, according to Northcliffe, the experimental equilibrinm charge distribution data for several heavy ions can seemingly be represented well by a single universal curve for each value of $z - z'$ (z: atomic number, z': net charge).[4] We have, therefore, calculated the average charge of ions entering solution, $\langle z \rangle_s$, by taking weighted means of each fraction of ions having a charge, z', in a charge-equilibrated monoenergetic beam. By using these quantities together with the number of ions determined with a Faraday cup, we could calculate the radiation-chemical yield which is defined by G, the number of molecules produced per 100 eV of energy deposited in solutions. The LET-values for ions with an energy of E_s and with a net charge of z' were calculated by the reduced Bethe equations:

$$-\frac{dE}{dx} = (A\, z'^2/E_s)\ \log\ (B\, E_s)$$

where A = 22.2, 25.9, and 29.6 and B = 2.75, 2.36, and 2.06 respectively for C-, N-, and O-ions. $(-dE/dx)$ is expressed in eV/Å where E_s is in MeV.

The oxidation yield of ferrous ions was found to be linearly dependent on the dose, and the results were even more reproducible than those for proton and helium-ion experiments.

(2) The limiting yield for net water decomposition at an infinite LET

The observed oxidation yields, $G(Fe^{3+})$, are shown in Fig. 1 as a function of the initial LET of heavy-ion radiation. It has been well-known that $G(Fe^{3+})$ decreases from G = 15.5 for ^{60}Co- γ rays (LET = 0.02 eV/Å) with increasing LET. However, quite a few data have been reported above LET ~5 eV/Å; these data are summarized together with the present ones in Fig. 2. Apparent discontinuities observed among different particles will be interpreted in the next section.

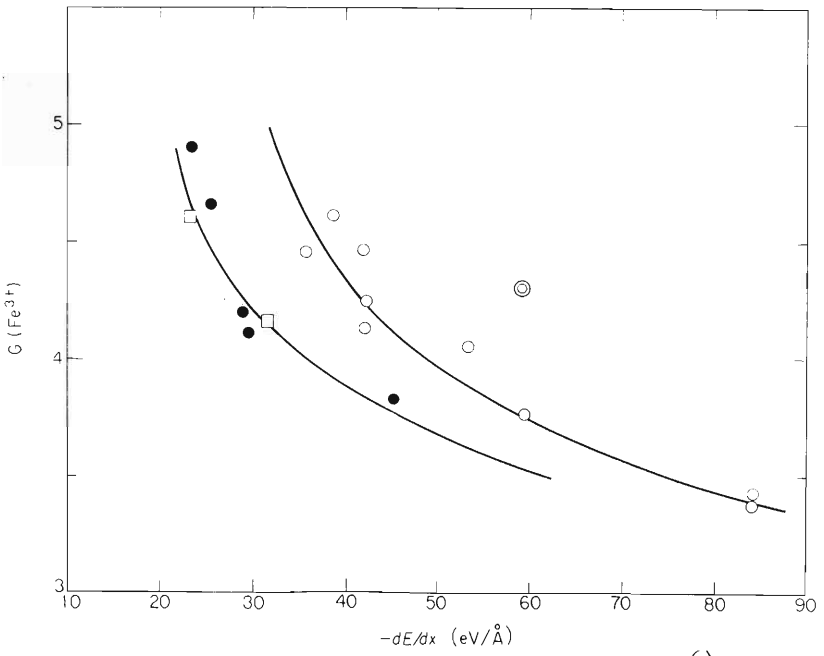

●: C-ions, □: C-ions by Schuler,[6]
○: N-ions, ◎: O-ions.

Fig. 1. The observed $G(Fe^{3+})$'s as a function of the initial LET of heavy-ion radiation.[2]

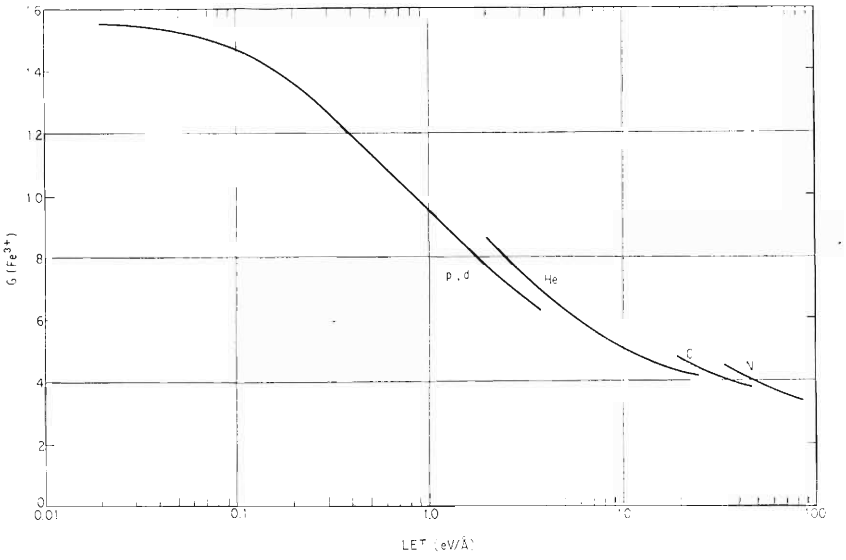

Fig. 2. Variation of $G(Fe^{3+})$ with LET over a wide range. Data shown in Fig. 1 are also included.

The ferric ion yield from Fricke solution is expressed by

$$G(Fe^{3+}) = G_{OH} + 3G_H + 2G_{H_2O_2} \quad (1)$$

where G_X stands for the 100 eV yield for initial species, X.
Using the material balance expected in water radiolysis:

$$G_H + 2G_{H_2} = G_{OH} + 2G_{H_2O_2} = G(-H_2O) \quad (2)$$

one can rewrite Eqn. (1) as

$$G(Fe^{3+}) = G(-H_2O) + 3G_H = 2G_{H_2} + 4G_H \quad (3)$$

where $G(-H_2O)$ represents the yield of net water decomposition.

According to the diffusion model in the radiation chemistry, at an infinite LET the radical yields, G_H and G_{OH}, should vanish. This assumption is based on the concept that all the free radicals recombine with each other in the dense ionization tracks before being homogenized, and has been evidenced by the experimental facts that G_H and G_{OH} decrease with increasing LET. At an infinite LET, therefore,

$$G(Fe^{3+}) = G(-H_2O) \quad (4)$$

The limiting $G(-H_2O)$ can also be deduced from the yields of free radicals at high LET. A lack of data at high LET's has led to higher value for $G(-H_2O)$ at a limiting LET; Schuler and Allen has estimated $G(-H_2O)^{\infty} = 3.6$.[5)]

Observed values for $G(Fe^{3+})$ are average ones for particles and the energies of which decrease from their incident values, E_s, to almost zero. The integrated yield of ferric ions along the path of a particle with incident energy E_s is given by

$$G(Fe^{3+}) \cdot E_s = \int_0^{E_s} G_i(Fe^{3+}) dE_s \quad (5)$$

where E_s is in 100 eV and G_i represents the "instantaneous" or "thin-target" yield. From Eqn. (5) one can derive

$$G_i(Fe^{3+}) = \frac{d\left[G(Fe^{3+}) \cdot E_s\right]}{dE_s} \quad (6)$$

Eqn. (6) shows that the instantaneous yield at a given E_s is given from the slope of the curve obtained by plotting $G(Fe^{3+}) \cdot E_s$ against E_s. Figure 3 shows such a plot of the present data and Schuler's ones with C-ions from HILAC.[6)] Apparently all the data with three heavy ions are represented well by a single universal curve. The dotted line in Fig. 3 is a slope at $E_s = 0$ or an infinite LET, which gives $G(-H_2O)^{\infty} = 2.9$

Being substantially lower than 3.6 estimated by Schuler and Allen,[5,6)] the present value of 2.9 must be more accurate than theirs. There have been some mechanistic discussions on the primary processes in the high-LET tracks on the basis of $G(-H_2O)^{\infty} = 3.6$. The high $G(-H_2O)^{\infty}$-value gives rise to the variation of $G(-H_2O)$ with LET that can not be readily explained by simple assumptions, whereas other products yields show monotonic variations with LET as expected from simple diffusion

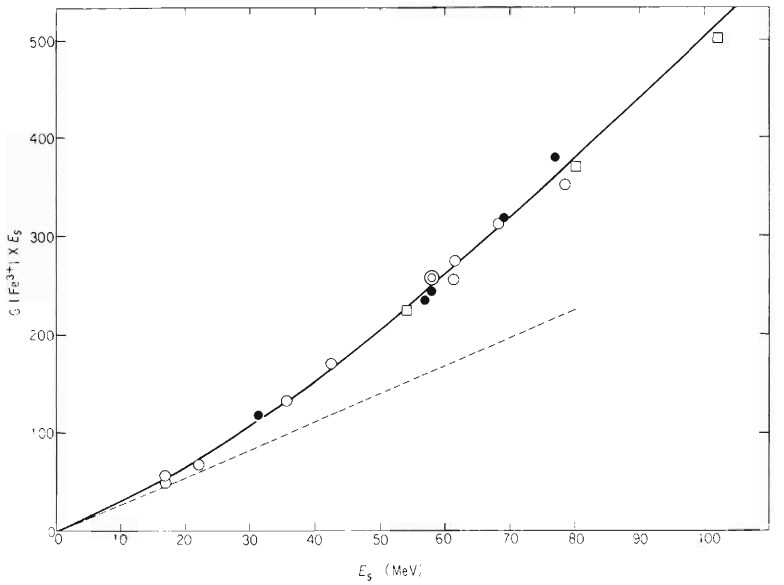

●: C-ions, □: C-ions by Schuler,[6]
○: N-ions, ◎: O-ions.

Fig. 3. A plot of the integrated yield of ferric ions vs. energy of the heavy ions entering the solution. The dotted line gives the limiting yield of $G(Fe^{3+})(2.9)$ at an infinite LET.[2]

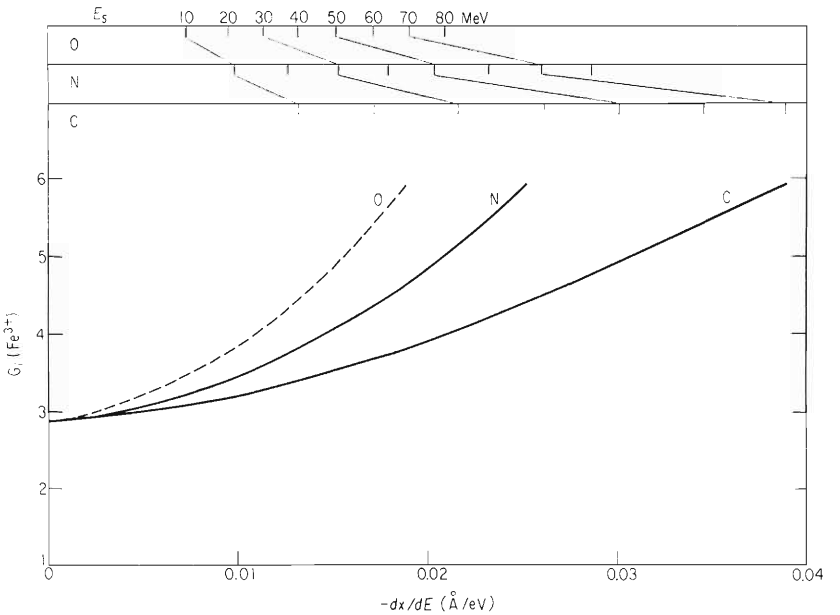

Fig. 4. Dependence on reciprocal LET of the instantaneous yields ($G_i(Fe^{3+})$) for C- and N- ions. Probable dependence for O- ions are shown by a dotted curve.[2]

model.[7] By assuming $G(-H_2O)^{\infty} = 2.9$, the variation of the yield for the net water decomposition may be expected to be also monotonic with respect to LET, no special explanations being required.

(3) The structure of heavy-ion tracks

From Fig. 3 the values of $G_i(Fe^{3+})$ at given energies (E_s) can be obtained graphically for the three heavy ions. These values are plotted in Fig. 4 as a function of the reciprocal LET. Figure 4 distinctly indicates the differences in $G_i(Fe^{3+})$ at the same LET-values among the three ions: the heavier the ion, the higher the yield.

Two heavy particles having the same ratio of z/v also have approximately the same LET. But the heavier of them has higher z and therefore higher v as well. The energy of the secondary electrons ejected by elastic collision of heavy particles is given by $E_e = 2mv^2\cos^2\theta$, which implies that the heavier particle ejects more energetic secondary electrons which may penetrate the main particle track (core) effectively and form more low-LET tracks outside the main track. It is also obvious, from Fig. 4, that $G(Fe^{3+})$ increases with decreasing LET.

The above track model has been assumed by Mozumder et al.,[8),9)] for heavy particles and seems to explain the present result given in Fig. 4. Regarding this point a set of results on the difference between yields for deaerated (nitrogen-saturated) and aerated solutions are summarized in Fig. 5, in which the ratios between these yields are shown as a function of LET.[10)] This result indicates that free radicals, H and OH, are diffusing more or less out of tracks up to the LET region as high as 100 eV/Å, above which the ratio becomes close to unity. The scavengeable free radicals may have their origin from the low-LET tracks formed by ejected electrons.

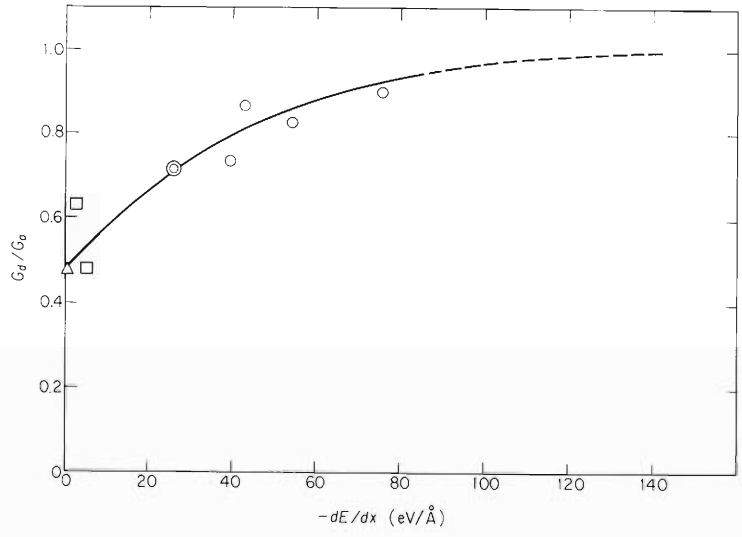

△ : ^{60}Co-γ, □ : He^{2+}-ions,
○ : N-ions, ◎ : O-ions.

Fig. 5. Variation with LET of the ratio of the yield for nitrogen-saturated solution to that for aerated solution.

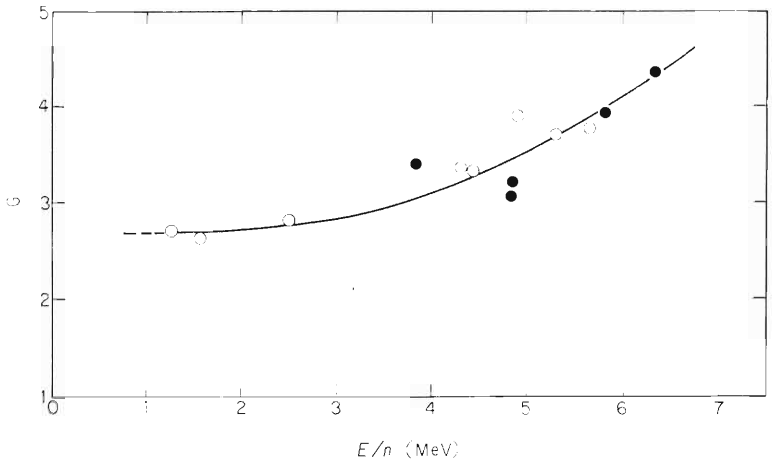

●: C-ions, ○: N-ions.

Fig. 6. The calculated yields in the track core as a function of energy per nucleon. Calculated according to Eqn. (7).

Assume that the observed $G(Fe^{3+})$ consists of the yields in the track core ($G(Fe^{3+})_{core}$) and in the low-LET electron track ($G(Fe^{3+})_e$):

$$G(Fe^{3+}) = f\ G(Fe^{3+})_{core} + (1-f) \cdot G(Fe^{3+})_e. \qquad (7)$$

If the fraction of energy deposited in the core in the total energy loss, f, and the $G(Fe^{3+})_e$ could be estimated appropriately, we can calculate the $G(Fe^{3+})_{core}$, which should agree with the value for $G_i(Fe^{3+})$ at an infinite LET. The fractions, f, have been calculated and illustrated by Mozumder et al. as a function of incident particle energy.[8),9)] The yields for $G(Fe^{3+})_e$ have been estimated from $G(Fe^{3+})$ vs. LET relation for protons or deuterons by ignoring the difference between proton and secondary electron, the average energy of the latter being estimated according also to Mozumder et al.[8),9)] The results is shown in Fig. 6, in which calculated $G(Fe^{3+})_{core}$-values are plotted as a function of energy per nucleon for C- and N-ions.[11)] All the values seem to be represented approximately by a single universal curve notwithstanding several assumptions and approximations. Furthermore, the extrapolation of this curve to zero energy appears to give a limiting value of $G(Fe^{3+})_{core}$ close to the value of $G(Fe^{3+})$ at an infinite LET (Fig. 3).

The experimental results and calculation described in this report may indicate that the discontinuities observed in the relationship between G and LET (Figs. 1 and 2) are accounted for quantitatively in terms of the secondary electron production by heavy-ion radiations. It is concluded, therefore, that the low-LET δ-tracks created by heavy-ion radiations outside their main tracks (cores) play a role in chemistry of aqueous solution depending upon their energies, no effect of charge exchange between charged particles and water molecules being aware.

References

1) M. Matsui, H. Seki, T. Karasawa, and M. Imamura : J. Nucl. Sci. Tech., 7, 97 (1970).
2) M. Imamura, M. Matsui, and T. Karasawa : Bull. Chem. Soc. Japan., 43, 2745 (1970).
3) L.C. Northcliffe : "Studies in Penetration of Charged Particles in Matter", Publication 1133, National Academy of Sciences-National Research Council, Washington, D.C.,p.173 (1964).
4) L.C. Northcliffe : Ann. Rev. Nucl. Sci., 13, 67 (1963).
5) R.H. Schuler and A.O. Allen : J. Am. Chem. Sco., 79, 1565 (1957).
6) R.H. Schuler : J. Phys. Chem., 71, 3712 (1967).
7) A.O. Allen : "The Radiation Chemistry of Water and Aqueous Solutions", Van Nostrand, Princeton, N. J., p. 58 (1961).
8) A. Mozumder, A. Chatterjee, and J. L. Magee : Advan. Chem. Ser., 81, 27 (1968).
9) A. Mozumder : Advan. Rad. Chem., 1, 1 (1969).
10) M. Matsui and M. Imamura : Unpublished.
11) T. Karasawa, M. Matsui, and M. Imamura : Unpublished.

8-2. LET Effect on the Hydrogen Formation in the Radiolysis of Liquid Tetrahydrofuran

M. Matsui, M. Imamura, and T. Karasawa

Hydrogen is, in general, one of the main products in the radiolysis of organic compounds, and is produced via different several processes characteristic of radiolysis. Most interesting of these is the process in which secondary electron is a precursor. Ionization of molecules gives rise to the formation of thermalized electrons, which may be recaptured rapidly by parent positive ions or react with other positive ions in spurs or trackes, or diffuse out of them to be free solvated electrons. While the behavior and the yield of the free solvated electrons have extensively been studied, little is known about the reactions in the spurs or tracks. The studies on the radiolysis by different kinds of radiations would be expected to give useful information, because, with increasing LET of radiations, the reactions in spurs or tracks may play an increasingly important role. Liquid tetrahydrofuran (THF) has been used simply because it is one of the compounds, the γ -radiolysis of which has extensively been studied by us.

The observed hydrogen yields for neat THF with helium ions (22.0 $\sim$ 23.0 MeV) and nitrogen ions (14.6 and 61.5 MeV) as well as with ^{60}Co- γ rays are summarized in Table 1. Hydrogen was determined by gaschromatography. The hydrogen yield, which is almost constant up to LET $\sim$ 3 eV/Å, shows a steep increase in the radiolysis with N-ions.

In Table 1 are also shown the dependence of the yield for free solvated electrons with LET. These yields have been determined by using maleic anhydride, which has been found by us to be capable of producing carbon monoxide quantitatively by capturing free electrons.[1] The yield of hydrogen decreases with increasing concentration of acid anhydride and levels off above 2×10^{-2} M acid anhydride, giving $G(H_2) \sim 3$ in both the γ-and helium-ion radiolysis.

The substantial decrease in $G(e_s^-)$ with increasing LET indicates that the more electrons are recaptured in denser ionization tracks prior to diffusing-out. These electrons may presumably be recaptured by two process:

$$e_s^- + THF^+ \longrightarrow THF^* \qquad (1)$$

$$e_s^- + THFH^+ \longrightarrow THF + H \qquad (2)$$

where THF^* represents the excited state of THF which may decompose to give hydrogen or other products and/or may be deactivated to give no products, and $THFH^+$ is the product of the ion-molecule reaction:

$$THF^+ + THF \longrightarrow THFH^+ + THF\,(-H).$$

The present results with γ -and ^{4}He-radiolysis indicate that there are little differences in $G(H_2)$ for neat THF and $G(H_2)$ for maleic anhydride solutions as well despite the substantial difference in $G(e_s^-)$. This may tentatively lead to the conclusion that, if Reaction (1) occurs, most of the resulting excited species THF^* should give rise to the formation of hydrogen. However, in the radiolysis with very high LET radiations

(^{14}N-ions), $G(H_2)$ amounts to very high values (Table 1), which can not be explained only by the assumed reactions mentioned above. Some specific actions characteristic of heavy-ion radiations should be taken into consideration. Experimental research on this point is in progress.

Table 1. The yields of hydrogen and free electron from liquid tetrahydrofuran radiolyzed with different kinds of radiations.

Radiation	LET (eV/Å)	$G(H_2)$[a]	$G(e_s^-)$[b]	$G(H_2)_{res}$[c]
^{60}Co-γ	0.02	3.51[d]	0.60[e]	2.90
22~23 MeV He^{++}	2.8 ~ 3.0	3.3	0.2	3.0
61.5 MeV N-ion	37	6.9	0	6.9
14.6 MeV N-ion	79	10.8	–	–

a) The total hydrogen yield for neat THF.
b) Determined with maleic anhydride as an electron scavenger. The value is equal to G(CO).
c) The limited yield of residual hydrogen in the presence of maleic anhydride.
d) Baxendale et al. have reported $G(H_2) = 3.60$.[2)]
e) Baxendale et al. have reported $G(e_s^-) = 0.66$ and 0.7 by pulse-radiolysis using respectively pyrene and anthracene.[3)]

References

1) M. Matsui and M. Imamura : Bull. Chem. Soc. Japan, 42, 3362 (1969).
2) J.H. Baxendale, D. Beaumond, and M.A.J. Rodgers : Intern. J. Radiat. Phys. Chem., 2, 39 (1970).
3) J.H. Baxendale, D. Beaumond, and M.A.J. Rodgers : Trans. Faraday Soc., 66, 1996 (1970).

8-3. LET Effects in Aqueous Solution of Polyvinylalcohol

S. Tagawa, Y. Tabata, M. Matsui, and M. Imamura

LET effects in aqueous solution of polyvinylalcohol (PVA) were studied by using γ-rays from a ^{60}Co source, α-ray from the cyclotron, and He, Li recoil particles from the reaction of $^{10}B(n,\alpha)^{7}Li$; LET values are 0.02, 3.2, and 28.0 eV/Å, respectively.

It was found that the molecular weight of PVA changes with irradiation dose, and the ratio of crosslinking to main chain scission increases with decreasing LET.

LET effects in aqueous solution of polymers have been reported by Schnabel et al.[1] and explained mainly by the difference in radical yields from water. However, in aqueous PVA solution, LET effects depend not only on the radical yields from water but also on the direct effects of radiation on polymers.

In this paper, the results obtained with α particles from the cyclotron are described.

(1) Experimental

PVA provided by Kura-ray Co. Ltd. was washed with distilled water for one day to eliminate residual sodium acetate. After being dissolved in water and filtrated, PVA was precipitated by pouring the aqueous solution into acetone. Then it was dried in vacuum to be constant in weight and stored over silica gel. The irradiation cell was made of quartz and its window was made of 10μm mica. The samples were sealed under vacuum or in the presence of air. Dosimetry was made as described before.[2] Solution was stirred violently by a magnetic stirrer during α-irradiation unless otherwise stated. The molecular weights of PVA were calculated from the following relationship:

$$[\eta] = 6.66 \times 10^{-4} \ M^{0.64}$$

were $[\eta]$ is the intrinsic viscosity in the unit of deciliters/gram. The intrinsic viscosity was measured at 30°C.

(2) Results

Aqueous PVA solution in a concentration of 1 % was irradiated with α-ray and with ^{60}Co γ-rays as well. As is shown in Fig. 1, the γ-irradiation, led to an increase in the molecular weight owing to crosslinking of PVA, and then finally to the formation of a three-dimentional, insoluble network at high doses (about 7×10^5 rad). On the other hand, when the solution was exposed to α-ray, the probability of crosslinking and that of scission of main chain were apparently equal.

Both effects of dose rate and oxygen were investigated. The results are shown in Fig. 2. No dose rate effect was observed in the absence of air over a range of dose rate 2 ~ 8 nA, but it was clearly observed in the presence of air. The dose rate effect in the presence of air may be due to the competition between oxygen-radical and radical-radical reactions. The competition reaction should be controlled by the diffusion of oxygen. The difference between in vacuum and in air became smaller at a higher dose rate.

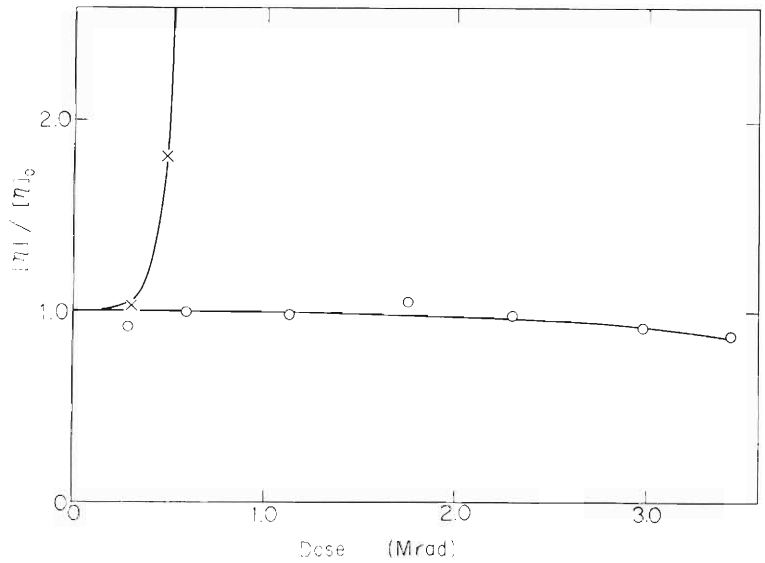

Fig. 1.

Relative intrinsic viscosities of PVA irradiated in 1 wt % aqueous solutions with (26.4 MeV α) (○) and γ-rays (×) as a function of irradiation dose. Irradiation with α-ray was carried out by using a magnetic stirrer during irradiation.

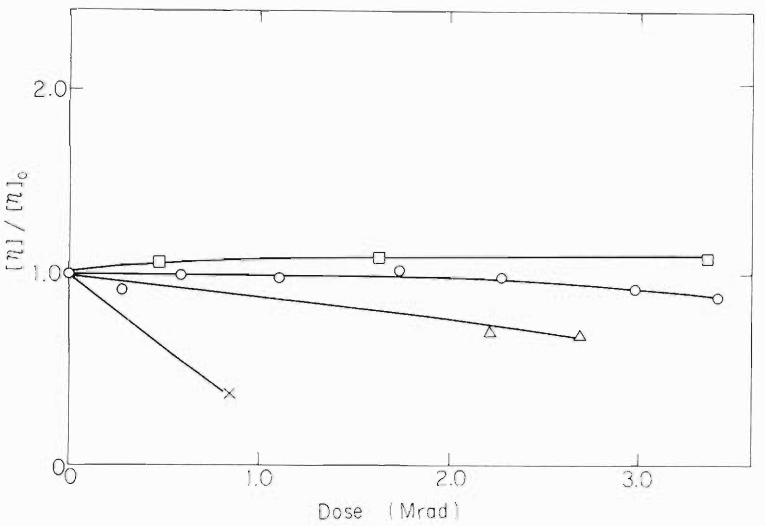

Fig. 2.

Relative intrinsic viscosities of irradiated in 1 wt % aqueous solutions with α-ray over a dose rate range from 5 to 8 nA as a function of irradiation dose. □ in vacuo, dose rate from 2～8 nA. ○ in air at 8 nA. △ in air at 4 nano A. × in air at 0.5 nA. The solution was stirred by a magnetic stirrer during irradiation.

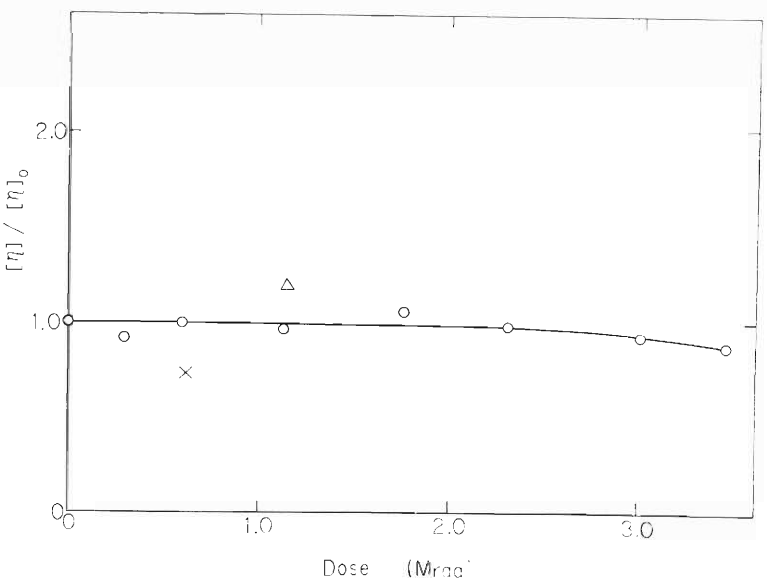

Fig. 3.

Relative intrinsic viscosities of PVA irradiated in different concentrations with α-ray as a function of irradiation dose. The solution was stirred by a magnetic stirrer during irradiation (△) 2 % PVA aqueous solution (○) 1 % aqueous PVA solution. (×) 0.5 % aqueous PVA solution.

Aqueous PVA solutions of different concentrations, 2, 1, and 0.5 wt %, were irradiated with α-ray in the presence of air. As is shown in Fig. 3, slight differences are observed over a range 0.5 ~ 2 wt %.

Aqueous solution of 1 wt % was irradiated with α-ray in the presence of air with and without stirring. The result is shown in Fig. 4. The ratio of scission to crosslinking is a little greater in the irradiation under stirring than in that without stirring. This may be explained by the difference in the diffusion rate of oxygen in the solution between the two cases. Dose rate effects on 1 wt % aqueous PVA solution without stirring were investigated in more detail. The result is shown in Fig. 5 ; the dose rate effect was almost the same as that in Fig. 2.

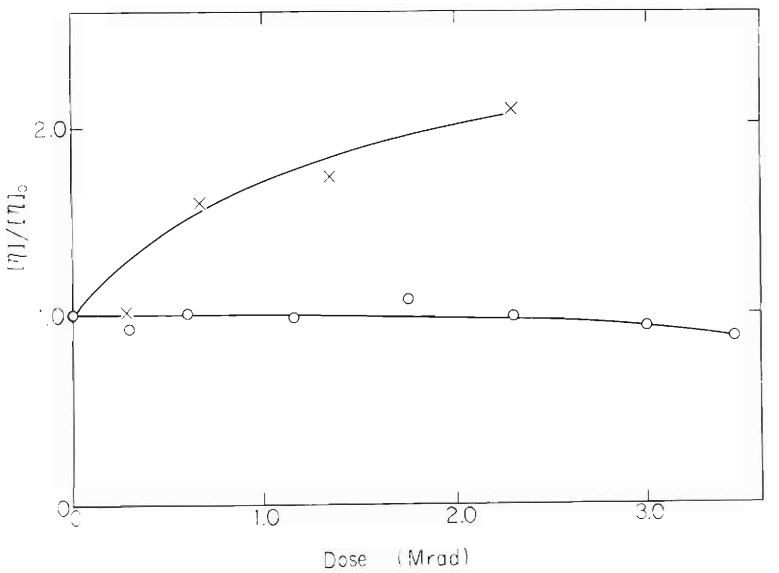

Fig. 4. Relative intrinsic viscosities of PVA irradiated in 1 wt % aqueous solutions with α-rays as a function of irradiation dose. (○) stirred. (×) not stirred.

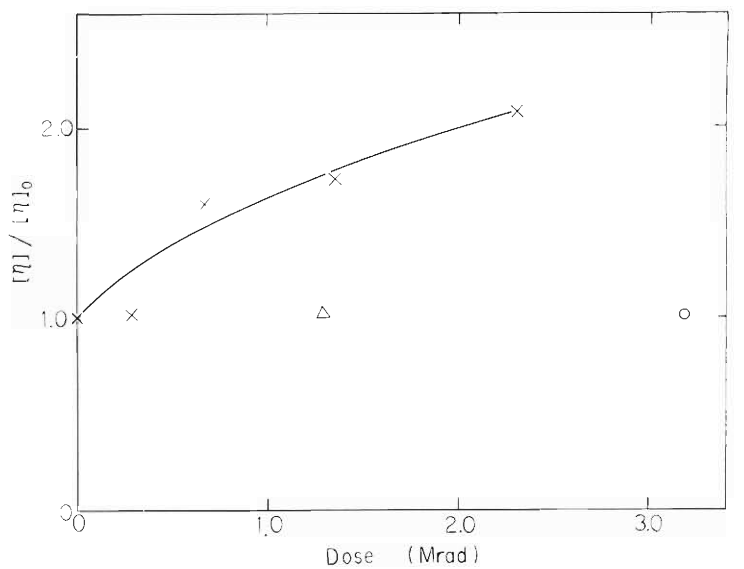

Fig. 5. Relative intrinsic viscosities of PVA irradiated in 1 wt % aqueous solutions with α-ray as a function of irradiation dose. Without stirring. (×) 8 nA (△) 4 nA, (□) 2 nA.

(3) Discussion

A number of work on the radiation effects of PVA have been reported. When dry PVA powder is irradiated with γ-rays, the scission of main chain occurs preferentially both in air and in vacuum the G-value of scission is about unity in both cases.[3),4)] When PVA is irradiated with γ-rays in aqueous solution, however, crosslinking occurs preferentially and gel is formed.[5)]

In our experiment, the G value of crosslinking was about 2.0 for 1.0 wt % aqueous PVA solution irradiated with γ-rays. The ratio of main chain scission to crosslinking in aqueous PVA solution is greater in α-irradiation than in γ-irradiation. Dose rate was higher in α-irradiation than in γ-irradiation. And the ratio of main chain scission to crosslinking decreased with increasing dose rate when aqueous PVA solution was irradiated in the presence of air. Therefore, the ratio of main chain scission to crosslinking should be smaller in α-irradiation than in γ-irradiation if the dose rate effect would occur preferentially. However, the overall effects are quite different from the expectation. Therefore, it can be said that the ratio of scission to crosslinking increases with increasing LET in aqueous PVA solution. Both direct and indirect effects should be considered to explain the LET effect on aqueous PVA solution. Indirect effects of irradiation on PVA in the solution are due to radiolysis of the solvent water.
A number of work have been done on the radiolysis of water, which revealed that the radical yields by α-irradiation are about one forth of those by γ-irradiation. To explain the direct effects of α-irradiation on PVA, its higher ionizing density, local temperature rising near the end of track, and knock-on collision should be taken into consideration. In our experimental condition, the energy loss due to knock-on collision is less than one thousandth of the total energy loss and the time of local temperature rise is very short. Therefore, two of these factors may be neglected, and the radiolytic products of water and the ionization density will be important factors for explanation of the LET effects of aqueous PVA solution.

The G-values of crosslinking is about 2.0 in the case of 1.0 wt % aqueous PVA solution for γ-irradiation. It is believed that crosslinking in this case is mainly caused by radicals from water. Since the radical yields from the radiolysis of water by α-irradiation is about one fourth of those by γ-irradiation, the G-value of crosslinking should be about 0.5 for the α-irradiation if the radical yields alone contributes to the LET effects of aqueous PVA solution. However, the ratio of crosslinking to scission was almost unity for deaerated samples. Therefore, the higher ionization density plays a significant role in LET effects.

The authors wish to express their thanks to Dr. K. Ishigure for his helps in the experiment.

References

1) W. Schnabel : Macromol. Chem., 77, 51 (1964)
2) S. Tagawa, Y. Tabata, K. Oshima, M. Matsui, and M. Imamura : Proc. 23th annual meeting of Chem. Soc. Japan. (1970).
3) Y. Hirano : Bull. Chem. Soc. Japan, 37, 1495 (1964).
4) I. Sakurada and S. Matsusawa : "Kobunshi Kagaku", 17, 689, 693 (1960).
5) A. Danno : J. Phys. Soc. Japan, 13, 722 (1958).

8-4. LET Effects on Biological Systems

A. Matsuyama, T. Karasawa, T. Takahashi, Y. Asano,
K. Igarashi, H. Kano, E. Fukada, and Y. Ando

(1) LET effects on cellular radiosensitivities of bacteria

In continuation of the study on liquid-phase irradiation,[1] the solid-phase irradiation of four different bacterial strains has been carried out to accumulate the sufficient data on the relationship between LET and RBE.[2),3)] Ionizing particles used in this study are as follows : protons (4.8 and 13.5 MeV), α-particles (1.2, 1.8, 3.6, 3.8, 6.1, 8.7, 11.7 and 26 MeV), carbon ions (14, 48, and 83 MeV) and nitrogen ions (33, 44, 47, 51, 53 , and 61 MeV). Bacterial cells used in this study were the log-phase cells of Escherichia coli B_{s-1} and B/r, those of Micrococcus radiodurans R_1 and dormant spores of a thymine-requiring mutant of Bacillus subtilis 168, thy^-, ind^-, leu^- (MY2Y1U2). The experimental procedure for irradiation and dosimetry was previously described.[2)] Immediately after irradiation, colony survivals were determined and the values of $1/D_{37}$ (for exponential survival curves) or $1/D_1$ % (for sigmoid curves of M. radiodurans) were calculated as a measure of RBE.

The results obtained are shown in Fig. 1 (a~d). In this figure some corrections for LET-RBE curves indicated in the preceding report[2)] are made. As shown in Fig. 1(d), recent determinations on M. radiodurans have revealed no peak on a LET-RBE curve in the LET region of 1 ~10 eV/A. It is noteworthy that, in comparison with the case of α-irradiation, the LET-RBE curve for carbon ions was found to shift toward higher sensitivity and an additional shift was observed in the case of nitrogen ions. In other words, bacterial cells increased their radiosensitivities with increasing mass numbers of ionizing particles with the same value of L_∞. The inactivation cross sections for three strains which give the exponential survival curve have been calculated from the data indicated in Fig. 1 and illustrated in Fig. 2 as functions of L_∞. The maximum inactivation cross sections for different particles were found to increase in the order α-particles, carbon ions and nitrogen ions. These observations may suggest an important role of δ-rays produced by these heavy particles in their biological actions, which can be referred to as the sheath effect. The analysis of experimental data is now under way from viewpoint of the target theory in order to elucidate the physical basis of these observations.

The device serving for the solid-phase irradiation of biological cells by particulate radiations is shown in Fig. 3. Using this unit, bacterial samples mounted on a piece of the membrane filter can be swung in both horizontal and vertical directions during irradiation to give the uniform dose over the area of the sample.

(2) Biochemical and biophysical studies on macromolecular components in irradiated bacteria

Double-strand scissions in DNA caused by radiations and their rejoining during postirradiation incubation in M. radiodurans have been studies by means of sedimentation analysis using neutral sucrose gradients.[4),5)] The result obtained with irradiation of M. radiodurans by 1400 krads of 44 MeV nitrogen ions (average charge number = 6.64, L_∞ = 53 eV/A) indicates that the rejoining of double-strand scissions

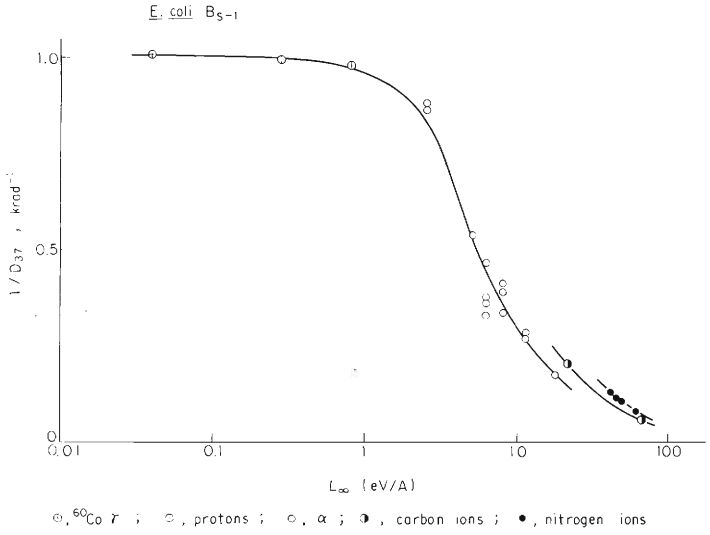

Fig. 1(a)

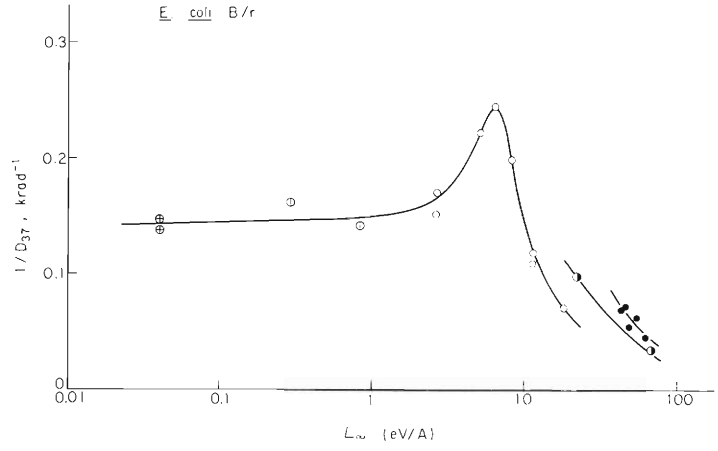

Fig. 1(b)

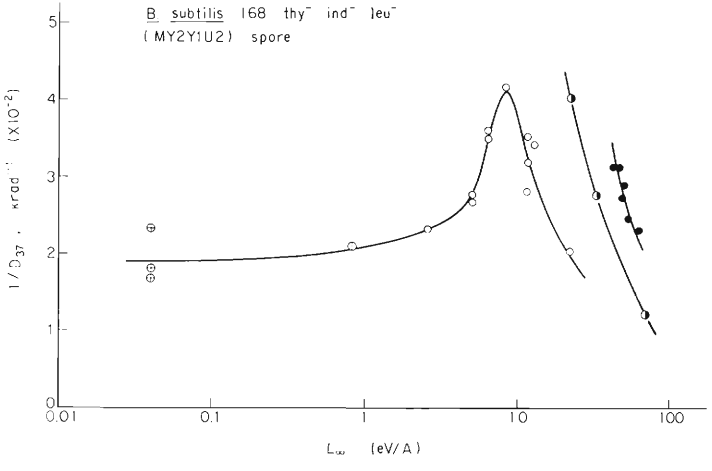

Fig. 1(c)

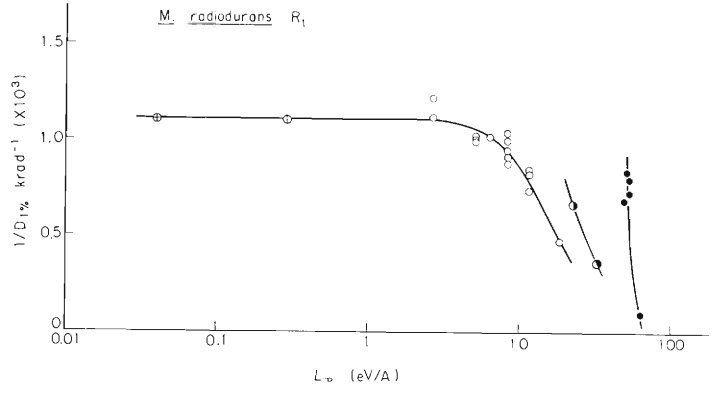

Fig. 1(d)

Fig. 1. Radiosensitivity of bacteria versus $L\infty$.

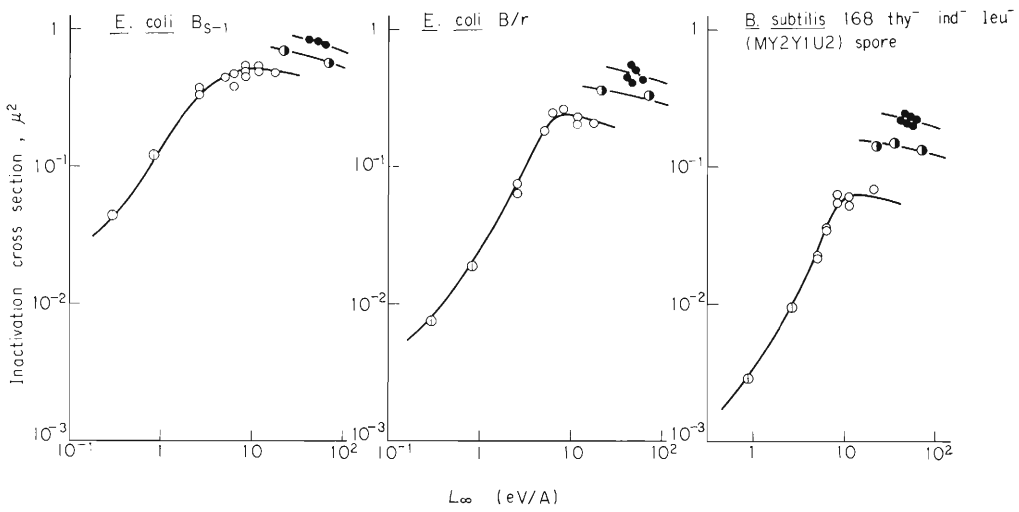

Fig. 2. Relationship between inactivation cross section and $L\infty$.

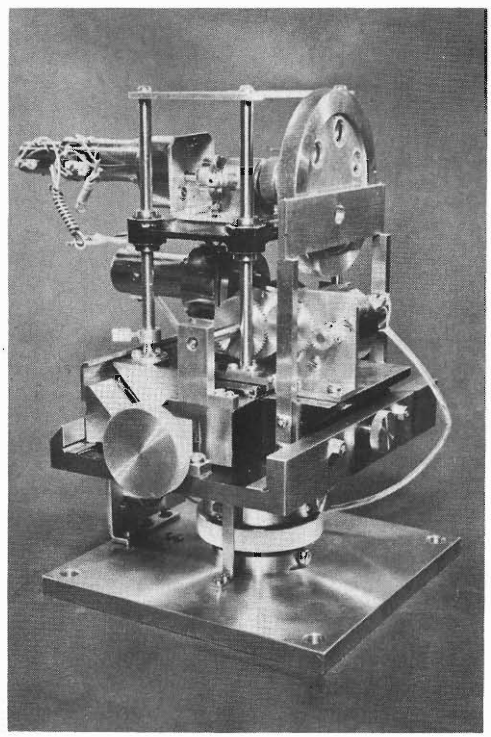

Fig. 3. Biological target.

in DNA take place in this radioresistant vegetative bacterium during reincubation after irradiation by such high-LET heavy ions. However, the rate of the rejoining of DNA-strand breakage after the bombardment by nitrogen ions was found much slower ($\sim$1/6) than that after gamma irradiation.

The RNA and protein syntheses were also reduced to the greater extent by high-LET particles as compared with the inhibition caused by gamma rays.

(3) Non-Newtonian viscosity of irradiated DNA

The solution of DNA extracted from E. coli was irradiated with 26 MeV α-particles and changes in the viscosity was measured by a coaxial cylinder viscometer.[6] The dependence of viscosities of DNA solutions upon radiation doses of α-particles has been studied to obtain informations on radiation damages in DNA molecules such as strand breakage and crosslink in comparison with the effect of gamma rays.

References

1) S. Kitayama, K. Igarashi, T. Karasawa, and A. Matsuyama : Agr. Biol. Chem., 34, 1346 (1970).
2) A. Matsuyama, T. Karasawa, S. Kitayama, and R. Takeshita : IPCR Cyclotron Progr. Rep., 3, 101 (1969).
3) A. Matsuyama, T. Karasawa, and T. Takahashi : In preparation.
4) A. Matsuyama and S. Kitayama : Abst. Papers 4th Intern. Cong. Radiat. Res., Evian, France, p.140 (1970).
5) S. Kitayama, K. Igarashi, H. Kano, T. Karasawa, and A. Matsuyama : In preparation.
6) Y. Ando, E. Fukada, Y. Okazawa, S. Kitayama, and A. Matsuyama : Rep. Progr. Polymer Phys Japan, 8, 525 (1970).

9. SOLID STATE PHYSICS

9-1. Mössbauer Effect of ^{61}Ni in Spinel Type Magnetic Oxides

H. Sekizawa, T. Okada, S. Okamoto, and F. Ambe

(1) Introduction

In spite of many experimentally undesirabel nuclear properties, ^{61}Ni can be a powerful probe in solid state physics as the only Mössbauer nuclide other than ^{57}Fe in the iron group transition elements,[1),2),3),4)] especially in the studies of internal magnetic fields.

The purpose of the present paper is to discuss the Mössbauer effect of ^{61}Ni in various Ni-containing oxides with spinel (or distorted spinel) structure.

(2) Experimental

The nuclear reactions, $^{58}Ni(\alpha,p)^{61}Cu$ and $^{58}Ni(\alpha,n)^{61}Zn \xrightarrow{\beta^+, EC} {}^{61}Cu$ were utilized to produce the source nuclide ^{61}Cu. A thin Ni_{84}-V_{16} alloy disc of about 20 mm in diameter was irradiated for several hours with 21 MeV α -particles from the IPCR Cyclotron, and was used as the source without annealing. The Ni_{84}-V_{16} alloy crystallizes in f.c.c. structure and paramagnetic in nature. The specimens of various oxides were prepared by the convenient ceramic method, using nickel enriched with ^{61}Ni up to 80 ~ 90 %. An NaI(Tl) scintillation counter was employed to detect the transmitted radiation. The Mössbauer spectrometer made by Elron or the one by Hitachi was operated in constant acceleration mode with a 400-channel pulse-height analyzer.

Because of the low resolution of the ^{61}Ni Mössbauer spectra, computer fitting of them to theoretical curves was an indispensable procedure to extract various parameters from the obtained spectra. Concerning the quadrupole moment of the excited state of ^{61}Ni, the rough estimate of -2 for the ratio Q_{ex}/Q_{gr} due to Erich, [3)] had been adopted tentatively in the analysis. Fortunately, the quadrupolar interactions in the spinels investigated turned out to be almost negligible compared with the magnetic interactions, except for a few cases mentioned in the text. The values of the isomer shift of the obtained spectra were also found to be of the order of the experimental uncertainty. Consequently, only the internal field is discussed in this paper, and the numerical values of the quadrupolar interaction and the isomer shift will not be presented.

(3) Results and discussion

The two groups of oxides with spinel (or distorted spinel) structure were investigated : the first group with the nickel ions in the octahedral site ($NiFe_2O_4$, $NiCo_2O_4$, $NiMn_2O_4$ and $GeNi_2O_4$), and the second group with the nickel ions in the tetrahedral site ($NiCr_2O_4$ and $NiRh_2O_4$).

(i) The spinels with nickel ions in the octahedral site

$NiFe_2O_4$: The Mössbauer spectrum at 80°K is shown in Fig. 1. It is an almost symmetric pattern with noticeable peaks on the top, characteristic to a case with appreciable internal magnetic field H_i and negligible electric field gradient (EFG) effect. The value of H_i was found to be 94 kOe. This coincided with the value reported in,[1)]

but the appreciable EFG effect reported therein had not been observed.

$NiCo_2O_4$: The absorption pattern at 80°K is shown in Fig. 1. The values of H_i were 73 kOe and 87 kOe at 80°K and at liquid-He temperature, respectively.

$NiMn_2O_4$: According to the recent report by Boucher et al.,[5] this spinel is incompletely inverse depending on the heat treatment. The fitting was made under the assumption of completely inverted ionic distribution, but the fitting at liquid-He temperature was not very unsatisfactory with H_i of 97 kOe as can be seen in Fig. 1, and at 80°K the best fit was obtained with H_i of 72 kOe.

$GeNi_2O_4$: The pattern at 80°K, which is far above its reported Neel temperature of 16°K, was slightly asymmetric, suggesting that the EFG effect is working.

(ii) The spinels with nickel ions in tetrahedral site

$NiCr_2O_4$: As is well known, this oxide has cubic spinel structure at temperatures higher than 310°K, below which it becomes tetragonal due to the Jahn-Teller effect of the Ni^{2+} ions in the tetrahedral sites. The ferrimagnetic Curie temperature is reported to be about 80°K. According to Prince,[6] the spin structure investigated by neutron diffraction is very complicated but the detailed spin structure is still unknown. At 80°K, the spectrum seems to be slightly asymmetric with a width wider than the single line cases, as can be seen in the upper part of Fig. 2.

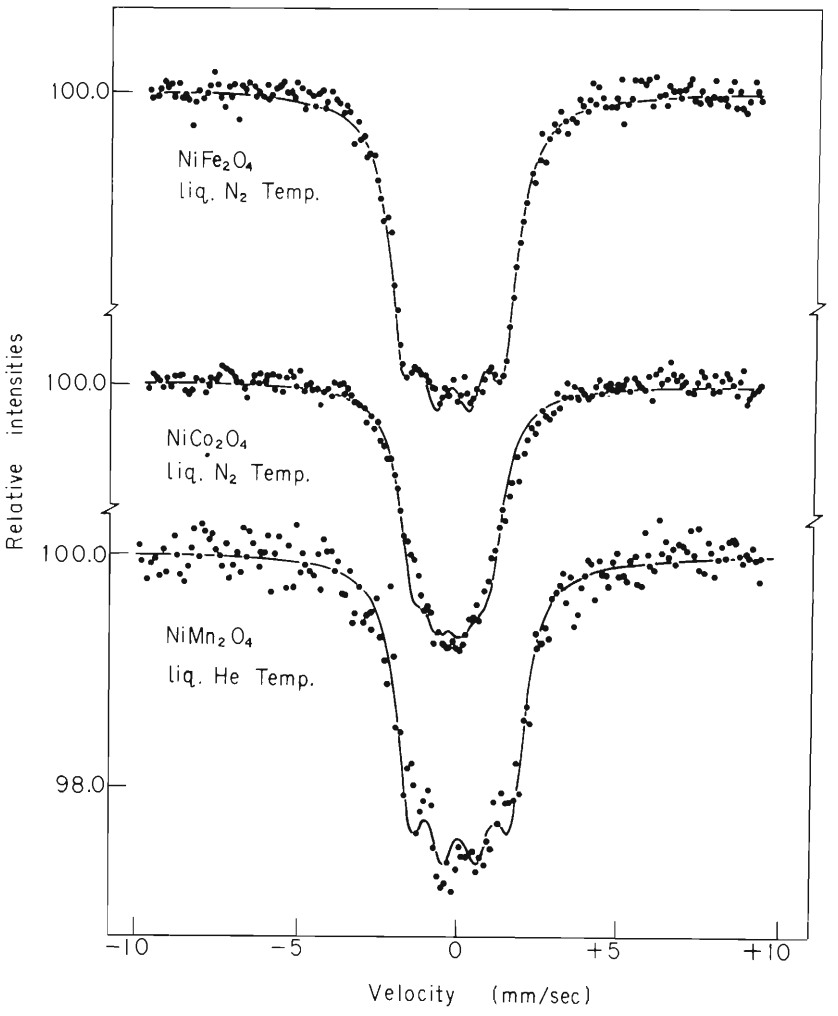

Fig. 1. The ^{61}Ni - Mössbauer spectra of $NiFe_2O_4$, $NiCo_2O_4$, and $NiMn_2O_4$.

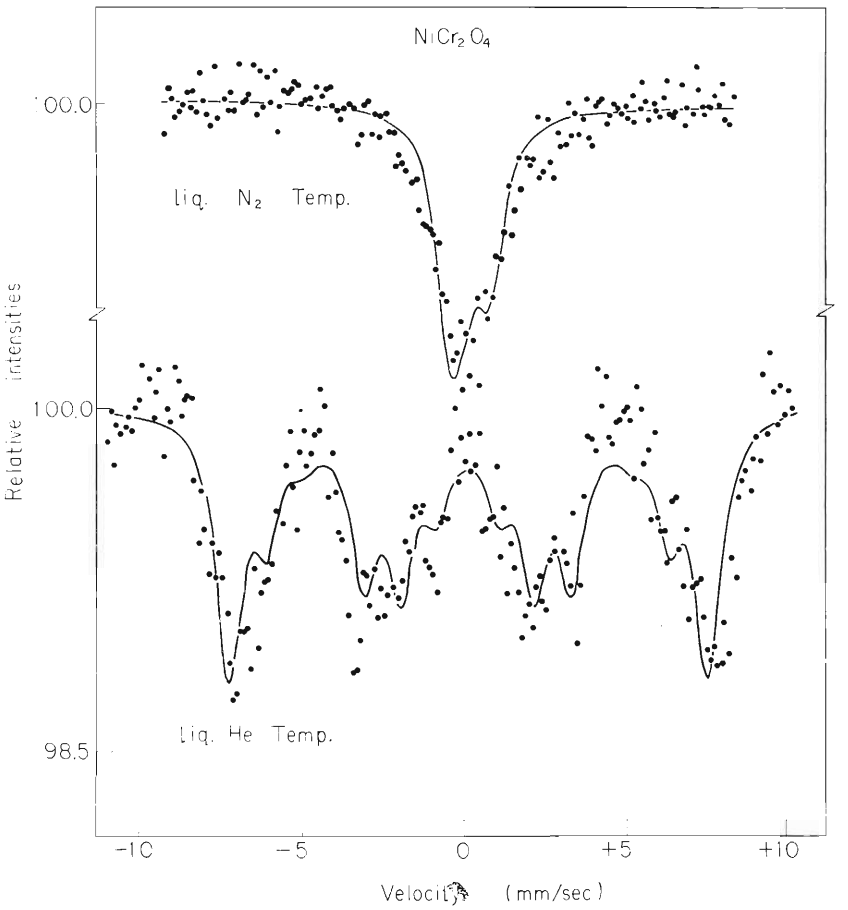

Fig. 2. The ^{61}Ni - Mössbauer spectra of $NiCr_2O_4$.

The most remarkable feature of this spinel is the widening of the pattern on cooling down to the liquid He temperature, as shown in the lower part of the same figure. The value of the internal magnetic field determined by the fitting amounted to 450 kOe, which seems to be the largest one ever reported for ^{61}Ni. Without data with an applied external magnetic field, detailed discussion of the possible origin of such a large field should be premature. However, contribution from the only incompletely quenched orbital moment of the Jahn-Teller distorted Ni^{2+} ions might be a possible mechanism to explain it.

$NiRh_2O_4$: The transition temperature from cubic to tetragonal symmetry is $380^{\circ}K$, and the antiferromagnetic Neel temperature is reported to be $18^{\circ}K$. The spectrum taken at $80^{\circ}K$ showed a noticeable asymmetry.

(4) Conclusion

A striking difference in magnitude of the internal magnetic field at ^{61}Ni nuclei has been observed between the spinel oxides with nickel ions in the octahedral site and $NiCr_2O_4$ with its nickel ions in the tetrahedral site. The former shows an internal magnetic field of the order of 70 ~ 100 kOe and a negligible EFG effect. The latter shows an internal magnetic field as high as 450 kOe, the origin of which is not yet established.

References

1) J. C.Travis, J. J. Spijkerman : Mössbauer Effect Methodology, Plenum Press, New York, 4, 237 (1968).
2) U. Erich, E. Kankeleit, H. Prange, and S. Hüfner : J. Appl. Phys., 40, 1391 (1969).
3) U. Erich : Z. Phys., 227, 25 (1969).
4) F.E.Obenshain, J. C. Love., and G.Czjzek : Proceedings of the 11th International Conference on Low Temperature Physics, Univ. of St. Andrews, 1, 532 (1968).
5) B. Boucher, R. Buhl, M.Perrin : J. Phys. Chem. Solids, 31, 363 (1970).
6) E. Prince : J. Appl. Phys., 32, 68S (1961).

9-2. Lattice Defects in Irradiated Cu_3Au

H. Sakairi, E. Yagi, T. Karasawa,
and R. R. Hasiguti

Lattice defects created in f.c.c. noble metals by irradiation at liquid helium temperature are annealed out mostly up to room temperatures. In usual isochronal annealing experiments, the annealing rate becomes rapid in two temperature ranges, which, for example in Cu, are $10^{o}\sim 50^{o}$K and $240^{o}\sim 300^{o}$K.[1] Between these two stages exists an wide stage in which annealing proceeds slowly. These annealing stages are generally called Stages I, II, and III. Though various interpretations were presented to assign each stage to some behavior of defects, none were supported by satisfactory experiments. Even the annihilation temperature of fundamental defects, such as interstitial atoms and vacancies, has not been ascertained.

To identify the defects contributing to the annealing at each stage, it is helpful to know a migration behavior of them. The physical properties of pure metals, however, are not affected by atomic replacements. So we examined the electrical resistivity of Cu_3Au which changes sensitively with the degree of atomic order. In all our experiments pure Cu was irradiated to compare it under the same condition with Cu_3Au. In this report the experimental results concerning the relation between the defect migration and the order formation are briefly described.

Stage I

Damage rate of Cu at helium temperature is three times larger than that at nitrogen temperature, that is, a large part of the defects created at liquid helium

Table 1. $\frac{d\rho}{d\phi}$ of Cu_3Au and Cu in the irradiation with alpha particles.
(10^{-23} ohm.cm/(α/cm^2))

irradiation energy (MeV)	Material	$\frac{d\rho}{d\phi}$ (He)* (A)	$\frac{d\rho}{d\phi}$ (N_2)* (B)	A − B	$\frac{A-B}{A}$
36	Cu_3Au	3.3	2.6	0.7	0.21
	Cu	0.64	0.23	0.41	0.67
16.5	Cu_3Au	12.3	9.8	2.5	0.20
	Cu	—	0.56	—	—

* $\frac{d\rho}{d\phi}$ (He) denotes the $\frac{d\rho}{d\phi}$ at liquid He temperature and so on.

temperature is annealed out at State I (Table 1). This agrees well with the isochronal annealing results.[1] On the other hand, damage rate of Cu_3Au at liquid helium temperature is slightly larger than that at nitrogen temperature (Table 1). As the stability of defects in Cu_3Au is considered to be nearly equal to that in Cu, it can be suggested that the resistivity increase of Cu_3Au is mainly caused by atomic disordering, instead of the presence of defects themselves. Another experimental result that the damage rate of Cu_3Au at helium temperature is 10 times larger than that of Cu (Table 1), also supports above suggestion, because it is not plausible that contribution of the presence of defects to resistivity increase of Cu_3Au differs largely from that of Cu. A possibility that the rate of defect production in Cu_3Au by irradiation differs largely from that in Cu, is also denied by an energetic consideration of collision events.

In conclusion a major part of the resistivity increase of irradiated Cu_3Au is caused by the disordering resulted from the atomic replacements which exert no effect on pure metals, and the migration of Stage I defects is not effective on the ordering of the disodered lattice.

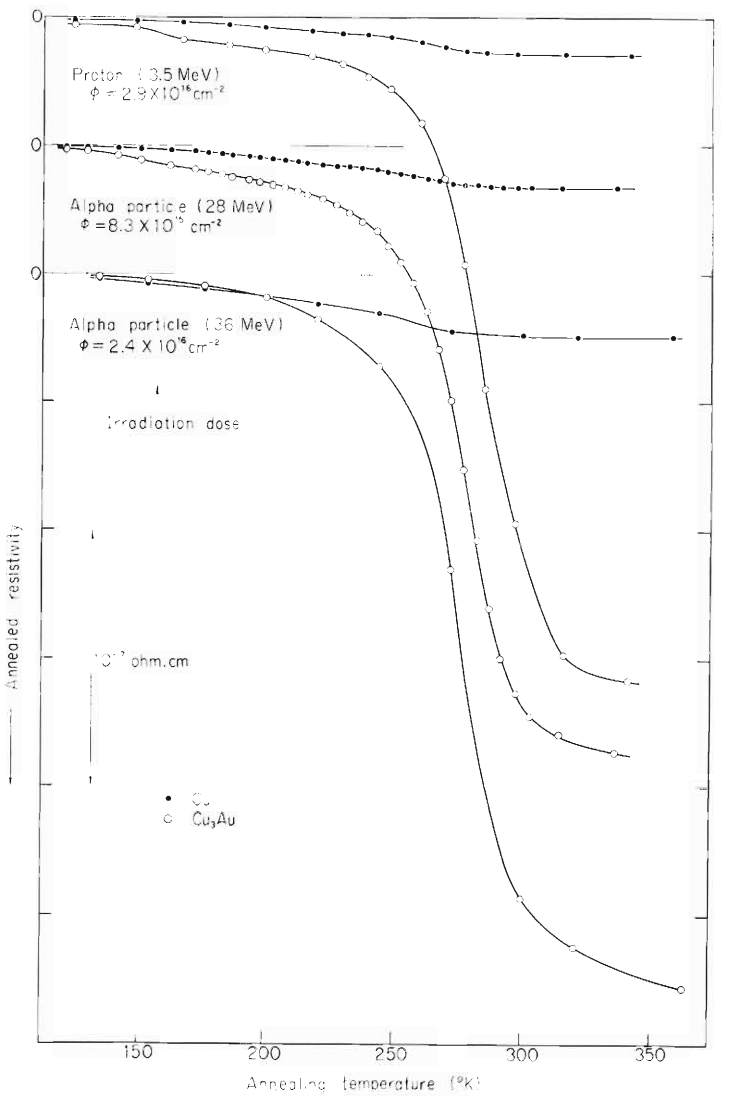

Fig. 1. Isochronal annealing curves of Cu_3Au and Cu irradiated with alpha particles at liquid nitrogen temperature.

Stage II

The amount of recovery of Cu_3Au at Stage II is only 1 ~ 5 % of the total resistivity increase by irradiation at liquid nitrogen temperature, while that of Cu reaches to 30 ~ 50 %. However the absolute amounts of recovery are almost the same for two metals. They agree within a factor of three (Fig. 1). So the amount of defects annihilating in this stage is considered to be nearly equal with two metals and migration of this defect in Cu_3Au does not help the reordering of the lattice. As a consequence the relative amount of recovery at this stage is small as compared with that of Cu.

Stage III

In contrast to Stages I and II, the recovery of Cu_3Au at Stage III differs largely from that of Cu (Fig. 1). The ratio of the amount of Stage III recovery of Cu_3Au to that of Cu under equal irradiating conditions is listed in Table 2. The migration of Stage III defects is undoubtedly accompanied by the atomic replacements.

A main factor determining above ratio for each irradiation is the defect concentration introduced into the lattice by irradiation. The interpretation is that the small concentration of introduced defects makes the defects to migrate over many lattice sites before the annihilation (interstitial-vacancy recombination), so that they can bring about many atomic replacements. (In a specimen more disorder than that introduced by irradiation happened to disappear (Fig. 2). This is a result of the presence of disorder, although small, prior to irradiation, which is inevitable because of the difficulty of preparing the perfectly ordered samples.)

Table 2. Stage III annealing of Cu_3Au irradiated at liquid nitrogen temperature.

$\Delta\rho_{total}$	$\Delta\rho_{III}/\Delta\rho_{total}$	$\Delta\rho_{III}(Cu_3Au)/\Delta\rho_{III}(Cu)$	Particle	Energy (MeV)	
1.77	0.20	25	alpha	16.5	*
0.84	0.30	25	alpha	36	*
0.58	0.40	30	alpha	28	*
0.43	0.55	–	alpha	16.5	
0.37	0.70	35	proton	3.5	*
0.36	0.60	–	alpha	28	
0.11	1.00	–	alpha	28	
0.09	1.70	90 ~ 100	proton	8	*

* The full curves of isochronal annealing are shown in Fig. 2.

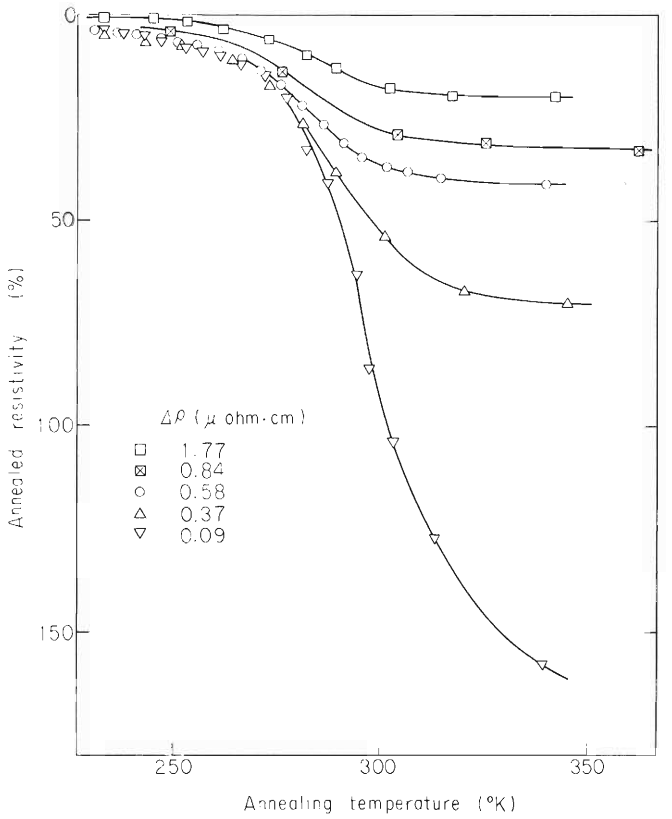

Fig. 2. Stage III annealing of Cu_3Au irradiated at liquid nitrogen temperature. ($\Delta\rho$ is a total increase of resistivity by the irradiation.)

(1) The resistivity increase by irradiation of Cu_3Au is mainly caused by the disordering by atomic replacements.

(2) The recovery of Cu_3Au at Stage I or II is nearly equal to that of Cu.

(3) The migration of Stage I defects or Stage II ones in Cu_3Au is not effective in the ordering.

(4) The recovery of Cu_3Au at Stage III is much larger than that of Cu.

(5) The migration of Stage III defects in Cu_3Au brings about the active ordering.

Reference

1) M. W. Thompson : "Defects and Radiation Damage in Metals", Cambridge Univ. Press, Chap. 6 (1969).

9-3. Electron Microscopic Observation on Helium Bubbles in Aluminum Irradiated by Alpha Particles

R. R. Hasiguti, E. Yagi, H. Sakairi,
M. Kobayashi, and T. Karasawa

Transmission electron microscopic observation of He bubbles in metals irradiated by alpha particles is being continued. The relations between bubbles and various lattice imperfections in pure alminum were summarized in the previous report. New relations were found by a subsequent observation, which are described below.

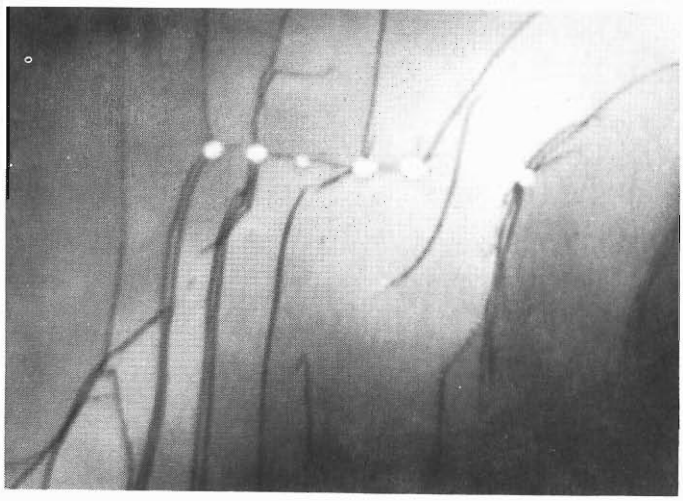

×13000

Fig. 1(a)

×20000

Fig. 1(b)

Fig. 1. Bubbles on dislocations in the specimen not heat-treated after irradiation.

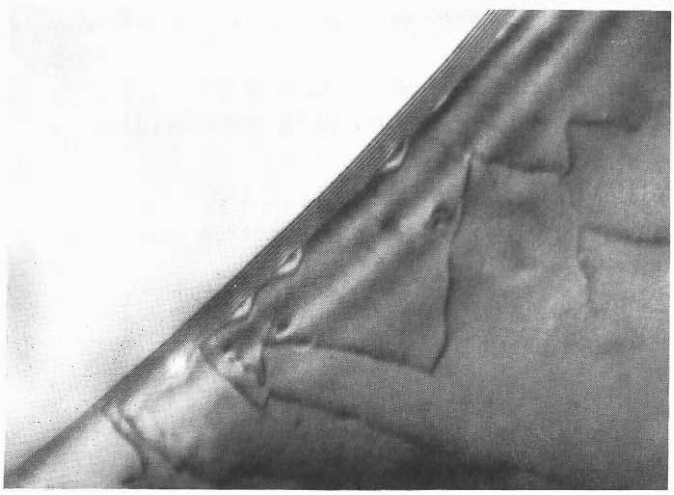

×13000

Fig. 2(a)

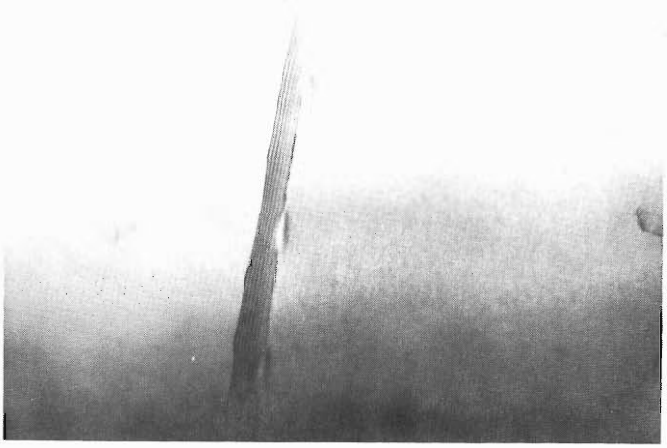

×13000

Fig. 2(b)

Fig. 2. Bubbles on tilt boundary in the specimen annealed at 400°C after irradiation.

(1) Bubble-dislocation interaction

No interaction between large visible bubbles and dislocations is observed previously. But an interaction between small invisible bubbles and dislocations was suggested by some facts. Later we found examples of bubble-dislocation interaction, some of which are shown in Fig. 1. They appear in specimens which are not heat-treated after irradiation, that is, they appear only at an early stage of bubble growth. This feature is interpreted in terms of weak interaction between bubbles and dislocations, which release the dislocations from the trapping by bubbles during thermal annealing processes.

(2) Bubble-boundary interaction

In previous observation the bubbles generated at grain boundaries disappear above 300°C. But recent experiment shows some bubbles on boundaries can survive up to 400°C. Examples are shown in Fig. 2. It is a distinctive feature that they are only such bubbles which are generated on tilt boundaries. The reason for this is not clear.

10. RI PRODUCTION AND ITS APPLICATIONS

10-1. Preparation of ^{90}Nb as a Positron Source

N. Shiotani, S. Ambe,
T. Okada, and T. Karasawa

^{90}Nb is one of useful positron sources which can be produced by a cyclotron, because

a) β^+ decay is over 50 % of the disintegration
b) half-life is suitable for bombarding time,
c) natural zirconium can be used as the target.

(1) Excitation curve

Natural zirconium plates (12.9 mg/cm^2 thick) were stacked and bombarded with 22 MeV deuterons. The integrated beam current was 168 μ coulomb.

The measured excitation curve for the formation of ^{90}Nb is shown in Fig. 1. The thick target yield was 16 mCi/μA.h for 22 MeV deuterons.

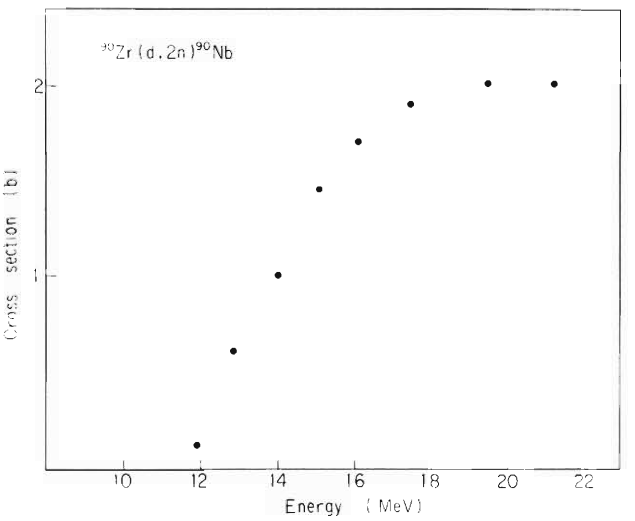

Fig. 1. Excitation curve for ^{90}Zr(d, 2n) ^{90}Nb.

(2) Chemical separation

A zirconium foil (500 mg) of natural isotopic abundance was bombarded with 22 MeV deuterons. The irradiated foil was dissolved in 4 mℓ of 12 M hydrofluoric acid. The solution was concentrated by evaporation to about 0.5 mℓ. Most of zirconium was precipitated by the addition of 5 mℓ of 10 M hydrochloric acid to the solution and removed by filtration. The filtrate was placed on the top of a column of an anion exchange resin, Diaion SA 100, 100 $\sim$ 200 mesh, 8 mm$\phi\times$ 50 mm, pretreated with 9 M hydrochloric acid. After zirconium was eluted with 100 mℓ of 7 M hydrochloric acid, carrier-free ^{90}Nb was eluted with 40 mℓ of 4 M hydrochloric acid. The effluent containing ^{90}Nb was evaporated to a drop. A ^{90}Nb positron source was obtained by

evaporation of the droplet in a small platinum planchet. Absence of significant radiochemical impurity other than niobium isotopes was confirmed by γ-ray spectrometry with a Ge-semiconductor detector. The amount of zirconium in the niobium fraction was found to be about 10 γ spectrophotometrically.

The time to obtain an about 350 mCi source for our positron annihilation experiment is about 10 h, 2 h for setting the target on the best position in the cyclotron, 1 h for bombarding the target with 25$\sim$30μA beam current and 6 h for chemical separation.

The source thus obtained gives us the rate of about 200 c.p.m. coincident γ-ray at the beginning of the angular correlation experiment. This rate is not poor compared with the rate using available positron sources such as ^{58}Co or ^{22}Na or ^{64}Cu.

10-2. The Separation of Carrier-free ^{203}Pb from a Deuteron-Bombarded Thallium Target

M. Inarida and A. Shimamura

The 52 h ^{203}Pb, which is useful as a chemical and medical tracer, was produced by a ^{203}Tl (d, 2n) ^{203}Pb reaction with a thallium-oxide target. This report describes the radiochemical isolation of carrier-free ^{203}Pb from a thallium target which had been bombarded with 16 MeV deuterons from the IPCR cyclotron.

The Tl_2O_3 target was wrapped in 10 μm-thick alminum foil and placed on a water-cooled brass target holder. The target was then bombarded with 16 MeV deuterons through a window of 50 μm-thick aluminum foil for 30 min at a beam intensity of 1 ~ 2 μA. After the bombardment, the target was dissolved in 10 mℓ of a 12 M hydrochloric acid solution. The method of separating the carrier-free ^{203}Pb from the thallium target is shown below :

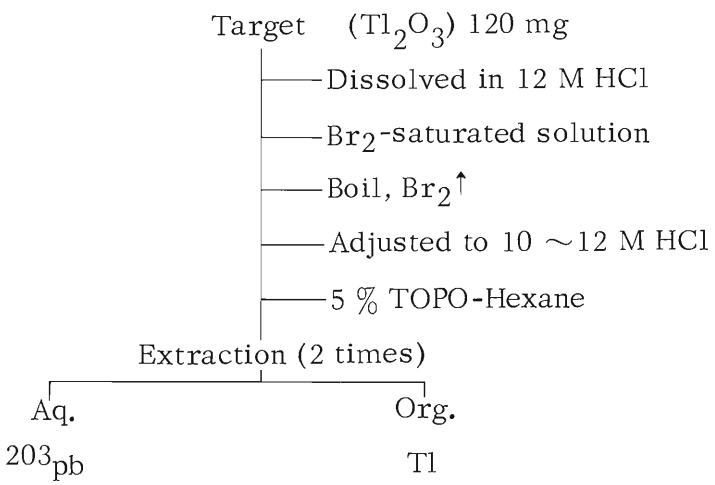

The radiochemical purity of the ^{203}Pb thus separated was checked by measuring its gamma spectrum and decay curve ; it was found to be higher than 99 %. The activity of the ^{203}Pb produced was about 2 mCi. The radiochemical yield was about 99 %, and the time for separation was 7 min.

10-3. The Separation of Carrier-free ^{133m}Ba from a Deuteron-Bombarded Cesium Target

M. Inarida and A. Shimamura

The deuteron bombardment of cesium produces $^{133, 133m}$Ba by the following nuclear reactions : ^{133}Cs(d, 2n) ^{133,133m}Ba, ^{133}Cs(d, p) $^{134, 134m}$Cs, ^{133}Cs(d, α) ^{131}Xe. This report describes the radio-chemical isolation of carrier-free ^{133m}Ba from a cesium target bombarded with 16 MeV deuteron particles.

The CsCl target was wrapped in 15 μm-thick aluminium foil and clamped to a water-cooled brass target holder attached to the IPCR cyclotron. The target was bombarded with 16 MeV deuterons for 30 min at a beam intensity of 2 $\sim$ 3 μA through a window of 50 μm-thick aluminium foil. After the bombardment, a 200-mg portion of the target was dissolved in 10 mℓ of a hydrochloric acid solution at pH3 (1 % cupferron solution). The method of separating carrier-free ^{133m}Ba from the cesium target is shown schematically :

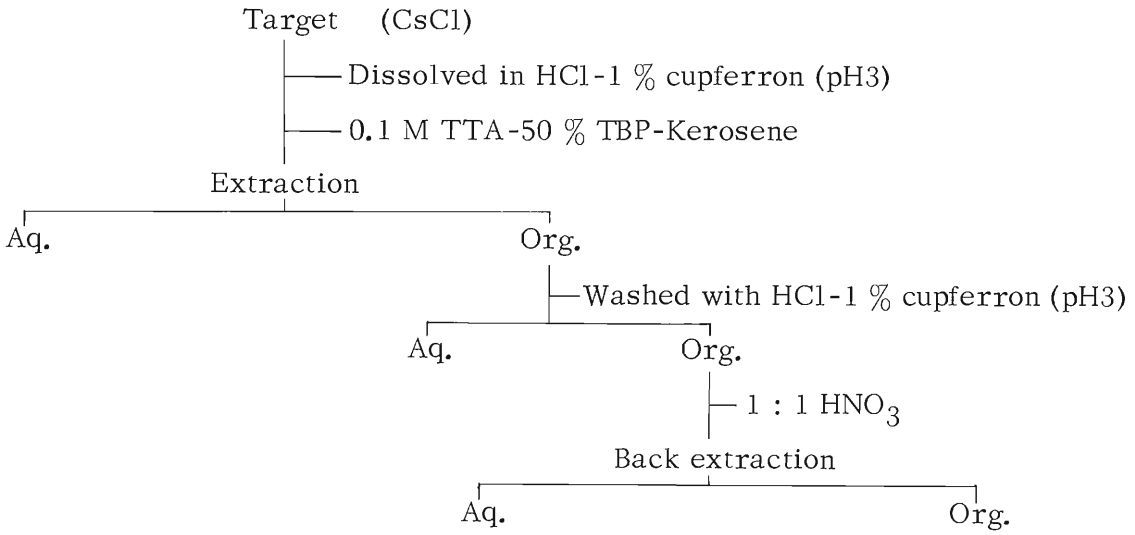

$^{133, 133m}$Ba

The procedure involves simple and rapid manipulation and can be completed in less than 15 minutes ; the time needed is important when the half-lives of the isotopes are short.

The activity in the carrier-free barium fraction was identified by its half-life (39 h) and by means of γ-ray spectrometry.

10-4. Production of Medical Use Isotopes

T. Nozaki, T. Karasawa, M. Okano
M. Inarida, and A. Shimamura

Since May 1970 we have begun to offer ^{18}F and ^{52}Fe to medical workers. Now ^{111}In can also be produced, and in near future ^{67}Ga, ^{87}Y - ^{87m}Sr, ^{203}Pb, and ^{28}Mg will rank among medical use isotopes made by the IPCR Cyclotron. The main production reactions, bombarding energies and practical yields are tabulated below. The isotopes have ever been used in the Cancer Research Institute, the Medical Department of Chiba University, the Medical Department of University of Tokyo, the National Cancer Centre and the Postal Services Ministry Hospital.

^{18}F is produced by the ^{3}He bombardment of oxygen gas[1] streaming from a cylinder through a Teflon bombardment box (6 cm diameter, 40 cm length) and a Teflon absorption tube (1.5 cm diameter, 10 cm length) which is filled with glass beads (3.5 mm diameter) coated as thinly as possible by NaOH in order to absorb the ^{18}F from the stream. Usually in 30 min, slightly over 10 mCi of ^{18}F accumulates in the absorption tube, which is then removed from the bombardment assembly and a new tube is attached to it. The ^{18}F with the tube is offered to the user, who elutes the ^{18}F with a small amount of water and neutralizes the solution prior to injection. This treatment is very simple and gives completely pure ^{18}F with negligible loss in the elution. Practical procedures for the preparation of millicurie amounts of various kinds of ^{18}F-labelled compounds, especially ^{18}F-steroids, have been under study.[2),3)]

Our production method for ^{52}Fe has been described.[3),4)] The remote chemical procedure has recently been improved and the separation has become easier and faster (within 1 h). In order to obtain really carrier-free ^{52}Fe, the chromium target must be free of iron. Efforts are now being made to obtain the iron-free target.

^{111}In is obtained as follows : (1) the bombarded silver plate is dissolved in warm HNO_3 and the solution is brought to close dryness ; (2) ^{111}In is extracted into methylisobutyl ketone as a thiocyanate complex and back-extracted into a dilute acid, and (3) further purified by an anion exchange column. The resultant solution is brought to dryness and supplied to the user.

Table 1. Radio isotopes produced by IPCR Cyclotron for medical use.

RI	Half life	Main production reaction	Bombardment energy (MeV)	Practical yield*
F-18	1.8 h	^{16}O (^{3}He, p) ^{18}F	14	0.4 mCi/min
Mg-28	21.2 h	^{27}Al (t, 2p) ^{28}Mg	>24	50 μCi/h
		^{26}Mg (t, p) ^{28}Mg	20	
Fe-52	8.2 h	^{52}Cr (^{3}He, 3n) ^{52}Fe	42	1 mCi/h
Ga-67	78 h	^{66}Zn (d, n) ^{67}Ga	22	3 mCi/h
In-111	68h	^{109}Ag (α, 2n) ^{111}In	42	5 mCi/h
Pb-203	52.1 h	^{203}Tl (d, 2n) ^{203}Pb	22	5 mCi/h

* For the target materical of the natural isotopic composition.

References

1) T. Nozaki : IPCR Cyclotron Progr. Rep., 1, 77 (1967).
2) T. Nozaki, A. Shimamura, and T. Karasawa : ibid., 2, 156 (1968).
3) T. Nozaki and A. Shimamura : ibid., 3, 114 (1969).
4) F. Akiha, T. Takeda, T. Aburai, T. Nozaki, and Y. Murakami : Radiochim. Acta (in press).

11. RADIATION MONITORING

11-1. Health Physics

K. Koda, I. Sakamoto, and I. Usuba

The results of measurements made during a period from Apr. 1969 to Mar. 1970 on the residual activities of the machine and the contamination on the floor etc. of the cyclotron room and the personnel monitoring are described.

(1) Residual activities

The surface dose rate at various parts of the machine due to residual activities showed a slow year-by-year increase as indicated in Table 1. Species of accelerated particles, their energies and the time of measurements after machine shutdown seem to have little effect on the dose rate values, and the fact shows that the residual activities would mainly be of nuclides of long half life accumulated during about 4 years' operation.

(2) Air and surface contamination

The radioactive contamination of the air in the cyclotron room was measured by absorption with charcoal placed on the several fixed places about 2 m in height. From its distribution the source of contamination was found to be the dees taken out from the acceleration chamber. The highest value has been obtained in 2 or 3 days after taking out of the dees.

Table 1. Fluctuation of surface dose rate with time at various parts of the machine. (mR/h)

Date	6/12 '68	8/5 '68	2/4 '69	4/17 '69	1/8 '70
Bellow Baffle box	800	600	6 000	8 000	10 000
BE magnet	250	20	1 500	2 500	500
Q_0 magnet	1 000	90	1 500	1 000	70
Helmholtx coil	30	20	35	40	25
Gate box	20	–	30	15	–
Time of measurement after machine shutdown	2 h	4 days	1 day	2 days	13 days

The surface contamination on the floor of the cyclotron room was kept to be about 10^{-5} $\mu Ci/cm^2$.

From the samples taken from the drainage in the cyclotron area, trace of ^{65}Zn which was clearly induced from the parts of the cyclotron was identified by the gamma-ray spectrometry.

(3) Personnel monitoring

The values of total dose in the present period of all cyclotron workers issued with the gamma-neutron film badge are shown in Table 2. Average annual dose per person per year is 318 mrem which is about two fifth of the value in the previous period.

As a result of the previous measurements with the body counter, concentration of ^{65}Zn was found in several parts of body of the workers, i.e. head, thorax and abdomen. The fact suggested a possibility of internal exposure of gonad. An experiment made with rats and rabbits, which inhaled ^{65}Zn-contaminated dust from the cyclotron, has shown, however, no concentration of ^{65}Zn in particular organs except lung. It may be concluded that the apparent concentration in the workers' body was due to local surface contamination especially toward hairs.

Table 2. Accumulated dose distribution of the staffs.
From Apr. 1969 to Mar. 1970.

Group Dose (mrem)	10 ~ 100	101 ~ 300	301 ~ 1,000	1001
Operators		1	4	1
Nuclear physicists	6	11	7	
Accelerator physicists		2	3	1
Nuclear chemists		2	2	
Radiochemists	3	1		
Health physicists	2			

Average does person per year : 318 mrem.
Maximum annual does : 1290 mrem.

12. LIST OF PUBLICATIONS

1) S. Yamaji and C. L. Lin : "The Effect of the Interaction Range on the Calculated Cross Section of the Two Nucleon Transfer Reaction" (in Japanese), Genshikaku Kenkyu, 14, 366 (1969).

2) S. Ambe, N. Shiotani, T. Okada and T. Karasawa : "Preparation of RI Sources by the IPCR Cyclotron for the Study of Solid Physics, (I)" (in Japanese), Reports of I. P. C. R., 46, 15 (1970).

3) S. Yamaji and S. Yoshida : "Calculation of the Heavy Particle Stripping Process in the Reaction $^{11}B(d, n)^{12}C$", Progr. Theor. Phys., 44, 125 (1970).

4) S. Kitayama, K. Igarashi, T. Karasawa, and A. Matsuyama : "LET Effects in Micrococcus radiodurans Irradiated with Alpha Particles in the Liquid Phase", Agr. Biol. Chem., 34, 1346 (1970).

5) Y. Ando, E. Fukada, Y. Okazawa, S. Kitayama, and A. Matsuyama : "Non-Newtonian Viscosity of γ-irradiated DNA", Rep. Progr. Polymer Phys. Japan, 8, 525 (1970).

6) M. Imamura, M. Matsui, and T. Karasawa : "Radiation Chemical Studies with Cyclotron Beams. II. The Radiolysis of an Aqueous Ferrous Ammonium Sulfate Solution with Carbon - and Nitrogen-Ion Radiations", Bull. Chem. Soc. Japan, 43, 2745 (1970).

7) M. Matsui, H. Seki, T. Karasawa, and M.Imamura : "Radiation Chemical Studies with Cyclotron Beams. I. Fricke Solutions", J. Nucl. Sci. Tech., 7, 97 (1970).

8) Y. Miyazawa, T. Tonuma, I. Kohno, S. Nakajima, T. Inoue, A. Shimamura, K. Yoshida, and T. Karasawa : "Acceleration of Multicharged Heavy Ions in IPCR (Riken) Ordinary 160 cm Cyclotron", Japan. J. Appl. Phys., 9, 532 (1970).

9) T. Tonuma, Y. Miyazawa, T. Karasawa, and I. Kohno : "Charge Exchange of Carbon and Nitrogen Ions in Nitrogen Gas", Japan. J. Appl. Phys., 9, 1306 (1970).

10) S. Kobayashi, S.Motonaga, Y. Chiba, K. Katori, A. Stricker, T. Fujisawa, and T. Wada : "Spin Flip in the Inelastic Scattering of Protons from ^{12}C at Energies around 13.1 MeV Resonance", J. Phys. Soc. Japan, 29, 1 (1970).

11) F. Ambe and N. Saito : "Chemical Effects of Neutron-Induced Nuclear Reactions in Halates and Related Compounds III, The (n, γ) and (n, 2n) Reactions in Iodates", Radiochim. Acta, 13, 105 (1970).

12) T. Nozaki, Y. Yatsurugi, and N. Akiyama: "Concentration and Behavior of Carbon in Semiconductor Silicon", J. Electrochem. Soc., 117, 1566 (1970).

13) T. Nozaki, Y. Yatsurugi, and N. Akiyama: "Charged Particle Activation Analysis for Carbon, Nitrogen and Oxygen in Semiconductor Silicon", J. Radioanal. Chem., 4, 87 (1970).

14) S. Nagamiya, T. Katou, T. Nomura, and T. Yamazaki : "Effective Spin and Orbital Magnetism of the Proton Studies from the Magnetic Moments of the 8^+ States of ^{90}Zr and ^{92}Mo", Phys. Letters, 33B, 574 (1970).

15) T. Yamazaki, T. Nomura, T. Katou, T. Inamura, A. Hashizume, and Y. Tendow : "Core Polarization Effect on the Magnetic Moment of the $(h^2_{9/2})$ 8^+ State of ^{210}Po", Phys. Rev. Letters, 24, 317 (1970).

16) T. Yamazaki, T. Nomura, S. Nagamiya, and T. Katou : "Aromalous Orbital Magnetism of Proton Deduced from the Magnetic Moment of the 11^- State of ^{210}Po", Phys. Rev. Letters, 25, 547 (1970).

17) N. Nakanishi, Y. Chiba, Y. Awaya, and K. Matsuda :"Elastic Scattering of ^3He Particles on Ca at Five Incident Energies between 18.8 and 39.3 MeV", Nucl. Phys., A140, 417 (1970).

18) S. Nagamiya, T. Nomura, and T. Yamazaki : "Stroboscopic Determination of the Magnetic Moment of the 8^+ Isomeric State of ^{208}Po", Nucl. Phys. (to be published).

19) T. Inamura, A. Hashizume, T. Katou, and Y. Tendow : "Identification of Neutron Deficient Isotopes ^{100}Ag and ^{104}In", J. Phys. Soc. Japan, 30, No. 3 (1971). (to be published)

20) I. Kohno, S. Nakajima, T. Tonuma, and M. Odera : "Elastic Scattering of Carbon and Nitrogen Ions", J. Phys. Soc. Japan, 30, No. 4 (1971) . (to be published)

13. LIST OF PERSONNEL

IPCR Cyclotron Administration Committee

KUMAGAI Hiroo 熊谷寛夫 (Chairman)
HAMADA Tatsuji 浜田達二
IMAMURA Masashi 今村昌
KARASAWA Takashi 唐沢孝
MATSUDA Kazuhisa 松田一久
MATSUYAMA Akira 松山晃
NOZAKI Tadashi 野崎正
SAITO Nobufusa 斎藤信房
SAKAIRI Hideo 坂入英雄
SEKIZAWA Hisashi 関沢尚

Managers of Users Group

HAMADA Tatsuji 浜田達二
NOZAKI Tadashi 野崎正
ODERA Masatoshi 小寺正俊

IPCR Cyclotron Operating Personnel

Management

KARASAWA Takashi 唐沢孝
KOHNO Isao 河野功
MIYAZAWA Yoshitoshi 宮沢佳敏
MOTONAGA Shoshichi 元永昭七
ODERA Masatoshi 小寺正俊

Operation

FUJITA Shin 藤田新
IKEGAMI Kumio 池上九三男
KAGEYAMA Tadashi 影山正
KOHARA Shigeo 小原重夫
NAKAJIMA Hisao 中島尚雄
OGIWARA Kiyoshi 荻原清
TERAJIMA Osamu 寺島為
YOSHIDA Kisaku 吉田喜作

Scientific and Engineering Personnel

Cyclotron Lab.

KUMAGAI Hiroo 熊谷寛夫
CHIBA Yoshiaki 千葉好明
FUJISAWA Takashi 藤沢高志
FUJITA Jiro 藤田二郎
HEMMI Masatake 逸見政武
INAMURA Takashi 稲村卓
INOUE Toshihiko 井上敏彦
KAMITSUBO Hiromichi 上坪宏道
KARASAWA Takashi 唐沢孝
KOHNO Isao 河野功
KUSUNO Sadao 楠野貞夫
MATSUDA Kazuhisa 松田一久
MIYAZAWA Yoshitoshi 宮沢佳敏
MOTONAGA Shoshichi 元永昭七
NAGAMIYA Shoji 永宮正治
NAKAJIMA Shunji 中島諄二
NAKANISHI Noriyoshi 中西紀喜
ODERA Masatoshi 小寺正俊
SHIMAMURA Akira 島村晃
TAKEDA Shigeru 竹田繁
TONUMA Tadao 戸沼正雄
YAMAJI Shuhei 山路修平
YAMAZAKI Yoshishige 山崎良成
YOSHIDA Fusako 吉田房子
WADA Takeshi 和田雄

(Visitors)

FUJITA Junichi 藤田純一 (Inst. for Nuclear Study, Univ. of Tokyo)
KATORI Kenji 鹿取謙二 (Tokyo Univ. of Educ.)
KOBAYASHI Shinsaku 小林晨作 (Inst. for Solid State Phys.)
NOMURA Toru 野村亨 (Univ. of Tokyo)
STRICKER Andreas (Univ. of Basel)
YAMAZAKI Toshimitsu 山崎敏光 (Univ. of Tokyo)

Radiation Lab.

AWAYA Yohko 粟屋容子
HAMADA Tatsuji 浜田達二
HASHIZUME Akira 橋爪朗
KATOU Takeo 加藤武雄
KONNO Satoshi 金野智
OKANO Masaharu 岡野真治
TAKAHASHI Tan 高橋旦
TENDOW Yoshihiko 天道芳彦

Nuclear Analytical Chemistry Lab.

AMBE Fumitoshi 安部文敏
AMBE Shizuko 安部静子
ARATANI Michi 荒谷美智
INARIDA Mariko 稲荷田萬里子
NOZAKI Tadashi 野崎正
SAITO Nobufusa 斎藤信房

(Visitors)

AKIYAMA Nobuyuki 秋山信之 (Komatsu Electronic Metals Co., Ltd.)
SHOJI Hitoshi 庄司準 (Tokyo Univ. of Educ.)
TAKEDA Masuo 竹田満洲雄 (Univ. of Tokyo)
YATSURUGI Yoshifumi 八剣吉文 (Komatsu Electronic Metals Co., Ltd.)

Radiobiology Lab.

ASANO Yoshio 朝野芳雄
IGARASHI Kazui 五十嵐一戊
KITAYAMA Shigeru 北山滋
MATSUYAMA Akira 松山晃

Radiation Chemistry Lab.

IMAMURA Masashi 今村昌
MATSUI Masao 松井正夫

Metal Physics Lab.

HASIGUTI R. Ryukiti 橋口隆吉
SAKAIRI Hideo 坂入英雄
SHIOTANI Nobuhiro 塩谷亘弘
YAGI Eiichi 八木栄一

(Visitors)

AOTA Kenichi 青田健一 (Univ. of Tokyo)
ISHINO Shiori 石野栞 (Univ. of Tokyo)
MISHIMA Yoshitsugu 三島良績 (Univ. of Tokyo)
SHIRAISHI Haruki 白石春樹 (Nat. Res. Inst. for Metals)
TANI Satoshi 谷賢 (Univ. of Tokyo)

Magnetic Materials Lab.

OKADA Takuya 岡田卓也
OKAMOTO Shoichi 岡本祥一
SEKIZAWA Hisashi 関沢 尚

Radiation Monitors

KODA Kugao 甲田陸男
SAKAMOTO Ichiro 坂本一郎
USUBA Isao 薄葉 勲

(Editors of the Progress Report)

IMAMURA Masashi 今村 昌
MATSUDA Kazuhisa 松田一久
NOZAKI Tadashi 野崎 正
SEKIZAWA Hisashi 関沢 尚

AUTHOR INDEX

IPCR Cyclotron Progress Report 1970

理化学研究所サイクロトロン年次報告 第4巻(1970)

印　刷　昭和46年（1971）3月25日
発　行　昭和46年（1971）3月30日
発行者　理化学研究所
　　代表者　星　野　敏　雄
　　351 埼玉県和光市広沢2番1号
　　電話（0484）62－1111
編集者　理化学研究所サイクロトロン運営委員会
　　委員長　熊　谷　寛　夫
印刷所　丸星印刷株式会社
　　101　東京都千代田区
　　神田神保町1丁目42番地

定価 2,000円

理化学研究所

埼玉県　和光市　広沢